TECHNISCHE UNIVERSITÄT MÜNCHEN

Lehrstuhl für Flugsystemdynamik

Precise Surface Aided Navigation

Dipl.-Ing. Philip Spiegel

Vollständiger Abdruck der von der Fakultät für Maschinenwesen der Technischen Universität München zur Erlangung des akademischen Grades eines

Doktor-Ingenieurs

genehmigten Dissertation.

Vorsitzender:	Prof. Dr.-Ing. Harald Klein
Prüfer der Dissertation:	1. Prof. Dr.-Ing. Florian Holzapfel
	2. Prof. Dr.-Ing. Peter Hecker

Die Dissertation wurde am 29.05.2017 bei der Technischen Universität München eingereicht und durch die Fakultät für Maschinenwesen am 12.03.2018 angenommen.

Preface

> "TERCOM development has been and continues to be an iterative process and at times appears to be more of an art than a science."
>
> J. P. Golden (1980) [45] - 22 years after Chance-Vought originally conceived TERCOM

This thesis was created during my employment at the Institute of Flight System Dynamics at the Technical University of Munich.

I want to thank Prof. Dr.-Ing. Florian Holzapfel for given me the opportunity to work at his institute and supporting this thesis in all respects. The work at the institute was very diversified including deep theoretical topics as well as their practical realization. The chance to assume responsibility for projects and infrastructure in my early work live was, apart from the scientific work, an outstanding experience and will strongly benefit my further activities.

My special thanks go to Dr.-Ing. Johann Dambeck for always having the patience to discuss all related topics of my thesis during the years. He always had an open ear for discussions and invested a huge amount of time in supporting me and the navigation group at the institute.

MBDA Germany supported this thesis and my employment at the institute with the founding of the first years within a cooperation, therefore I am thankful.

I greatly appreciated the helpful and positive working atmosphere at the institute. Especially the interesting debates at the coffee table and the intensive trips to Wiener Neustadt will be remember. Thanks to the initial crew, as well as the second generation, of our room MW3615 for all kinds of technical discussions and especially for the off-topic talks.

I want to thank Prof. Dr. Alfred Schöttl for offering his help and supporting this thesis, especially in the final phase.

I'm very thankful for the continuous personal support of my life partner Verena and my parents Hans and Inge.

Munich, May 2017

Abstract

In this thesis, methods to improve the accuracy and robustness of terrain aided navigation systems are addressed. First, the functional principles of the three surface-ranging sensor types: altimeters, range-scanning and range-imaging sensors are analyzed. A sophisticated simulation model, covering geometric, beam-shape and signal propagation effects, is developed and validated with recorded real data. To detect and eliminate erroneous altimeter measurements, a validity assessment concept is introduced, as well as a compensation algorithm for erroneous slant range measurements. The compensated height above ground measurement is applied as vertical aiding in an integrated navigation system. The exploitation of the surface's information content is used to enhance conventional matching-based surface navigation systems. A closed-loop compensation method using the slant-range compensation algorithm in surface aided navigation brings further improvements, as well as the extension by a linear drift estimation and a multi-beam sensor setup. For unknown or fast changing surfaces, a dead-reckoning approach to surface aided navigation using overlapping measurements is introduced to provide a position drift aiding. The flight test instrumentation on the Institute of Flight System Dynamic's research aircraft including a suite of reference sensors and an in-flight visualization is introduced and explained. The thesis is completed with a simulation study and a real data evaluation of the introduced methods.

In dieser Arbeit werden Methoden zur Verbesserung der Genauigkeit und Robustheit von Geländenavigationssystemen behandelt. Als Erstes werden die Funktionsprinzipien der drei abstandsgebenden Sensortypen: Höhenmesser, entfernungsabtastende und entfernungsabbildende Sensoren analysiert. Ein detailliertes Simulationsmodell, das geometrische, Strahlform- und Signalausbreitungseffekte abdeckt, wird entwickelt und mit aufgezeichneten realen Daten validiert. Zur Erkennung und Beseitigung fehlerhafter Höhenmessungen wird ein Bewertungskonzept zur Messgültigkeit eingeführt, sowie ein Kompensationsalgorithmus für fehlerhafte Schrägmessungen vorgestellt. Die kompensierte Höhe über Grund wird als vertikale Stützung in einem integrierten Navigationssystem angewendet. Eine Methode zur gesteigerten Ausnutzung des Oberflächeninformationsinhalts wird verwendet um konventionelle geländeabgleichsbasierte Navigationssysteme zu verbessern. Durch eine integrierte Kompensationsmethode, die die Schrägmessungskompensation in der Geländenabgleichsalgorithmik beinhaltet, kann eine weitere Verbesserung erreicht werden, wie auch durch die Erweiterung des Algorithmus durch eine lineare Driftschätzung und einen Mehrstrahlsensoraufbau. Bei unbekannten oder schnell verändernden Erdoberflächen wird ein Koppelnavigations-Ansatz zur Geländenavigation, basierend auf überlappenden Messungen eingeführt, um einen inertialen Positionsdrift zu reduzieren. Die Flugtestinstrumentierung des Forschungsflugzeug des Lehrstuhls für Flugsystemdynamik, bestehend aus einem Datenaufzeichnungsgerät, verschiedenen Referenzsensoren und einer Visualisierung, wird vorgestellt und erläutert. Die Arbeit wird mit einer Simulation der vorgestellten Methoden sowie einer Echtdatenauswertung abgeschlossen.

Contents

Nomenclature

Acronyms

ADC	Air Data Computer
AIL	Aircraft-in-the-Loop
APC	Automation PC
ASTER	Advanced Spaceborne Thermal Emission and Reflection Radiometer
ATC	Air Traffic Control
B&R	Bernecker & Rainer
CAN	Controller Area Network
CRC	Cyclic Redundancy Check
CW	Continuous Wave
DBF	Digital Beam Forming
DEM	Digital Elevation Map
DRSAN	Dead-Reckoning Surface Aided Navigation
DSM	Digital Surface Model
DTED	Digital Terrain Elevation Data
DTM	Digital Terrain Model
ECEF	Earth-Centered Earth-Fixed
EFCS	Experimental Flight Control System
EGM08	Earth Gravitational Model 2008
FCC	Flight Control Computer
FDM	Flight Dynamic Model
FL	Flight Level
FMCW	Frequency Modulated Continuous Wave
FTE	Flight Test Engineer
FTI	Flight Test Instrumentation
GBAS	Ground Based Augmentation System
GNSS	Global Navigation Satellite System
GPS	Global Positioning System
GPWS	Ground Proximity Warning System
HIL	Hardware in the Loop
HPBW	Half Power Beam Width
ICN	Intelligent Controlled Node
IFSAR	Interferometric Synthetic Aperture Radar

ILS	Instrument Landing System
IMU	Inertial Measurement Unit
InGaAs	Indium Gallium Arsenide
INS	Inertial Navigation System
KF	Kalman-Filter
Ladar	Laser Detection and Ranging
Laser	Light Amplification by Stimulated Emission of Radiation
Lidar	Light Detection and Ranging
LOAT	Local Oscillator Automatic Tuning
LPP	Laser Position Pickup
MEMS	Micro-Electro-Mechanical System
MSL	Mean Sea Level
NEXTMap	Intermap NEXTMap
PDU	Power Distribution Unit
PFD	Primary Flight Display
PMD	Photonic Mixing Device
PPSAN	Precise Positioning Surface Aided Navigation
PVT	Position-Velocity-Time
QNE	Global Altimeter Pressure Setting
QNH	Local Altimeter Pressure Setting
Radar	Radio Detection and Ranging
RAOA	Radio Altimeter Operating Area
RLG	Ring Laser Gyroscope
RMS	Root Mean Square
SAN	Surface Aided Navigation
SDA	Strapdown Algorithm
SoW	Seconds-of-Week
SRTM	Shuttle Radar Topography Mission
SSB	Single Sideband
TA	Transition Altitude
TAN	Terrain Aided Navigation
TanDEM-X	TerraSAR-X add-on for Digital Elevation Measurement
TerraSAR-X	Terra Synthetic Aperture Radar - X (Band)
TL	Transition Level
ToF	Time-of-Flight
TSS	Total System Simulation
UART	Universal Asynchronous Receiver Transmitter
UAV	Unmanned Aerial Vehicle
UDP	User Datagram Protocol
VSAN	Vertical Surface Aided Navigation
WGS84	World Geodetic System 1984

Coordinate Systems

b body fixed frame, with
- x-axis pointing towards the nose of the aircraft
- y-axis pointing towards starboard wing
- z-axis pointing down within aircraft's symmetry plane

e ECEF frame, with Earth's center as origin,
- x-axis pointing towards Greenwich meridian
- y-axis perpendicular to x-axis
- z-axis along Earth's rotation axis

i Inertial frame, unrotated coordinate system with Earth's center as origin

m measurement frame with sensor center as origin, z-axis pointing in measurement direction

n navigation frame with x-axis pointing to North, y-axis pointing to East and z-axis pointing downwards

s sensor frame with origin in the sensor center, tilted by the mounting angle

Symbols

$A_{rx,eff}$	Effective antenna aperture size
GM	Earth's gravitational constant
G_{rx}	Receiver antenna gain
G_{tx}	Transmitter antenna gain
$\mathbf{H}$	Kalman filter measurement matrix
$\mathbf{K}$	Kalman filter gain matrix
$P_{rx/tx}$	Receive/transmit power
$\mathbf{P}$	Covariance matrix
S_{target}	Power density at the target
T_p	Pulse duration
ΔT_m	Modulation duration
Δf_m	Modulation frequency ramp
$\boldsymbol{\lambda}(P)$	WGS84 position vector
$\boldsymbol{v}_n$	Velocity in navigation frame
$\breve{q}_{nb}$	Quaternion representation of the Euler angles
$\lambda(P)$	WGS84 longitude
$\mathbf{M}$	SAN matching matrix
$\mathbf{R}_{xy}$	Rotation matrix from y-frame to x-frame
$\mathbf{d}_m$	Distance measurement in m-frame
$\mathbf{x}_b(S)$	Sensor lever arm
$\mathbf{x}_e(P)$	Cartesian position vector
ω	Earth's angular velocity
$\phi(P)$	WGS84 latitude
σ	Radar cross section
τ	Signal runtime
a	Semi-major axis
c	Speed of light
f_b	Beat frequency
f_c	Center frequency
f_d	Doppler frequency
f_{if}	Intermediate frequency
f_{lo}	Local oscillator frequency
f	Ellipsoidal flattening
$h(P)$	WGS84 height
h_{agl}	Height above ground level
h_{geoid}	height geoid
$h_{msl}(P)$	height MSL
h_{topo}	Topographic height in reference to WGS84
h_{undul}	Undulation height
l	Free-space damping
$f_{rx/tx}$	Receive/transmit frequency
$s_{rx/tx}$	Receive/transmit signal

Chapter 1

Introduction

1.1 Motivation

The estimation of the platform velocity and attitude is as important for aerospace applications as the estimation of the position. These tasks are condensed in the discipline of navigation. Inertial Navigation Systems (INSs) have a long history beginning in the second world war. Gimballed gyrostabilized platforms were applied in the past and have been further developed to today's strapdown systems. These systems can provide an attitude, velocity and position estimation, but are however instable due to sensor measurement errors. For the long-term aiding of the instable INS navigation solution, Global Navigation Satellite Systems (GNSSs) have been established and are today's state-of-the-art when jamming or spoofing attacks are out of scope. The history of Terrain Aided Navigation (TAN) began long before Global Positioning System (GPS) was operational in 1985 and still is of great value in GNSS degraded or denied environments.

During the last few decades terrain aided navigation has been developed from an art to a science. Due to the advent of remote sensing the globally available digital terrain and surface models have been much improved, in global coverage, resolution and precision. Since about the turn of the millennium most research work has been dedicated to extend data fusion for multi-modal probability distributions (terrain ambiguity), non-Gaussian probability distributions (skewness, correlation and peakedness) and elongated probability distributions (terrain preference directions) by applying nonlinear Bayesian filtering theory. In contrast this thesis entitled "Precise Surface Aided Navigation" is dedicated to complement nonlinear filtering theory, by analyzing and exploiting the ranging altimeter transceiver principles of operation and the range-imaging measurement modes of operation.

The measurement of the height above ground is an obvious additional information for airborne vehicles for low-level flight or landing applications. There are various principles for height above ground measurements available today using Radio Detection and Ranging (Radar) and Light Amplification by Stimulated Emission of Radiation (Laser) based methods. Even multi-dimensional range-scanning and range-imaging sensors became available. The widespread established integration of surface-ranging sensors in all kinds of airborne platforms opens the opportunity for further applications.

The most common Radar altimeter application is the support in landing scenarios of civil aircraft. The surface-ranging sensor is applied in addition to an Instrument Landing System (ILS) under poor visibility conditions to ensure a safe landing. In military appli-

cations, surface-ranging sensors have been established to be already used as navigation aiding system, for terrain following flight modes or as Ground Proximity Warning System (GPWS). In general aviation aircraft, Radar altimeters are used as additional height indication for the pilot.
Due to the GNSS satellite operation principle, the accuracy of the height estimation is weaker than the accuracy of the horizontal position estimation. Therefore, the application of a height above ground measurement in combination with GNSS provides several benefits by directly aiding the weak height channel.
The application of surface-ranging sensors is thus in some sense complementary to the use of GNSS. The visible satellite constellation degrades for low-level flights due to terrain shadowing or tracking loss due to high attitude dynamics caused by bank-to-turn flight control laws. The surface-ranging sensor is in low-level flights right within its operating range. Additionally, the probability of spoofing or jamming of the GNSS signal increases with lower ground-clearance. The required energy for an intentional GNSS disturbance decreases in low-level flight which benefits an intentional disturbance as well as a beneficial angle between the antenna and aggressor.
The height above ground cannot always be measured easily and the measurement is error-prone. The measurement is affected by platform attitude dynamics, surface variations and signal propagation effects. These effects must be analyzed to understand the surface-ranging sensor measurements. The error characteristics influence the way how they are integrated and processed in a navigation system. A detailed sensor model is required which covers the mentioned effects for this analysis. The height aiding of INSs can be improved with a better understanding of the error characteristics of surface-ranging sensors. For several applications, the height above ground can directly be used, but for the data fusion with an absolute height, a Digital Elevation Map (DEM) is required.
Surface-ranging sensor measurements have a complementary availability compared to GNSSs. In GNSS denied environments, surface-ranging sensors can be used to compensate the outage when operating close enough to the terrain. The measurement of surface-ranging sensors cannot only be used for a vertical aiding of the navigation estimation, but also for a horizontal position aiding. TAN systems collect the height above ground measurements of the surface-ranging sensor and relates the measurement to an existing DEM. The position estimation can be obtained with a matching metric and can be provided to the INS as position aiding. Contrary to GNSS, this method is independent of external signals and can therefore not be jammed or spoofed easily. This independence also allows the usage as integrity monitor for other navigation components. Contrary to a camera-based navigation aid, TANs can provide a full position aiding without being dependent on the daylight or the weather conditions.
The accuracy of existing TAN systems is limited by the accuracy of the surface-ranging sensor measurements and the accuracy of the DEMs. Additionally, the elevation profile matching function requires powerful computers, which have not been available in the early development stages of these systems. Nowadays, precise DEMs with a high resolution and good vertical accuracies are available with a world-wide coverage. The computational power has increased dramatically in the last decades and opens the opportunity to improve TAN. With the better understanding of the measurement error characteristics obtained with the simulation model, novel approaches for TAN can be established.
In GNSS denied situations with a good DEM representation of the local surface, TAN can be used as navigation aiding system in low-level operation. Environments with fast

changing surfaces like dunes or cost areas affected by tides cannot be represented by a DEMs with a high accuracy. The water level of rivers, strongly seasonal depending fields with vegetations or forest are also hard to measure representatively. For aiding INSs in unknown surroundings, a dead-reckoning TAN can provide a completely self-sufficient aiding information.

1.2 Scope of Work

Three main problems are addressed in this thesis:

1. **How can surface-ranging sensors improve the height aiding of INS/GNSS**
   In flight situations with small ground clearance and degraded vertical GNSS precision, surface-ranging-based vertical aiding can significantly improve the height estimation. These situations can be a low-level flight of a fighter aircraft or the runway approach of a passenger aircraft for example. The conventional processing of an on-board altimeter in combination with a Digital Terrain Model (DTM) contributes to significant height errors above rough surfaces areas or in unleveled flight situations.

2. **How can the positioning accuracy of TAN algorithms be increased**
   The position aiding accuracy using a TAN system can not keep up with the positioning performance of GNSS due to altimeter and DEM errors. In situations with degraded GNSS or GNSS outages, TAN is a fall back option. The improvement of the aiding accuracy to offer a real alternative to GNSS is very desirable. The use of altimeters with their measurement errors above rough surface is thereby one error source which degrades the accuracy of TAN algorithms. Another problem is the processing of redundant surface information which degrades the estimation precision.

3. **How can a DEM independent TAN method be provided**
   TAN algorithms intrinsically dependent on DEM and thereby on their availability, resolution, accuracy and currentness. If one of these requirements is not fulfilled, for example the flight above unknown regions or above a fluted areas, TAN can not be applied. A dead-reckoning approach to TAN which is GNSS and DEM independent can be a suitable aiding to compensate short-term GNSS outages.

1.3 Contributions

The solution approaches of the adressed Surface Aided Navigation (SAN) problems are illustrated in figure 1.1 with their uses case scenarios and are annotated following.

Vertical aiding using an altimeter This aspect of the thesis aims to improve the accuracy of a vertical aiding of an INS/GNSS using an altimeter with a DEM. Therefore, the altimeter measurement characteristics are analyzed using a detailed simulation model. With the obtained knowledge by the simulation model, several methods to improve a vertical aiding of INSs with surface-ranging sensors are developed.

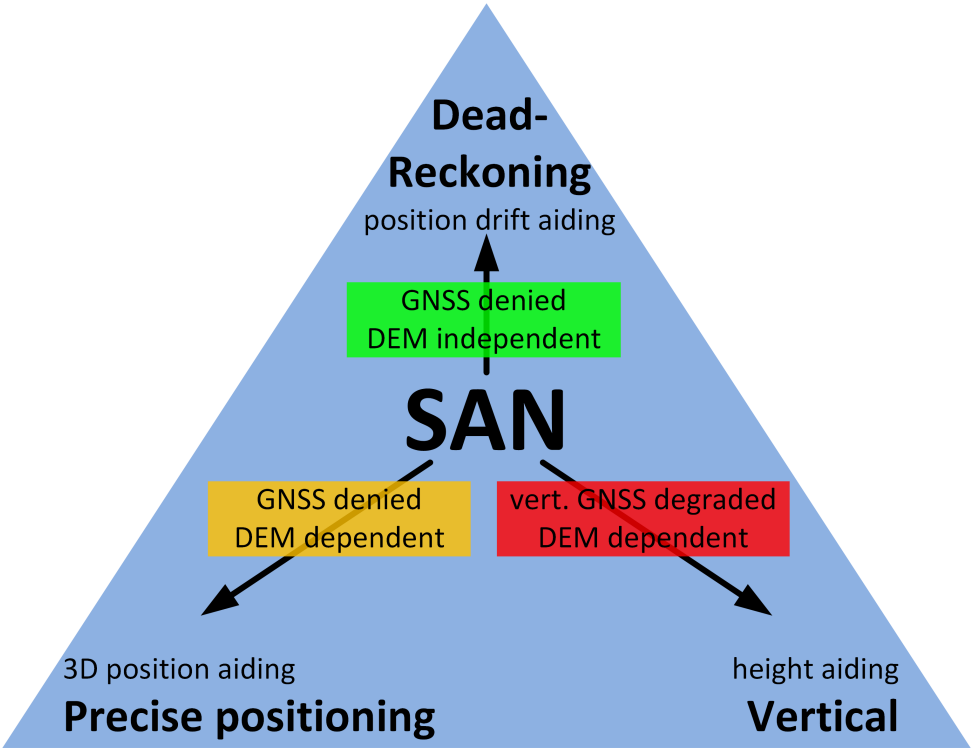

Figure 1.1: Vertical, precise positioning and dead-reckoning SAN

The simulation model not only covers geometric effects from the platform attitude dynamics and surface variations, but also signal propagation effects and the antenna beam-shape. The simulated results are compared to recorded altimeter flight test data to evaluate the simulation model. The model is afterwards used in simulations to identify the dominating error influences of surface-ranging sensors.
A method to determine the validity of sensor measurements based on the simulation model is introduced. The estimation of the measurement variance is also covered. The variance is derived for three cases, the height above ground variance, the slant range variance and the georeferenced footprint variance. The main dominating error influences, the platform attitude, the surface variations and the signal propagation effects are compensated using a compensation algorithm with three complexity levels. The compensation algorithm is applied on recorded real data, as well as on simulated data to show its performance in comparison to an uncompensated raw measurement. The aiding of an INS using the raw and the compensated altimeter measurement is compared in simulation. The introduced validity estimation and slant range compensation algorithms are also applied in a recorded flight test campaign.

Improvement of SAN The methods combined in this topic aim to improve the position estimation accuracy of batch-based TAN. Therefore, the methods developed for the vertical improvement are used and complemented by methods which aim to improve the horizontal positioning.
In this thesis, a grid-search based algorithm using a matching metric is applied to isolate the information problem of this application. The information content of the Earth's surface is analyzed to derive sampling policies for the surface-ranging sensors. A method

to exploit the information of the measurements is presented and combined with an efficient sampling of the surface. The consideration of the position error drift within the comparison algorithm is introduced and its benefits are analyzed. The grid-search algorithm is extended by the slant range compensation algorithm for further improvements. TAN methods using multi-beam sensor setups are developed to increase the measured information content.

Dead-reckoning approach to SAN The methods which have been applied to improve vertical and horizontal SAN are used in the third aspect of this thesis to provide a dead-reckoning SAN. The similarities and peculiarities of the dead-reckoning SAN approach to a conventional DEM-based method are focused in this aspect.
Especially the characteristics and benefits of the two different sensor setups using either a range-imaging or two range-scanning sensors is focused. The specialties of both measurements are considered with their effects on the data processing. In this context, the consideration of the position drift effect on the comparison results is also discussed. The integration of the dead-reckoning measurement is derived and applied in simulation.

1.4 Outline

The thesis is organized as follows: chapter 2: "Surface-Ranging Sensor Modeling and Validation" discusses the functional principles of the three relevant surface-ranging sensor classes, altimeters, range-scanning and ranging-imaging sensors. A simulation model for these sensors is presented, covering geometric and signal propagation effects and the concepts of operation for these sensors are discussed. Three concepts to improve the vertical aiding of INSs using surface-ranging sensors are presented in chapter 3: "Vertical SAN". The main focus of this chapter is the assessment of surface-ranging measurements and their error compensation. In chapter 4: "Precise Positioning SAN" several methods to improve the position aiding of INSs using a DEM are introduced. The aiding of INSs with an TAN system without a DEM is discussed in chapter 5: "Dead Reckoning SAN". The main focus of this chapter is the processing of redundant surface-ranging measurements. The integration of surface-ranging sensors in a research aircraft with the necessary reference sensors is explained in chapter 6: "Flight Test Instrumentation". It especially focuses the aspect of data-logging with industrial automation components. In chapter 7: "Flight Emulation and Simulation", the presented methods of the former chapters are applied to recorded data and in simulation. The thesis concludes with a summary in chapter 8. Some results of this thesis have been prepublished in [82], [83], [84] and [85]

Chapter 2

Surface-Ranging Sensor Modeling and Validation

In this chapter, the functional principles of surface-ranging sensors are explained, including their measurement principle and the corresponding reference systems. A classification of the discussed surface-ranging sensors is illustrated in figure 2.1 depending on their ranging and imaging information content.

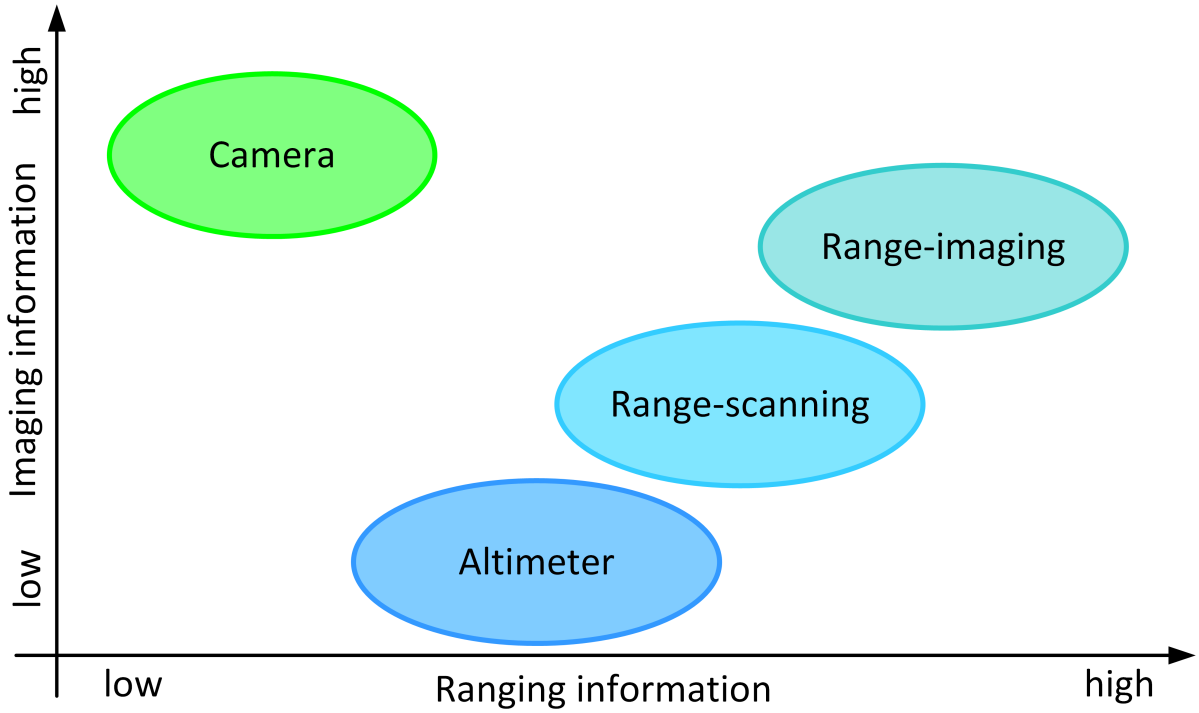

Figure 2.1: Surface-ranging sensors classes overview

While altimeters provide a one-dimensional range-only measurement, their ranging and imaging information content is small. Range-scanning sensors can provided up to a range information in two directions, thereby their ranging and their imaging information content is larger. Range-imaging sensors output a full imaging measurement including a ranging information for each pixel and provide the maximum of range-imaging sensor capabilities. Compared to a camera with an imaging only measurement, its resolution is significantly smaller and thereby its imaging information content. Cameras without

ranging measurement are not discussed in this thesis.
The specifics of the three considered sensor classes altimeters (Laser and Radar), range-scanning and range-imaging sensors are discussed. In the second section, the theoretical basics of the sensor principles are applied to model and simulate the sensor measurement and error characteristics. The most complex model, the Radar altimeter simulation model, is validated with recorded altimeter data from a flight test campaign. The chapter concludes with the concepts of operation, where the limits and error characteristics of surface ranging sensors are considered. A simulation study demonstrating the vulnerabilities of surface-ranging sensor measurements complements the chapter. Another approach for sensor simulation is given in [93] with the Laser scanner synthesizer. Some results of this chapter have been prepublished in [82], [83], [84] and [85]. Some student theses in this field ([44], [41], [8]) haven been supervised during the work on this thesis.

2.1 Functional Concepts

2.1.1 Measurement Principle

The height of an airborne platform with respect to a defined coordinate system is one of the most important information for navigation, flight control and flight guidance purposes. There are several definitions of the platform height that have to be distinguished, taking into account various reference systems, measurement principles and error characteristics. After introducing the relevant reference systems, the following sections discuss different height measurement methods and characteristics. The height above ground measurement, which is the focus of this thesis, is considered in detail. Subsequently, the error characteristics of the different height measurement methods are compared.

2.1.1.1 Geodetic Reference Systems

The most common global geodetic reference system is called World Geodetic System 1984 (WGS84), it defines an ellipsoid with the semi-major axis a, the flattening f, the Earth's gravitational constant GM (with mass of Earth's atmosphere) and the angular velocity of the Earth ω. An overview of the four defined parameters is given in the table 2.1. All other geometric parameters related to an ellipsoid, such as the semi-minor axis b or the first eccentricity e, can be derived [63]. For other geographic coordinate systems see [77]. Especially the application of GNSS receivers, where the horizontal position and height are provided with respect to WGS84, supports the usage of WGS84 in other navigation tasks. GNSS receivers typically provide two kinds of height quantities: the platform height with

Parameter	**Variable**	**Value**
Semi-major axis	a	$6\,378\,137.0\,\mathrm{m}$
Flattening	$\frac{1}{f}$	$298.257\,223\,563$
Earth's gravitational constant	GM	$3\,986\,004.418 \times 10^{8}\,\mathrm{m}^3/\mathrm{s}^2$
Angular velocity of the Earth	ω	$7\,292\,115.0 \times 10^{-11}\,\mathrm{rad\,s}^{-1}$

Table 2.1: WGS84 parameter definitions

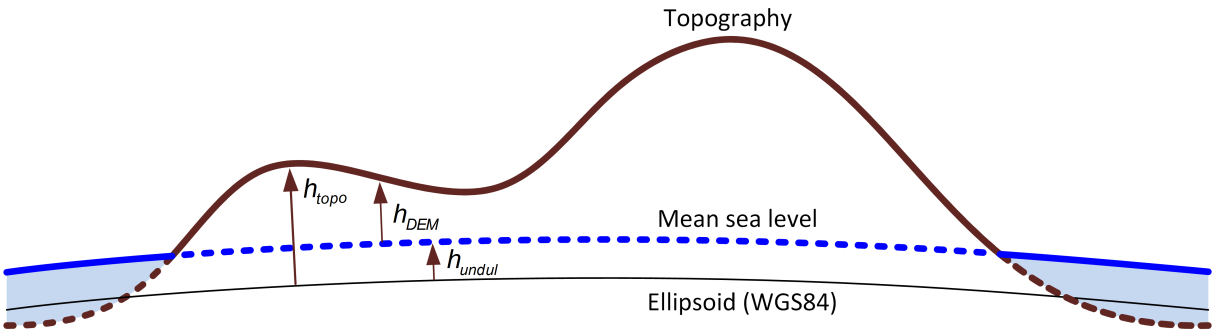

Figure 2.2: Undulation height

respect to WGS84 $h_{wgs}(P)$ or Mean Sea Level (MSL) $h_{msl}(P)$ and the undulation (geoid) $h_{undul}(P)$ height. The difference between MSL and WGS84 height can be approximated with the undulation height. The undulation height describes an equipotential surface called geops. A detailed consideration of this topic is given in [6].
In aerospace applications, the MSL height is often used to describe the platform height $h_{msl}(P)$. Apart from local influences on the sea level like winds, ocean currents or melt water, the geoid height is close to the time averaged sea surface, which is exposed to the Earth's gravity field [30]. The undulation height h_{undul} can be determined using a lookup table created with the Earth Gravitational Model 2008 (EGM08). The relation between the platform height in reference to MSL and the platform height in reference to WGS84 is described by equation 2.1. Figure 2.2 illustrates the reference ellipsoid, the MSL and the corresponding heights. Additionally, it provides the topographic height h_{topo}, describing the height of the Earth's surface and the DEM height d_{dem}.

$$h_{wgs}(P) = h_{msl}(P) + h_{undul}(P) \tag{2.1}$$

The platform height with respect to WGS84 $h_{wgs}(P)$ varies up to 100 m from the platform height with respect to MSL $h_{msl}(P)$, which requires the consideration of the undulation height for all low level flight operations. It will turnout to be convenient to take the WGS84 height $h_{wgs}(P)$ as default height $h(P)$, if no further frame is specified. The topographic height is denoted by h_{topo} and is, whenever no other frame is given, with respect to WGS84.

2.1.1.2 Height Measurement Basics

Passive as well as active sensors for height measurement are discussed in this section. While passive sensors detect a physical quantity of the surrounding environment, active sensors emit a signal by themselves and analyze the signal after interaction with the environment. The most common passive aeronautic height measurement is based on the barometric measurement principle. Therefore, a barometric pressure measurement with a pitot-static probe provides a relation to the current flight altitude using the barometric height formula in reference to the pressure setting. In low level flight phases, like departure and approach, the altimeter pressure reference is set to a local weather dependent parameter. This parameter is described be the Q-code QNH. The pressure setting of the altimeter is aligned to show the correct airfield height $h_{msl}(P)$ when standing on the ground. Even though the QNH setting provides an accurate indication of the aircraft's

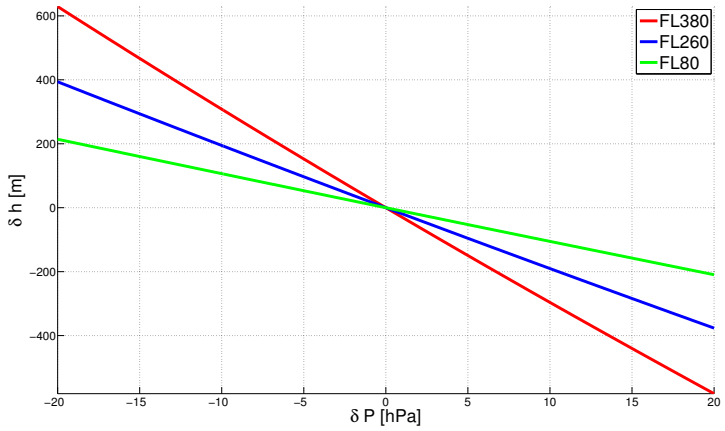

Figure 2.3: Barometric height measurement error

height, it is mandatory for interaction with the Air Traffic Control (ATC) and the integration in the airspace, to ensure that all participating aircraft use the same pressure setting. Therefore, a global pressure setting described by the Q-code QNE with the pressure of 1013.25 hPa is used.
Obviously, the height $h_{msl}(P)$ indicated with a Global Altimeter Pressure Setting (QNE) is incorrect due to local pressure and temperature differences, but guarantee the Flight Level (FL) separation of different aircraft. The height indicated by a barometric altimeter with a QNE setting matches the GNSS height (with respect to MSL), if the assumption of a standard atmosphere is fulfilled in the current situation. The transition from the flight altitude with QNH setting to a FL with QNE setting after take-off is called Transition Altitude (TA), the transition from FL back to flight altitude in an approach situation is called Transition Level (TL). The height measurement error using a barometric measurement principle is depicted in figure 2.3. The figure shows the considerable sensitivity of the barometric height indication to local pressure deviations. This height error δP is caused by the interpretation of the measured pressure with the standard atmosphere height formula (see equation 2.2).

$$p(h) = 1013.25 \left(1 - \frac{0.0065\,\mathrm{K\,m^{-1}} \cdot h}{288.15\,\mathrm{K}}\right)^{5.255} \mathrm{hPa} \tag{2.2}$$

2.1.1.3 Height Above Ground Measurement

The height above ground measurement has a long history in aerospace, beginning with the invention of traditional pulsed Radar altimeters. These altimeters are based on the transmission of an electromagnetic pulse, the reflection of the pulse on the Earth's surface and the detection of the reflected signal onboard. The Time-of-Flight (ToF) measurement principle is illustrated in figure 2.4. The drawings of the DA42 are published with the kind permission of Diamond Aircraft Systems [35].
The received signal s_{rx} differs in two ways from the transmitted signal s_{rx}. The signal runtime τ delays the received signal with respect to the transmitted signal, the signal energy is reduced by environmental disturbances, distortion and free-space loss. These effects are summarized in the damping factor l. The relation between transmitted and

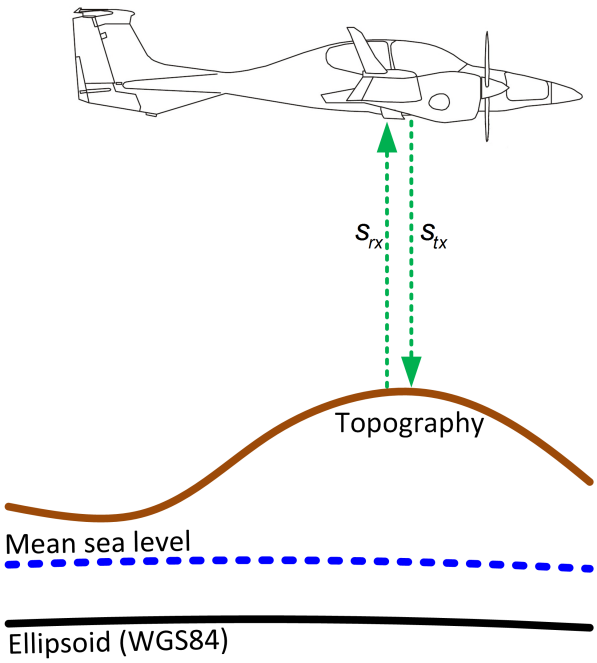

Figure 2.4: Runtime measurement

received signal is given by equation 2.3 and is additionally illustrated in figure 2.5. The illustration additionally introduces the definition of the pulse length T_p.

$$s_{rx}(t) = I s_{tx}(t - \tau) \tag{2.3}$$

The measurement of the distance to the reflected surface, for airborne altimeters the height above ground h_{agl}, can be calculated with the signal runtime τ (equation 2.4) neglecting the airborne altimeter antenna motion. For electromagnetic measurement principles, the propagation speed of the signal is given by the speed of light c.

$$h_{agl} = \frac{c}{2}\tau \tag{2.4}$$

One of the main disadvantages of a pulse based Radar distance measurement is caused by the requirement of transmitting at least as much energy to be able to detect the reflected response. The signal energy is defined by the product of the signal pulse length T_p and the signal amplitude. To fulfill the energy requirement, the signal has to be transmitted with a sufficient amplitude and pulse length, to ensure the detection of a reflection. The receiver is not capable to detect a reflected signal within this transmission interval. The reflected signal cannot be distinguished from the transmitted signal, and hence not be detected. Thereby, short surface reflections within the transmission pulse length, cannot be resolved with the pulse based measurement principle. The minimum resolvable measurement height of a pulsed altimeter is given by equation 2.5.

$$h_{agl,min} = \frac{c \cdot T_p}{2} \tag{2.5}$$

A typical pulse length of $T_p = 100\,\mathrm{ns}$ yields an unresolved minimum height measurement of $h_{agl,min} = 15\,\mathrm{m}$. While this is sufficient for a high-altitude measurement, applications with small ground-clearance cannot be realized. Hence, the minimum height above ground

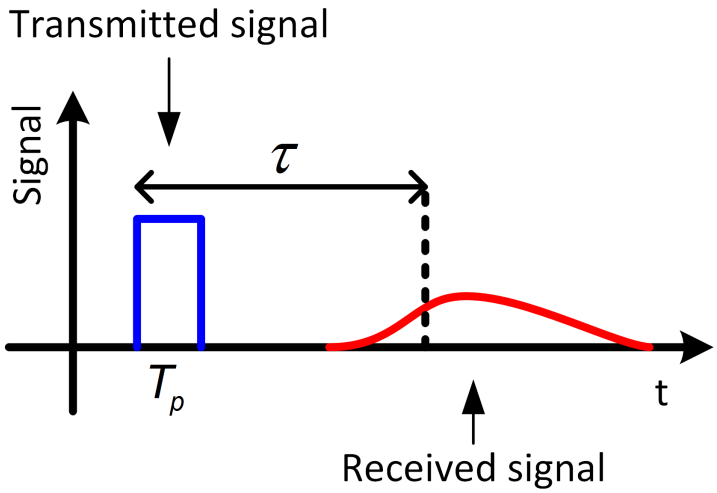

Figure 2.5: Pulsed response

resolution is a critical factor for altimeter applications. The requirements on the minimum and maximum measurement range are defined in the Technical Standard Order C87 [40]. A pulsed Radar altimeter is not suitable in these flight situations, while an altimeter based on the phase-shift measurement principle, which is introduced in the following section, does overcome this problem.

2.1.1.4 Height Measurement Error Characteristics

Inertial, GNSS and integrated navigation systems are typically based on an ellipsoidal reference system, usually WGS84. These systems provide the platform height either as ellipsoidal height $h(P)$ or as sum of undulation height h_{undul} and MSL height $h_{msl}(P)$. Both formulations have their advantages depending on the application. For inertial based navigation using an Inertial Measurement Unit (IMU), it is important to formulate the equations of motion in a reference system, in which the gravity measurement can be compensated. While GNSS provides a long time stable height measurement, inertial navigation underlies a position and velocity drift depending on the quality of the sensors. Especially the height channel of INSs is instable due to the central gravity field of the Earth. The accuracy of GNSS is mainly dependent on (pseuro-)range measurement accuracy, the current satellite constellation and atmospheric effects.

Contrary to inertial or GNSS navigation systems, the measurement of the height above ground h_{agl} with a Radar or Laser altimeter is referenced to the overflown topographic height h_{topo}. The error of height above ground measurements is influenced by the characteristics of the overflown surface (rough, moderate, smooth, flat) and the beam-shape of the sensor. To provide an absolute height measurement, a reference DEM is required with a sufficient resolution and accuracy. An overview of the different discussed height measurement methods is given in figure 2.6, table 2.2 gives additionally the dominating errors of the measurement methods.

The following section presents a detailed view of the different functional designs and specific characteristics of surface-ranging sensors. Laser altimeters, Radar altimeters, range-scanning sensors, and range-imaging sensors are considered.

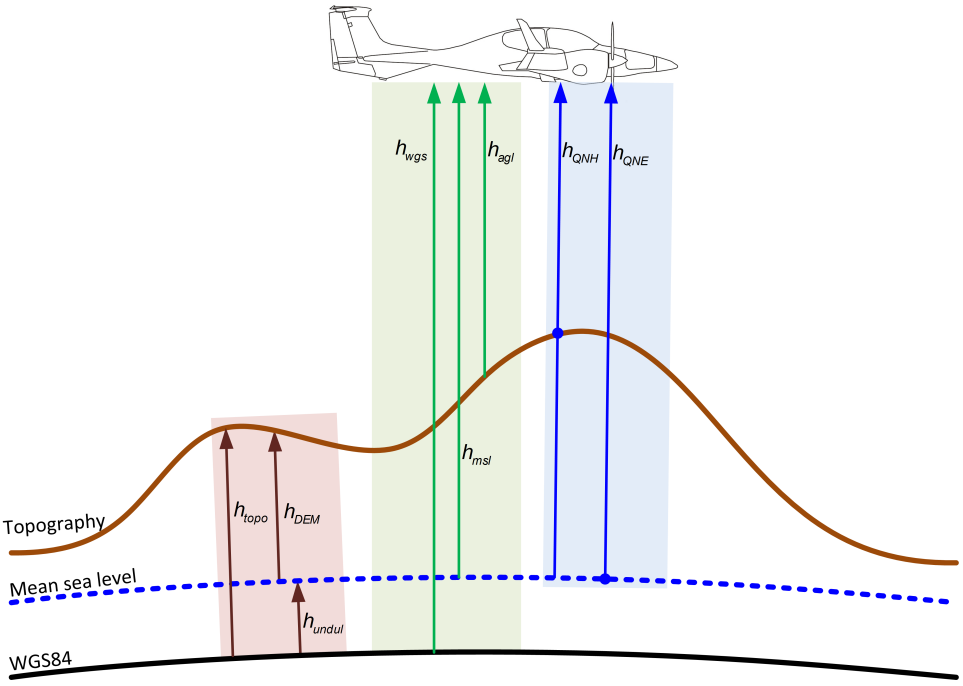

Figure 2.6: Altimeter measurement comparison

Measurement	Reference	Error Characteristic
Barometric	Pressure setting	Weather dependent height offset
Inertial	Reference ellipsoid	Position error drift, instable height channel, schulering horizontal channel
GNSS	Reference ellipsoid	Bias-like, constellation dependent, vertical worse
Radar/Laser Altimeter	Earth's surface	Scaling with h_{agl}

Table 2.2: Height measurement sources

2.1.2 Laser Altimeter Functional Design

Laser altimeters provide distance measurements to the illuminated reflection point on the Earth's surface by using the ToF principle described above. The transmitted Laser signal provides a short pulse length of about $\Delta T_p \approx 10\,\mathrm{ns}$ with an energy E of about $1\,\mathrm{mJ}$. This signal is emitted by a Laser diode, for ranging applications typically Indium Gallium Arsenide (InGaAs) diodes are used. These altimeters normally work at a wavelength λ of about $900\,\mathrm{nm}$ and are thereby out of the human visibility range, which is limited to about $\lambda_{max} = 750\,\mathrm{nm}$. Due to the high transmission energy within the short pulse length, the pulse measurement principle can be applied for Laser altimeters without restrictions concerning the minimum measurement distance. The unresolved height for a pulse length of $T_p = 10\,\mathrm{ns}$ is calculated to $h_{agl,min} = 1.5\,\mathrm{m}$. This small minimum measurement range is acceptable for the application in airborne platforms. A frequency modulated signal can be used, if the application requires a more detailed minimum measurement range resolution. The principle of distance measurement using frequency modulated signals is explained in

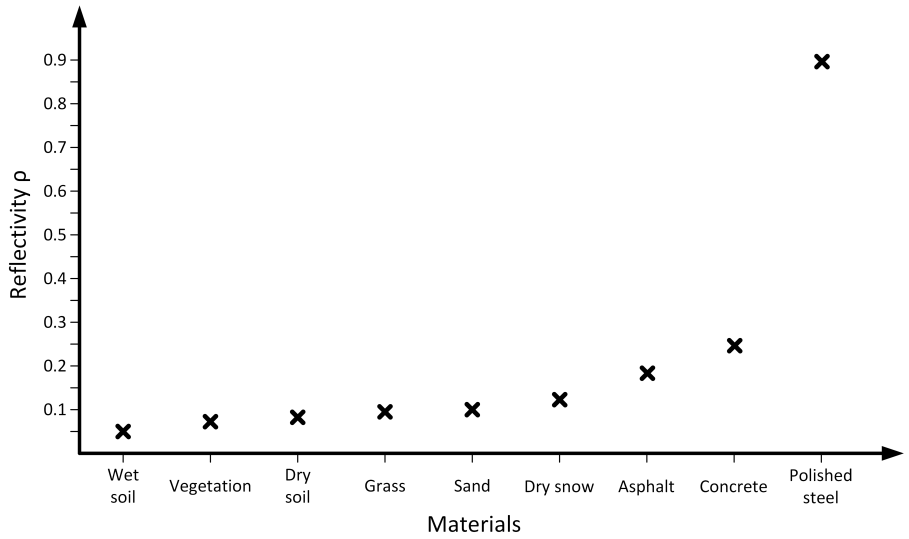

Figure 2.7: Reflectivity for various materials [20]

the following section in the context of Radar altimeters.

The maximum measurement range of Laser altimeters dependents strongly on the reflectivity of the overflown and illuminated surface. The surface material reflectivity is the major influencing factor on the measurement range. For material with high absorption or stealth characteristics, the reflected power is reduced to a minimum and thereby the maximum measurement range, too. On the other hand, the nominal maximum measurement range is increased when the reflected object provides a good reflectively characteristic. Figure 2.7 illustrates the reflectivity of various materials which are of interest for this thesis. The reflectivity values and more details to Laser ranging can be found in [20].

Furthermore, Laser altimeters underlie a strong weather dependency, especially foggy or cloudy weather reduces the maximum range of the device considerably. Laser altimeters provide a pencil beam measurement with a typical beam divergence of about $1\,\mathrm{mrad}$ to $3\,\mathrm{mrad}$. The foot print at a range of $500\,\mathrm{m}$ thereby increases to a size of $0.5\,\mathrm{m}$ to $1.5\,\mathrm{m}$. The distance accuracy of Laser altimeters is normally within a few centimeters for planar reflectors, but the measurement is exposed to the platform's attitude dynamics. Fixed mounted Laser altimeters cannot provide a sufficiently accurate nadir height measurement in an unleveled flight situation without compensation of the platform attitude. The integration of a gimbaled sensor mounting can solve this problem, but is associated with high cost and structural changes in the platform. A detailed view on the measurement error characteristics of all altimeter types is given in section 2.3.

Apart from range measurements, Laser technology is also applied for vehicle speed measurements. For this application, a Continuous Wave (CW) signal is applied instead of a pulsed signal. While the distance to the reflected object cannot be measured with the CW signal, the reflected signal can be used to measure the relative velocity between the sensor and the object. The frequency of the reflected signal is shifted by the Doppler frequency, if the object is moving with respect to the sensor. This so-called Doppler shift can directly be used to determine the relative velocity between object and sensor antenna setup. There are also sensors which can measure both, the distance and the velocity of an object, by transmitting a signal with a frequency ramp and an additional constant frequency part afterwards. These sensors are often applied in automotive applications,

where both information are required. Sensors with the capability to measure velocities are not in the focus of this thesis.

2.1.3 Radar Altimeter Functional Design

High precision Radar altimeters make use of Frequency Modulated Continuous Wave (FMCW) signals for performing a range measurement. With a continuous signal, the transmitted energy can be increased dramatically compared to a pulsed signal. Thereby, FMCW Radars combine the advantages of measuring large ranges with a high accuracy.

2.1.3.1 Modulated Signal

The transmitted signal $s_{tx}(t)$ with the frequency $f_{tx}(t)$ consists of two parts. The carrier signal with the frequency f_c provides a continuous transmission power. The frequency modulation $f_m(t)$ provides a time varying signal, it is modulated with a frequency saw tooth. The transmitted signal $s_{tx}(t)$ is given by equation 2.6. The gradient of the saw tooth frequency $\dot{f}_m$ is due to the linear ramp given by the difference ratio of the modulation frequency bandwidth Δf_m and the ramp interval ΔT_m (see equation 2.7). The total frequency including both parts of the signal is given by equation 2.8.

$$s_{tx}(t) = P_{tx} \cos\left(2\pi f_{tx}(t)\, t\right) \tag{2.6}$$

$$\dot{f}_m = \frac{\Delta f_m}{\Delta T_m} \tag{2.7}$$

$$\begin{aligned} f_{tx}(t) =& f_c + f_m(t) \\ =& f_c + \mathrm{mod}\left(\dot{f}_m \cdot t, \Delta f_m\right) \end{aligned} \tag{2.8}$$

The transmitted signal is propagated through free-space and reflected on the Earth's surface. The reflected signal is propagated back to its origin and detected on the reception antenna with a delay. The transmitted and received signal frequencies with their phase difference, but for the sake of simplicity without signal loss, are illustrated in figure 2.8. This phase difference between the current transmission signal and the received signal is used to calculate the distance to the reflected surface.
Let $f_{rx}(t)$ be the frequency of the received signal $s_{rx}(t)$. The received signal is given by equation 2.9. Methods to extract the phase shift by comparing the transmitted and received signal and the calculation of the distance are shown in the following section.

$$\begin{aligned} f_{rx}(t) &= f_{tx}(t-\tau) \\ &= f_c + f_m(t-\tau) \\ &= f_c + mod\left(\dot{f}_m \cdot (t-\tau), \Delta f_m\right) \end{aligned} \tag{2.9}$$

The damping of the signal is summarized in the coefficient l, which contains the free-space path loss and the absorption of the signal depending on the surface reflectivity. Apart from the physical free-space path loss, this coefficient covers all kinds of environmental

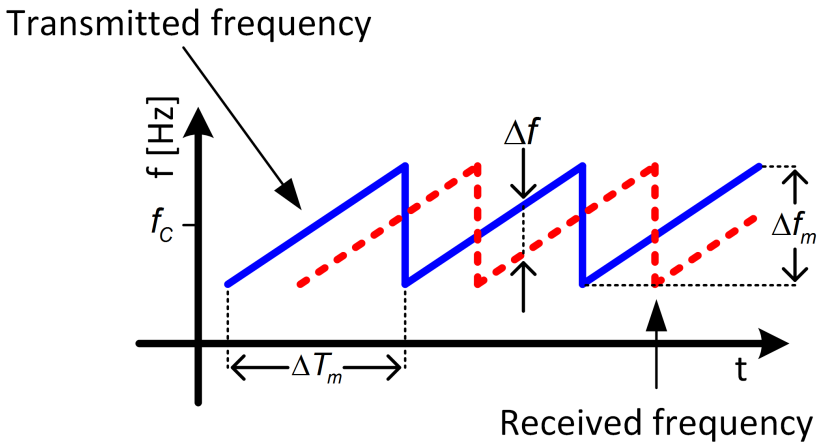

Figure 2.8: Transmitted and received (lossless) FMCW signal

damping influences like temperature and general weather conditions. The received signal is given by equation 2.10.

$$\begin{aligned} s_{rx}(t) &= P_{rx} \cos\left(2\pi f_{rx}(t)\, t\right) \\ &= I P_{tx} \cos\left(2\pi f_{tx}(t-\tau)\, t\right) \end{aligned} \tag{2.10}$$

2.1.3.2 Radar Equation

In this chapter, the propagation of the Radar signal is explained in detail beginning at the device antenna output. The cable damping between receiver and antenna with possible additional connectors and a specific cable length has to be considered individually. The power density at a illuminated target S_{target}, resulting from a isotropic radiation of the transmission power P_{tx} at the distance d to the target, is given by equation 2.11. See appendix A for the derivation of the isotropic radiation power density.

$$S_{target} = \frac{P_{tx}}{4\pi d^2} \tag{2.11}$$

Radar altimeters do usually not use an isotropic antenna characteristic, mainly because the antenna is mounted at the bottom of the fuselage and the measurement direction of an altimeter is pointing downwards. For aerospace applications, an isotropic radiation is even not desired, due to the loss by radiating the power equally in all directions. The benefit of a power concentration and a defined radiation direction is provided by a directional antenna. The power density at the target is proportional to the antenna gain G_{tx} (see equation 2.12).

$$S_{target} = \frac{P_{tx} G_{tx}}{4\pi d^2} \tag{2.12}$$

The reflected power from the surface depends on the Radar cross section σ. The Radar cross section is an indicator for the reflectivity of the illuminated target and gives the size of an equivalent isotropic radiating area. It is defined as the equivalent area of a completely reflecting surface. Thereby, the cross section can be much smaller than the geometric illuminated area in case of stealth shaped surfaces or surfaces with high natural

absorption. The Radar cross section of a surface is defined by directly illuminating the object with the power P_t and measuring the returned power P_s at a distance d (see equation 2.13).

$$\sigma = 4\pi d^2 \frac{P_s}{P_t} \tag{2.13}$$

The total power at the target is given by equation 2.14.

$$P_{target} = \frac{P_{tx} G_{tx} \sigma}{4\pi d^2} \tag{2.14}$$

The reflected signal with the power P_{target} is propagated isotropically through free-space. The signal power density S_{rx} of the reflected signal, reduces the power at the origin (see equation 2.15).

$$S_{rx} = \frac{P_{tx} G_{tx} \sigma}{(4\pi d^2)^2} \tag{2.15}$$

The effective antenna area $A_{rx,eff}$ is decisive for the antenna reception gain. The received power P_{rx} of the antenna output is written by equation 2.16.

$$P_{rx} = \frac{P_{tx} G_{tx} \sigma A_{rx}}{(4\pi d^2)^2} \tag{2.16}$$

The relation of antenna gain G, effective antenna area A_{eff} and the wavelength of the received signal λ is given by equation 2.17.

$$A_{rx,eff} = \frac{G_{rx} \lambda^2}{4\pi} \tag{2.17}$$

The received power P_{rx} at the Radar receiver can be decomposed by the radar equation (see equation 2.18). A more detailed Radar explanation is given in [99].

$$P_{rx} = \frac{P_{tx} G_{tx} G_{rx} \sigma \lambda^2}{(4\pi)^3 d^4} \tag{2.18}$$

2.1.3.3 Antenna Characteristics

The characteristics of antennas describe the direction dependent gain. Usually a rotation symmetrical diagram or a diagram with two graphs for the antenna azimuth and elevation is used to describe the characteristics. The diagram is visualized in a radial reference system with logarithmic scale. The antenna pattern is hereby referenced to an isotropic antenna. The gain of the antenna is given in the unit dBi with respect to an isotropic radiation pattern. An exemplary of a Radar altimeter antenna pattern is given in figure 2.9. The example antenna provides a maximum gain of $G_{el} = G_{az} = 10\,\mathrm{dBi}$ at $az = el = 0\,\mathrm{rad}$, which corresponds to a linear gain factor of 10. The transformation from a linear gain factor to logarithmic relation and vice versa is given by equation 2.19.

$$\begin{aligned} G_{lin} &= 10^{\left(\frac{G_{dBi}}{10}\right)} \\ G_{dBi} &= 10 \log_{10}(G_{lin}) \end{aligned} \tag{2.19}$$

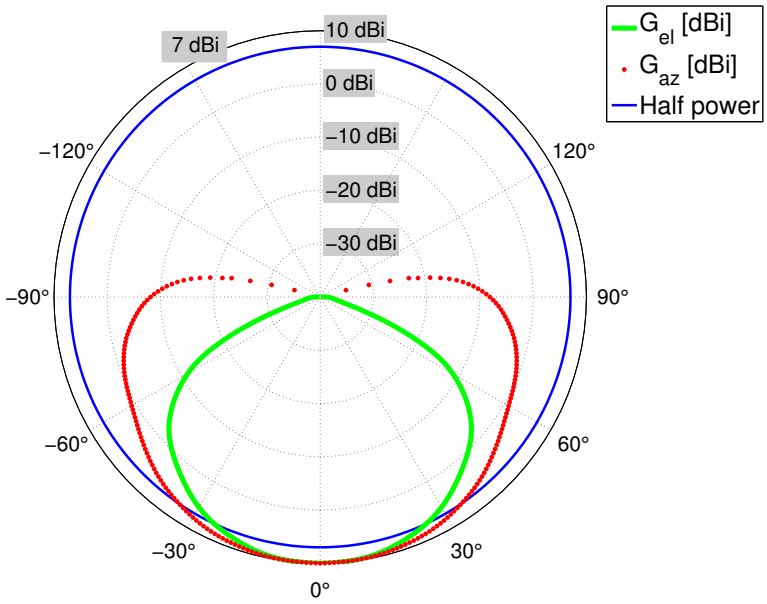

Figure 2.9: Example antenna pattern

The exemplary antenna diagram depicts a constant half power indication. The angle of intersection between the antenna pattern and the half power line is called Half Power Beam Width (HPBW) θ_{HPBW}. The antenna pattern shows a HPBW of $\theta_{HPBW,az} = 35°$ in azimuth and $\theta_{HPBW,el} = 26°$ in elevation. The design intention of a large HPBW is to compensate the roll and pitch attitude of the aircraft for an attitude independent measurement of the nadir height above ground. Usually, Radar altimeter antennas exhibit a larger HPBW in the roll axis and a smaller in the pitch axis due to the higher roll dynamics.

2.1.3.4 Receiver Structures

The internal Radar receiver signal processing is described in this section. Two approaches to isolate the phase shift indicating the height measurement are introduced. Detailed information about the internal Radar receiver signal processing can be found in [65].

Local Oscillator Automatic Tuning The Local Oscillator Automatic Tuning (LOAT) receiver structure is one method to isolate the so-called beat signal s_b, a low frequency signal containing the phase shift including the height information. A diagram of the structure is given in figure 2.10. The LOAT receiver uses a tunable local oscillator with the time-dependent frequency $s_{lo}(t)$ consisting of the current transmit frequency $f_{tx}(t)$ (including the saw tooth ramp) reduced by an intermediate frequency f_{if}. The local oscillator frequency is given by equation 2.20.

$$f_{lo}(t) = f_{tx}(t) - f_{if} \tag{2.20}$$

Both signals, the currently transmitted s_{tx} and the received s_{rx}, are initially downscaled by mixing them with the local oscillator signal. The theory of signal mixing is explained in appendix B. The down-converted transmit signal contains two frequency shares $f_{tx,if,1}$ and $f_{tx,if,2}$, which are given by equation 2.21.

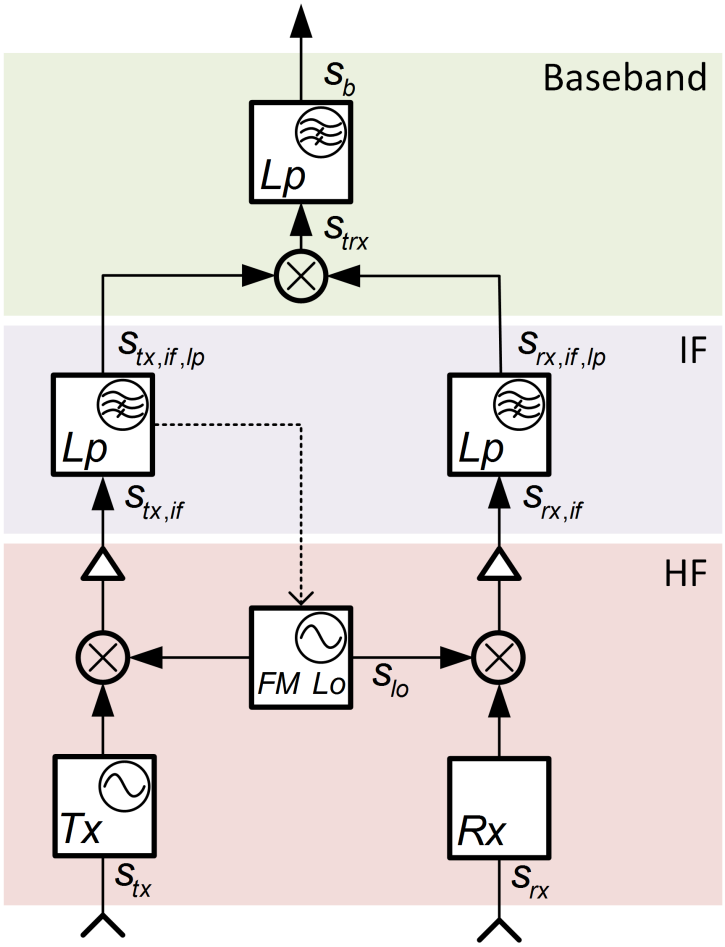

Figure 2.10: Local oscillator automatic tuning receiver architecture

$$\begin{aligned} f_{tx,if}(t) &= |f_{tx}(t) \pm (f_{tx}(t) - f_{if})| \\ f_{tx,if,1}(t) &= f_{tx}(t) + (f_{tx}(t) - f_{if}) = 2f_{tx} - f_{if} \\ f_{tx,if,2}(t) &= f_{tx}(t) - (f_{tx}(t) - f_{if}) = f_{if} \end{aligned} \tag{2.21}$$

The frequency $f_{tx,if,1}$, containing the doubled carrier frequency, is in upper part of the signal's frequency domain, while the frequency $f_{tx,if,1}$ is exactly the frequency of the local oscillator. The same down-conversion principle is applied to the received signal with the result given by equation 2.22. The lower frequency $f_{rx,if,2}$ can be rearranged with the definition of the beat frequency $f_b = f_{tx} - f_{rx}$.

$$\begin{aligned} f_{rx,if}(t) &= |f_{rx}(t) \pm (f_{tx}(t) - f_{if})| \\ f_{rx,if,1}(t) &= f_{rx}(t) + (f_{tx}(t) - f_{if}) = f_{rx}(t) + f_{tx}(t) - f_{if} \\ f_{rx,if,2}(t) &= f_{rx}(t) - (f_{tx}(t) - f_{if}) = f_{rx}(t) - f_{tx}(t) + f_{if} \\ &= f_{tx}(t) - f_b(t) - f_{tx}(t) + f_{if} = f_{if} - f_b(t) \end{aligned} \tag{2.22}$$

The phase of the received signal is delayed with respect to the transmitted signal due to the time-of-flight to the surface and backwards to the antenna. Therefore, the frequency $f_{rx,if,1}$ contains the received and transmitted frequencies. A low pass filter eliminates the higher frequency parts of both signals, the resulting frequencies of the filtered signals $s_{tx,if,lp}$ and $s_{rx,if,lp}$ are given by equation 2.23 and equation 2.24.

$$f_{tx,if,lp}(t) = f_{if} \tag{2.23}$$
$$f_{rx,if,lp}(t) = f_{if} - f_b(t) \tag{2.24}$$

To extract the beat signal $s_b(t)$, the down-converted, low pass filtered received signal $s_{rx,if,lp}$ is mixed with its transmit signal pendant $s_{tx,if,lp}$. The resulting signal is denoted s_{trx} and it's frequency is given by equation 2.25.

$$f_{trx} = |f_{if} \pm (f_{if} - f_b(t))| \tag{2.25}$$

Again, the resulting signal owns a higher and a lower frequency part. The associated frequencies $f_{trx,1}$ and $f_{trx,2}$ are given in 2.26.

$$\begin{aligned} f_{trx,1}(t) &= 2f_{if} - f_b(t) \\ f_{trx,2}(t) &= f_b(t) \end{aligned} \tag{2.26}$$

The final low pass filter isolates the beat signal s_b and eliminates the high frequency shares.

Single Sideband Receiver Structure The Single Sideband (SSB) receiver does not require a tunable local oscillator as advantage to the introduced LOAT receiver. Its principle structure is shown in figure 2.11. The received signal s_{rx} is mixed with the current down-converted and sideband filtered signal $s_{tx,lo,sbf}$. This signal results from mixing the current transmitted signal s_{tx} with the constant frequency signal s_{lo}, generated by the local oscillator with the frequency $f_{lo} = \text{const}$. The frequency of the signal $f_{tx,lo}$ is given by equation 2.27.

$$\begin{aligned} f_{tx,lo}(t) &= |f_{tx}(t) \pm f_{lo}| \\ f_{tx,lo,1}(t) &= f_{tx}(t) + f_{lo} \\ f_{tx,lo,2}(t) &= f_{tx}(t) - f_{lo} \end{aligned} \tag{2.27}$$

The frequency of the sideband filtered signal, where the higher frequency part $f_{tx,lo,1}$ is eliminated, is given by equation 2.28.

$$f_{tx,lo,sbf}(t) = f_{tx}(t) - f_{lo} \tag{2.28}$$

As already mentioned, the signal $s_{tx,lo,sbf}$ is used for an initial mix-down of the received signal, resulting in the signal s_{trx}. Its frequency structure is given by equation 2.29. The frequencies of s_{trx} can be computed using the beat signal frequency definition $f_b(t) = f_{tx}(t) - f_{rx}(t)$.

$$\begin{aligned} f_{trx}(t) &= |f_{rx}(t) \pm f_{tx,lo,sbf}| = |f_{rx}(t) \pm (f_{tx}(t) - f_{lo})| \\ f_{trx,1}(t) &= f_{rx}(t) + (f_{tx}(t) - f_{lo}) = f_{rx}(t) + f_{tx}(t) - f_{lo} \\ f_{trx,2}(t) &= f_{rx}(t) - (f_{tx}(t) - f_{lo}) \\ &= f_{tx}(t) - f_b(t) - f_{tx}(t) + f_{lo} = f_{lo} - f_b(t) \end{aligned} \tag{2.29}$$

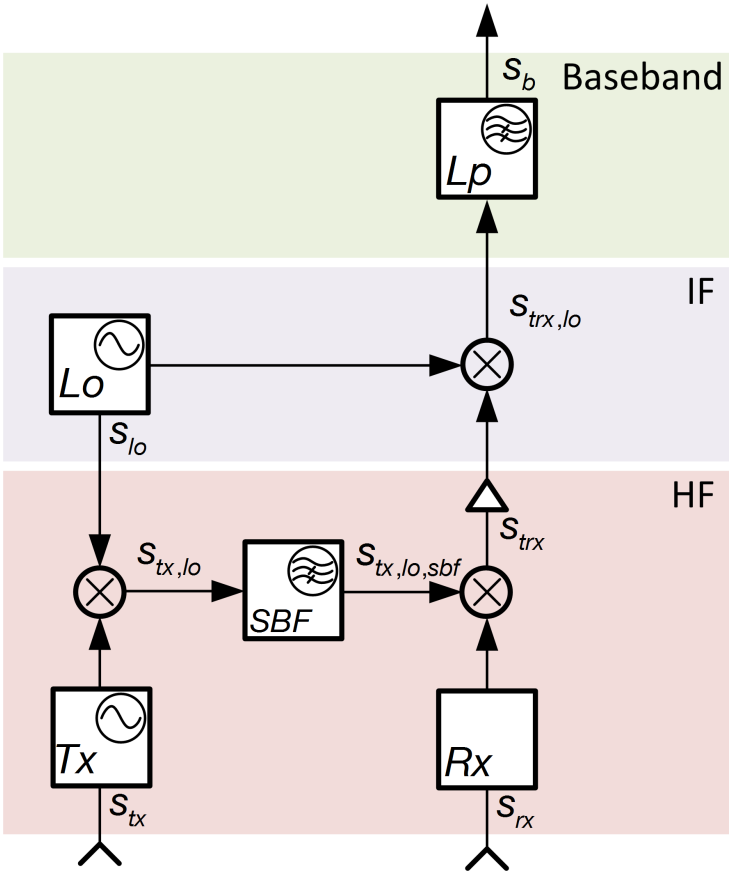

Figure 2.11: Single-sideband receiver architecture

The signal s_{trx} is once again mixed with the local oscillator signal s_{lo} without a prior low pass filtering. Therefore, four different frequency parts remain in the signal $s_{trx,lo}$. The mixing of the signals is given in 2.30.

$$f_{trx,lo}(t) = |t_{trx}(t) \pm f_{lo}| \tag{2.30}$$

It consists of four parts with the frequencies given by equations 2.31.

$$\begin{aligned} f_{trx,lo,1} &= f_{trx,1}(t) + f_{lo} = f_{rx}(t) + f_{tx}(t) \\ f_{trx,lo,2} &= f_{trx,1}(t) - f_{lo} = f_{rx}(t) + f_{tx}(t) - 2f_{lo} \\ f_{trx,lo,3} &= f_{trx,2}(t) + f_{lo} = 2f_{lo} - f_b(t) \\ f_{trx,lo,4} &= |f_{trx,2}(t) - f_{lo}| = f_b(t) \end{aligned} \tag{2.31}$$

The four resulting mix frequencies, as well as the transmit, receive and local oscillator frequency are illustrated in figure 2.12.
Finally, the signal $s_{trx,lo}$ has to be low-pass filtered to isolate the beat signal s_b. This low-pass filter is depicted in the figure, too.

Height Calculation The introduced receiver structures LOAT and SSB provide the isolation of the frequency difference between transmitted and received signals, the so-called beat frequency $f_b(t)$. The time-of-flight of the signal can directly be derived with the frequency ramp gradient $\dot{f}_m$, for a measurement interval within one saw tooth ramp interval (equation 2.32).

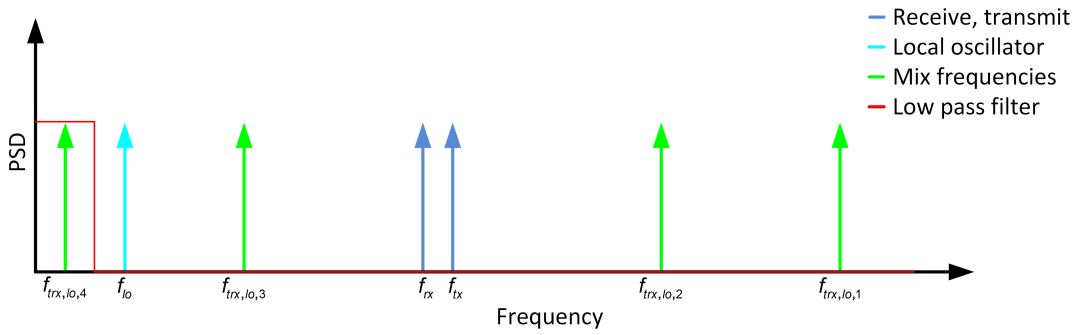

Figure 2.12: Mix frequency of a SSB receiver

$$\tau = \frac{f_b}{\dot{f}_m} \tag{2.32}$$

The height above ground h_{agl} is given by equation 2.33.

$$h_{agl} = \frac{c}{2}\tau \tag{2.33}$$

Doppler Assessment A disadvantage of the measurement principle, based on a frequency modulated signal, is the sensitivity to a Doppler frequency shift. The Doppler shift can be caused by the relative velocity between the antenna and the reflecting target. This section investigates whether Doppler induced measurement errors are significant in altimeter applications. In an altimeter application, the vertical velocity v_d of the aircraft and the surface variation can lead to erroneous measurements. The Doppler shift Δf_d can be calculated with the relative velocity $v_{d,rel}$ of the altimeter antenna and the surface by equation 2.34.

$$\Delta f_d = f_c \frac{v_{d,rel}}{c} \tag{2.34}$$

Assuming a Doppler induced frequency shift in the received signal of $f_{rx,doppler} = f_{rx} + \Delta f_d$ the resulting measurement error $\delta h_{agl,doppler} = h_{agl,doppler} - h_{agl}$ can be calculated by substituting equation 2.32 into equation 2.33 and subsequent error propagation by equation 2.35.

$$\delta h_{agl,doppler} = \frac{\Delta f_d \cdot c}{2\dot{f}_m} \tag{2.35}$$

Assuming a standard three degree approach and oscillating surface variations up to $\delta h = 100\,\mathrm{m}$ beneath the approach path, figure 2.13 illustrates the height measurement error $\delta h_{agl,doppler}$ caused by the Doppler shift. For this simulation example, a standard Radar altimeter with a center frequency of $f_c = 4.3\,\mathrm{GHz}$ and a modulation frequency of $\dot{f}_m = 100\,\mathrm{GHz}$ is assumed.
The height measurement error caused by Doppler frequency shifts are limited to a few centimeters. As a result, the Doppler effect can be neglected for altimeter applications and for the common position and topographic height accuracy.

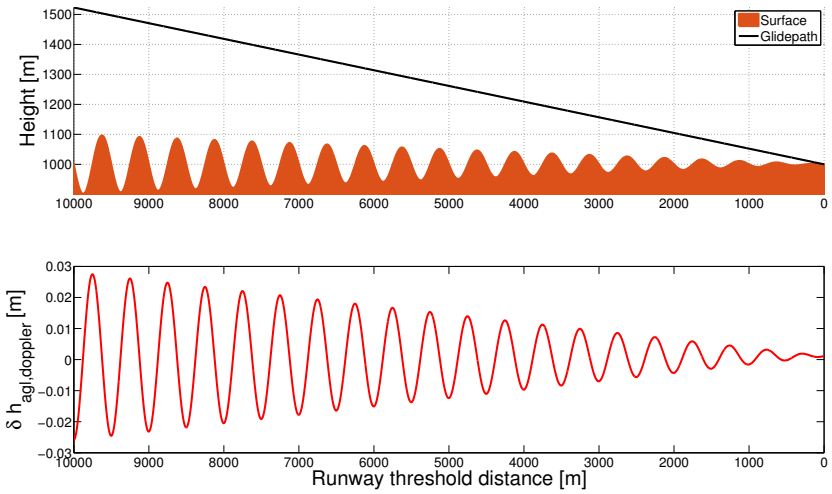

Figure 2.13: Doppler shift influence on height measurement

2.1.4 Range-Scanning Sensors Functional Design

Ranging sensors with one or more directional degrees of freedom are called range-scanning sensors. These sensors do not only provide the distance to the reflecting target in a body-fixed direction, but in addition a directional variation relative to the body frame. This directional information can be one-dimensional, for example using a Laser scanner which can deflect the Radar beam in one direction. A sensor with two degrees of directional freedom, for example a phased array Radar, provides two angular information about the deflection. The range measurement of a Laser scanner can use the pulsed signal principle similar to the altimeter approach. This measurement method limits the maximum update frequency. Expecting a maximal range measurement of $d_{max} = 1000\,\mathrm{m}$, which is a typical range for common Laser and Radar altimeters, the maximum measurement frequency is calculated by equation 2.36.

$$f_{max} = \frac{c}{2d_{max}} = 150\,\mathrm{kHz} \tag{2.36}$$

Laser scanners providing higher update rates are using a frequency modulated transmit signal, comparable to the signal used for FMCW Radars. Both measurement principles can provide accuracies better than $10\,\mathrm{cm}$, which is at least one order of magnitude above the accuracy of typically available DEMs and thereby totally sufficient. Laser scanners commonly use a rotating mirror to deflect the Laser ray in the requested direction. The schematic principle is illustrated with a polygon shaped deflection mirror in figure 2.14.
In this thesis, the basic design of rotating mirror-based Laser scanners is discussed, more advanced mirror shapes and mirror movement principles like oscillating mirrors or nutating mirrors are considered in [18]. Laser scanners with a polygon-shaped mirror cannot measure distances for one full circumvolution. This is not an issue for the down-looking application in airborne platforms. For automotive applications, other designs enable the measurement in a total revolution.
The most important design factors for Laser scanners are the range measurement frequency f_s and the angular speed of the rotating mirror. These two parameters control the number n_l of scanned lines per second, the in-line distance of measurements and the line distance. An exemplary footprint of a Laser scanner measurement is illustrated in figure

2.15.
Apart from the obvious error sources like ranging or angular measurement errors, Laser scanners are influenced by other effects. Structural bending or vibration between the sensor position and the b frame reference point can degrade the high precision range measurement. Another aspect concerning the georeferencing of the range measurement are the different update frequencies. While Laser scanners provide an output with several kilohertz, the position is often available with several hundred hertz. Therefore, the position and attitude reference has to be interpolated for the georeferencing of high frequency range measurements.
The reflected signal of a pulsed Laser scanner may consist of several responses, depending on the characteristics of the reflecting surface. Whenever the Laser is reflected first by an object, which reflects parts of the transmitted power and the remaining power is reflected by the surface, two peaks, a first response and a last response are received. This situation is illustrated in figure 2.16. Often, Laser scanner can distinguish multiple responses and can provide them as measurement.
Since the detection of a pencil beam surface response does not require to be simulated on signal level, the receiver internal signal processing of Laser scanners is not part of this work. Therefore, the distance measurement can be interpreted as point distance from platform to surface.
Another range-scanning sensor, which provides ranging measurements to the reflecting target with an angular deflection, is a phased-array radar. This sensor is based on the Radar measurement principle using phased-array antenna elements and Digital Beam Forming (DBF). With this technology, the Radar signal is transmitted through an antenna array with different phases and hence can be angularly deflected. However, the beam-size exceeds the pencil beam-shape of a Laser scanner due to the finite size of the antenna element and the mounting restrictions inside or on an airframe. The techniques introduced in this thesis can also be applied to variable beam Radar altimeters but are not discussed explicitly further on. The use of Laser scanners for geo-mapping applications is considered in [76] and [96].

2.1.5 Range-Imaging Sensors Functional Design

Range-imaging sensors are well-known under several terms such as:

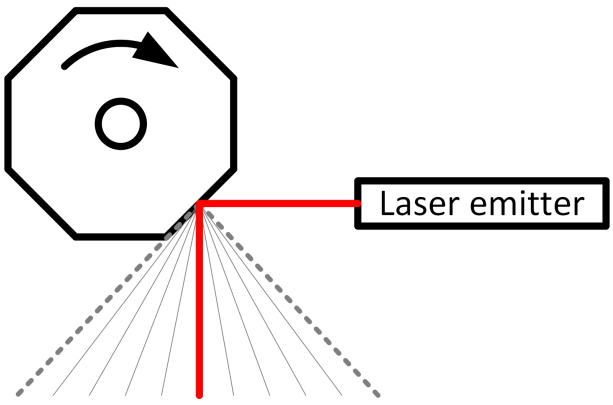

Figure 2.14: Rotating polygon Laser deflection

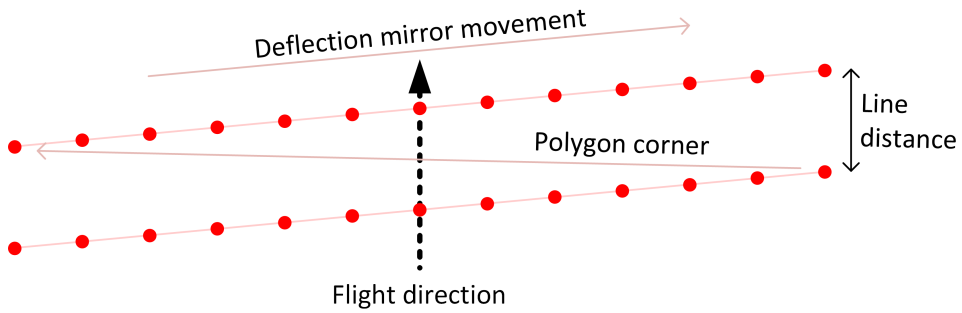

Figure 2.15: Laser scanner footprint over planar terrain

- Time-of-Flight (ToF) Camera
- Photonic Mixing Device (PMD) Camera
- (Flash) Laser Detection and Ranging (Ladar)
- (Flash) Light Detection and Ranging (Lidar)
- 3D Camera.

The different terms are related to different aspects of these sensors, the functional principle is based on a basic ToF measurement and for detection of the signal runtime a Photonic Mixing Device (PMD) sensor is applied. The basic principle of this sensor class is based on an active illumination of the scenery. Therefore, either a pulsed infrared light signal with a short pulse width or a continuous modulated light signal is applied. Both measurement principles, pulsed and continuous wave phase measurement are used for sensors of this class. The reflected light of the illuminated objects is projected through a optical lens onto a PMD sensor. This sensor can determine the signal runtime for each image pixel resulting in a distance matrix measurement.
The synchronous range determination for several pixels is quite challenging, which is one reason why range-imaging sensors are not available with the high resolutions offered for classic digital cameras. Range-Imaging sensors are available with resolutions up to $p_x = 200 \times p_y = 200$ pixels and with update rates up to $f_s = 160\,\text{Hz}$. Equivalent

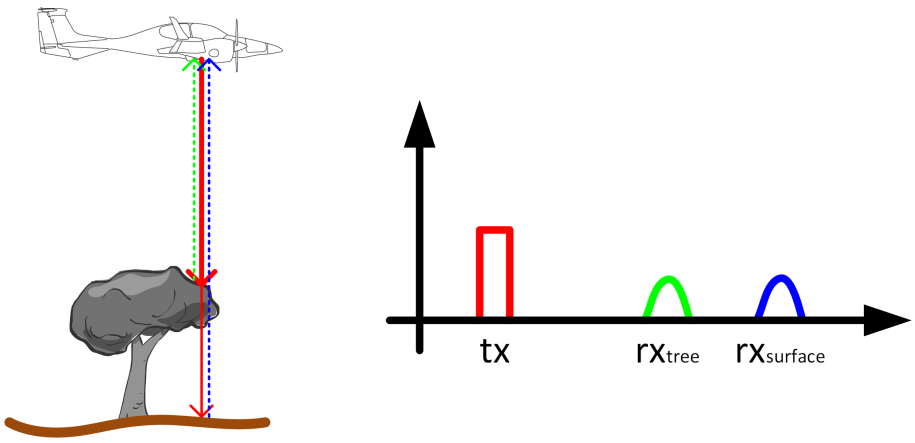

Figure 2.16: First and last Laser response

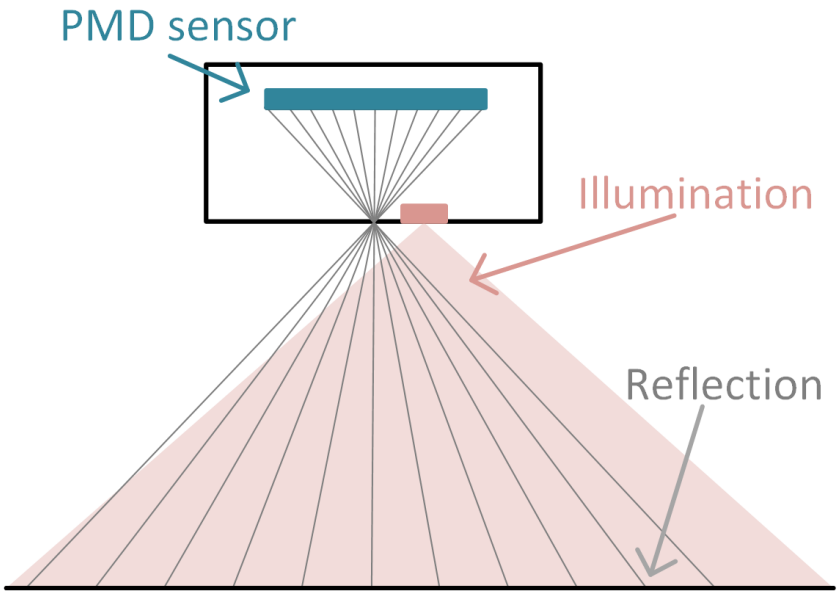

Figure 2.17: 2D functional principle of range-imaging sensors

range-scanning sensors would need a sampling rate of $f_s \cdot p_x \cdot p_y = 6.4\,\mathrm{MHz}$ to provide a comparable information content. Even for top-of-the-class Laser scanners, this high sampling frequency is out of scope. The measurement principle is illustrated in figure 2.17.
The key feature and basic advantage compared to range-scanning sensors is the instantaneous measurement of the distance matrix. Range-scanning sensors provide sequential surface ranging with the major disadvantage that the coverage of the surface depends on the velocity of the platform. Additionally, for SAN or georeferencing purposes, it is beneficial if the surface is measured at one instant point in time rather than scanning within a certain time interval for data handling simplicity. Another beneficial aspect of a range-imaging sensor compared to a scanner setup is the absence of movable parts in the sensor construction and hence system reliability.

2.1.6 Formal Measurement Description

This section introduces the formal description of a direction dependent range measurement to the surface. Let m be the measurement frame with it's origin at the sensor device and it's z-axis in the measurement direction. The m is introduced to cover directional depending effects of the measurement. The distance to the surface in m frame is denoted by d_m.
Let s be the sensor frame with the same origin as the m frame in the sensor device origin. It's axis are aligned to the sensor device to describe the mounting of the sensor with respected to the platform. The transformation is given by the rotation matrix $\mathbf{R}_{sm}$. The distance measurement in the s frame is given by equation 2.37.

$$\mathbf{d}_s = \mathbf{R}_{sm} \begin{pmatrix} 0 \\ 0 \\ d_m \end{pmatrix} = \mathbf{R}_{sm}\mathbf{d}_m \tag{2.37}$$

The leverarm from b frame to s frame is denoted by $\mathbf{x}_b\,(S)$ and the rotation matrix from

b frame to the sensor frame s is given with $\mathbf{R}_{bs}$. The distance measurement in the body frame b is given by equation 2.38.

$$\mathbf{d}_b = \mathbf{R}_{bs}\mathbf{R}_{sm}\mathbf{d}_m - \mathbf{x}_b(S) \tag{2.38}$$

To provide a height information, the measurement in the b frame has to be converted into the navigation frame n. Since the navigation frame's origin can be assumed to be identical to the body frame origin, the transformation can be calculated by rotating $\mathbf{d}_b$ by $\mathbf{R}_{nb}$ (see equation 2.39).

$$\mathbf{d}_n = \mathbf{R}_{nb}\left(\mathbf{R}_{bs}\mathbf{R}_{sm}\mathbf{d}_m - \mathbf{x}_b(S)\right) \tag{2.39}$$

For an absolute georeferencing, the equation has to be transformed into the Earth frame e. Let $\mathbf{x}_e(P)$ be the platform position in Earth-Centered Earth-Fixed (ECEF) coordinates. The measured point $\mathbf{x}_e(M)$ on the Earth's surface, expressed in ECEF coordinates by applying the rotation matrix $\mathbf{R}_{en}$, is given by equation 2.40.

$$\mathbf{x}_e(M) = \mathbf{x}_e(P) + \mathbf{R}_{en}\mathbf{R}_{nb}\left(\mathbf{R}_{bs}\mathbf{R}_{sm}\mathbf{d}_m - \mathbf{x}_b(S)\right) \tag{2.40}$$

For later processing tasks, as for example the application of table lookup functions for comparison reasons, it is useful to transform the georeferenced measurement into geodetic coordinates. The transformation of a Cartesian vector to a geodetic distance is established by the matrix $\mathbf{D}^{-1}$ (equation 2.41, [30]) .

$$\mathbf{D} = \begin{pmatrix} M(\phi)+h & 0 & 0 \\ 0 & (N(\phi)+h)\cos\phi & 0 \\ 0 & 0 & -1 \end{pmatrix} \tag{2.41}$$

Let $\boldsymbol{\lambda}(P)$ be the platform position and $\boldsymbol{\lambda}(M)$ the georeferenced measurement position, both in geodetic coordinates. The measurement expressed in geodetic coordinates is then given by equation 2.42.

$$\boldsymbol{\lambda}(M) = \boldsymbol{\lambda}(P) + \mathbf{D}^{-1}\mathbf{R}_{en}\mathbf{R}_{nb}\left(\mathbf{R}_{bs}\mathbf{R}_{sm}\mathbf{d}_m - \mathbf{x}_b(S)\right) \tag{2.42}$$

The vector equation is transformed into a height-only representation for a table lookup function and the comparison with a DEM. The topographic height with respect to WGS84 of the measurement footprint $h_{topo}(\phi(M), \lambda(M))$ is given by equation 2.43 with the platform height $h(P)$.

$$h_{topo}(\phi(M), \lambda(M)) = h(P) + \begin{pmatrix}0 & 0 & 1\end{pmatrix}\mathbf{D}^{-1}\mathbf{R}_{nb}\left(\mathbf{R}_{bs}\mathbf{R}_{sm}\mathbf{d}_m - \mathbf{x}_b(S)\right) \tag{2.43}$$

With the relation

$$\begin{pmatrix}0 & 0 & 1\end{pmatrix}\mathbf{D}^{-1} = -\begin{pmatrix}0 & 0 & 1\end{pmatrix}, \tag{2.44}$$

the equation can be simplified to 2.45.

$$h_{topo}(\phi(M), \lambda(M)) = h(P) - \begin{pmatrix}0 & 0 & 1\end{pmatrix}\mathbf{R}_{nb}\left(\mathbf{R}_{bs}\mathbf{R}_{sm}\mathbf{d}_m - \mathbf{x}_b(S)\right) \tag{2.45}$$

Equation 2.40 can be rearranged to isolate for the distance vector measurement, which will turn out to be useful for a formal description of slant range distance measurements (equation 2.46).

$$\mathbf{d}_m = \mathbf{R}_{ms}\mathbf{R}_{sb}\left(\mathbf{R}_{bn}\mathbf{R}_{ne}\left(\mathbf{x}_e\left(M\right) - \mathbf{x}_e\left(P\right)\right) + \mathbf{x}_b\left(S\right)\right) \tag{2.46}$$

The distance magnitude can similarly be derived by a rearrangement of equation 2.43 resulting in 2.47 for later integration aspects. The perturbations of the measurement equations are derived in appendix C.2.

$$d_m = -\begin{pmatrix}0\\0\\1\end{pmatrix}^T \mathbf{R}_{ms}\mathbf{R}_{sb}\left(\mathbf{R}_{bn}\begin{pmatrix}0\\0\\1\end{pmatrix}\left(h\left(P\right) - h_{topo}\left(\phi\left(M\right), \lambda\left(M\right)\right)\right) - \mathbf{x}_b\left(S\right)\right) \tag{2.47}$$

2.2 Modeling and Simulation

In this section, the modeling and simulation of surface-ranging sensors is discussed in general. A sophisticated sensor model is required for the simulation analysis of the sensor error characteristics. Existing simulation models for surface ranging sensors have shown limitations regarding their signal layer simulation capability. The simulation of the beam-shape is another important aspect for the analysis and has to be modeled, too. The general problem motivation is summarized in the following box:

Motivation

- Simulation model required for measurement characteristic analysis
- Existing sensor simulation model do not cover:
  - beam-shape characteristics
  - internal receiver processing

The introduced simulation model can cover all kinds of surface-ranging sensors and provides a modular architecture for highest reusability. The simulation model can be used both with recorded flight trajectories and simulated trajectories, the architecture is shown in figure 2.18. It consists of a geometric layer, which covers all geometric aspects of the range measurement and a signal layer, which includes the beam-shape modeling and the internal signal processing.

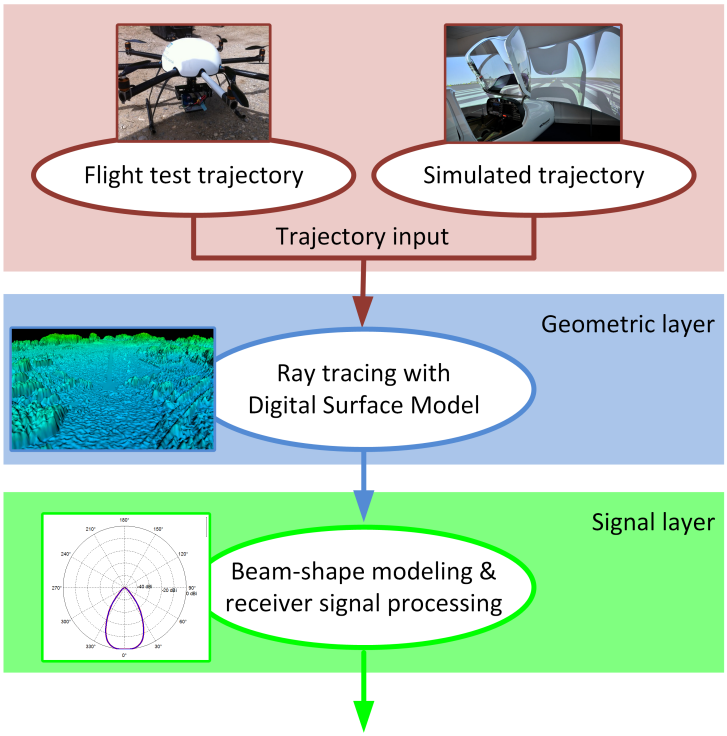

Figure 2.18: Simulation model block diagram

This section first discusses the use of DEM in the simulation model and the interpretation of a DEM. A ray tracing approach for an accurate determination of the sensor-to-surface distance is introduced. Finally, the beam-shape modeling and the simulation of the internal receiver processing of Radar altimeters is described. While the geometric layer is

	Geometric layer		Signal layer	
	Ray tracing	Error model	Beam-shape	Signal processing
Laser altimeter	✓	✓	✗	✗
Radar altimeter	✓	✓	✓	✓
Range-scanning	✓	✓	✗	✗
Range-imaging	✓	✓	✗	✗

Table 2.3: Sensor model overview

parameterizable for every sensor class, the beam-shape and signal propagation simulation is exclusively introduced for the Radar altimeter. While the simulation of pencil beam-shape sensors do not require a signal layer simulation, due to their point measurement principle, wide beam-shape Radar altimeters do so. For sensors with a close to pencil beam measurement, geometric error characteristics are considered. Table 2.3 gives an overview of the sensors and the modeled effects. This section is concluded with a validation of the most complex simulation model, the Radar altimeter simulation model. The validation is based on collected flight test data, recorded in an octo-copter test campaign.

2.2.1 Digital Elevation Models

Databases which include the topographic height of the Earth with respect to the latitudinal and longitudinal position are called DEMs. These DEMs are specified by their sampling resolution, the horizontal and vertical accuracy and the covered area. DEMs which represent the Earth's surface without buildings, vegetation and other obstacles are called DTMs and are normally available with a coarser resolution. Digital Surface Models (DSMs) are DEMs which additionally include objects on the Earth's surface. To cover vegetation and smaller obstacles, the resolution of DSMs has to be higher than the resolution of DTM. An illustration of a DTM and a DSM explaining the difference is given in figure 2.19. A deeper consideration of DTMs is given in [36].
DEMs are available with different resolutions and tile sizes, the National Imagery and Mapping Agency (NIMA) proposed five Digital Terrain Elevation Data (DTED) levels to characterize different databases. Taking into account the ellipsoidal shape of the Earth,

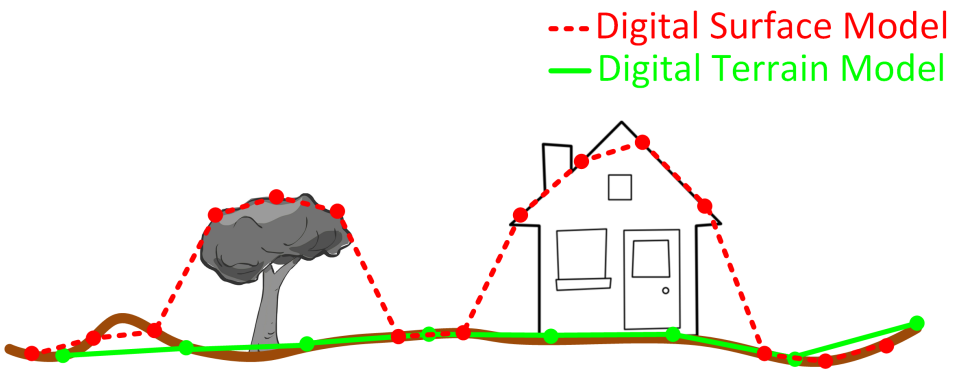

Figure 2.19: Digital terrain and digital surface model

Zone	Latitude
I	$0° - 50°$ N/S
II	$50° - 70°$ N/S
III	$70° - 75°$ N/S
IV	$75° - 80°$ N/S
V	$80° - 90°$ N/S

Table 2.4: DTED zones

the latitudinal coordinates are clustered into five zones, the zones are given in table 2.4. The DTED levels are given with the zone-dependent longitudinal resolutions in table 2.5. The latitudinal resolution is always equal to the longitudinal resolution of zone I, the longitudinal distance is additionally indicated at the equator, the specifications are given in [64]. The DTED levels 3, 4 and 5 are defined with increasing resolutions, but are not standardized.
The Shuttle Radar Topography Mission (SRTM) of 2000 was a Space Shuttle mission (STS-99), which recorded global elevation data up to DTED level 2 quality with a two-antenna Radar setup. For public use, only a DTED level 1 quality is available [52]. The Advanced Spaceborne Thermal Emission and Reflection Radiometer (ASTER) database is available in DTED level 2 resolution from a mission with the Earth surveying satellite Terra [3]. Both databases are available for research and education purposes for free. Another campaign, which aims to record a global DEM, is denoted TerraSAR-X add-on for Digital Elevation Measurement (TanDEM-X) mission. This mission is based on two similar satellites, the Terra Synthetic Aperture Radar - X (Band) (TerraSAR-X) and the TanDEM-X satellite [62]. The recorded data is post-processed and provide a worldwide elevation model with a resolution of about 12 meters which is denoted WorldDEM [100]. A more detailed database, however not globally available, is the Intermap NEXTMap (NEXTMap) with resolutions up to 5 meters recorded with an Interferometric Synthetic Aperture Radar (IFSAR). This database is available in DTM as well as in DSM quality for the U.S. and Europe [49]. Apart from the introduced models, there are various local databases with higher resolutions. The main disadvantage of those models with higher resolutions up to several decimeters is their partial coverage. Additionally, depending on country and district, the data is referenced to different geodetic datums, which complicates the compatibility with other DEMs. While global DEMs are recorded by a satellite campaign, local DEMs are recorded with airborne sensors like Laser scanners. The land

DTED	Resolution					Longitudinal	Tile
Level	I	II	III	IV	V	Distance	Size
0	$30''$	$60''$	$90''$	$120''$	$180''$	$\sim 900\,\mathrm{m}$	$1° \times 1°$
1	$3''$	$6''$	$9''$	$12''$	$18''$	$\sim 90\,\mathrm{m}$	$1° \times 1°$
2	$1''$	$2''$	$3''$	$4''$	$6''$	$\sim 30\,\mathrm{m}$	$1° \times 1°$

Table 2.5: DTED levels

Model	Coverage	Resolution	Accuracy
SRTM	Global	90 m	~ 20 m
ASTER	Global	30 m	~ 20 m
WorldDEM (TanDEM-X)	Global	12 m	~ 4 m
Intermap NEXTMap	Europe, USA	5 m	~ 1 m
Local land surveying offices	Local regions	< 1 m	~ 0.2 m

Table 2.6: DEM classes

surveying offices of the federate states in Germany often provide very detailed DEMs with resolution smaller than 1 meter [7]. An overview of the considered DEMs with their resolutions and accuracies is given in table 2.6. In future a more global high resolution 3D map will become available from 3D reconstruction using optical remote sensing imaginary. A comparison of a DTM, recorded from the ASTER mission, and a local Laser scan DSM of the same surface is provided in figure 2.20 for a better impression.
A high resolution DEM means large amounts of data which have to be stored in an access friendly way. For the later processing, a lookup table is the preferred concept with the latitude and longitude as axis and the elevation as information. Apart from a fast table lookup, the latitude ϕ and longitude λ are stored as grid raster to save memory space. For the following calculation, the coordinates are saved in double floating point precision variables requiring 8 bytes each. The necessary memory space in Bytes for a tile with N latitudinal and M longitudinal elevation grid points is calculated by equation 2.48. For larger DEM tiles, the lookup memory concept saves up to factor 3 of the mass storage. However, the lookup table provides advantages, the equidistantly spaced grid requirement is a disadvantage.

$$\begin{aligned} Mem_{array} &= 8\,(3NM) \\ Mem_{lookup} &= 8\,(N + M + NM) \end{aligned} \tag{2.48}$$

The error characteristics of DEMs can be categorized into horizontal and vertical error sources. Obviously, a vertical error provides an erroneous elevation information δh_{dem} on the requested horizontal position (ϕ, λ). A horizontal error $(\delta\phi, \delta\lambda)$ provides an erroneous assignment Δh_{dem} of the measured vertical information to the horizontal information. This relation is given by equation 2.49 [59]. While vertical errors are caused by ranging measurement errors, horizontal errors are caused by an erroneous georeferencing of the ranging information. The error source can be the reference navigation system or the post-processing.

$$\delta h_{dem}\,(\phi, \lambda) = \Delta h_{dem}\,(\delta\phi, \delta\lambda) + \delta h_{dem} \tag{2.49}$$

2.2.2 Bilinear Surface Interpolation

The correct interpretation of the elevation data contained in DEMs is discussed in this section. The data provided by DEMs is normally based on a regular grid. Each tile is defined by the horizontal position of the four corner points and their elevation. An

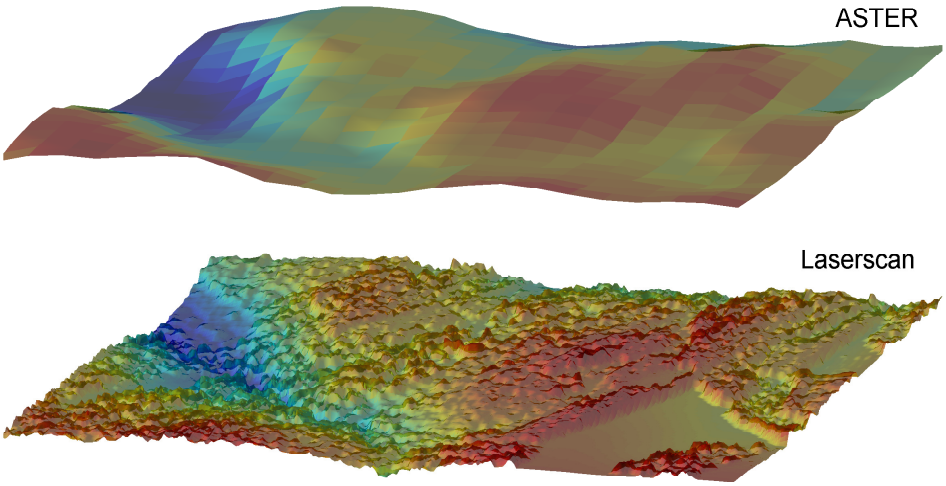

Figure 2.20: Comparison of DEM resolutions

analytic representation of a plane requires only three corner points. For a surface model, this approach would lead to sharp bends on the tile boarders, which should be avoided. Therefore, a bilinear interpretation of the surface of a regularly gridded DEM is preferable. A schematic illustration of one DEM tile is provided in figure 2.21.

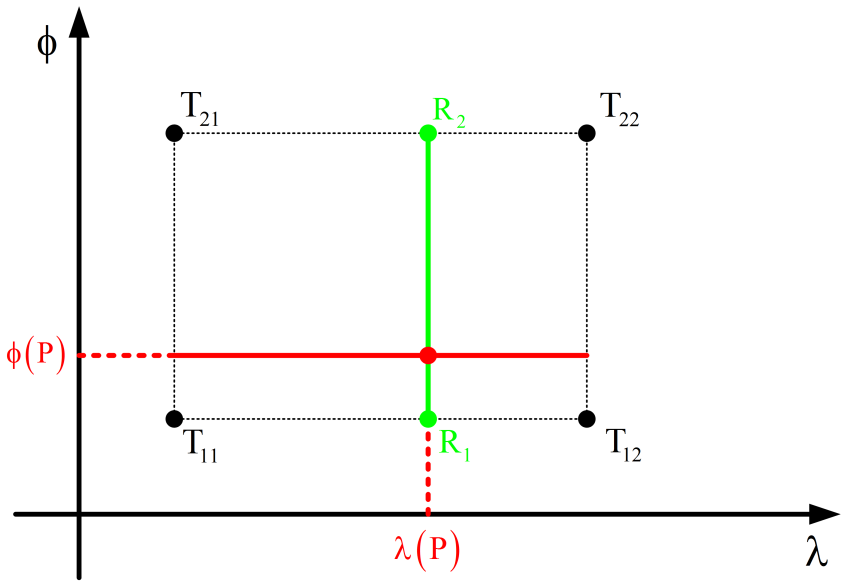

Figure 2.21: Bilinear interpolation

The bilinear height interpolation at the horizontal position $(\phi(P), \lambda(P))$ makes use of two auxiliary points R_1 and R_2. The coefficients to determine the elevation on the auxiliary points with the coefficients a_1, a_2, b_1 and b_2 is given by equation 2.50.

$$
\begin{aligned}
R_1 : h_{topo}\left(\phi\left(T_{11}\right), \lambda\left(P\right)\right) =& a_1 \cdot \lambda\left(P\right) + b_1 \\
a_1 =& \frac{h_{topo}\left(T_{12}\right) - h_{topo}\left(T_{11}\right)}{\lambda\left(T_{12}\right) - \lambda\left(T_{11}\right)} \\
b_1 =& h_{topo}\left(T_{11}\right) - a_1 \cdot \lambda\left(T_{11}\right) \\
R_2 : h_{topo}\left(\phi\left(T_{21}\right), \lambda\left(P\right)\right) =& a_2 \cdot \lambda\left(P\right) + b_2 \\
a_2 =& \frac{h_{topo}\left(T_{22}\right) - h_{topo}\left(T_{21}\right)}{\lambda\left(T_{22}\right) - \lambda\left(T_{21}\right)} \\
b_2 =& h_{topo}\left(T_{21}\right) - a_2 \cdot \lambda\left(T_{21}\right)
\end{aligned}
\tag{2.50}
$$

The interpolation formula of the height h_{topo} at the position P is given in 2.51.

$$
\begin{aligned}
P : h_{topo}\left(\phi\left(P\right), \lambda\left(P\right)\right) =& a_3 \cdot \phi\left(P\right) + b_3 \\
a_3 =& \frac{h_{topo}\left(R_2\right) - h_{topo}\left(R_1\right)}{\lambda\left(R_2\right) - \lambda\left(R_1\right)} \\
b_3 =& h_{topo}\left(R_1\right) - a_3 \cdot \phi\left(R_1\right)
\end{aligned}
\tag{2.51}
$$

2.2.3 Ray Tracing

The geometric sensor model has the primary task to calculate the distance between the sensor mounted on the platform and a DEM surface in the required direction. This distance is determined with a ray tracing algorithm to handle the non-linear characteristics of DEMs which cannot be solved analytically. The problem is illustrated in figure 2.22 in a two-dimensional simplification.
While the exact determination of the intersection point can be solved analytically, the determination of the exact tile has to be solved with a non-analytic approach. The following sections investigate a solution based on a tile prediction to identify either the tile or the near surrounding of the searched tile. For strong non-linear surfaces, the tile prediction provides the near surrounding of the most probable intersection position and has to be complemented by a subsequent tile search algorithm. The analytic intersection determination is finally solved with a bilinear intersection.

2.2.3.1 Tile Prediction

The major task of the tile prediction is to identify the most probable intersection of a ray with the surface. While a classical tile search algorithm will consume enormous calculation time, the introduced tile prediction is optimized for a fast identification. The prediction algorithm checks the ray for surface penetration with a refining resolution. This fine search grid-resolution is parametrized dependent on the resolution of the DEM used. The tile prediction principle is illustrated in figure 2.23.
Whenever the ray approaches the surface beneath a defined threshold, the section is analyzed in detail to avoid ignored intersections (see figure 2.24).

2.2.3.2 Tile Search and Intersection

The tile prediction typically estimates the tile of intersection correctly and an extended tile search is not required. In rare cases over rough surfaces, the tile prediction can become

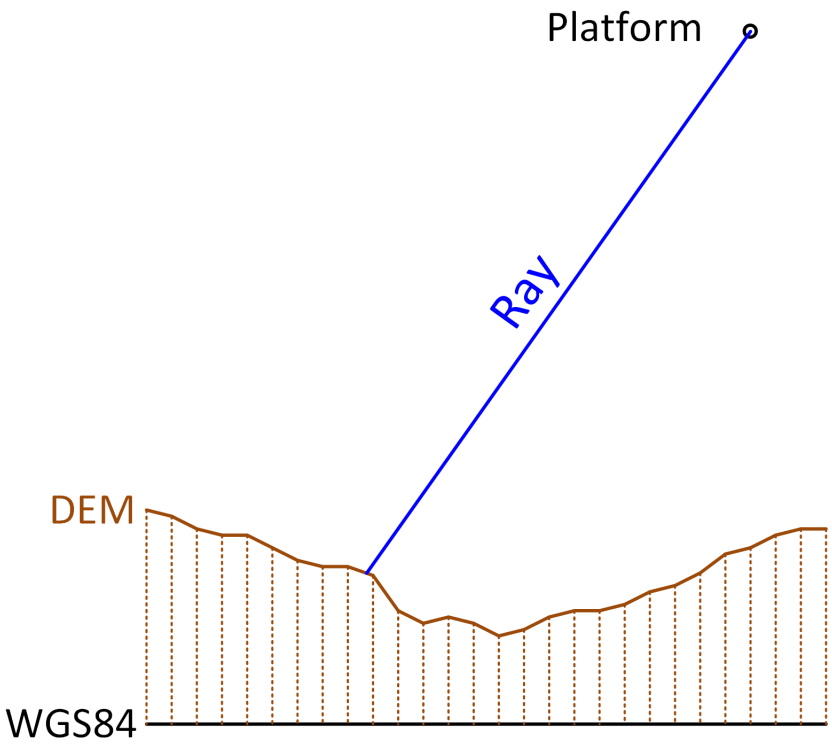

Figure 2.22: DEM intersection problem

inaccurate and selects a tile which is neighbored to the true intersection tile. Therefore, the intersection algorithm checks the prediction for correctness inside the tile. If the first intersection is invalid, the tile search algorithm in the vicinity of the proposed tile is executed. First, the intersection of a bilinear DEM tile with a vector is computed by checking the most probable tile with the corner points $\mathbf{x}_e(A), \mathbf{x}_e(B), \mathbf{x}_e(C), \mathbf{x}_e(D)$ for an inlying intersection. The bilinear surface is given in a vectorial denotation with the two factors s_1 and s_2 in equation 2.52.

$$\begin{aligned} E_{bilin} : \mathbf{x}_{bilin} = &\mathbf{x}_e(A) + s_1 \left(\underbrace{\mathbf{x}_e(B) - \mathbf{x}_e(A)}_{\mathbf{r}_{e,BA}} \right) + s_2 \left(\underbrace{\mathbf{x}_e(C) - \mathbf{x}_e(A)}_{\mathbf{r}_{e,CA}} \right) \\ &+ s_1 s_2 \left(\underbrace{\mathbf{x}_e(A) - \mathbf{x}_e(B) - \mathbf{x}_e(C) + \mathbf{x}_e(D)}_{\mathbf{r}_{e,bilin}} \right) \end{aligned} \tag{2.52}$$

As the definition of the bilinear plane shows, there are 2 independent variables s_1 and s_2 and their combination $s_1 s_2$. This non-linear equation cannot be solved for s_1 and s_2 with a linear approach, and thereby an auxiliary construction is used for a closed analytic determination. The ray vector $\mathbf{r}_e$is represented by the intersection of two planes E_1 and E_2 with their normal vectors $\mathbf{k}_1$ and $\mathbf{k}_2$. The auxiliary construction and the ray representation is illustrated in figure 2.25
The first orthogonal vector can be chosen out of a various number of allowed vectors, only the dot product of the vector and the ray $\mathbf{r}_e$ has to be zero to fulfill orthogonality (see equation 2.53).

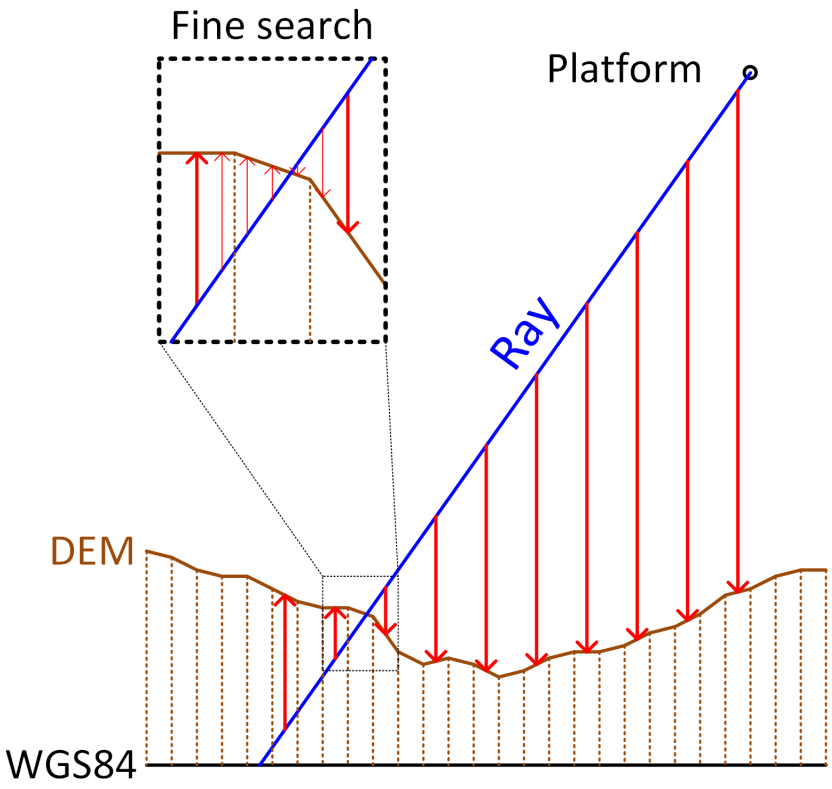

Figure 2.23: Ray tracing tile prediction

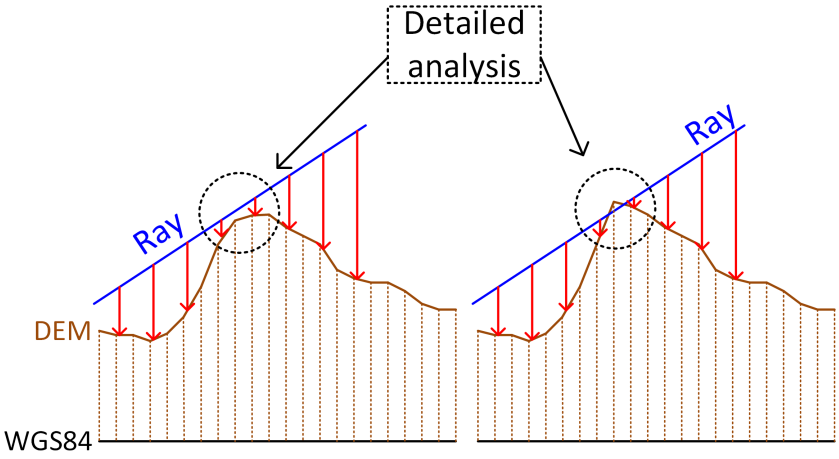

Figure 2.24: Ray tracing shadowing effects

$$\langle \mathbf{k}_1, \mathbf{r}_e \rangle = k_1 r_{e,1} + k_2 r_{e,2} + k_3 r_{e,3} = 0 \tag{2.53}$$

An obvious and simple solution for this requirement and the determination of the second orthonormal vector $\mathbf{k}_2$ with the cross product is given by equation 2.54.

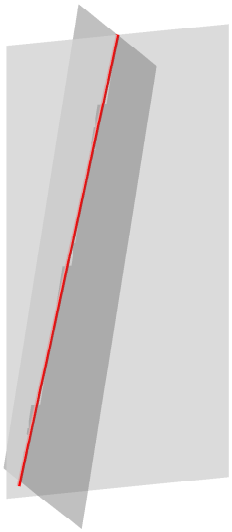

Figure 2.25: Auxiliary planes representing the beam ray

$$\begin{aligned} \mathbf{k}_1 &= \begin{pmatrix} -r_{e,2} \\ r_{e,1} \\ 0 \end{pmatrix} \\ \mathbf{k}_2 &= \mathbf{k}_1 \times \mathbf{r}_e \end{aligned} \tag{2.54}$$

With these two orthogonal vectors, the two auxiliary planes E_1 and E_2, which define the ray $\mathbf{r}_e$ with their intersection, are in the following defined by introducing the factors n_1, n_2, n_3 and n_4. The origin of the planes is chosen in the sensor measurement center $\mathbf{x}_e(P_m)$, the planes are given by equation 2.55.

$$\begin{aligned} E_1 : \mathbf{x} &= \mathbf{x}_e(P_m) + n_1 \begin{pmatrix} -k_{1,2} \\ k_{1,1} \\ 0 \end{pmatrix} + n_2 \begin{pmatrix} 0 \\ -k_{1,3} \\ k_{1,2} \end{pmatrix} \\ E_2 : \mathbf{x} &= \mathbf{x}_e(P_m) + n_3 \begin{pmatrix} -k_{2,2} \\ k_{2,1} \\ 0 \end{pmatrix} + n_4 \begin{pmatrix} 0 \\ -k_{2,3} \\ k_{2,2} \end{pmatrix} \end{aligned} \tag{2.55}$$

Now, both planes are intersected with the bilinear surface. These intersections describe two curves on the DEM and are given by equation 2.56 and equation 2.57. Both equations are solved for the second bilinear surface variable s_2.

$$\begin{aligned} \langle \mathbf{x}_e(A) + s_1\mathbf{r}_{e,BA} + s_2\mathbf{r}_{e,CA} + s_1s_2\mathbf{r}_{e,bilin}, \mathbf{k}_1 \rangle &= \langle \mathbf{x}_e(P_m), \mathbf{k}_1 \rangle \\ s_2(\langle \mathbf{r}_{e,CA}, \mathbf{k}_1 \rangle + s_1 \langle \mathbf{r}_{e,bilin}, \mathbf{k}_1 \rangle) &= \langle \mathbf{x}_e(P_m), \mathbf{k}_1 \rangle - \langle \mathbf{x}_e(A), \mathbf{k}_1 \rangle - s_1 \langle \mathbf{r}_{e,BA}, \mathbf{k}_1 \rangle \\ s_2 &= \frac{\langle \mathbf{x}_e(P_m), \mathbf{k}_1 \rangle - \langle \mathbf{x}_e(A), \mathbf{k}_1 \rangle - s_1 \langle \mathbf{r}_{e,BA}, \mathbf{k}_1 \rangle}{\langle \mathbf{r}_{e,CA}, \mathbf{k}_1 \rangle + s_1 \langle \mathbf{r}_{e,bilin}, \mathbf{k}_1 \rangle} \end{aligned} \tag{2.56}$$

$$\begin{aligned}
\langle \mathbf{x}_e(A) + s_1\mathbf{r}_{e,BA} + s_2\mathbf{r}_{e,CA} + s_1 s_2 \mathbf{r}_{e,bilin}, \mathbf{k}_2\rangle &= \langle \mathbf{x}_e(P_m), \mathbf{k}_2\rangle \\
s_2\left(\langle \mathbf{r}_{e,CA}, \mathbf{k}_2\rangle + s_1\langle \mathbf{r}_{e,bilin}, \mathbf{k}_2\rangle\right) &= \langle \mathbf{x}_e(P_m), \mathbf{k}_2\rangle - \langle \mathbf{x}_e(A), \mathbf{k}_2\rangle - s_1\langle \mathbf{r}_{e,BA}, \mathbf{k}_2\rangle \\
s_2 &= \frac{\langle \mathbf{x}_e(P_m), \mathbf{k}_2\rangle - \langle \mathbf{x}_e(A), \mathbf{k}_2\rangle - s_1\langle \mathbf{r}_{e,BA}, \mathbf{k}_2\rangle}{\langle \mathbf{r}_{e,CA}, \mathbf{k}_2\rangle + s_1\langle \mathbf{r}_{e,bilin}, \mathbf{k}_2\rangle}
\end{aligned} \tag{2.57}$$

These two curves are again intersected with each other to isolate the intersection point of the ray with the bilinear DEM interpretation. The basic equation is given in 2.58 and the rearrangement as quadratic equation in 2.59.

$$\frac{\langle \mathbf{x}_e(P_m), \mathbf{k}_1\rangle - \langle \mathbf{x}_e(A), \mathbf{k}_1\rangle - s_1\langle \mathbf{r}_{e,BA}, \mathbf{k}_1\rangle}{\langle \mathbf{r}_{e,CA}, \mathbf{k}_1\rangle + s_1\langle \mathbf{r}_{e,bilin}, \mathbf{k}_1\rangle} = \frac{\langle \mathbf{x}_e(P_m), \mathbf{k}_2\rangle - \langle \mathbf{x}_e(A), \mathbf{k}_2\rangle - s_1\langle \mathbf{r}_{e,BA}, \mathbf{k}_2\rangle}{\langle \mathbf{r}_{e,CA}, \mathbf{k}_2\rangle + s_1\langle \mathbf{r}_{e,bilin}, \mathbf{k}_2\rangle} \tag{2.58}$$

$$\begin{aligned}
&s_1^2 \underbrace{\left(\langle \mathbf{r}_{e,BA}, \mathbf{k}_2\rangle \langle \mathbf{r}_{e,bilin}, \mathbf{k}_1\rangle - \langle \mathbf{r}_{e,BA}, \mathbf{k}_1\rangle \langle \mathbf{r}_{e,bilin}, \mathbf{k}_2\rangle\right)}_{\eta} + \\
&s_1 \Big(\langle \mathbf{x}_e(P_m), \mathbf{k}_1\rangle \langle \mathbf{r}_{e,bilin}, \mathbf{k}_2\rangle - \langle \mathbf{r}_{e,BA}, \mathbf{k}_1\rangle \langle \mathbf{r}_{e,CA}, \mathbf{k}_2\rangle - \langle \mathbf{x}_e(A), \mathbf{k}_1\rangle \langle \mathbf{r}_{e,bilin}, \mathbf{k}_2\rangle \\
&\quad \underbrace{- \langle \mathbf{x}_e(P_m), \mathbf{k}_2\rangle \langle \mathbf{r}_{e,bilin}, \mathbf{k}_1\rangle + \langle \mathbf{x}_e(A), \mathbf{k}_2\rangle \langle \mathbf{r}_{e,bilin}, \mathbf{k}_1\rangle + \langle \mathbf{r}_{e,BA}, \mathbf{k}_2\rangle \langle \mathbf{r}_{e,CA}, \mathbf{k}_1\rangle\Big)}_{\kappa} \\
&+ \Big(\langle \mathbf{x}_e(P_m), \mathbf{k}_1\rangle \langle \mathbf{r}_{e,CA}, \mathbf{k}_2\rangle - \langle \mathbf{x}_e(A), \mathbf{k}_1\rangle \langle \mathbf{r}_{e,CA}, \mathbf{k}_2\rangle \\
&\quad \underbrace{- \langle \mathbf{x}_e(P_m), \mathbf{k}_2\rangle \langle \mathbf{r}_{e,CA}, \mathbf{k}_1\rangle + \langle \mathbf{x}_e(A), \mathbf{k}_2\rangle \langle \mathbf{r}_{e,CA}, \mathbf{k}_1\rangle\Big)}_{\xi} = 0
\end{aligned} \tag{2.59}$$

This quadratic equation can be solved using the formula in 2.60.

$$\begin{aligned}
s_1^2\eta + s_1\kappa + \xi &= 0 \\
s_{1_{1/2}} &= -\frac{\kappa}{2\eta} \pm \sqrt{\left(\frac{\kappa}{2\eta}\right)^2 - \frac{\xi}{\eta}}
\end{aligned} \tag{2.60}$$

For determination of the two possible intersection points on the DEM, the parameter $s_{2_{1/2}}$ has to be calculated additionally, equation 2.61 provides the solution.

$$s_{2_{1/2}} = \frac{\langle \mathbf{x}_e(P_m), \mathbf{k}_1\rangle - \langle \mathbf{x}_e(A), \mathbf{k}_1\rangle - s_{1_{1/2}}\langle \mathbf{r}_{e,BA}, \mathbf{k}_1\rangle}{\langle \mathbf{r}_{e,CA}, \mathbf{k}_1\rangle + s_{1_{1/2}}\langle \mathbf{r}_{e,bilin}, \mathbf{k}_1\rangle} \tag{2.61}$$

The intersection with the bilinear DEM surface, the two auxiliary planes and the ray is illustrated in figure 2.26.
A valid intersection of the selected DEM tile has to fulfill the criterion in equation 2.62. If the criterion is not fulfilled, the determined intersection point with the DEM lies outside the tile and is invalid. For the rare cases, where the tile prediction algorithm identifies a wrong tile, a search algorithm is implemented which analyze the neighboring tiles for a possible intersection.

$$\begin{aligned}
0 \leq s_{1_{1/2}} \leq 1 \\
0 \leq s_{2_{1/2}} \leq 1
\end{aligned} \tag{2.62}$$

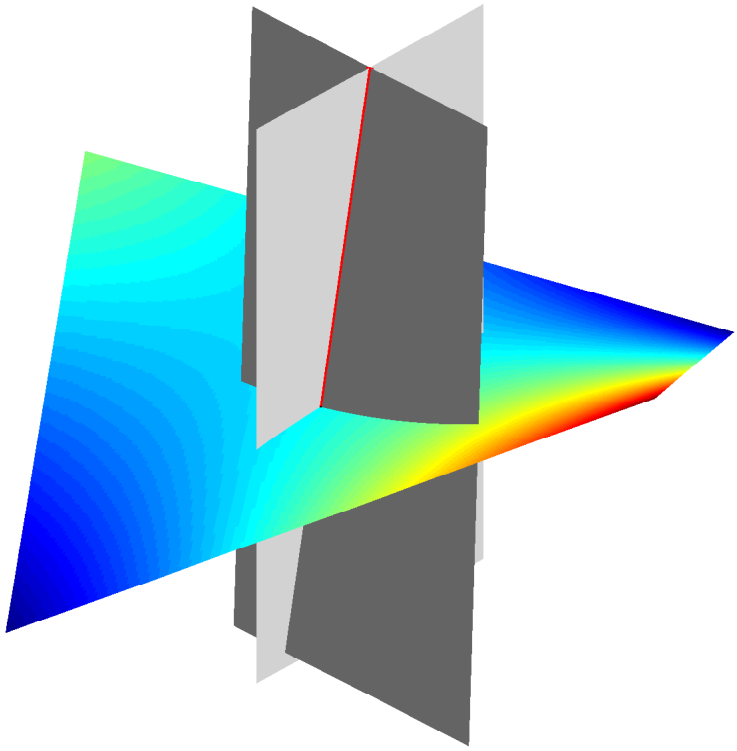

Figure 2.26: Bilinear surface model intersection construction

2.2.4 Simple Error Model

The perturbation analysis of the slant range measurement equation 2.40 and 2.42 is derived in appendix C.1. The basic georeferenced slant range measurement equation have already been discussed and are given in Cartesian coordinates in equation 2.40 and in geodetic coordinates in 2.42. It reveals main geometric error sources which are listed in table 2.7 with their influence on the slant range measurement.
The sensor lever-arm error $\delta\mathbf{x}_b(S)$ as well as the sensor misalignment error $\boldsymbol{\psi}_{\tilde{s}s}$ can be minimized by a careful installation and alignment of the equipment. Especially the location of installation has to be chosen carefully in terms of structural strength, vibrations and deflections. The platform position error $\delta\mathbf{x}_e(P)/\delta\boldsymbol{\lambda}(P)$ and orientation error $\boldsymbol{\psi}_{n\tilde{n}}$ are dependent on the quality of the used reference navigation system. The two remaining errors describe the main sensor characteristics and depend on the sensor category. The

Error description	**symbol**
Platform position	$\delta\mathbf{x}_e(P)/\delta\boldsymbol{\lambda}(P)$
Platform orientation	$\boldsymbol{\psi}_{n\tilde{n}}$
Ranging	δd_m
Sensor mounting misalignment	$\boldsymbol{\psi}_{\tilde{s}s}$
Sensor lever-arm error	$\delta\mathbf{x}_b(S)$
Measurement direction	$\boldsymbol{\psi}_{\tilde{m}m}$

Table 2.7: Geometric error overview

ranging error can be divided into a bias-like component b_d, a scale factor component s_d and a noise-like component n_d. The total ranging error model is given by equation 2.63.

$$\delta d_m = d_m \cdot s_d + b_d + n_d \tag{2.63}$$

The dominating ranging error contributor for altimeters is the scale factor error s_d, especially if no distinction between platform attitude and ranging error sources is made. In this case, attitude caused slant range measurement errors are counted to the scale factor error share in addition to the measurement principle-based scale factor errors, since both scale with range. This approach is usually taken for Radar altimeters, where a ranging accuracy is declared to depend on the absolute ranging value. Often, this specification is related to an attitude constraint, which allows a certain roll and pitch angle without accuracy loss. The ToF measurement principle brings the benefit of a high precision measurement for small distances due to the high amount of reflected power. Therefore, constant biased and noise error parts are comparatively small for this sensor class. While the bias error is constant over the complete measurement range, the noise component is assumed to be proportional to the measurement range and has thereby also a scale factor component which has to be considered. An correspondingly adjusted ranging sensor error model is given by equation 2.64. The model is extended by a scale factor dependent noise component n_s which increases with the measurement range. The noise component n_d is remaining to cover the constant noise effects.

$$\delta d_m = d_m (s_d + n_s) + b_d + n_d \tag{2.64}$$

If a separate attitude error component is considered in the error model, the scale factor error components and the attitude error components can exchange their error shares. While the model is suitable for a pencil beam Laser measurement, where the platform attitude provides a geometric error, and the ranging error can be quantified depending on the absolute measurement error with equation 2.64, the model is not suitable for wide-beam shapes. For example, a slant measurement with a wide-beam cone Radar altimeter provides a scale factor error due to the signal disturbance and an attitude dependency due to the slant measurement. These effects have a complex interaction and cannot be considered isolated. Therefore, for beam cones which exceed pencil beam characteristics, the beam-shape modeling, which is introduced in the following chapter, is a suitable simulation model.

2.2.5 Beam-Shape Modeling

Simulating the beam shape of a Radar altimeter is challenging. The antenna gain characteristics have to be approximated and the surface ranges within the beam cone have to be calculated in the geometric layer. Furthermore, the surface elevation is strongly nonlinear depending on the roughness of the considered area. Dependent on the applied DEM a linearization of the elevation data can be sensible, but results in a loss of height accuracy. Therefore, the solution of the Radar receiver signal response with a defined beam shape cannot be calculated analytically.
This section introduces an approach for an integral solution for the beam-shape simulation using the ray distance vector to represent the entire beam-shape. The angular directions of the parameterizable amount N of rays are equidistantly arranged on a half

sphere. Therefore, an equidistant distribution on a half dome, representing the lower half of the antenna pattern, can be obtained by applying a geodesic dome. This special geometric shape is assembled from equilateral triangles resulting in shapes which have equal distances between all neighboring vertices. The amount of triangles, and thereby the number of vertices, cannot be chosen independently, which is a small disadvantage. The construction of an icosahedron and a geodesic dome is derived subsequently.
A geodesic dome is basically based on a geometric shape called icosahedron consisting of 20 equilateral triangles with a total of 12 corner points located on a circle with radius r from the center. The usage of equilateral triangles ensures that all corner points are at the same distance to their direct neighbors. The icosahedron shape is illustrated in figure 2.27(a). The basic icosahedron can be constructed using the angular distance of the upper and lower five corner points of $\Delta\alpha = 72°$. Additionally, the upper five corner points are rotated by $\Delta\beta = 36°$ versus the lower ones. The top view given in figure 2.27(b) illustrates the angles of the corner points of one layer and the shift between the upper and lower level. The upper level points are colored in red, the lower layer points are colored in blue.

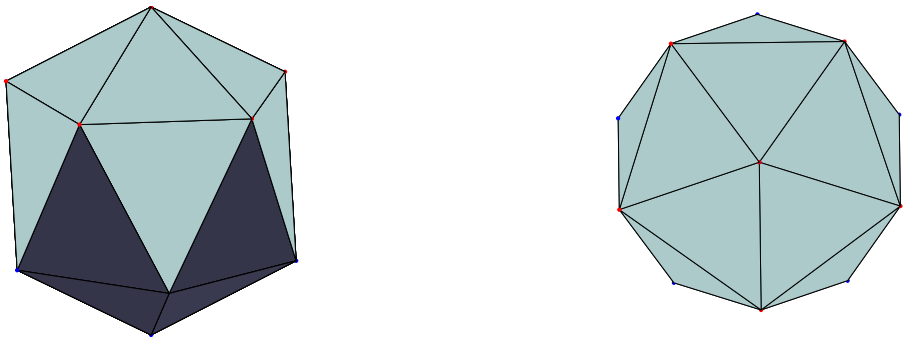

(a) Side view (b) Top view

Figure 2.27: Icosahedron

The icosahedron is a geodesic dome with the order one. Figure 2.28 shows an unwrapped first order icosahedron with 20 triangles and 12 vertices. The vertices, which are shared by multiple triangles are plotted unfilled, the unique ones are plotted filled. For example, the upper and lower row features only one unique corner point.

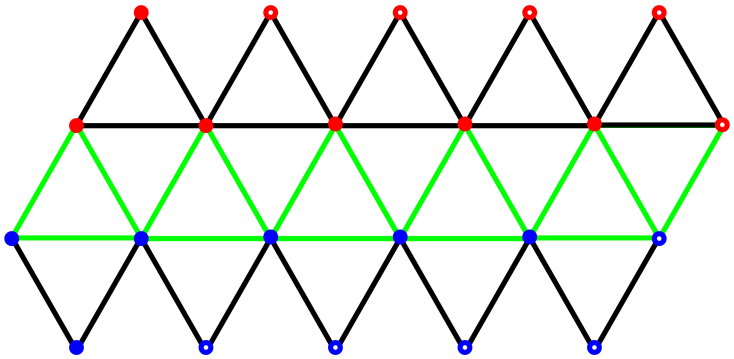

Figure 2.28: Icosahedron flat view

To refine a first order to a second order geodesic dome, each equilateral triangle is split into four smaller ones. The newly created vertices are chosen to be on the sphere. The shape

of a geodesic dome converges to a sphere as the order tends to infinity. The extension of a first order basic triangle to a second order results in four new triangles. The extension to a third order geodesic dome results in nine triangles per origin triangle. Generally, the number N_{tr} of triangles follows equation 2.65.

$$N_{tr} = 20 \cdot n^2 \tag{2.65}$$

The number of vertices N_p, which is more important for the beam-shape modeling, depends on the number of triangles. The relation between the number of triangles N_{tr} and the number of corner points N_p is given by equation 2.66. Figure 2.29 shows the extension of a icosahedron to a second order geodesic dome, which consists of 80 triangles and 42 vertices.

$$N_p = 2 + \frac{N_{triangles}}{2} \tag{2.66}$$

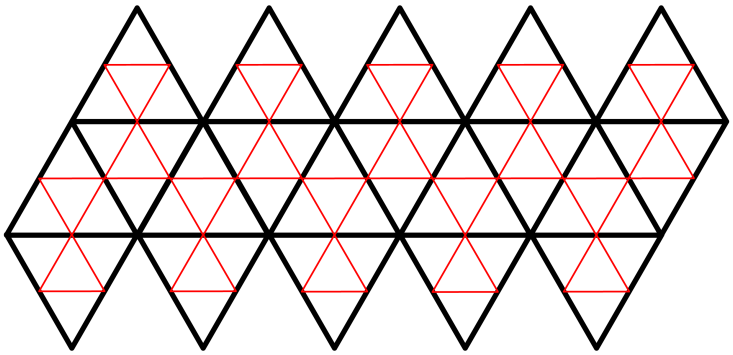

Figure 2.29: Geodesic dome flat view

The number N_{ray} of rays depends on several factors. The available computational power, the characteristics the overflown surface and the resolution of the DEM are the main influencing factors. While the calculation power is the limiting factor concerning the maximum number of simulated rays, a flat surface characteristic or a low resolution DEM can be used as argument to reduce the number of rays. As rule for thumb, the footprint distance of the rays should be of similar magnitude as the resolution of the used DEM. The strong damping of Radar altimeter antennas for azimuth angles $\phi_{az} \gtrsim 70°$ and elevation angle $\phi_{el} \gtrsim 70°$ can limit the number of simulated rays. An implemented half dome resolution with $N_p = 751$ is illustrated in figure 2.30.
To simulate the beam-cone, first the distance to the surface in elevation and azimuth direction has to be calculated. Therefore, the introduced ray tracing algorithm of section 2.2.3 is applied for all ray directions with the measurement angle $\boldsymbol{\psi}_{sm}$. Figure 2.31 gives an example of the footprint of the different rays of one Radar beam measurement.
The distance d_m to a flat surface at the azimuth angle ϕ_{sm} can be calculated using equation 2.67 at a specific height above ground h_{agl}. The calculated curve is compared to a ray-based simulation in figure 2.32 to proof the correctness of the ray-tracing and beam-shape modeling approach.

$$d_m = \frac{h_{agl}}{\cos(\phi_{sm})} \tag{2.67}$$

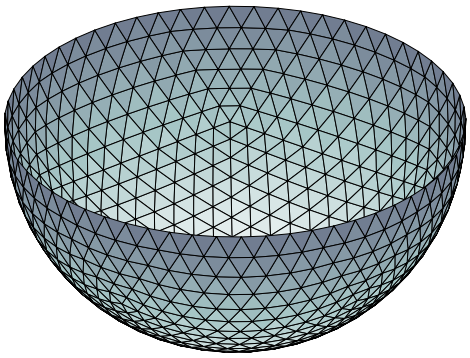

Figure 2.30: Antenna modeling using a geodesic dome

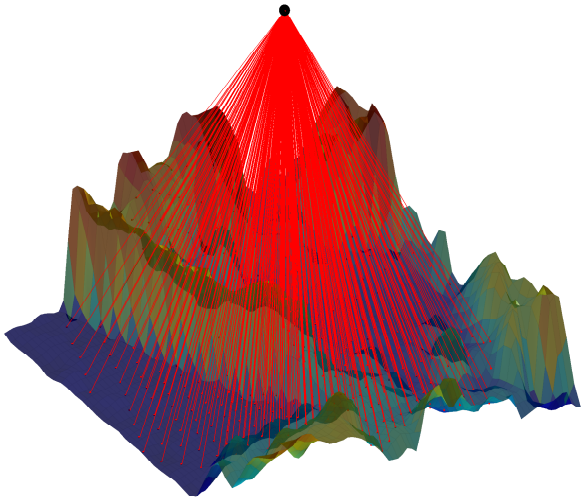

Figure 2.31: Ray-representation of the beam-shape

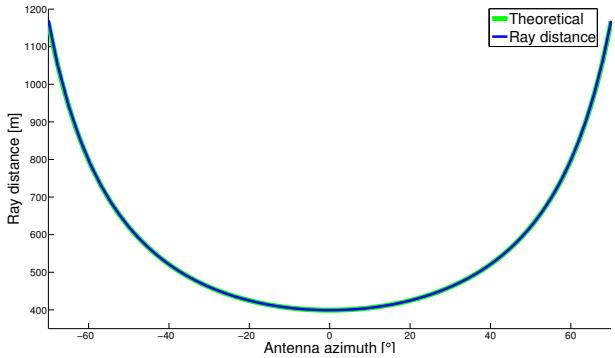

Figure 2.32: Ray distances

The antenna pattern of the simulated antenna is used to calculate the gain of the antenna in the specific direction of the ray. An example of a wide-shaped antenna characteristic is given in figure 2.33.
This antenna diagram provides a section view of the elevation and azimuth antenna gain. Before calculating the antenna gain for a specific direction, the antenna diagram has to be transformed into a representation which can be interpolated. First, the antenna characteristics for roll and pitch are transformed individually into a rotational symmetric representation. The representation for the both direction $G_{az}(z)$ and $G_{el}(z)$ is rotation-

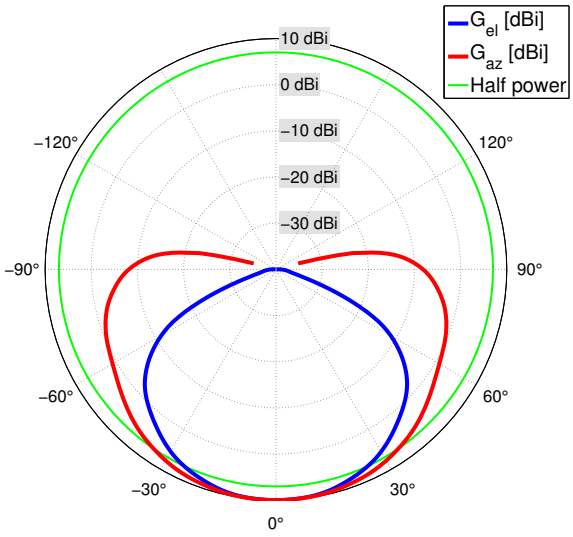

Figure 2.33: Antenna characteristics

ally symmetric around the down-axis z. In a second step, an ellipsoidal representation covering both, elevation and azimuth, is interpolated from the one-dimensional representations (see figure 2.34).

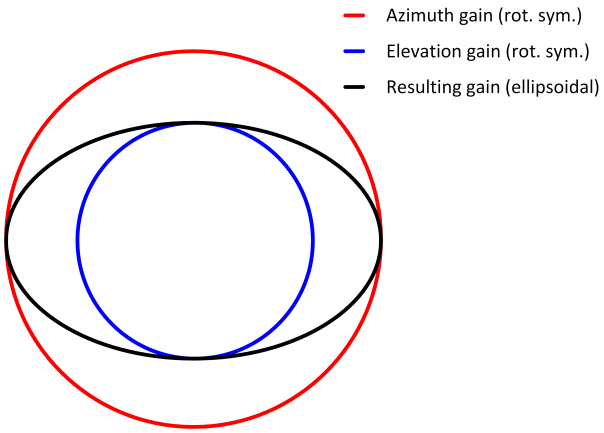

Figure 2.34: Azimuth and elevation gain interpolation

With this interpolation, the antenna gain can be calculated for all existing elevation and azimuth angles. For visualization purposes, the obtained gains can be plotted three-dimensionally to illustrated the beam pattern of the antenna (see figure 2.35).

The required information, the direction dependent distance $d_n(\boldsymbol{\psi}_{sm})$ and the direction dependent antenna gain $G_n(\boldsymbol{\psi}_{sm})$ are used to re-assemble the antenna reception signal. The directions are referred to the measurement frame m with respect to the sensor frame s. The re-assembled Radar signal can be calculated by summing up the different rays and substitute them into the Radar equation 2.18, the result is shown in equation 2.68.

$$P_{rx} = \sum_{n=1}^{N} \frac{P_{tx,n} G_{tx,n}(\boldsymbol{\psi}_{sm})\, G_{rx,n}(\boldsymbol{\psi}_{sm})\, \sigma \lambda^2}{(4\pi)^3\, d_n(\boldsymbol{\psi}_{sm})^4} \tag{2.68}$$

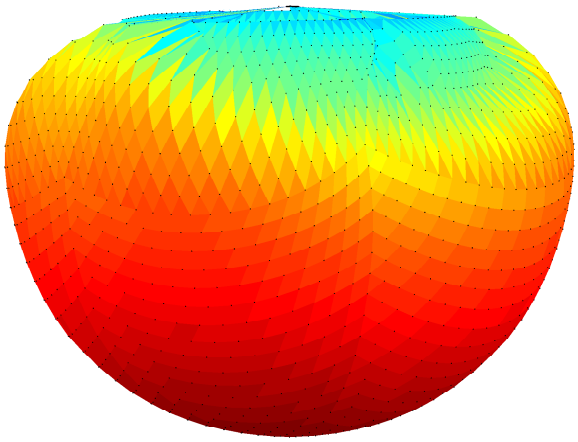

Figure 2.35: 3D antenna model

2.2.6 Receiver Signal Processing

The internal processing of the received signal was described in detail in section 2.1.3.4. The simulation and implementation aspects of the high frequency parts of the Radar receiver are introduced in this section. The two different internal receiver structures are implemented and simulated on signal layer. Furthermore, a baseband representation of the signal processing is derived and simulated to reduce the required computational power. The parameters of the examples refer to real altimeter parameters, which underlie the regulations of the "Frequenznutzungsplan" in Germany [22].

2.2.6.1 Simulation: Local Oscillator Automatic Tuning Receiver

This section describes the different internal mixing stages of a LOAT Radar receiver and their implementation in a simulation model. Figure 2.36 provides the simulation results and is divided into two columns.
The left column depicts the time series of the signal, the right column shows the associated frequency-domain representation. The five rows correspond to the five internal mixing stages of the internal receiver processing and can be explained as follows:

1. The first row illustrates a short extract of the received Radar signal. In this example, the signal has a center frequency of $f_c = 4.3\,\mathrm{GHz}$ and a modulation frequency of $f_m \approx 64\,\mathrm{MHz}$. Therefore, the frequency of the received signal adds up to $f_{rx} \approx 4.364\,\mathrm{GHz}$. Due to the beam-shape simulation with about $N = 1000$ beam rays with different signal runtime to the surface, the modulation frequency can only be approximated as was explained in section 2.2.5. The time series extract shows a duration of $T_{max} = 2\,\mathrm{ns}$, the frequency spectrum is plotted in a range up to $f_{max} \approx 9\,\mathrm{GHz}$. The corresponding transmit signal s_{tx}, which is not plotted in the simulation, has a current frequency of $f_{tx} = 4.3666\,\mathrm{GHz}$, the difference of the both signals is about $f_b \approx 2.6\,\mathrm{MHz}$.

2. The second row illustrates the resulting signal, directly after mixing with the local oscillator. In this example, a intermediate frequency of $f_{if} = 200\,\mathrm{MHz}$ has been

used. The total local oscillator frequency f_{lo} is given by:

$$f_{lo} = f_{tx} - f_{if} = 4.1666\,\text{GHz}$$

The mix of the received signal with the local oscillator provides the signal $s_{rx,if}$ by two different frequency components given by equation 2.69.

$$\begin{aligned} f_{rx,if,1} &= f_{rx} + f_{lo} = f_{rx} + f_{tx} - f_{if} \\ &= 8.5306\,\text{GHz} \\ f_{rx,if,2} &= f_{rx} - f_{lo} = f_{rx} - f_{tx} + f_{if} \\ &= f_{tx} - f_b - f_{tx} + f_{if} = f_{if} - f_b \\ &= 197.4\,\text{MHz} \end{aligned} \tag{2.69}$$

The time period is stretched to $T_{max} = 20\,\text{ns}$ to capture the resulting lower frequency signal $s_{rx,if,1}$.

3. Row three shows the low pass filtered signal $s_{rx,lo,lp}$. Both the time and the frequency domain plots show the resulting signal with frequency $f_{rx,if,2}$ without the eliminated upper mixing frequency $f_{rx,if,1}$.

4. The signal s_{trx} illustrated in the fourth row results from the second mix-down of the signal $s_{rx,if,lp}$ with its corresponding transmit signal $s_{tx,if,lp}$. While the frequency of the mixed down receive signal is known, the frequency of the transmit signal is calculated by equation 2.70. The transmit signal s_{tx} is also mixed by the local oscillator which yields the frequencies $f_{tx,if,1}$ and $f_{tx,if,2}$.

$$\begin{aligned} f_{tx,if,1} &= f_{tx} + f_{lo} = f_{tx} + f_{tx} - f_{if} \\ &= 8.5332\,\text{GHz} \\ f_{tx,if,2} &= f_{tx} - f_{lo} = f_{tx} - f_{tx} + f_{if} = f_{if} \\ &= 200\,\text{MHz} \end{aligned} \tag{2.70}$$

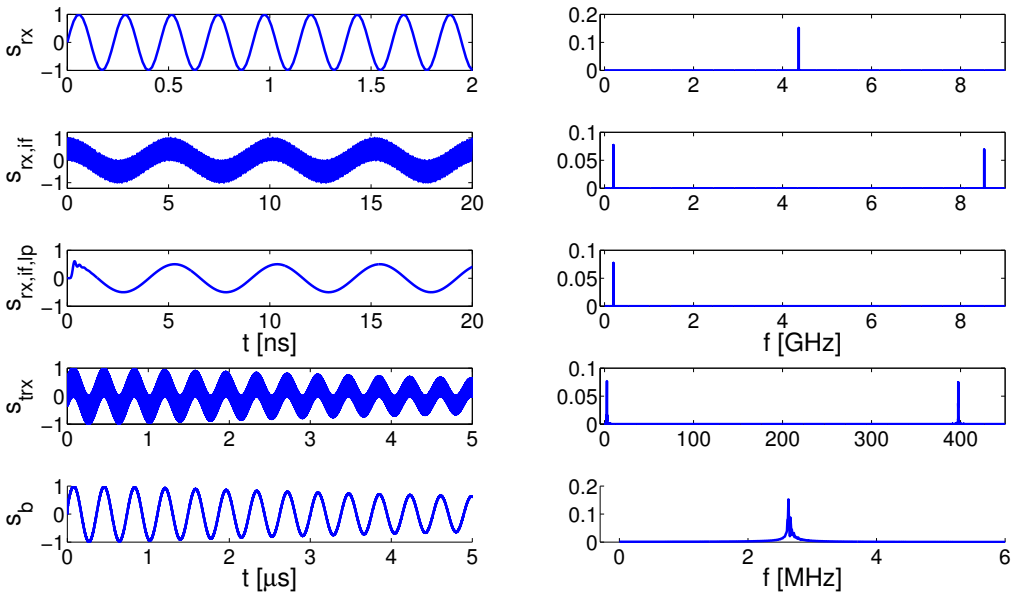

Figure 2.36: Simulation - Local Oscillator Automatic Tuning receiver

The subsequent low pass filter isolates the frequency $f_{tx,if,lp} = f_{tx,if,2}$. This internal step is not provided by the simulation example figure to focus on the received signal shares. The resulting frequencies of the final mix down to the signal s_{trx} can now be calculated by equation 2.71.

$$\begin{aligned} f_{trx,1} &= f_{tx,if,lp} + f_{rx,if,lp} = f_{if} + f_{if} - f_b \\ &= 2f_{if} - f_b \approx 397.4\,\mathrm{MHz} \\ f_{trx,2} &= f_{tx,if,lp} - f_{rx,if,lp} = f_{if} - f_{if} + f_b \\ &= f_b \approx 2.6\,\mathrm{MHz} \end{aligned} \tag{2.71}$$

5. Finally, the low pass filter isolates the beat signal s_b. The frequency gradient of the sawtooth modulation is parametrized according to equation 2.72.

$$\dot{f}_m = \frac{300}{\Delta T_m}\mathrm{GHz\,s^{-1}} \tag{2.72}$$

The time-of-flight τ of the signal can be calculated by equation 2.73.

$$\tau \approx \frac{f_b}{\dot{f}_m} = 866\,\mathrm{ns} \tag{2.73}$$

With the speed of light $c = 299\,792\,458\,\mathrm{m\,s^{-1}}$, the measured distance h_{agl} can be calculated by equation 2.74.

$$h_{agl} = \frac{c}{2}\tau \approx 130\,\mathrm{m} \tag{2.74}$$

2.2.6.2 Simulation: Single Sideband Receiver

The same step-by-step simulation is now applied to the SSB Radar receiver. The simulation example is given in figure 2.37. The plot structure is similar to the introduced LOAT simulation: the first column showing the time representation of the signal, the second is showing its frequency-domain representation. The SSB receiver processes the received signal in four main steps as follows:

1. The first row shows the signal at the receiver antenna input. The SSB example uses the same center frequency $f_c = 4.3\,\mathrm{GHz}$, but with another absolute modulation frequency of $f_m \approx 63\,\mathrm{MHz}$, due to the deviating height above ground for this simulation. The frequency of the received signal s_{rx} can be added up to $f_{rx} \approx 4.363\,\mathrm{GHz}$. The corresponding transmit signal s_{tx}, which is not plotted in the simulation, has a current frequency of $f_{tx} = 4.3666\,\mathrm{GHz}$. The difference of the both signals is about $f_b \approx 4\,\mathrm{MHz}$.

2. The second row illustrates the time and frequency domain of the mixed signal s_{trx}, which results from the mix of the received signal with a signal denoted by $s_{tx,lo,sbf}$. This signal is the sideband filtered signal of the current transmit signal s_{tx} using the constant local oscillator signal s_{lo}. For this simulation, the local oscillator frequency

has been chosen to $f_{lo} = 500\,\text{MHz}$. The two frequency shares of the unfiltered signal $s_{tx,lo}$ are calculated by equation 2.75.

$$\begin{aligned} f_{tx,lo,1} &= f_{tx} + f_{lo} = 4.863\,\text{GHz} \\ f_{tx,lo,2} &= f_{tx} - f_{lo} = 4.363\,\text{GHz} \end{aligned} \tag{2.75}$$

The band pass filter eliminates the upper frequency, the resulting signal $s_{tx,lo,sbf}$ has the frequency $f_{tx,lo,sbf} = f_{tx,lo,2}$. The frequency components of the signal s_{trx} are given by equation 2.76 and can be decomposed with the relation $f_{rx} = f_{tx} - f_b$.

$$\begin{aligned} f_{trx,1} &= f_{rx} + f_{tx,lo,sbf} = f_{tx} - f_b + f_{tx} - f_{lo} \\ &= 2f_{tx} - f_b - f_{lo} = 8.2292\,\text{GHz} \\ f_{trx,2} &= f_{rx} - f_{tx,lo,sbf} = f_{tx} - f_b - f_{tx} + f_{lo} \\ &= f_{lo} - f_b = 496\,\text{MHz} \end{aligned} \tag{2.76}$$

3. The resulting signal s_{trx} is again mixed with the local oscillator signal without prior low-pass filtering. A signal with four frequency components occurs. The four main frequencies of the signal $s_{trx,lo}$ are calculated by equation 2.77.

$$\begin{aligned} f_{trx,1} &= f_{trx,1} + f_{lo} = 2f_{tx} - f_b = 8.729\,\text{GHz} \\ f_{trx,2} &= f_{trx,1} - f_{lo} = 2f_{tx} - 2f_{lo} - f_b = 7.729\,\text{GHz} \\ f_{trx,3} &= f_{trx,2} + f_{lo} = 2f_{lo} - f_b = 996\,\text{MHz} \\ f_{trx,4} &= f_{trx,2} - f_{lo} = f_b = 4\,\text{MHz} \end{aligned} \tag{2.77}$$

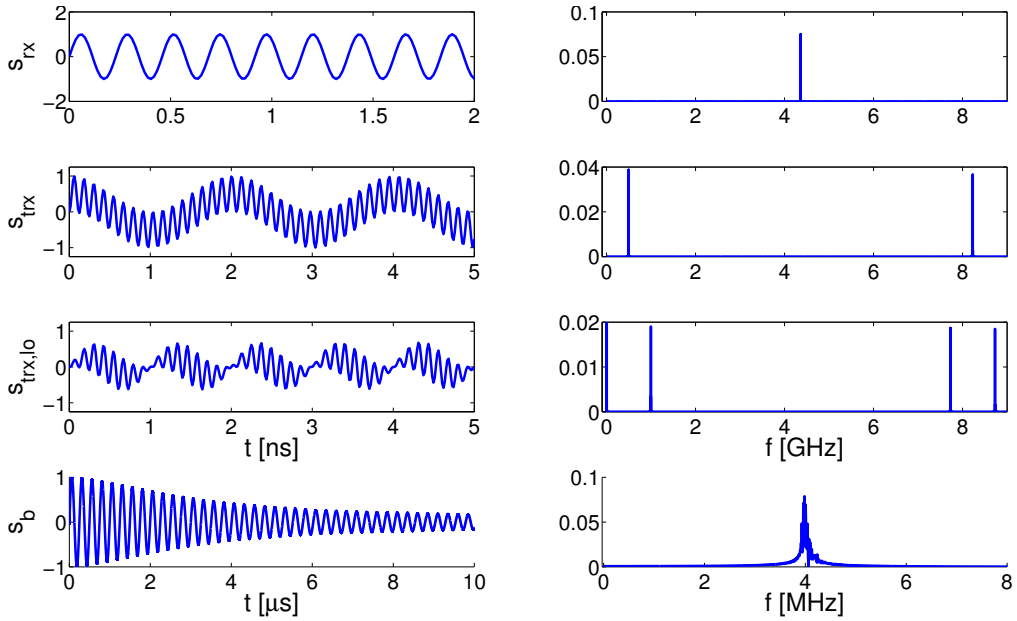

Figure 2.37: Simulation - Single-Sideband receiver

4. The final low-pass filter eliminates the frequencies $f_{trx,1}$, $f_{trx,2}$ and $f_{trx,3}$ to isolate the beat frequency. The further calculation of the height is similar to the LOAT receiver. It start with the calculation of the time-of-flight of the signal by equation 2.78.

$$\tau \approx \frac{f_b}{\dot{f}_m} = 1.33\,\mu s \tag{2.78}$$

The corresponding height above ground level is calculated by equation 2.79

$$h_{agl} = \frac{c}{2}\tau \approx 200\,m \tag{2.79}$$

2.2.7 Receiver Baseband Representation

The simulation of a high frequency signal, such as the carrier signal with the frequency f_c of a Radar altimeter, allocates a huge amount of digital memory and the signal processing generates a high computational burden. As shown in the chapter 2.1.3.4 and in chapter 2.2.6, the internal receiver signal processing generates signals with a maximum frequency of $f_{max} \approx 2f_c \approx 8.6\,GHz$. Fulfilling the Nyquist theorem, the signal has to be simulated at minimum with twice of f_{max}. This leads to a sample frequency of at least $f_{sample} \geq 2f_{max} \geq 4f_c \geq 17.2\,GHz$. One second of signal simulation would allocate a vector with 17.2×10^9 data fields. Assuming double precision vectors for the time stamp and the signal amplitude, the signal with a time duration of $\Delta t = 1\,s$ would allocate 275 GB. One approach to limit the computational burden and to reduce the allocated memory space can be the formulation of the signal in the baseband representation.
In equation 2.80 the calculation of the beat frequency is done in the baseband, the approach is derived for one beam ray with the delay τ_n and the assumption $f_{tx} > f_{rx}$. This assumption requires that the current transmit frequency and the received frequency can be compared within the same saw tooth cycle.

$$\begin{aligned} f_b(t) =& f_{tx}(t) - f_{rx}(t) \\ =& \dot{f}_m t - \dot{f}_m (t - \tau_n) \\ =& \dot{f}_m \tau_n \end{aligned} \tag{2.80}$$

The beat signal, representing the complete beam-shape, can now be reassembled in the baseband with the corresponding transmit power share $P_{tx,n}$, the different ray damping coefficient L_n and the runtime dependent beat frequency $f_{b,n}$. The summed up signal is given by equation 2.81.

$$s_b(t) = \sum_n^N L_n P_{tx,n} \cos\left(2\pi \left(\dot{f}_m \tau_n\right) t\right) \tag{2.81}$$

The case of a saw tooth cycle slip within the measurement duration can be detected by checking the condition $f_{tx} < f_{rx}$. In this case, the beat frequency is calculated by equation 2.82, the rearranged baseband signal is given in 2.83.

$$\begin{aligned} f_b(t) =& f_{tx}(t) + \Delta f_m - f_{rx}(t) \\ =& \dot{f}_m t + \Delta f_m - \dot{f}_m (t - \tau_n) \\ =& \dot{f}_m \tau_n + \Delta f_m \end{aligned} \tag{2.82}$$

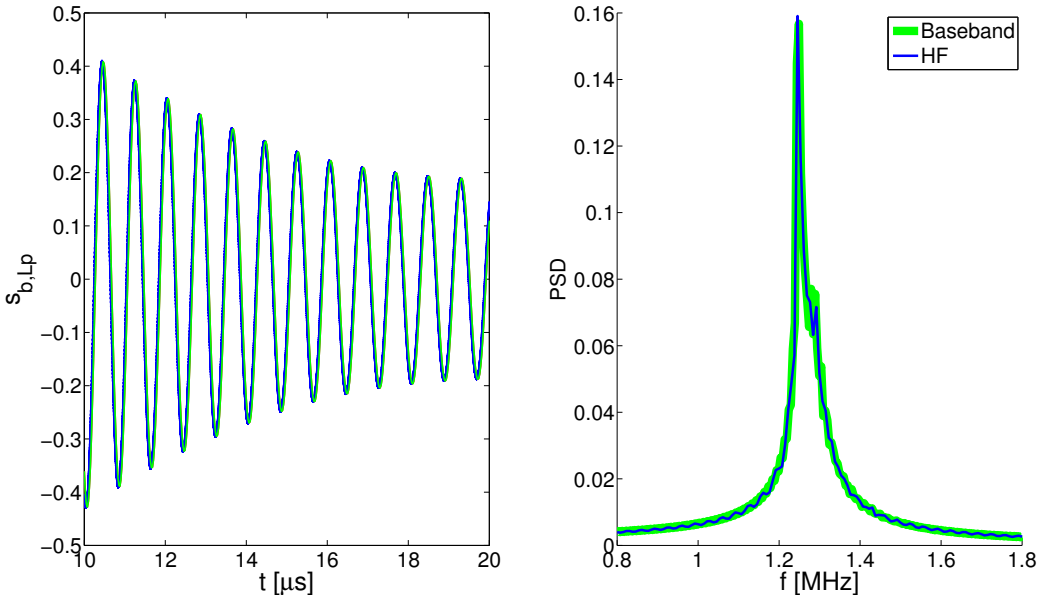

Figure 2.38: Baseband signal representation

$$s_b(t) = \sum_{n}^{N} L_n P_{tx,n} \cos\left(2\pi \left(\dot{f}_m \tau_n + \Delta f_m\right) t\right) \tag{2.83}$$

A comparison of the high frequency simulation on the carrier frequency f_c with the direct baseband simulation is illustrated in figure 2.38. In this example, the perfect match of the beat frequencies demonstrate that the signal simulation can be calculated in the baseband. This abstraction is the key technique to enable a signal simulation of a Radar altimeter.

2.2.8 Real Data Validation

An altimeter flight test campaign was realized to validate the previously derived detailed altimeter simulation model. Therefore, an altimeter measurement campaign has been realized, using a Quantum Systems [71] octo-copter Geo-X8000 and a Smart Micro Radar altimeter. The Radar altimeter UMRR-0A is a lightweight device with an integrated transmit and receive antenna. The Radar waveform is modulated on a 24 GHz carrier frequency, the altimeter has a measurement range up to 500 m and a measurement accuracy of 0.25 m or 2 % of height above ground, whichever is larger. A detailed technical specification can be found in [79]. The octo-copter is additionally equipped with an integrated navigation system including a Micro-Electro-Mechanical System (MEMS)-based IMU, a μBlox GPS receiver and a barometer. The position accuracy of the integrated navigation system is within two meters under good satellite constellation and visibility conditions. The navigation and altimeter data were recorded and analyzed in post processing. A picture of the flight test setup is given in figure 2.39.
The results of this real data study have first been published in [85]. The performance of the altimeter simulation model is shown with respect to three trajectories above varying surface types. First an approach trajectory has been realized, followed by a vertical ramp trajectory and a trajectory with constant altitude.
Detailed knowledge about the antenna characteristics could not be provided by the manufacturer. The antenna characteristics was interpolated from four known gain values. The

Figure 2.39: Flight test setup

resulting narrow beam-shaped antenna pattern is illustrated in figure 2.40.

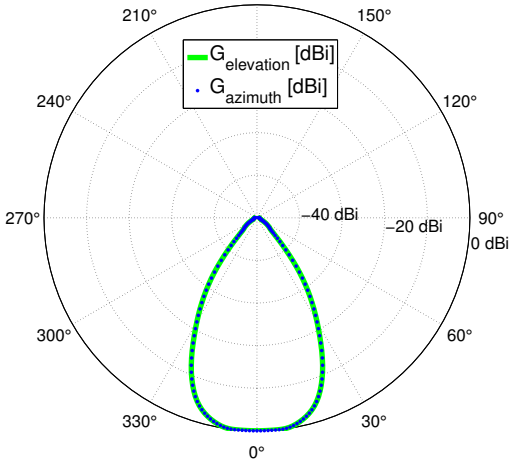

Figure 2.40: Estimated altimeter antenna transmission/reception characteristic

To compare the simulation with the recorded real data, the settings in table 2.8 have been chosen for the simulation model.

Parameter	**Value**
DEM source	NEXTMAP DSM
DEM resolution	$\Delta\lambda \times \Delta\phi = 5\,\mathrm{m} \times 5\,\mathrm{m}$
DEM vertical accuracy	$\delta h_{topo} < 1.5\,\mathrm{m}$
Number of rays	$N_{ray} = 2000$
Center frequency	$f_c = 24.125\,\mathrm{GHz}$
Update frequency	$f_s = 10\,\mathrm{Hz}$

Table 2.8: Validation: altimeter simulation model settings

The upcoming three flight test evaluations are provided in an equal structure. First, the trajectory is shown in a three-dimensional Google Earth visualization followed by the

measurement and evaluation time series plots. The upper graph of the result plots shows the absolute height of the reference trajectory with a solid DSM below it in reference to WGS84. The middle plot compares the measured Radar altimeter height above ground h_{agl} and the results of the simulation model and the lower plot indicates the errors between recorded h_{agl} and simulated height above ground in reference to the nadir height above ground.

2.2.8.1 Approach Trajectory

The performance of the simulation model is first shown on a trajectory imitating a fixed-wing aircraft approach. When reaching the initial height and position fix, the octo-copter is descending with a constant approach angle. To cover the requirement of a non-flat surface of an approach application, the trajectory leads above a small forest and continues over farm land. The flight tests took place in summer, while the data visualized in Google Earth have been recorded in springtime. A three-dimensional visualization of the approach trajectory with Google Earth is given in figure 2.54.

Figure 2.41: Approach trajectory - 3D track

The simulation model results are illustrated in figure 2.42.
The Radar altimeter simulation model matches the recorded data within an accuracy of a few meters, depending on the surface characteristics. Especially the height above the forest is only as good as the used digital surface model covers the real situation. In this case, the elevation database has a resolution of 5m in Northern and Eastern direction and an accuracy of about 1.5 m, which entails that smaller vegetation is not mapped exactly. Furthermore, seasonal differences have a huge impact on the simulation model performance. For a quantization of the simulation model performance, the Root Mean Square (RMS) error of the simulated height above ground is calculated with respect to the measured height. This quantity may not serve as quality indicator for the height measurement, it however indicates the quality of the simulation model. The RMS error is

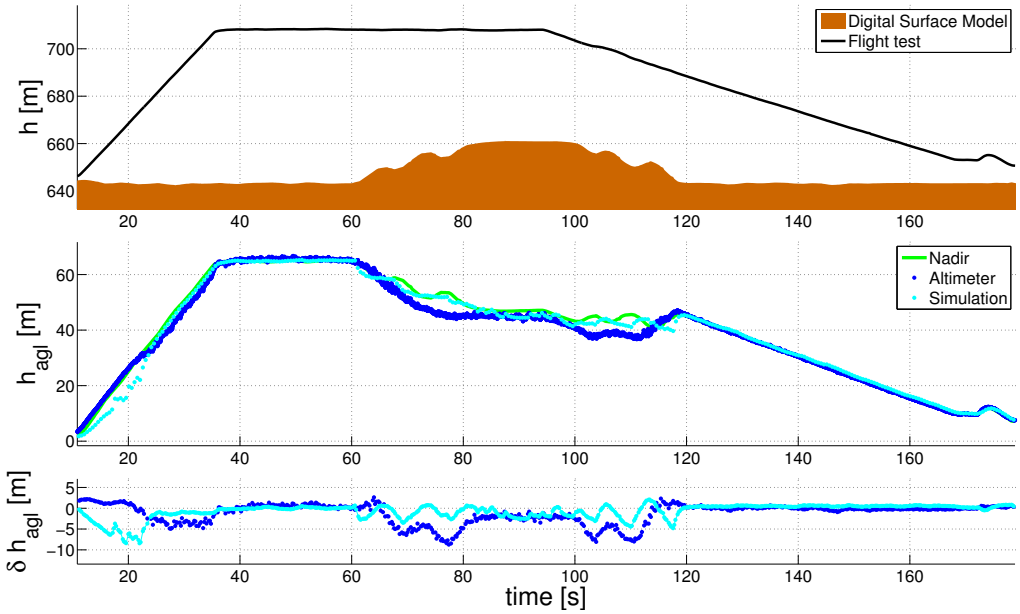

Figure 2.42: Approach trajectory - simulation vertical comparison

calculated to $\delta h_{rms} = 2.67\,\mathrm{m}$. Especially the flight above the forested area shows a bias-like deviation between the simulation model error and measurement error with respect to the nadir height ($60\,\mathrm{min} < t < 80\,\mathrm{min}$ and $100\,\mathrm{min} < t < 120\,\mathrm{min}$). Apart from this offset error, the simulated height above ground error seems to follow the measurement error. This observation affirms that the error source is caused by seasonal recording issues, which describes the major impact of the used DEM for the simulation model.

2.2.8.2 Vertical Ramp

In the second trajectory, the simulation model is compared to a recorded vertical ramp flight path above different surfaces. The first vertical ramp up to $h_{agl} \approx 100\,\mathrm{m}$ above ground level and back to the ground is flown once above a grass vegetated area, afterwards the same ramp is flown above a concrete area. A three dimensional visualization of the vertical ramp trajectory with Google Earth is depicted in figure 2.43.
The absolute height, the measured and simulated height above ground and the errors between simulation and recorded data are given in figure 2.44.
The accuracy of the simulation results regarding a scale factor error promise a linear, scale factor error free behavior, also for higher altitudes. The results for the first ramp, which were flown above grass ($t \approx 70\,\mathrm{s}$), are about $\delta h_{agl} \approx 2\,\mathrm{m}$ less accurate than the result for the ramp flown above an asphalt covered area ($t \approx 175\,\mathrm{s}$). While the measured height above the grass are systematically larger than the nominal height above ground, the good reflection characteristics of the asphalt provide slightly lower raw measurements. The RMS error of the altimeter simulation model with respect to the measured height is calculated to $\delta h_{rms} = 1.4\,\mathrm{m}$. It is remarkable that the model error depends on the properties of the overflown area. The RMS error above the asphalt area turn out to be $\delta h_{rms} = 1.2\,\mathrm{m}$, while the error increases to $\delta h_{rms} = 1.6\,\mathrm{m}$ above grass.
The dispersion of the radar wave due to grass vegetation surface area is one reason for this deviation, while an asphalt area provides a defined reflection. This result affirms the degradation of the simulation model performance above vegetated areas. Especially

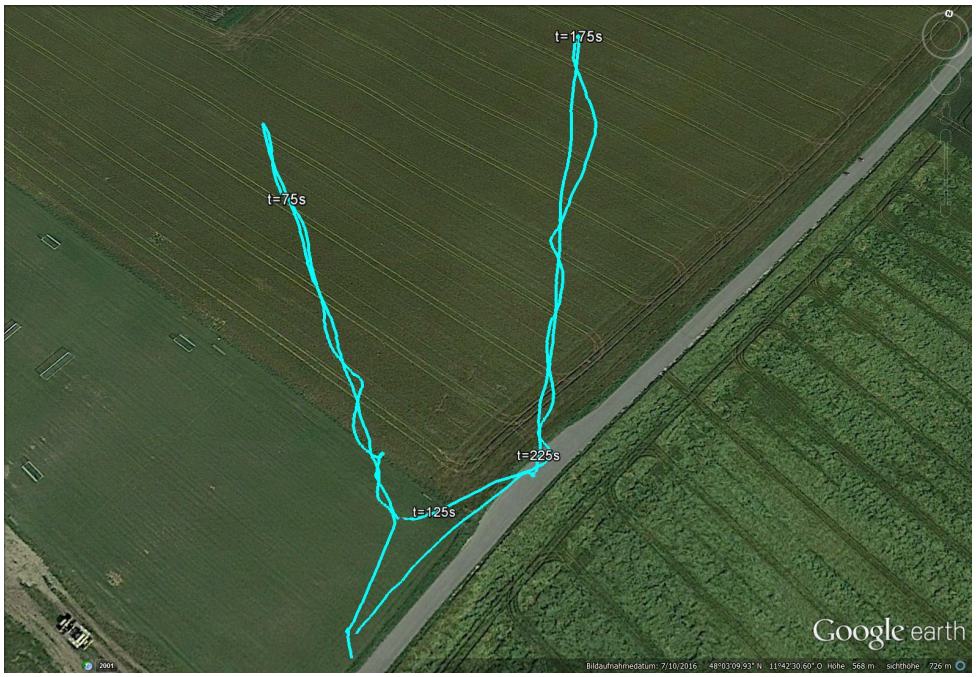

Figure 2.43: Vertical ramp - 3D track

areas with higher grass are strongly seasonal dependent. Those surface characteristics are difficult to cover in a simulation model, since the introduction of material properties would be required. A detailed description of Radar scattering is given in [86]. As conclusion, the results of this flight test confirm a good match between measurement and simulation concerning scale factor errors. The performance is in general degrading with increasing influence of the surface vegetation.

2.2.8.3 Constant Altitude

The campaign was concluded by a straight-and-leveled flight over different surfaces in a constant altitude. Especially the flight over and parallel to a forest is a specific challenge for the simulation model. A three dimensional visualization of the constant altitude trajectory with Google Earth is depicted in figure 2.45.
The vertical profile of the test flight is given in the established plot sequence in figure 2.46.
The simulation model shows a good performance compared to the recorded data. Especially, the entry and exit points of the forested area at $t = 100\,\mathrm{s}$ and $t = 150\,\mathrm{s}$ show a very good match between the altimeter model and the true altimeter receiver and antenna characteristic. In this situation, the quality of the used DEM has the major influence. At these time points, the platform is still over flat surface, while the antenna already measures the slant range to the tree tops. The RMS error of the simulated height above ground shows an error of $\delta h_{rms} = 1.72\,\mathrm{m}$ with respect to the measured height. This example demonstrates the performance of the simulation model, while the model strongly depends on the currentness and accuracy of the DSM. The altimeter antenna and signal processing behavior is covered quite accurately. The RMS error of the nadir height with respect to the measurement is calculated to $\delta h_{rms} = 3.72\,\mathrm{m}$. Summarizing the simulation model validation with respect to the applied DSM with a height accuracy of $\delta h_{agl} < 1.5\,\mathrm{m}$.

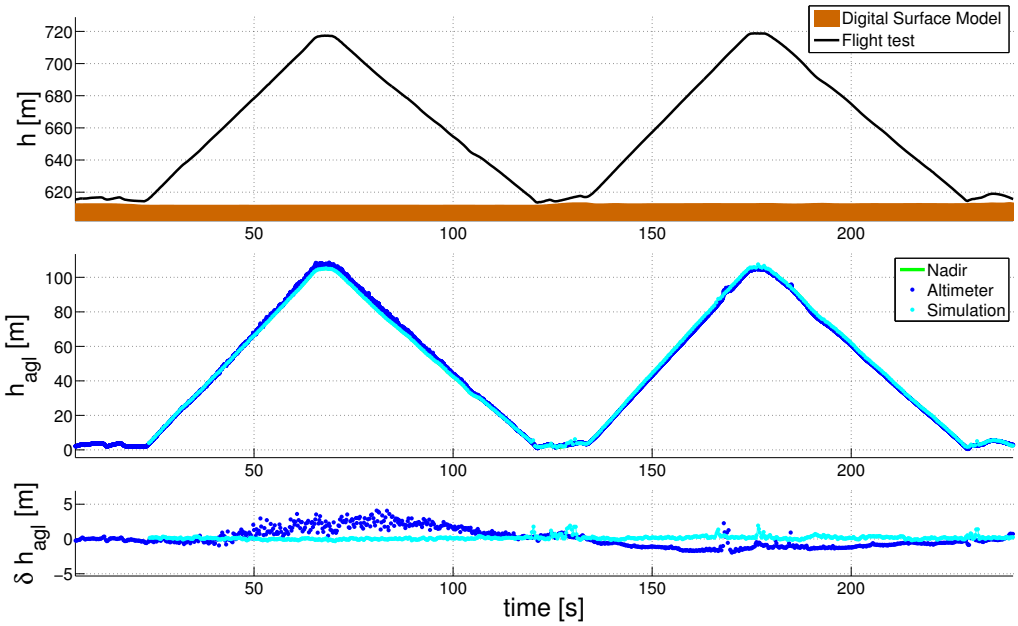

Figure 2.44: Vertical ramp - simulation vertical comparison

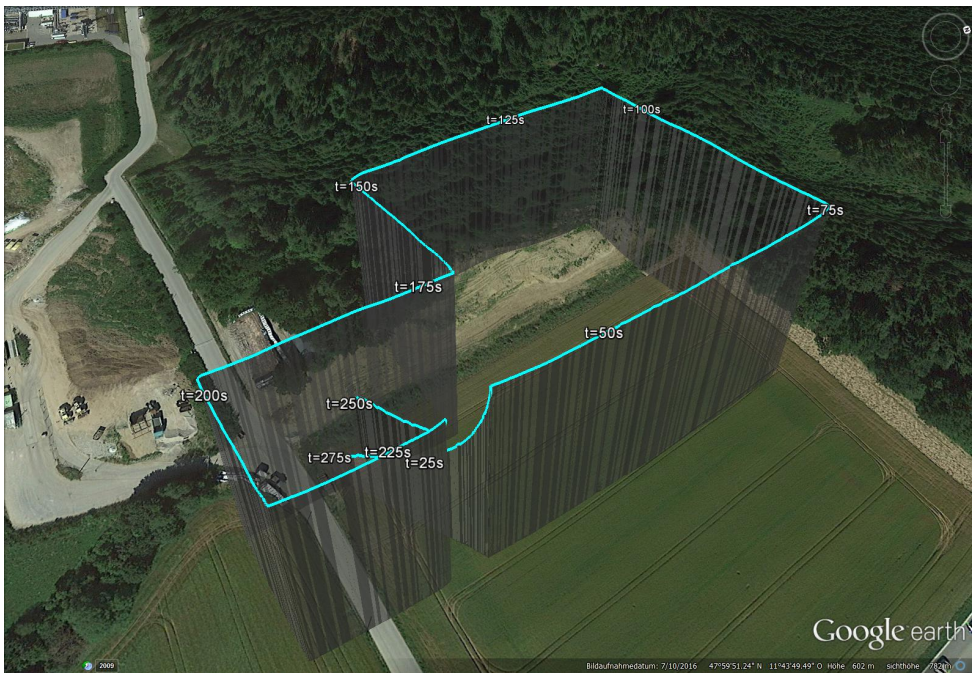

Figure 2.45: Constant altitude - 3D track

The following box summarizes the results:

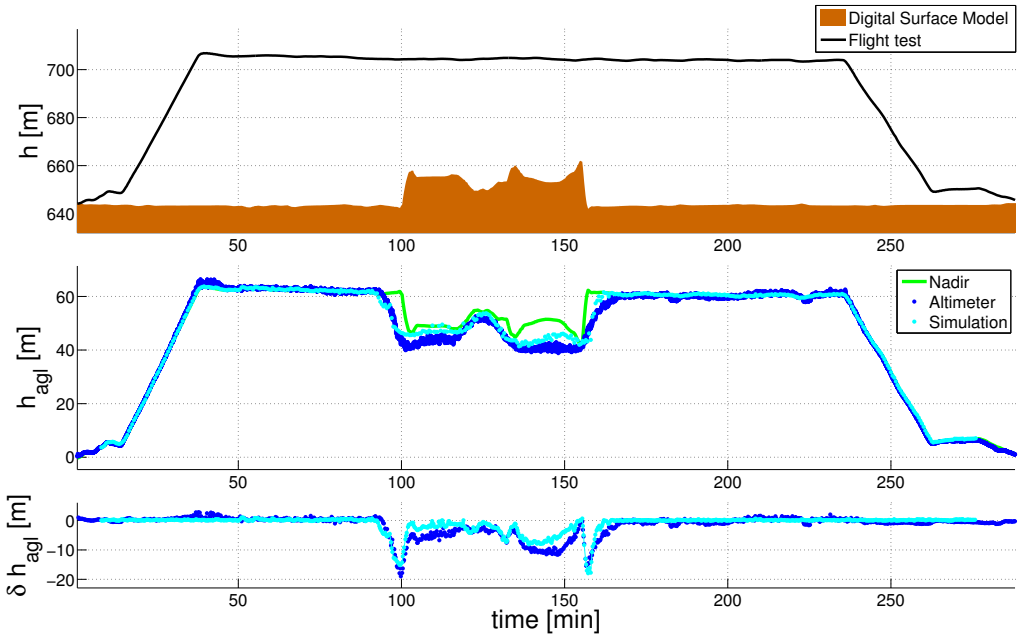

Figure 2.46: Constant altitude - simulation vertical comparison

Results

- Currentness of DSM is most important
- Seasonal differences have to be considered
- Surface reflectivity is not covered by the simulation model
- Scale factor errors are covered by the beam-shape simulation
- Good coverage of the beam-shape characteristic
- Performance is limited by DSM resolution, accuracy and currentness

2.3 Concept of Operation

The use of surface-ranging sensors in an airborne platform provides different challenges which will be discussed in this section. The problems of a height above ground measurement are various and strongly dependent on the nature of the measurement. Apart from general environmental error sources, a distance to ground or height above ground can be influenced by several geometric and wave propagation effects. In the first section, operating limitations are discussed followed by the analysis of slant-range measurement errors. A formal error description complements the theoretical part of this section followed by a simulation study. Parts of this analysis have first been published in [82], a student thesis has been supervised in this topic ([8]). The problem motivated by:

Motivation

- Surface-ranging sensors cannot provide a situation-independent nadir height measurement
- Influencing factors have to be identified for further improvements.

2.3.1 Operating Limitations

Active ranging sensors based on the ToF measurement principle generally depend on the reflectivity of the overflown surface. The surface characteristics define the maximum measurement range as well as the achievable accuracy. Apart from the surface characteristics, the weather conditions may also influence the measurement depending on the signal type of the sensor. While electromagnetic waves in a frequency range used for Radar altimeters are almost independent of the weather conditions, Laser light can be disturbed easily and cannot be used under poor visibility conditions for larger distances. Another challenging task is the integration of the altimeter in the aircraft fuselage. Laser altimeters and range-imaging sensors require a mounting with a direct line-of-sight to the surface. Normally, a cut-out has to be made in the fuselage, which can be a challenging task in terms of structural strength. For military applications, a cut-out at the platform bottom side is an even bigger problem, since the Radar cross section increases and hence the detectability. Radar altimeters do not require a cut-out in the platform fuselage, but an outside mounting of the antennas. From a structural point of view, this is a smaller effort compared to a cut-out. However, the antenna positioning in or on the fuselage provides additional challenges. Another aspect which can be important for the sensor selection is the capability of duplex or triplex operation. If the aircraft design or the certification regulations require more than a single altimeter, the altimeters have to be prepared to be synchronizable. Otherwise a measurement of one of the altimeters can disturb or even lead to an erroneous measurement of the other altimeters [83].

2.3.2 Slant-Range Measurement Errors

The height above ground is defined as the distance between the sensor platform and the nadir point on the surface below the platform. Due to different geometric effects, Radar altimeters do often not measure the vertical height above ground, but a slant range to the closest lateral surface. Three types of geometric effects are responsible for erroneous measurements, which are attitude dependent, beam-shape dependent and

surface variations dependent effects. The attitude dependency is caused by the limited Radar beam-cone aperture angle. Radar altimeter antennas with a sufficient half power beam-width are designed to compensate small roll and pitch angles over a flat horizontal surface. For attitude angles larger than the maximum allowed antenna compensation angles, the radar altimeter will measure a slant range. Designed to compensate for attitude angles, the beam-cone size can even increase the slant range measurement error in an unfavorable situation. If a surface variation (e.g. hills, buildings or vegetation) is within the beam-cone, the altimeter will likely measure a slant range, and thereby the shorter distance to the closest object. An example, illustrating an obstacle caused slant range measurement error, is given in figure 2.47 [83].

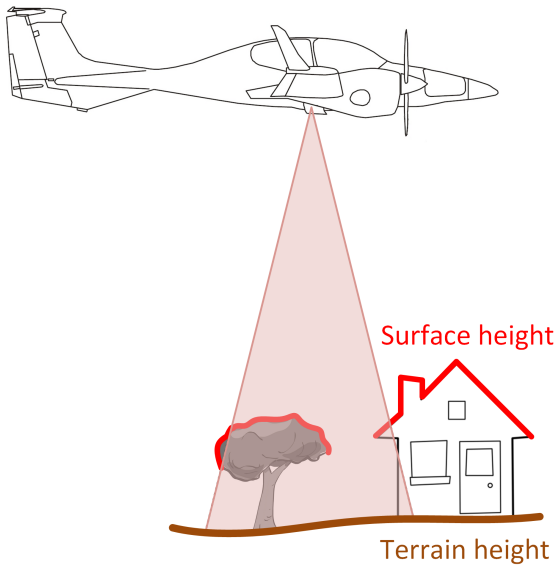

Figure 2.47: Obstacles measurement

Consequently, a narrow beam-cone is less influenced by surface variations, but to attitude caused slant range effects, while an antenna with wide characteristics is more tolerable to attitude dependent slant range causes, but has a higher risk of erroneous measurements due to surface variations. Apart from geometrical error sources in combination with surface dependent effects, the internal signal processing of a Radar receiver is another error source [83]. Radar and Laser altimeters are compared considering the beam-size in [21].
Dependent on the geometrical situation, the reflectivity of the surface and multi-path signal reflections leads to disturbed, distorted or spread received signals at the receiver antenna. These interferences are influencing the signal processing and can lead to erroneous height measurements. A graphical explanation of the different ranges is given in figure 2.48.
The latitude and longitude dependent platform nadir (P) and the attitude dependent platform perpendicular are exclusively determined by the platform geometry. The antenna beam-center is additionally tilted by the sensor mounting angles, while the first reflection of the Radar is also influenced by the geometric shape of the surface. The real measured slant range is furthermore influenced by signal propagation, reflection and processing effects. The following subsections give a detailed explanation of the three main error sources [83].

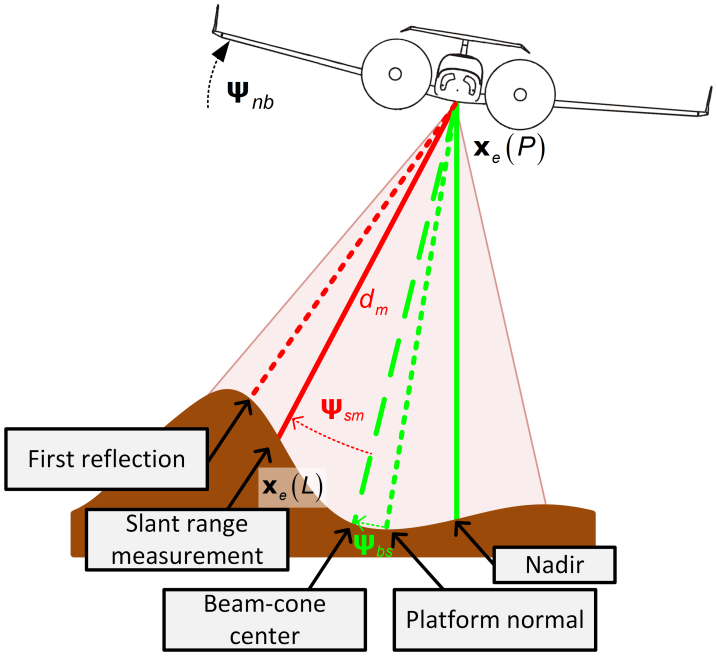

Figure 2.48: Altimeter measurement description

2.3.2.1 Attitude Dependency

The most obvious slant range-causing situation occurs when the platform is flying unleveled. In flight phases such as departure, bank-to-turn or final approach, where either the platform is changing the flight level or the heading, the platform perpendicular is not pointing to the platform nadir. Figure 2.49 shows the effect of a small roll angle on the altimeter measurement with an antenna providing a narrow beam-cone shape. While the antenna center points to the side, the beam-cone can compensate a part of the slant range measurement, whereas there is however still a remaining height error.
An isolated evaluation of the attitude casued slant range errors is given in figure 2.50. The illustration shows the attitude dependency of the height measurement over a roll angle range of $\phi = 0°..75°$ for the three different nominal heights above ground $h_{agl,1} = 100\,\mathrm{m}$, $h_{agl,2} = 400\,\mathrm{m}$ and $h_{agl,3} = 800\,\mathrm{m}$. Additionally, the illustration covers the effects of the increasing roll angle for a narrow shaped beam-cone and a wide shaped beam characteristic. The red area highlights the exceedance of the maximum measurement range d_{max} described by equation 2.84.

$$d_{max}(\phi) = h_{agl}\cos(\phi) \tag{2.84}$$

The analysis shows different attitude and height dependent effects. First, the spreading of the two different beam-shapes is remarkable even with no rotation. While the narrow shaped beam-cone provides a comparatively small spreading of the received signal, the received signal of the wide beam-cone shape spreads up to $\Delta h \approx 100\,\mathrm{m}$ for the nominal height $h_{agl,3}$. The analysis of the responses with higher rotations of about $\phi > 30°$ shows the benefits of the antenna with the wide beam characteristics. While the rising edge of the signal received by the wide beam-cone provides the nominal height above ground, the signal of the narrow beam antenna is delayed and hence erroneous. This effect increases with increasing attitude angle. On the other hand, the falling edge of the wide beam-cone

shaped antenna is dramatically more distorted compared to the signal received with the narrow beam shaped antenna. Summarizing, a narrow beam shape antenna has benefits when the platform is in a leveled flight phase. In this situation, the smaller illuminated surface area results in a more defined reflection signal, compared to the wide beam-cone pendant. A wide beam shape antenna provides a vice versa behavior. The disadvantage of this antenna type is the huge spreading of the received signal in a leveled situation. On the other hand, this effects enables the capability of compensating slant range measurement. A narrow beam shaped antenna provides a smaller defined measurement direction and opens opportunities for an algorithmic compensation of the attitude caused slant range measurement.

2.3.2.2 Surface Variations

While for attitude caused slant range errors, a wide beam-cone shape can compensate for slant range errors, the error could also increase with a wider beam-cone shape in unfavorable situations. Due to the increased field-of-view of the wider beam-shape altimeter, the probability of surface variations within the illuminated area increases. These variations of the Earth's surface or reflecting obstacles lead to slant range measurements and hence to errors which cannot be easily compensated for.
Figure 2.51 illustrates a situation where the surface variations are responsible for a shortened height above ground measurement due to the hilly surface characteristics within the beam-cone. While this aspect considers the surface variation, in the next section the main focus is on the interaction of these causes and the corresponding effects on the received signal.

2.3.2.3 Signal Dependency

For flat surfaces, a wide beam-cone is designed to compensate for platform attitudes, i.e. is not vulnerable for slant range measurements. For narrow beam-cone shaped antennas,

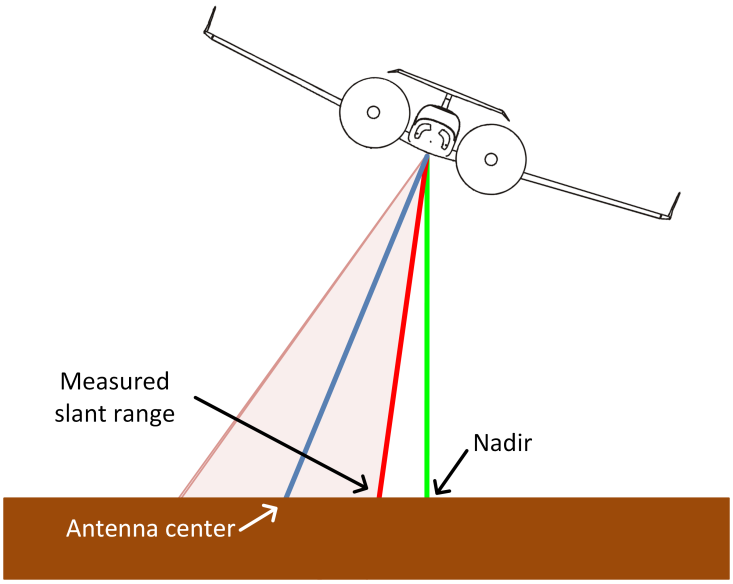

Figure 2.49: Slant range - attitude dependency

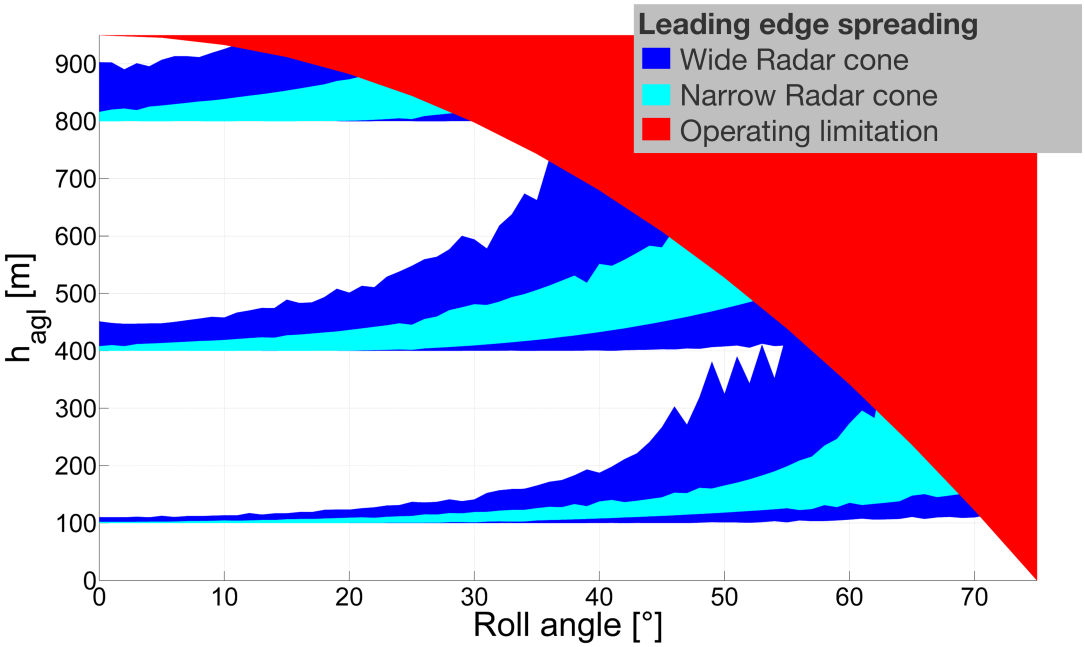

Figure 2.50: Attitude dependency error characteristics

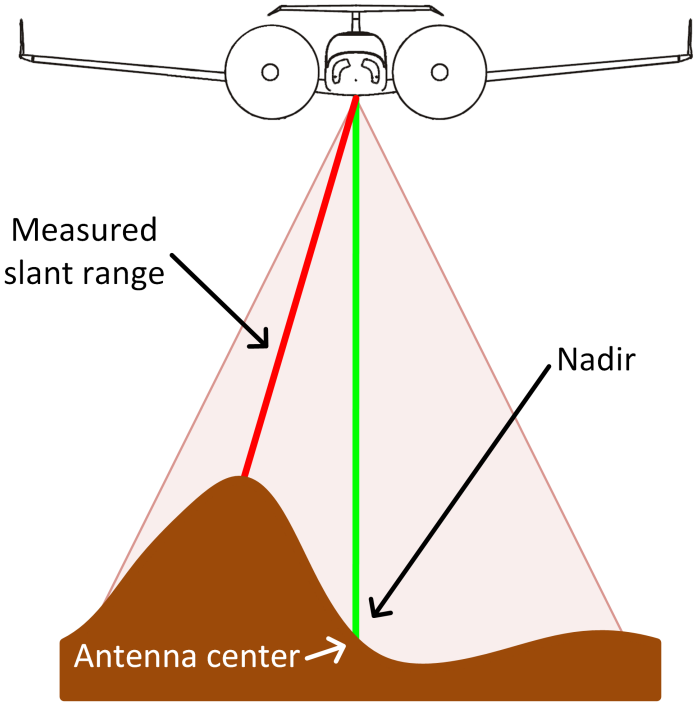

Figure 2.51: Slant range - surface variations

rough surface is also an error source by measuring non-representative areas, for example the top of a local hill or the bottom of a valley. A combination of the three slant range causing effects is shown in figure 2.52.

Apart from the geometrical error sources, the signal processing of a Radar receiver is an additional error source. Beginning with the radiation at the transmit antenna, the signal underlies the environmental conditions and signal propagation effects. Additionally,

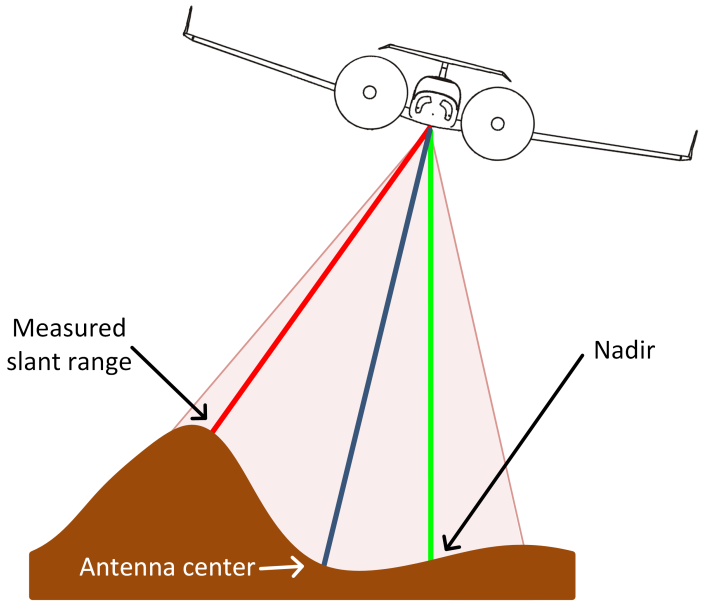

Figure 2.52: Slant range - combined effects

different reflectivity characteristics of the measured area can distort the signal reception by over-weighting specific well reflecting areas and under-weighting others. Receiving the signal at the antenna, the signal and the existing noise are being processed receiver internally to find a representative distance measurement. Figure 2.53 illustrates a representative Radar altimeter response including the noise level, a rising and a falling edge.

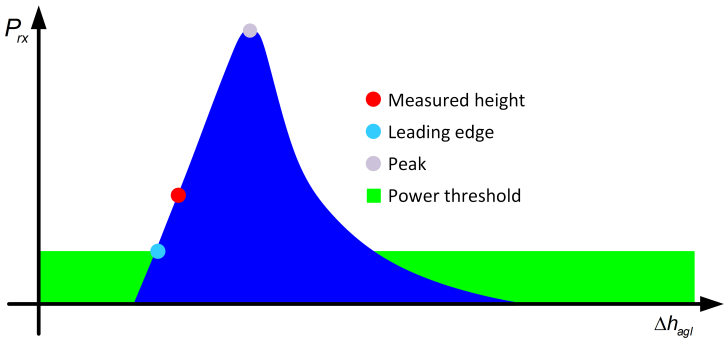

Figure 2.53: Leading edge detection

2.3.3 Simulation Study

This section exemplifies the concept of operations consideration and the entire surface-ranging sensor chapter with a simulation study. Two scenarios, an approach trajectory and a fighter aircraft trajectory, are considered to quantify the slant range error influences on altimeters. The approach trajectory is characterized by smooth platform dynamics and a surface typical for a smaller rural airfield. To provide also a consideration of military applications of Radar altimeter, a high dynamic trajectory above a rough surface in a hilly environment is analyzed. The fighter aircraft trajectory features high platform

dynamics, especially in the roll axis, flown with a small ground clearance. Both scenarios are simulated with a pencil beam Laser altimeter, a narrow beam-cone Radar altimeter and a wide beam-cone Radar altimeter.

2.3.3.1 Approach Trajectory Scenario

The trajectory starts in the South-West with the downwind sector heading North-East at an altitude of about $h \approx 8000\,\text{ft}$. The trajectory provides a bank-to-turn maneuver onto the airfield base leg and a final bank-to-turn for the localizer interception with a stepwise descend to the final approach. The three-dimensional Google Earth illustration of the approach trajectory is given in figure 2.54. The trajectory is flown with typical dynamics of an airliner aircraft.

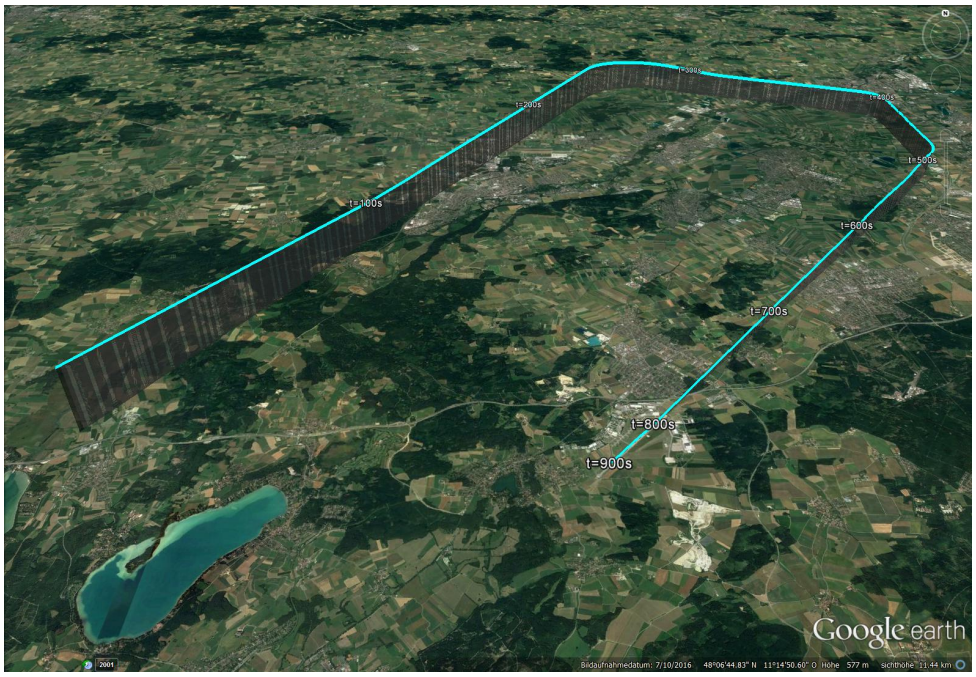

Figure 2.54: Approach trajectory - 3D track

To isolate the platform and beam-cone shape caused effects from the surface dependent effects, this trajectory is also simulated above a virtual flat Earth surface. The local topographic height is assumed to coincide with the airfield elevation and is virtually added to the simulation environment. Figure 2.55 illustrates the absolute height h, the height above ground h_{agl} and the height error δh_{agl} in reference to the nadir height of the three sensors. Additionally, the aircraft roll and pitch are plotted in the lower row plot. As expected, the beam-cone shape has a significant influence on the measured height above ground. The pencil beam of the Laser altimeter causes large measurement errors during the bank-to-turn maneuvers of the platform. The point measurement to the surface does not provide any compensation for the roll angle. Especially over flat surface, these error characteristics can be observed due to the missing influence of surface variations. Both Radar altimeters can compensate the bank-to-turn maneuvers in a very good way. However, the benefit of the wide beam-cone can further reduce the measurement error compared to the narrow beam-cone, especially during the second bank-to-turn maneuver. While the first and the third maneuvers are flown within the roll limitation specifications

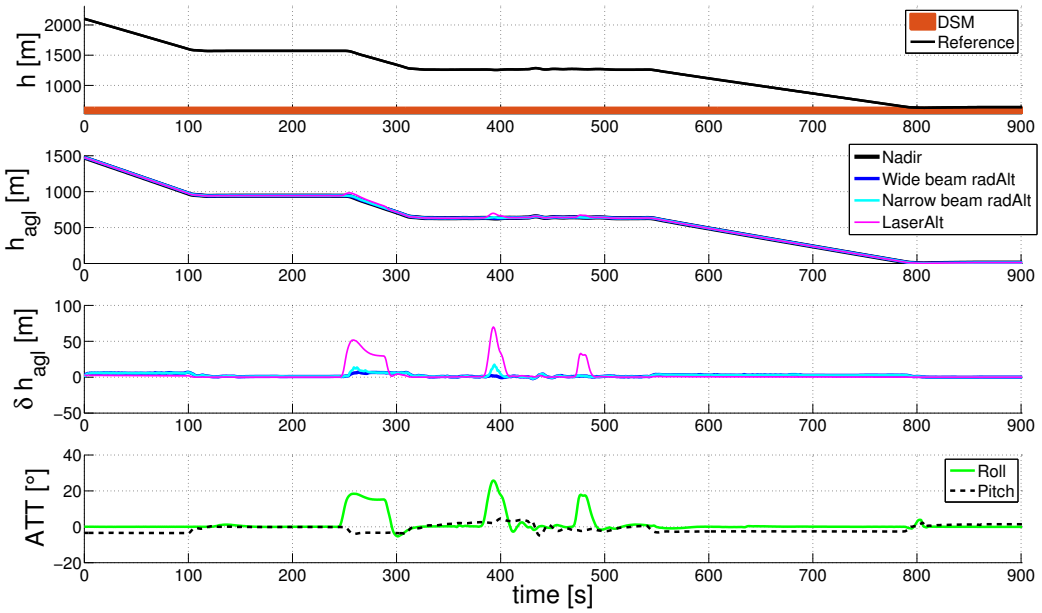

Figure 2.55: Approach trajectory - vertical situation (flat surface)

of both altimeters, the second one exceeds the specification of the narrow beam-cone altimeter. As predicted in figure 2.50, this exceedance causes a slant range measurement and thereby a measurement error. Another observable effect is a small scale factor error of both Radar altimeters for larger heights above ground. Due to the wide enlargement of the Radar footprint, the Laser altimeter is beneficial is this situation.
Following, the simulation results are shown for the same approach trajectory above the realistic elevation profile. The absolute height h, the height above ground h_{agl}, the height errors δh_{agl} and the platform attitude are shown in figure 2.56.

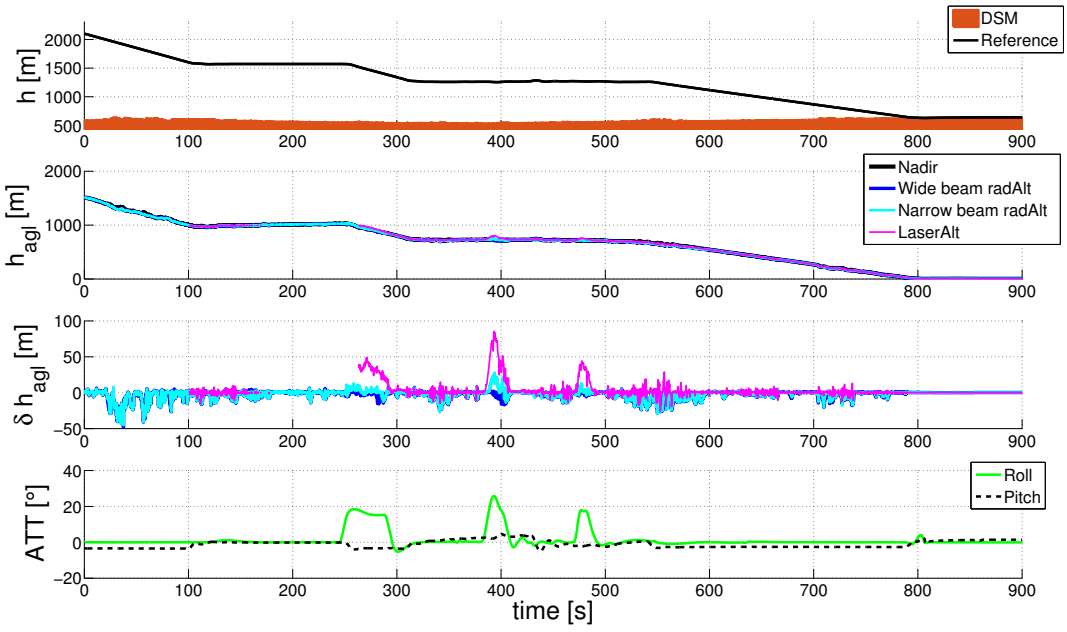

Figure 2.56: Approach trajectory - vertical situation

Applying the realistic surface elevation to the same trajectory provides the same error

characteristics of the altimeters as for the virtual flat Earth. The Laser altimeter errors are still dominating the error spectrum. Not only in the situation with an unleveled platform, but also dependent on the surface variations on the ground. Also, both Radar altimeters exhibit additional errors. At the beginning of the trajectory, both Radar altimeters measure the top of the illuminated surface area. Thereby, the measured distance is shorter than the current nadir height above ground. Especially, above rough areas where the energy is reflected first by exposed hills or similar formations, the same effect can be observed along the trajectory. Another example of this effect can be observed at $t = 550\,\mathrm{s}$. The attitude caused effects however dominate the error spectrum compared to the surface dependent errors. The effects of a rough surface are analyzed in the second simulation example.

2.3.3.2 Low-Level Flight Trajectory

The second simulation example features significantly higher flight dynamics. Since the previous simulations showed the inappropriateness of the Laser altimeter for this kind of dynamics, only the Radar altimeters are compared. The considered trajectory starts in the East with a low-level flight path heading West first and North-West afterwards. The three-dimensional Google Earth representation of the trajectory is given in figure 2.57.

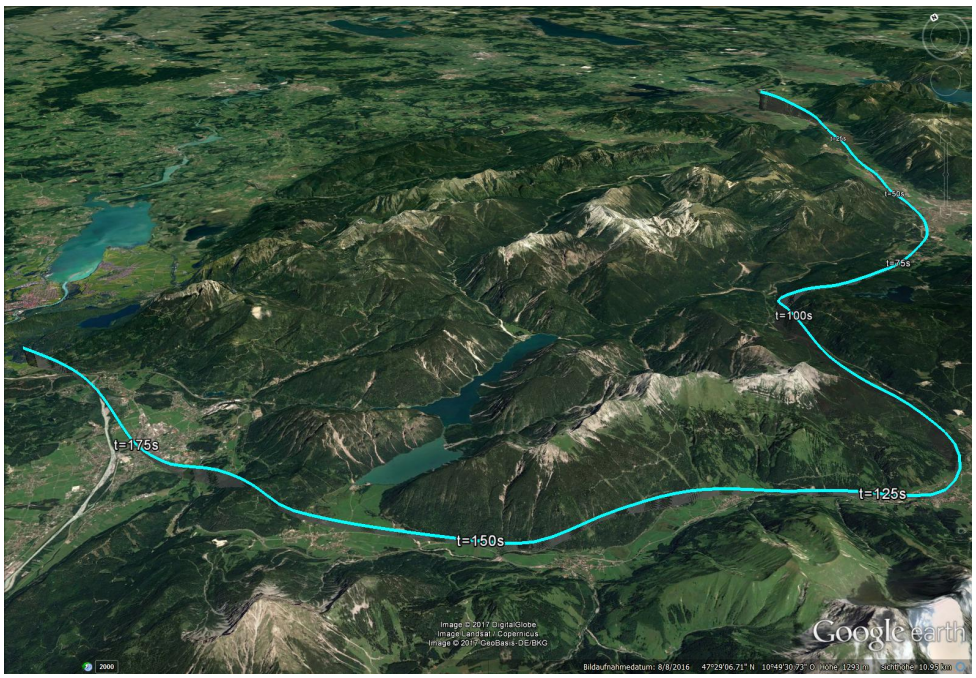

Figure 2.57: Low-level trajectory - 3D track

First, the simulation results are again shown for the virtual flat Earth for a better isolation of the error effects. The height h, the height above ground h_{agl}, the height errors δh_{agl} and the platform attitude are given in figure 2.58.
The effects discussed in the first simulation example are exposed more obvious in this simulation. Due to the high platform dynamics with large roll angles, the benefits of the wide beam-cone altimeter become obvious. The results in figure 2.59 in contrast provides the flight path above the true elevation profile.

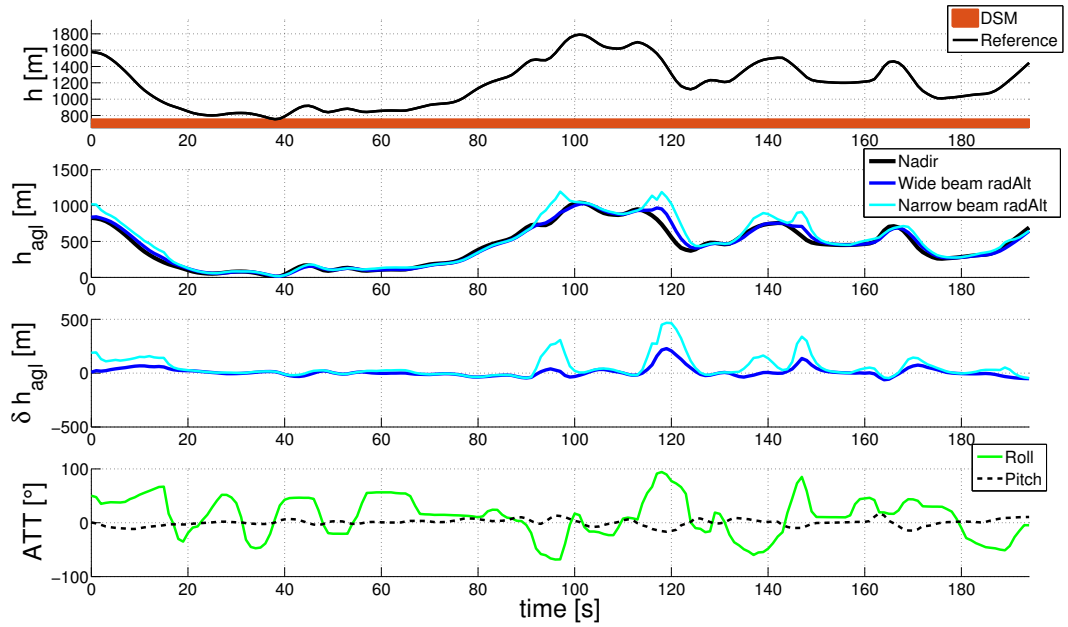

Figure 2.58: Low-level trajectory - vertical situation (flat surface)

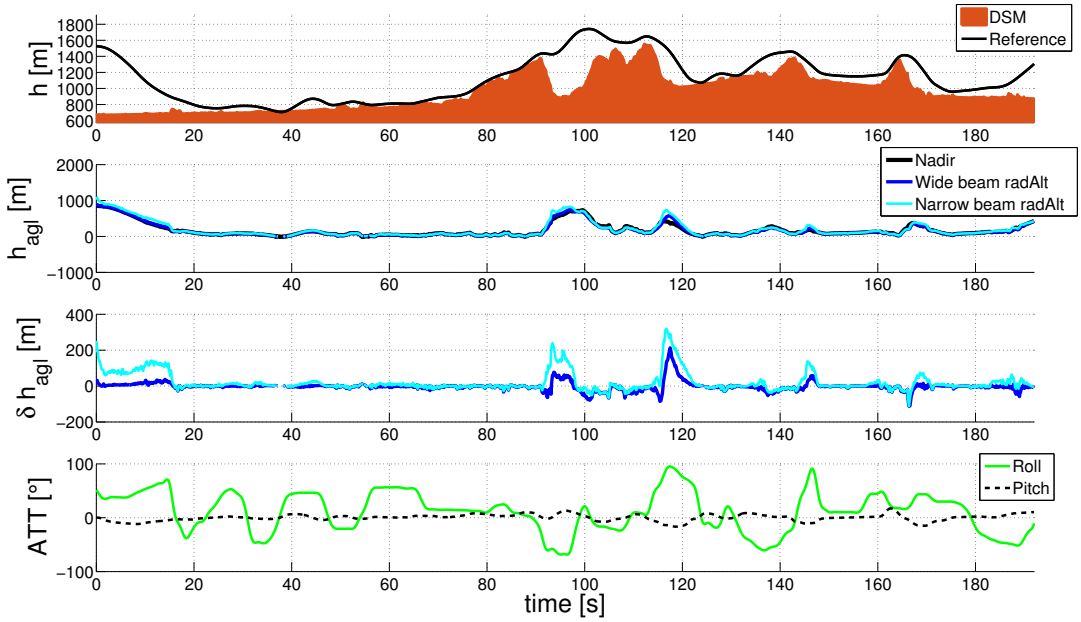

Figure 2.59: Low-level trajectory - vertical situation

Obviously, the height above ground decreases for the realistic surface and hence the observed slant range effects are reduced, too. The main characteristics of both altimeters are affirmed with this simulation results. The narrow beam-cone altimeter performs well within its attitude limitations where the majority of signal energy is still reflected by the surface. For larger roll angles $\phi > 50°$, this requirement is not fulfilled anymore. In such situations, the wide beam-cone altimeter is beneficial. The wide beam-cone allows larger roll angles without losing the reflecting surface. Both altimeter however stop working when the roll angle exceeds $\phi \approx 90°$ without facing a reflection surface.
Finally, the simulation results show advantages and disadvantages of the three altimeters in different situations. While the narrow beam-cone altimeter is beneficial when the majority of the signal energy is reflected, it is vulnerable to larger roll angles. The wide beam-cone altimeter provides a complementary characteristic. While the vulnerability to measurement errors is larger for smaller roll angles, the altimeter can provide a valid measurement for larger roll angles. While the pencil beam-cone dominates the error characteristics, a defined point-distance measurement Laser from a Laser altimeter or narrow beam-cone shaped Radar altimeter in a compensation friendly measurement. This designated slant range measurement can be compensated more accurately due to the smaller and defined reflecting surface. Conclusively, the type of altimeter has to be chosen under consideration of the application requirements, platform dynamics and surface characteristics, since no best sensor for all situations has been identified. The main results of this section are concluded in the following box:

Results

- Wide beam-cones are beneficial for high platform dynamics
- Narrow beams concentrate the signal energy and provide a defined response
- Pencil beams provide a defined and compensation friendly measurement direction
- The sensor has to be selected under consideration of the platform dynamics, the mission profile and the expected surface characteristics

Chapter 3

Vertical SAN

For a safe landing under poor visibility conditions, larger airfields offer navigation aiding systems like an ILS or a Ground Based Augmentation System (GBAS). Small or temporary airfields cannot offer expensive ground infrastructure, and the pilot has to navigate with the aircraft internal sensors to the minimum decision height. In this case the pilot has to decide whether the runway is visible and a safe landing is guaranteed or has to divert to an alternate airport. A diversion is often associated with increasing costs as far as a return flight to the origin airport in case of an island. There are three categories to cluster the approach conditions for instrument guided landings under poor visibility conditions. The visibility conditions are given in table 3.1, more detailed information is provided in [50]. The approach situation with a characteristic surface of a smaller airfield below the approach path is illustrated in figure 3.1.
Radar altimeter measurements are often applied in the landing control algorithms for an automatic landing under CAT II/III conditions. Not only the aircraft has to be certified for an automatic landing, but also the airfield has to be prepared for an operation under those conditions. Apart from wide aircraft separations and special taxiway hold positions in the ATC procedures, the airfield has to provide a Radio Altimeter Operating Area (RAOA). Smaller airfields often do not provide such an obstacle free reflection area and the surface below the approach pattern can contain vegetation, terrain variation and buildings. A schematic visualization of the RAOA is given in figure 3.2 [1].

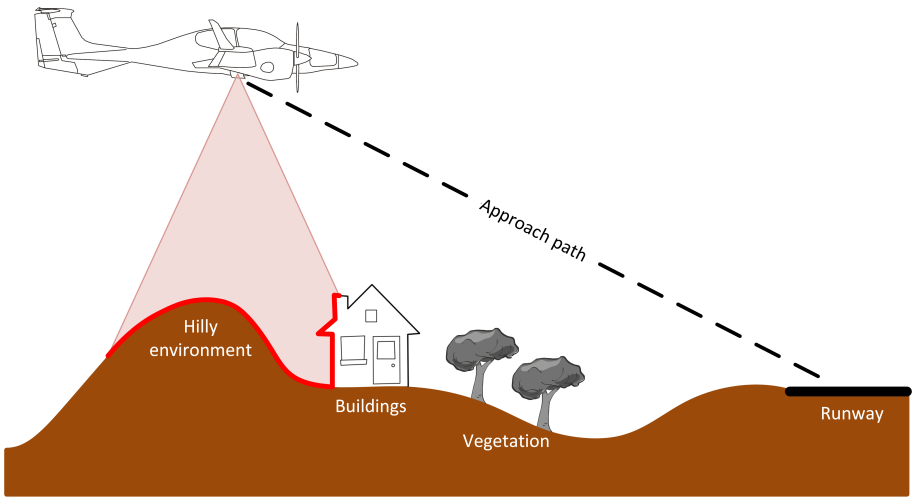

Figure 3.1: General aviation aircraft approach on small airfield

CAT	Decision height	Runway visual range
I	$> 200\,\text{ft}$	$> 1800\,\text{ft}$
II	200 ft-100 ft	$> 1000\,\text{ft}$
IIIa/IIIb/IIIc	$< 100\,\text{ft}/< 50\,\text{ft}$/no limit	$< 600\,\text{ft}/< 150\,\text{ft}$/no limit

Table 3.1: CAT visibility conditions

Low-level trajectories have generally similar requirements and preconditions as airfield approaches, for example a fighter aircraft in a terrain-following flight mode. These flight situations often occur in military aviation, where the low-altitude profile is a requirement to decrease the probability of detection. In this scenario, the vertical accuracy of a GNSS aided integrated navigation system is degraded by the high attitude dynamics. The high dynamics especially in the roll axis cause satellite signal losses due to the GNSS antenna beam-shape. Furthermore, the topographic surrounding of a low-altitude trajectory restricts the visibility to the satellites with low elevations due to terrain shading. Conclusively, whenever a platform flies with a low ground-clearance, the probability of degradation of the important vertical navigation accuracy is increased. The geometrical degradation of the satellite constellation is indicated with the Vertical Dilution of Precision (VDOP). The motivation is summarized in the following box. Parts of the following chapter have already been published in [82], [83], [84] and [85]. In [16] a method for vertical aiding using GPS, Radar and barometric measurements and a fade-over algorithm is introduced. In [15] a Radar altimeter based method to reduced vertical navigation errors is introduced.

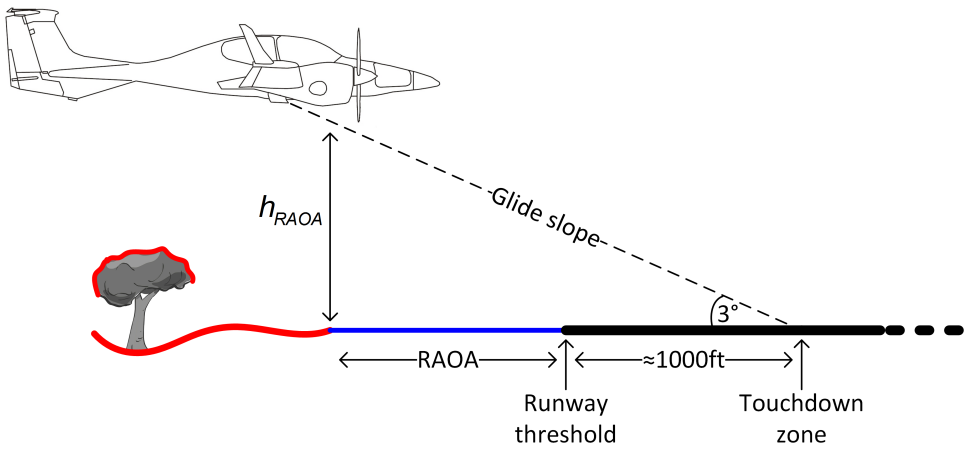

Figure 3.2: Radio Altimeter Operating Area

Motivation

- High satellite shading effects by surface elevation in low-level flights
- Degraded GNSS vertical position accuracy
- Altimeter measurement errors caused by surface variations, obstacles, platform attitude and beam-cone shape
- Altimeter measurement validity and variance information missing

Four methods to handle the described problems are introduced in this chapter. Beginning with a measurement validity assessment, which decides whether a measurement is valid and can be used for further processing or is invalid and has to be excluded from further processing. The measurement variance estimation provides a quality assessment of the measurement considering the entire platform and sensor situation and additionally the surface characteristics. As third method, the slant range compensation algorithm providing several compensation methods to improve the measurement accuracy is introduced. Not only the measurement accuracy can be increased with this method, but also the measurement availability is improved. The solution approach is summarized in the following box.

Solution Approach

- Validity assessment considering the aircraft states and surface characteristics
- Situation dependent measurement quality estimation
- Accuracy improvement by compensation algorithms

3.1 Measurement Validity

The measurement errors and limitations of Radar and Laser altimeters have been explained and discussed in section 2.3. These slant range measurement errors occur due to a combination of the three main influencing effects: the platform attitude, the beam-cone shape and the surface variation. Navigation systems which use external measurements rely on a consistent validity assessment and measurement covariance information. The exclusion of degraded measurements improves the accuracy of navigation systems. By excluding erroneous measurements, they cannot directly influence the integrated navigation system, however the update rate of the sensor is reduced or the measurements are excluded for a certain time period. Figure 3.3 shows the block diagram of an in-flight validity assessment algorithm using an altimeter simulation model coincident to the measurement.
Invalid altimeter measurements can have multiple reasons. Physically caused reasons, for example the extensions of the maximum measurement range will result in a reduction of the reflected power. If the reflected signal is not powerful enough to be distinguished from the noise floor, the height cannot be measured. In this case, a conventional sensor will not provide a measurement and the invalidity can easily be detected. Furthermore, sensor internal checks may provide a validity flag or another information within the transmission protocol indicating the measurement validity. In this chapter, invalid sensor measurements, that cannot be detected by the sensor itself, will be discussed. It is necessary to

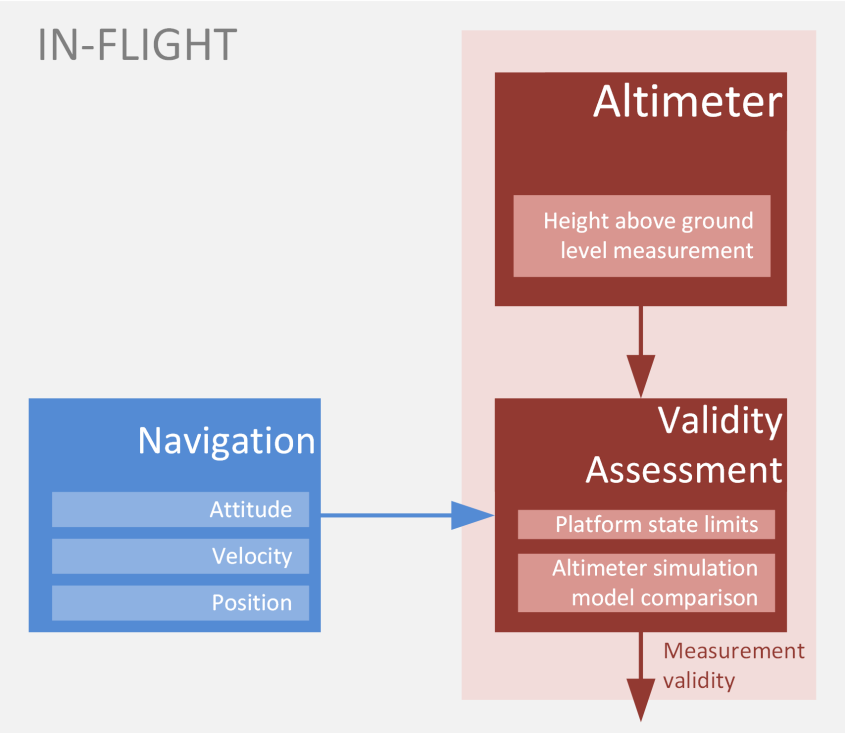

Figure 3.3: Validity assessment - architecture

analyze the sensor and the specific applications to find requirements for valid and invalid measurements. From sensor perspective, one reason for invalidity could be the exceedanca of the measurement range. Some sensors however continue transmitting erroneous measurements in this scenario, while the measured value exceeds the defined maximum measurement range. The measurement integrity cannot be guarantied and the measurement has to be excluded from further processing. With the same reason, a measurement dropping below the minimum measurement range should be ignored to ensure the operation within intended signal strength limits. Another reason for erroneous measurements is the platform roll and pitch angle. Depending on the beam-shape, the platform attitude angles may cause enormous measurement errors. Even the compensation of the slant range errors caused by the platform attitudes cannot ensure a measurement error within the specifications due to the surface roughness, figure 3.4 illustrates this situation. A Radar altimeter can compensate parts of those slant range measurement errors but Laser altimeter are vulnerable to the platform depending errors due to their pencil beam shape. The slant range causing effects have been discussed in section 2.3. Strategies for slant range compensation are going to be introduced in section 3.3. Apart from sensor range and platform attitude indications, the altimeter simulation model can be introduced to analyze the validity of the measurements. The distribution of the simulated distances of the single rays representing the beam shape, can be used to define a validity requirement.

Furthermore, the reflection angle between surface and measurement line-of-sight is an indicator for the measurement validity. Figure 3.5 left shows good signal reflection conditions, while the signal in the situation of the right figure is diverted. The orthogonality of surface gradients, mainly effecting the signal diversion are also illustrated as small arrows on the surface.

The selection of suitable validity criteria is primarily sensor dependent, therefore the re-

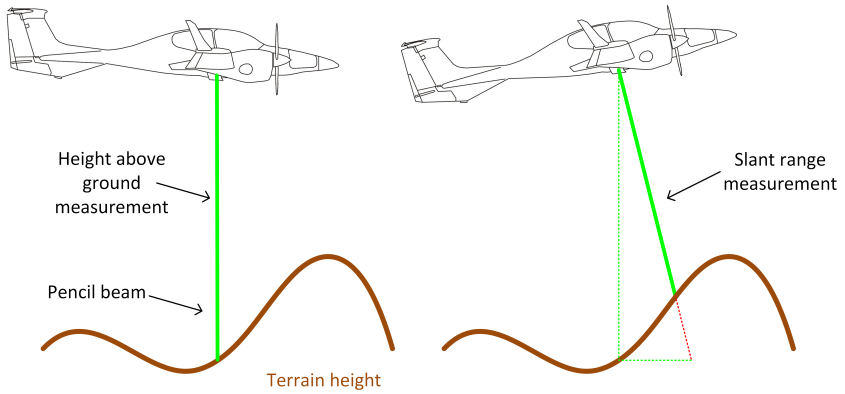

Figure 3.4: Attitude sensitivity of a pencil beam-shape

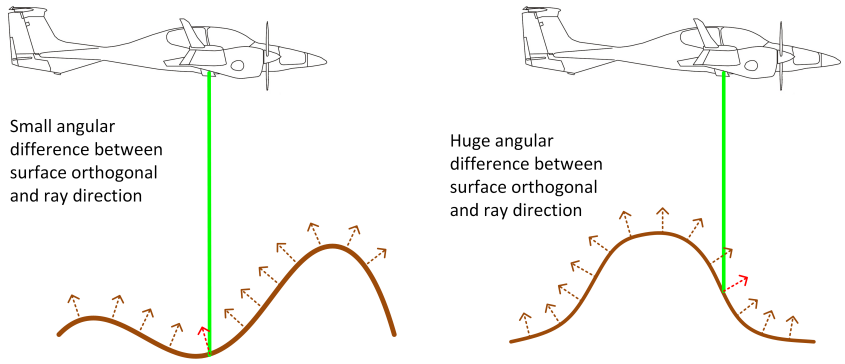

Figure 3.5: Surface gradient

quirements for Laser and Radar altimeters are discussed. The major influencing factor for the validity of a height measurement of a Laser altimeter is the platform attitude. Attributable to the thin pencil beam of the Laser altimeter, the measurement error increases with the platform roll and pitch angles. Additionally to the slant range measurement, the surface height at the footprint is unknown and can even increase the error. For a robust validity assessment, the output of the altimeter simulation model is compared to the real measurements. If the simulated measurement strongly disagrees with the real measurement, the measurement is also declared invalid. This metrics are equally applied on the Radar altimeter with a wider tolerance for roll and pitch attitude angles due to the wider Radar beam-cone. The HPBW θ_{hpbw} of the used antenna is the design parameter for this parametrization. The dispersion of the altimeter simulation model distance results are evaluated in addition to the altimeter validity check. The result can identify abnormal measurements and the limitation scaled on the height above ground. For example, the distance dispersion increases if obstacles or strong surface variations are within the beam cone. The designing factors are summarized in table 3.2. Chapter 7 gives performance examples of the algorithm using recorded flight test data.

Criteria	Laser altimeter	Radar altimeter
Roll angle	$\leq 10°$	ϕ_{hpbw}
Pitch angle	$\leq 10°$	θ_{hpbw}
Simulation model deviation	$\leq 5m$	$\leq 10m$
Received signal dispersion	-	$\sim h_{agl}$

Table 3.2: Validity criteria

3.2 Measurement Variance

The elimination of erroneous measurements leads to discontinuous aiding which is not suitable for navigation systems which rely on a continuous and frequency stable aiding information. Another solution, which can be used for weighting and measurement quality assessment, is the estimation of the measurement covariance. For example, GNSS receivers provide position and velocity covariance estimates based on the satellite constellation, the satellite signals and the tracking loop noise values. Receivers prepared for a tightly coupled integration also provide pseudo-range and delta-range covariance estimations. Conventional Radar or Laser altimeters do not provide a comparable measurement quality indicator, which is fundamental for any navigation system data fusion. The covariance of the integrated navigation system, which is an indicating factor for the system accuracy, strongly depends on the consistency of single measurement covariance estimations. Figure 3.6 shows the architecture of an in-flight variance estimation of an altimeter measurement.

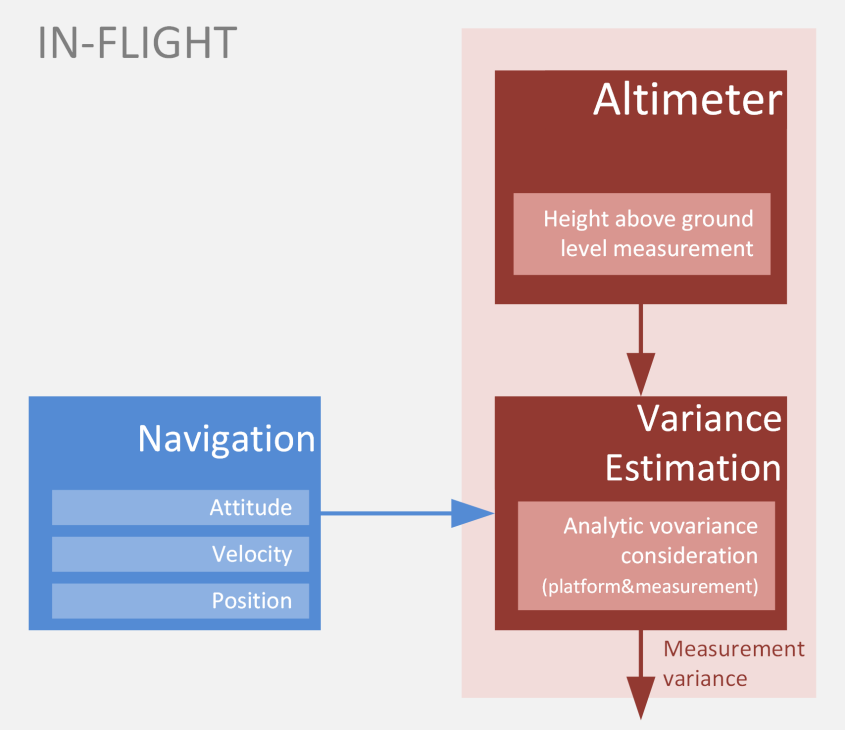

Figure 3.6: Variance estimation - architecture

The covariance value of a measurement is absolutely required as quality indication to

weight the information in a data fusion filter. Without a sensor internal covariance estimation, the covariance has to be estimated outside the sensor. If no estimation is available, the covariance would have to be otherwise chosen as constant. This approach can lead to inconsistencies of the navigation filter, since the good and the bad measurements can not be distinguished. Choosing a too optimistic covariance matrix of a measurement will converge the integrated navigation system into a situation where new measurements have minor influence on the estimation state and the filter becomes inconsistent. On the other side, if the covariance of the measurement is chosen too pessimistic, the filter will reduce the influence of the information and the benefit of the measurement is lost.
The covariance can be obtained by considering a simplified altimeter model with the three main dominating error components, the sensor bias b_{agl}, the scale factor s_{agl}, and the noise error n_{agl}. A simplified approach is given by equation 3.1.

$$\begin{aligned} h_{agl} &= \tilde{h}_{agl} + \delta h_{agl} \\ &= \tilde{h}_{agl} + s_{agl} \cdot \tilde{h}_{agl} + b_{agl} + n_{agl} \end{aligned} \tag{3.1}$$

This error model does not take the platform states and the surface environment explicitly into account. This model does not provide any platform attitude angles or surface characteristics. A possible perfect nadir measurement of a leveled aircraft above flat surface is rated equal to a slant range measurement above rough surface. Additionally, this model does not cover the exceedance of the maximum measurement attitude angles specified for altimeter operation. A covariance estimation based on this model, provides pessimistic results for ideal situation and too optimistic for worst case situations.
In the following three sections, a platform dependent in-flight variance estimation for altimeter measurements is derived. First, the variance for the height above ground measurement is calculated, the second section considers the covariance of the slant range distance, and finally the measurement footprint covariance, which is required for SAN systems, is determined.

3.2.1 Height above Ground Variance

The error parts of a slant range measurement and the surface variation, which have been discussed in section 2.3, are included in this consideration. The height above ground error δh_{agl} can be interpreted as the difference of the true nadir height h_{agl} and the altimeter measurement d_m. The relation with the topographic height of the platform nadir $h(N)$ and the absolute height of the platform $h(P)$ is given by equation 3.2. The consideration of the height above ground variance does not take map errors into account by definition. The situation is additionally illustrated in figure 3.7.

$$\begin{aligned} \delta h_{agl} &= h_{agl} - d_m \\ &= h(P) - h(N) - d_m \end{aligned} \tag{3.2}$$

The scalar height above ground can be described with the slant range distance $\mathbf{d}_m$ rotated into the n frame and the topographic height difference between the nadir height $h(N)$ and the measurement height $h(M)$, which is denoted by $\Delta h(N, M)$. The equation is given in 3.3.

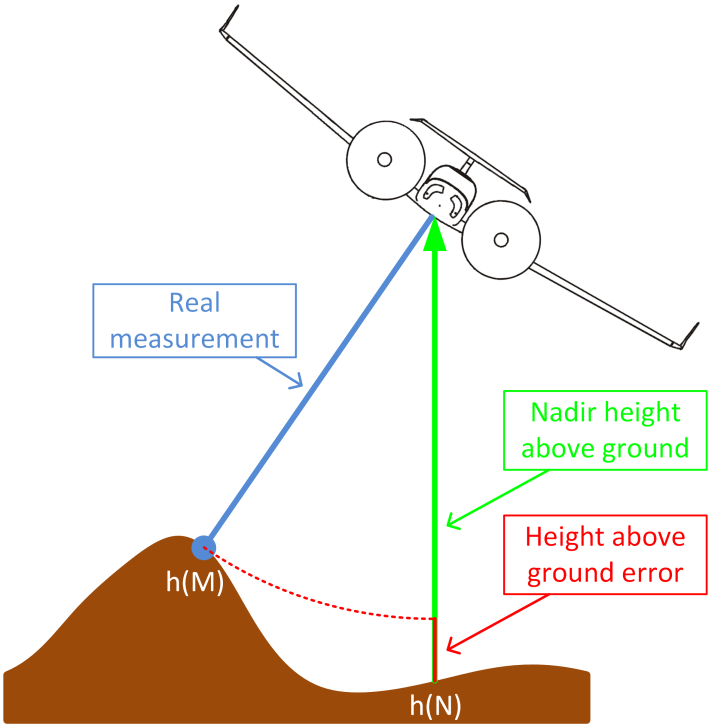

Figure 3.7: Height above ground error parts

$$h_{agl} = \begin{pmatrix} 0 & 0 & 1 \end{pmatrix} \mathbf{R}_{nm} \mathbf{d}_m + \Delta h\,(N, M) \tag{3.3}$$

Substituting equation 3.3 into equation 3.2 leads to equation 3.4. The two error parts can be grouped into an attitude dependent and a surface dependent error part. The attitude dependent error part defines the slant range error caused by the platform attitude, sensor mounting or measurement direction influence. These influences are combined in the rotation matrix from the measurement frame m into the navigation frame n. The second error part describes the surface variation between the nadir and the measurement point. While this influence can be neglected for flat surfaces, it has to be considered for rough surface variations. The covariance of the height above ground measurement is given by equation 3.5.

$$\begin{aligned} \delta h_{agl} &= \begin{pmatrix} 0 & 0 & 1 \end{pmatrix} \mathbf{R}_{nm} \mathbf{d}_m + \Delta h\,(N, M) - d_m \\ &= \begin{pmatrix} 0 & 0 & 1 \end{pmatrix} (\mathbf{R}_{nm} - \mathbf{I})\, \mathbf{d}_m + \Delta h\,(N, M) \end{aligned} \tag{3.4}$$

$$\mathrm{Cov}\left[\delta h_{agl}\right] = \mathrm{Cov}\left[\begin{pmatrix} 0 & 0 & 1 \end{pmatrix} (\mathbf{R}_{nm} - \mathbf{I})\, \mathbf{d}_m\right] + \mathrm{Cov}\left[\Delta h\,(N, M)\right] \tag{3.5}$$

For the determination of the height above ground variance, the slant range error part is modeled depending on the measured distance d_m. The distance dependent term can be modeled dependent on the rotation matrix $\mathbf{R}_{mn}$. This matrix is a composition of three different rotations, the transformation from n frame into b frame, from b frame into the sensor frame s and finally into the measurement frame m. The rotation matrix may be decomposed as given by equation 3.6. The body and sensor frame poses are well known

from the navigation system and the mounting of the sensor, whereas the measurement frame rotation is sensor specific. While the measurement frame coincides with the sensor frame for Laser altimeters with their pencil beam-shape characteristics, Radar altimeters wide beam-cone antennas measure into an unknown direction within the beam-cone in case of known DEM, but insufficiently good known position or vice versa. The rotation of the measurement direction has either to be modeled generically or the rotation has to be determined with the simulation model. This approach is shown in the section dealing with the compensation methods.

$$\mathbf{R}_{nm} = \mathbf{R}_{nb}\mathbf{R}_{bs}\mathbf{R}_{sm} \tag{3.6}$$

This rotation matrix is the main dominating factor, scaled by measurement range, which influences the height above ground error and its covariance. The second error contribution is the surface variation between the measured topography and platform nadir topographic height. This error part is depending on the surface variation of the overflown area. The rotation matrix also contributes to the distance between these two points and can increase the error probability. Using this equation for the integration of an altimeter in a navigation system, depending on the altimeter type, the error parts have to be parametrized.
For sensors providing an intentional slant range measurement such as Laser scanners, this approach is not suitable. For these sensors the distance variance calculation, introduced in the following section, has to be applied. The influences on the two error parts are given in table 3.3 and have to be parametrized according to the given altimeter specification.

Influence		**Pencil beam-shape**	**Wide beam-shape**
Slant range	$\mathbf{R}_{sm}$	Pencil beam: neglectable	Attitude & surface
	$\mathbf{R}_{bs}$	Structural deformation (aeroelasticity)	
	$\mathbf{R}_{nb}$	Platform attitude	
Surface	Δh	Local surface characteristics	

Table 3.3: Influences on height above ground variance

3.2.2 Slant Range Variance

While the height above ground variance considers only a nadir height measurement of the altimeter, the slant range measurement variance does also cover slant range measurements. On the one side, this section deals with the variance of intentional slant range measurements, provided for example by Laser scanners. On the other side, the variance for mistakenly measured slant range is calculated. The mathematical derivation is performed twofold, once for pencil beam-shape characteristics and once for wide beam shape characteristics to cover both, Radar and Laser measurements. For the measurement variance consideration, the perturbation result of appendix C.2 is used. The approximation of the rotation matrices with skew symmetric matrices is introduced in the appendix, as well. This perturbation is based on the basic measurement equation, introduced by equation 2.46. The covariance calculation is given by equation 3.7. The references M (measurement), S (sensor origin) and N (nadir) are similar to figure 3.7.

$$\begin{aligned}\mathrm{Cov}\left[\delta\mathbf{d}_m\right] \approx \mathrm{Cov}\,[&\mathbf{R}_{\tilde{m}s}\mathbf{R}_{\tilde{s}b}\mathbf{R}_{b\tilde{n}}\mathbf{R}_{ne}\delta\mathbf{x}_e\left(M\right) - \mathbf{R}_{\tilde{m}s}\mathbf{R}_{\tilde{s}b}\mathbf{R}_{b\tilde{n}}\mathbf{R}_{ne}\delta\mathbf{x}_e\left(P\right)\\ &+ \mathbf{R}_{\tilde{m}s}\mathbf{R}_{\tilde{s}b}\mathbf{R}_{b\tilde{n}}\boldsymbol{\Psi}_{\tilde{n}n}\mathbf{R}_{ne}\tilde{\mathbf{x}}_e\left(M\right) - \mathbf{R}_{\tilde{m}s}\mathbf{R}_{\tilde{s}b}\mathbf{R}_{b\tilde{n}}\boldsymbol{\Psi}_{\tilde{n}n}\mathbf{R}_{ne}\tilde{\mathbf{x}}_e\left(P\right)\\ &+ \mathbf{R}_{\tilde{m}s}\mathbf{R}_{\tilde{s}b}\delta\mathbf{x}_b\left(S\right) + \boldsymbol{\Psi}_{m\tilde{m}}\mathbf{R}_{\tilde{m}s}\mathbf{R}_{\tilde{s}b}\mathbf{R}_{b\tilde{n}}\mathbf{R}_{ne}\tilde{\mathbf{x}}_e\left(M\right)\\ &- \boldsymbol{\Psi}_{m\tilde{m}}\mathbf{R}_{\tilde{m}s}\mathbf{R}_{\tilde{s}b}\mathbf{R}_{b\tilde{n}}\mathbf{R}_{ne}\tilde{\mathbf{x}}_e\left(P\right) + \boldsymbol{\Psi}_{m\tilde{m}}\mathbf{R}_{\tilde{m}s}\mathbf{R}_{\tilde{s}b}\tilde{\mathbf{x}}_b\left(S\right)\\ &+ \mathbf{R}_{\tilde{m}s}\boldsymbol{\Psi}_{s\tilde{s}}\mathbf{R}_{\tilde{s}b}\mathbf{R}_{b\tilde{n}}\mathbf{R}_{ne}\tilde{\mathbf{x}}_e\left(M\right) - \mathbf{R}_{\tilde{m}s}\boldsymbol{\Psi}_{s\tilde{s}}\mathbf{R}_{\tilde{s}b}\mathbf{R}_{b\tilde{n}}\mathbf{R}_{ne}\tilde{\mathbf{x}}_e\left(P\right)\\ &+\mathbf{R}_{\tilde{m}s}\boldsymbol{\Psi}_{s\tilde{s}}\mathbf{R}_{\tilde{s}b}\tilde{\mathbf{x}}_b\left(S\right)]\end{aligned} \tag{3.7}$$

In the sequel, the covariance terms which are small or equivalent to zero are eliminated. First, the covariance of the sensor frame misalignment can be neglected due to the fix mounting of the sensor to the aircraft. The static rotation angles can be determined with a high accuracy, and the s frame is expected to have no motion due to vibrations, therefore it is neglected in equation 3.8. If the sensor mounting location is suspended to vibrations, the term has to be considered in the further calculations. Second, the covariance of the lever-arm error can be neglected for a similar reason. The lever arm of between coordinate frame origin and sensor frame origin can be measured or determined out of the constructions planes with a high accuracy. This term is also not considered further, but has to be considered if the sensor mounting location is suspended to vibrations or bending effects. The neglected term is given by equation 3.9.

$$\mathrm{Cov}\left[\boldsymbol{\psi}_{\tilde{s}s}\right] \approx \mathbf{0}_{3x3} \tag{3.8}$$

$$\mathrm{Cov}\left[\delta\mathbf{x}_b\left(S\right)\right] \approx \mathbf{0}_{3x3} \tag{3.9}$$

The platform position and attitude covariances are well-known from the navigation filter. The corresponding entries in the covariance matrix $\mathbf{P}$ are given by equation 3.10

$$\begin{aligned}\mathrm{Cov}\left[\delta\mathbf{x}_e\left(P\right)\right] &= \mathbf{P}_{pos}\\ \mathrm{Cov}\left[\boldsymbol{\psi}_{n\tilde{n}}\right] &= \mathbf{P}_{att}\end{aligned} \tag{3.10}$$

The resulting terms in equation 3.11 are now determined sequentially and are discussed afterwards. Table 3.4 gives an description of the terms and the corresponding equation number.

Term	**Description**	**Equation**
1	Footprint position error	3.12
2	Platform position error	3.13
3	Platform attitude influence on footprint	3.14
4	Platform attitude error	3.15
5	m frame misalignment influence on footprint position	3.16
6	m frame misalignment influence on platform position	3.17
7	m frame misalignment influence on lever-arm	3.18

Table 3.4: Dependencies on the slant range covariance

Introducing the described assumptions into equation 3.7 results in following equations.

$$\begin{aligned}\mathrm{Cov}\left[\delta\mathbf{d}_m\right] \approx \mathrm{Cov}\,[&\mathbf{R}_{\tilde{m}s}\mathbf{R}_{\tilde{s}b}\mathbf{R}_{b\tilde{n}}\mathbf{R}_{ne}\delta\mathbf{x}_e\left(M\right) - \mathbf{R}_{\tilde{m}s}\mathbf{R}_{\tilde{s}b}\mathbf{R}_{b\tilde{n}}\mathbf{R}_{ne}\delta\mathbf{x}_e\left(P\right)\\ &+ \mathbf{R}_{\tilde{m}s}\mathbf{R}_{\tilde{s}b}\mathbf{R}_{b\tilde{n}}\boldsymbol{\Psi}_{\tilde{n}n}\mathbf{R}_{ne}\tilde{\mathbf{x}}_e\left(M\right) - \mathbf{R}_{\tilde{m}s}\mathbf{R}_{\tilde{s}b}\mathbf{R}_{b\tilde{n}}\boldsymbol{\Psi}_{\tilde{n}n}\mathbf{R}_{ne}\tilde{\mathbf{x}}_e\left(P\right)\\ &+ \boldsymbol{\Psi}_{m\tilde{m}}\mathbf{R}_{\tilde{m}s}\mathbf{R}_{\tilde{s}b}\mathbf{R}_{b\tilde{n}}\mathbf{R}_{ne}\tilde{\mathbf{x}}_e\left(M\right) - \boldsymbol{\Psi}_{m\tilde{m}}\mathbf{R}_{\tilde{m}s}\mathbf{R}_{\tilde{s}b}\mathbf{R}_{b\tilde{n}}\mathbf{R}_{ne}\tilde{\mathbf{x}}_e\left(P\right)\\ &+\boldsymbol{\Psi}_{m\tilde{m}}\mathbf{R}_{\tilde{m}s}\mathbf{R}_{\tilde{s}b}\tilde{\mathbf{x}}_b\left(S\right)]\end{aligned} \tag{3.11}$$

$$\mathrm{Cov}\left[\mathbf{R}_{\tilde{m}s}\mathbf{R}_{\tilde{s}b}\mathbf{R}_{b\tilde{n}}\mathbf{R}_{ne}\delta\mathbf{x}_e\left(M\right)\right] = \mathbf{R}_{\tilde{m}s}\mathbf{R}_{\tilde{s}b}\mathbf{R}_{b\tilde{n}}\mathbf{R}_{ne}\,\mathrm{Cov}\left[\delta\mathbf{x}_e\left(M\right)\right]\left(\mathbf{R}_{\tilde{m}s}\mathbf{R}_{\tilde{s}b}\mathbf{R}_{b\tilde{n}}\mathbf{R}_{ne}\right)^T \tag{3.12}$$

$$\begin{aligned}\mathrm{Cov}\left[\mathbf{R}_{\tilde{m}s}\mathbf{R}_{\tilde{s}b}\mathbf{R}_{b\tilde{n}}\mathbf{R}_{ne}\delta\mathbf{x}_e\left(P\right)\right] &= \mathbf{R}_{\tilde{m}s}\mathbf{R}_{\tilde{s}b}\mathbf{R}_{b\tilde{n}}\mathbf{R}_{ne}\,\mathrm{Cov}\left[\delta\mathbf{x}_e\left(P\right)\right]\left(\mathbf{R}_{\tilde{m}s}\mathbf{R}_{\tilde{s}b}\mathbf{R}_{b\tilde{n}}\mathbf{R}_{ne}\right)^T\\ &= \mathbf{R}_{\tilde{m}s}\mathbf{R}_{\tilde{s}b}\mathbf{R}_{b\tilde{n}}\mathbf{R}_{ne}\mathbf{P}_{pos}\left(\mathbf{R}_{\tilde{m}s}\mathbf{R}_{\tilde{s}b}\mathbf{R}_{b\tilde{n}}\mathbf{R}_{ne}\right)^T\end{aligned} \tag{3.13}$$

$$\begin{aligned}\mathrm{Cov}\left[\mathbf{R}_{\tilde{m}s}\mathbf{R}_{\tilde{s}b}\mathbf{R}_{b\tilde{n}}\boldsymbol{\Psi}_{\tilde{n}n}\mathbf{R}_{ne}\tilde{\mathbf{x}}_e\left(M\right)\right] &= \mathrm{Cov}\left[-\mathbf{R}_{\tilde{m}s}\mathbf{R}_{\tilde{s}b}\mathbf{R}_{b\tilde{n}}\left(\mathbf{R}_{ne}\tilde{\mathbf{x}}_e\left(M\right)\times\right)\boldsymbol{\psi}_{\tilde{n}n}\right]\\ &= \mathbf{R}_{\tilde{m}s}\mathbf{R}_{\tilde{s}b}\mathbf{R}_{b\tilde{n}}\left(\mathbf{R}_{ne}\tilde{\mathbf{x}}_e\left(M\right)\times\right)\mathbf{P}_{att}\left(\mathbf{R}_{\tilde{m}s}\mathbf{R}_{\tilde{s}b}\mathbf{R}_{b\tilde{n}}\left(\mathbf{R}_{ne}\tilde{\mathbf{x}}_e\left(M\right)\times\right)\right)^T\end{aligned} \tag{3.14}$$

$$\begin{aligned}\mathrm{Cov}\left[\mathbf{R}_{\tilde{m}s}\mathbf{R}_{\tilde{s}b}\mathbf{R}_{b\tilde{n}}\boldsymbol{\Psi}_{\tilde{n}n}\mathbf{R}_{ne}\tilde{\mathbf{x}}_e\left(P\right)\right] &= \mathrm{Cov}\left[-\mathbf{R}_{\tilde{m}s}\mathbf{R}_{\tilde{s}b}\mathbf{R}_{b\tilde{n}}\left(\mathbf{R}_{ne}\tilde{\mathbf{x}}_e\left(P\right)\times\right)\boldsymbol{\psi}_{\tilde{n}n}\right]\\ &= \mathbf{R}_{\tilde{m}s}\mathbf{R}_{\tilde{s}b}\mathbf{R}_{b\tilde{n}}\left(\mathbf{R}_{ne}\tilde{\mathbf{x}}_e\left(P\right)\times\right)\mathbf{P}_{att}\left(\mathbf{R}_{\tilde{m}s}\mathbf{R}_{\tilde{s}b}\mathbf{R}_{b\tilde{n}}\left(\mathbf{R}_{ne}\tilde{\mathbf{x}}_e\left(P\right)\times\right)\right)^T\end{aligned} \tag{3.15}$$

$$\begin{aligned}\mathrm{Cov}\left[\boldsymbol{\Psi}_{m\tilde{m}}\mathbf{R}_{\tilde{m}s}\mathbf{R}_{\tilde{s}b}\mathbf{R}_{b\tilde{n}}\mathbf{R}_{ne}\tilde{\mathbf{x}}_e\left(M\right)\right] &= \mathrm{Cov}\left[-\left(\mathbf{R}_{\tilde{m}s}\mathbf{R}_{\tilde{s}b}\mathbf{R}_{b\tilde{n}}\mathbf{R}_{ne}\tilde{\mathbf{x}}_e\left(M\right)\times\right)\boldsymbol{\psi}_{m\tilde{m}}\right]\\ &= \left(\mathbf{R}_{\tilde{m}s}\mathbf{R}_{\tilde{s}b}\mathbf{R}_{b\tilde{n}}\mathbf{R}_{ne}\tilde{\mathbf{x}}_e\left(M\right)\times\right)\mathrm{Cov}\left[\boldsymbol{\psi}_{m\tilde{m}}\right]\left(\mathbf{R}_{\tilde{m}s}\mathbf{R}_{\tilde{s}b}\mathbf{R}_{b\tilde{n}}\mathbf{R}_{ne}\tilde{\mathbf{x}}_e\left(M\right)\times\right)^T\end{aligned} \tag{3.16}$$

$$\begin{aligned}\mathrm{Cov}\left[\boldsymbol{\Psi}_{m\tilde{m}}\mathbf{R}_{\tilde{m}s}\mathbf{R}_{\tilde{s}b}\mathbf{R}_{b\tilde{n}}\mathbf{R}_{ne}\tilde{\mathbf{x}}_e\left(P\right)\right] &= \mathrm{Cov}\left[-\left(\mathbf{R}_{\tilde{m}s}\mathbf{R}_{\tilde{s}b}\mathbf{R}_{b\tilde{n}}\mathbf{R}_{ne}\tilde{\mathbf{x}}_e\left(P\right)\times\right)\boldsymbol{\psi}_{m\tilde{m}}\right]\\ &= \left(\mathbf{R}_{\tilde{m}s}\mathbf{R}_{\tilde{s}b}\mathbf{R}_{b\tilde{n}}\mathbf{R}_{ne}\tilde{\mathbf{x}}_e\left(P\right)\times\right)\mathrm{Cov}\left[\boldsymbol{\psi}_{m\tilde{m}}\right]\left(\mathbf{R}_{\tilde{m}s}\mathbf{R}_{\tilde{s}b}\mathbf{R}_{b\tilde{n}}\mathbf{R}_{ne}\tilde{\mathbf{x}}_e\left(P\right)\times\right)^T\end{aligned} \tag{3.17}$$

$$\begin{aligned}\mathrm{Cov}\left[\boldsymbol{\Psi}_{m\tilde{m}}\mathbf{R}_{\tilde{m}s}\mathbf{R}_{\tilde{s}b}\tilde{\mathbf{x}}_b\left(S\right)\right] &= \mathrm{Cov}\left[-\left(\mathbf{R}_{\tilde{m}s}\mathbf{R}_{\tilde{s}b}\tilde{\mathbf{x}}_b\left(S\right)\times\right)\boldsymbol{\psi}_{m\tilde{m}}\right]\\ &= \left(\mathbf{R}_{\tilde{m}s}\mathbf{R}_{\tilde{s}b}\tilde{\mathbf{x}}_b\left(S\right)\times\right)\mathrm{Cov}\left[\boldsymbol{\psi}_{m\tilde{m}}\right]\left(\mathbf{R}_{\tilde{m}s}\mathbf{R}_{\tilde{s}b}\tilde{\mathbf{x}}_b\left(S\right)\times\right)^T\end{aligned} \tag{3.18}$$

For calculation of the covariance terms, the position error covariance $\mathbf{P}_{pos}$ and attitude error covariance $\mathbf{P}_{att}$ of the central navigation filter have been used. The rotation matrices $\mathbf{R}_{b\tilde{n}}$ and $\mathbf{R}_{ne}$ can be calculated with the navigation state solution, which are sensor independent. The rotation into the sensor mounting frame $\mathbf{R}_{\tilde{s}b}$ is static and can be determined once for the current setup. The rotation into the measurement frame $\mathbf{R}_{\tilde{m}s}$ is strongly sensor dependent. Now the distinction between pencil beam and wide beam sensors is presented to determine the measurement frame rotation.

3.2.2.1 Pencil Beam Shape

The measurement distance covariance can be simplified furthermore for pencil beam sensors. All covariance terms including the measurement frame misalignment, which describe slant range effects can be eliminated. The simplification is given by equation 3.19. The distance covariance can then be simplified to equation 3.20.

$$\mathrm{Cov}\left[\boldsymbol{\psi}_{m\tilde{m}}\right] \approx \mathbf{0}_{3x3} \tag{3.19}$$

$$\begin{aligned}\mathrm{Cov}\left[\mathbf{d}_m\right] =& \mathbf{R}_{\tilde{m}s}\mathbf{R}_{\tilde{s}b}\mathbf{R}_{b\tilde{n}}\mathbf{R}_{ne}\,\mathrm{Cov}\left[\delta\mathbf{x}_e\left(M\right)\right]\left(\mathbf{R}_{\tilde{m}s}\mathbf{R}_{\tilde{s}b}\mathbf{R}_{b\tilde{n}}\mathbf{R}_{ne}\right)^T \\ &- \mathbf{R}_{\tilde{m}s}\mathbf{R}_{\tilde{s}b}\mathbf{R}_{b\tilde{n}}\mathbf{R}_{ne}\mathbf{P}_{pos}\left(\mathbf{R}_{\tilde{m}s}\mathbf{R}_{\tilde{s}b}\mathbf{R}_{b\tilde{n}}\mathbf{R}_{ne}\right)^T \\ &+ \mathbf{R}_{\tilde{m}s}\mathbf{R}_{\tilde{s}b}\mathbf{R}_{b\tilde{n}}\left(\mathbf{R}_{ne}\tilde{\mathbf{x}}_e\left(M\right)\times\right)\mathbf{P}_{att}\left(\mathbf{R}_{\tilde{m}s}\mathbf{R}_{\tilde{s}b}\mathbf{R}_{b\tilde{n}}\left(\mathbf{R}_{ne}\tilde{\mathbf{x}}_e\left(M\right)\times\right)\right)^T \\ &- \mathbf{R}_{\tilde{m}s}\mathbf{R}_{\tilde{s}b}\mathbf{R}_{b\tilde{n}}\left(\mathbf{R}_{ne}\tilde{\mathbf{x}}_e\left(P\right)\times\right)\mathbf{P}_{att}\left(\mathbf{R}_{\tilde{m}s}\mathbf{R}_{\tilde{s}b}\mathbf{R}_{b\tilde{n}}\left(\mathbf{R}_{ne}\tilde{\mathbf{x}}_e\left(P\right)\times\right)\right)^T\end{aligned} \tag{3.20}$$

3.2.2.2 Wide Beam Shape

The determination of the measurement distance covariance is much more complicated for wide beam-shaped sensors, such as Radar altimeters. The measurement direction of a Radar altimeter is not compulsory equal to the antenna center direction, the reasons for the deviation have already been described in the section 2.3. Contrary to the approach for a Laser altimeter, the m frame error of a Radar altimeter measurement cannot be neglected. Furthermore, the m frame error cannot be calculated analytically. One method which can provide an approximation, is the application of the altimeter simulation model to calculate the measurement direction of the synthetic measurement. Therefore, the simulation model is executed with the input parameters regarding the current flight state and a DEM. The simulation model provides the simulated distance, which is not requested for this application, and the measurement direction. For the determination of the distance variance, the covariance of the simulation model error $\boldsymbol{\psi}_{m\tilde{m}}$ has additionally to be considered.
The problem could also be solved with a generic geometric model for measurement direction determination. This approach will not cover all influencing effects and will lead to a optimistic covariance estimate. The covariance of the measurement orientation error covers the errors of the model which is used to determine the measurement orientation.
The complete formula to calculate the Radar altimeter covariance is given by equation 3.21.

$$\begin{aligned}\mathrm{Cov}\left[\mathbf{d}_m\right] =& \mathbf{R}_{\tilde{m}s}\mathbf{R}_{\tilde{s}b}\mathbf{R}_{b\tilde{n}}\mathbf{R}_{ne}\,\mathrm{Cov}\left[\delta\mathbf{x}_e\left(M\right)\right]\left(\mathbf{R}_{\tilde{m}s}\mathbf{R}_{\tilde{s}b}\mathbf{R}_{b\tilde{n}}\mathbf{R}_{ne}\right)^T \\ &- \mathbf{R}_{\tilde{m}s}\mathbf{R}_{\tilde{s}b}\mathbf{R}_{b\tilde{n}}\mathbf{R}_{ne}\mathbf{P}_{pos}\left(\mathbf{R}_{\tilde{m}s}\mathbf{R}_{\tilde{s}b}\mathbf{R}_{b\tilde{n}}\mathbf{R}_{ne}\right)^T \\ &+ \mathbf{R}_{\tilde{m}s}\mathbf{R}_{\tilde{s}b}\mathbf{R}_{b\tilde{n}}\left(\mathbf{R}_{ne}\tilde{\mathbf{x}}_e\left(M\right)\times\right)\mathbf{P}_{att}\left(\mathbf{R}_{\tilde{m}s}\mathbf{R}_{\tilde{s}b}\mathbf{R}_{b\tilde{n}}\left(\mathbf{R}_{ne}\tilde{\mathbf{x}}_e\left(M\right)\times\right)\right)^T \\ &- \mathbf{R}_{\tilde{m}s}\mathbf{R}_{\tilde{s}b}\mathbf{R}_{b\tilde{n}}\left(\mathbf{R}_{ne}\tilde{\mathbf{x}}_e\left(P\right)\times\right)\mathbf{P}_{att}\left(\mathbf{R}_{\tilde{m}s}\mathbf{R}_{\tilde{s}b}\mathbf{R}_{b\tilde{n}}\left(\mathbf{R}_{ne}\tilde{\mathbf{x}}_e\left(P\right)\times\right)\right)^T \\ &+ \left(\mathbf{R}_{\tilde{m}s}\mathbf{R}_{\tilde{s}b}\mathbf{R}_{b\tilde{n}}\mathbf{R}_{ne}\tilde{\mathbf{x}}_e\left(M\right)\times\right)\mathrm{Cov}\left[\boldsymbol{\psi}_{m\tilde{m}}\right]\left(\mathbf{R}_{\tilde{m}s}\mathbf{R}_{\tilde{s}b}\mathbf{R}_{b\tilde{n}}\mathbf{R}_{ne}\tilde{\mathbf{x}}_e\left(M\right)\times\right)^T \\ &- \left(\mathbf{R}_{\tilde{m}s}\mathbf{R}_{\tilde{s}b}\mathbf{R}_{b\tilde{n}}\mathbf{R}_{ne}\tilde{\mathbf{x}}_e\left(P\right)\times\right)\mathrm{Cov}\left[\boldsymbol{\psi}_{m\tilde{m}}\right]\left(\mathbf{R}_{\tilde{m}s}\mathbf{R}_{\tilde{s}b}\mathbf{R}_{b\tilde{n}}\mathbf{R}_{ne}\tilde{\mathbf{x}}_e\left(P\right)\times\right)^T \\ &+ \left(\mathbf{R}_{\tilde{m}s}\mathbf{R}_{\tilde{s}b}\tilde{\mathbf{x}}_b\left(S\right)\times\right)\mathrm{Cov}\left[\boldsymbol{\psi}_{m\tilde{m}}\right]\left(\mathbf{R}_{\tilde{m}s}\mathbf{R}_{\tilde{s}b}\tilde{\mathbf{x}}_b\left(S\right)\times\right)^T\end{aligned} \tag{3.21}$$

3.2.3 Footprint Variance

Often the footprint position information is considered for the processing of altimeter measurements in SAN systems. For this application, the covariance of the measured footprint is derived in this section. The perturbation, which is the basis for the further calculation is given in appendix C.1, the covariance calculation is given in 3.22. The calculations are based on the basic georeferenced height measurement equation, introduced by equation 2.40.

$$\begin{aligned}\mathsf{Cov}\left[\delta\mathbf{x}_e\left(M\right)\right] \approx \mathsf{Cov}\big[&\delta\mathbf{x}_e\left(P\right) - \mathbf{R}_{en}\mathbf{R}_{\tilde{n}b}\delta\mathbf{x}_b\left(S\right) - \mathbf{R}_{en}\boldsymbol{\Psi}_{n\tilde{n}}\mathbf{R}_{\tilde{n}b}\tilde{\mathbf{x}}_b\left(S\right)\\ &+ \mathbf{R}_{en}\mathbf{R}_{\tilde{n}b}\mathbf{R}_{b\tilde{s}}\mathbf{R}_{s\tilde{m}}\delta\mathbf{d}_m + \mathbf{R}_{en}\boldsymbol{\Psi}_{n\tilde{n}}\mathbf{R}_{\tilde{n}b}\mathbf{R}_{b\tilde{s}}\mathbf{R}_{s\tilde{m}}\tilde{\mathbf{d}}_m\\ &+ \mathbf{R}_{en}\mathbf{R}_{\tilde{n}b}\mathbf{R}_{b\tilde{s}}\boldsymbol{\Psi}_{\tilde{s}s}\mathbf{R}_{s\tilde{m}}\tilde{\mathbf{d}}_m + \mathbf{R}_{en}\mathbf{R}_{\tilde{n}b}\mathbf{R}_{b\tilde{s}}\mathbf{R}_{s\tilde{m}}\boldsymbol{\Psi}_{\tilde{m}m}\tilde{\mathbf{d}}_m\big]\end{aligned} \tag{3.22}$$

The dependencies of the lever-arm error and the sensor frame misalignment are not considered for the same reasons discussed in the previous section. The simplifications are given by equation 3.8 and 3.9 in the previous section. The simplified covariance is given by equation 3.23

$$\begin{aligned}\mathsf{Cov}\left[\delta\mathbf{x}_e\left(M\right)\right] \approx \mathsf{Cov}\big[&\delta\mathbf{x}_e\left(P\right) - \mathbf{R}_{en}\boldsymbol{\Psi}_{n\tilde{n}}\mathbf{R}_{\tilde{n}b}\tilde{\mathbf{x}}_b\left(S\right) + \mathbf{R}_{en}\mathbf{R}_{\tilde{n}b}\mathbf{R}_{b\tilde{s}}\mathbf{R}_{s\tilde{m}}\delta\mathbf{d}_m\\ &+ \mathbf{R}_{en}\boldsymbol{\Psi}_{n\tilde{n}}\mathbf{R}_{\tilde{n}b}\mathbf{R}_{b\tilde{s}}\mathbf{R}_{s\tilde{m}}\tilde{\mathbf{d}}_m + \mathbf{R}_{en}\mathbf{R}_{\tilde{n}b}\mathbf{R}_{b\tilde{s}}\mathbf{R}_{s\tilde{m}}\boldsymbol{\Psi}_{\tilde{m}m}\tilde{\mathbf{d}}_m\big]\end{aligned} \tag{3.23}$$

The platform position and platform attitude covariance are again substituted by the relation in equation 3.10. The remaining covariance terms are rearranged separately. Table 3.5 gives an overview and a description of the terms.

Term	Description	Equation
1	Platform position error	3.24
2	Platform attitude error with lever-arm	3.25
3	Ranging error	3.26
4	Platform attitude error with range	3.27
5	Measurement orientation error	3.28

Table 3.5: Dependencies on the footprint covariance

$$\mathsf{Cov}\left[\delta\mathbf{x}_e\left(P\right)\right] = \mathbf{P}_{pos} \tag{3.24}$$

$$\begin{aligned}\mathsf{Cov}\left[\mathbf{R}_{en}\boldsymbol{\Psi}_{n\tilde{n}}\mathbf{R}_{\tilde{n}b}\tilde{\mathbf{x}}_b\left(S\right)\right] &= \mathsf{Cov}\left[-\left(\mathbf{R}_{\tilde{n}b}\tilde{\mathbf{x}}_b\left(S\right)\times\right)\mathbf{R}_{en}\boldsymbol{\psi}_{n\tilde{n}}\right]\\ &= \left(\mathbf{R}_{\tilde{n}b}\tilde{\mathbf{x}}_b\left(S\right)\times\right)\mathbf{R}_{en}\mathbf{P}_{att}\left(\left(\mathbf{R}_{\tilde{n}b}\tilde{\mathbf{x}}_b\left(S\right)\times\right)\mathbf{R}_{en}\right)^T\end{aligned} \tag{3.25}$$

$$\mathsf{Cov}\left[\mathbf{R}_{en}\mathbf{R}_{\tilde{n}b}\mathbf{R}_{b\tilde{s}}\mathbf{R}_{s\tilde{m}}\delta\mathbf{d}_m\right] = \mathbf{R}_{en}\mathbf{R}_{\tilde{n}b}\mathbf{R}_{b\tilde{s}}\mathbf{R}_{s\tilde{m}}\,\mathsf{Cov}\left[\delta\mathbf{d}_m\right]\left(\mathbf{R}_{en}\mathbf{R}_{\tilde{n}b}\mathbf{R}_{b\tilde{s}}\mathbf{R}_{s\tilde{m}}\right)^T \tag{3.26}$$

$$\begin{aligned}\mathrm{Cov}\left[\mathbf{R}_{en}\boldsymbol{\Psi}_{n\tilde{n}}\mathbf{R}_{\tilde{n}b}\mathbf{R}_{b\tilde{s}}\mathbf{R}_{s\tilde{m}}\tilde{\mathbf{d}}_m\right] &= \mathrm{Cov}\left[-\mathbf{R}_{en}\left(\mathbf{R}_{\tilde{n}b}\mathbf{R}_{b\tilde{s}}\mathbf{R}_{s\tilde{m}}\tilde{\mathbf{d}}_m\times\right)\boldsymbol{\psi}_{n\tilde{n}}\right] \\ &= \mathbf{R}_{en}\left(\mathbf{R}_{\tilde{n}b}\mathbf{R}_{b\tilde{s}}\mathbf{R}_{s\tilde{m}}\tilde{\mathbf{d}}_m\times\right)\mathbf{P}_{att}\left(\mathbf{R}_{\tilde{n}b}\mathbf{R}_{b\tilde{s}}\mathbf{R}_{s\tilde{m}}\tilde{\mathbf{d}}_m\times\right)^T\mathbf{R}_{en}^T\end{aligned} \tag{3.27}$$

$$\begin{aligned}\mathrm{Cov}\left[\mathbf{R}_{en}\mathbf{R}_{\tilde{n}b}\mathbf{R}_{b\tilde{s}}\mathbf{R}_{s\tilde{m}}\boldsymbol{\Psi}_{\tilde{m}m}\tilde{\mathbf{d}}_m\right] &= \mathrm{Cov}\left[-\mathbf{R}_{en}\mathbf{R}_{\tilde{n}b}\mathbf{R}_{b\tilde{s}}\mathbf{R}_{s\tilde{m}}\left(\tilde{\mathbf{d}}_m\times\right)\boldsymbol{\psi}_{\tilde{m}m}\right] \\ &= \mathbf{R}_{en}\mathbf{R}_{\tilde{n}b}\mathbf{R}_{b\tilde{s}}\mathbf{R}_{s\tilde{m}}\left(\tilde{\mathbf{d}}_m\times\right)\mathrm{Cov}\left[\boldsymbol{\psi}_{\tilde{m}m}\right]\left(\tilde{\mathbf{d}}_m\times\right)^T\left(\mathbf{R}_{en}\mathbf{R}_{\tilde{n}b}\mathbf{R}_{b\tilde{s}}\mathbf{R}_{s\tilde{m}}\right)^T\end{aligned} \tag{3.28}$$

The entire covariance result is given by equation 3.29. For the further calculation, the platform states and platform covariances from the navigation solution and navigation filter are used. For the determination of the measurement orientation $\boldsymbol{\psi}_{\tilde{m}m}$, the sensor characteristics have to be considered. This approach has been discussed in the previous section.

$$\begin{aligned}\mathrm{Cov}\left[\delta\mathbf{x}_e\left(M\right)\right] \approx\ & \mathbf{P}_{pos} + \mathbf{R}_{en}\left(\mathbf{R}_{\tilde{n}b}\mathbf{R}_{b\tilde{s}}\mathbf{R}_{s\tilde{m}}\tilde{\mathbf{d}}_m\times\right)\mathbf{P}_{att}\left(\mathbf{R}_{\tilde{n}b}\mathbf{R}_{b\tilde{s}}\mathbf{R}_{s\tilde{m}}\tilde{\mathbf{d}}_m\times\right)^T\mathbf{R}_{en}^T \\ & + \mathbf{R}_{en}\mathbf{R}_{\tilde{n}b}\mathbf{R}_{b\tilde{s}}\mathbf{R}_{s\tilde{m}}\,\mathrm{Cov}\left[\delta\mathbf{d}_m\right]\left(\mathbf{R}_{en}\mathbf{R}_{\tilde{n}b}\mathbf{R}_{b\tilde{s}}\mathbf{R}_{s\tilde{m}}\right)^T \\ & + \mathbf{R}_{en}\mathbf{R}_{\tilde{n}b}\mathbf{R}_{b\tilde{s}}\mathbf{R}_{s\tilde{m}}\left(\tilde{\mathbf{d}}_m\times\right)\mathrm{Cov}\left[\boldsymbol{\psi}_{\tilde{m}m}\right]\left(\tilde{\mathbf{d}}_m\times\right)^T\left(\mathbf{R}_{en}\mathbf{R}_{\tilde{n}b}\mathbf{R}_{b\tilde{s}}\mathbf{R}_{s\tilde{m}}\right)^T \\ & - \left(\mathbf{R}_{\tilde{n}b}\tilde{\mathbf{x}}_b\left(S\right)\times\right)\mathbf{R}_{en}\mathbf{P}_{att}\left(\left(\mathbf{R}_{\tilde{n}b}\tilde{\mathbf{x}}_b\left(S\right)\times\right)\mathbf{R}_{en}\right)^T\end{aligned} \tag{3.29}$$

The footprint covariance does not include surface dependencies. It models the effects of the platform position and orientation variance, the measurement direction and ranging variance on the measurement footprint. The surface characteristic is not included in the derivation.
The three approaches provide templates for different altimeter measurement interpretations. They can be applied whenever the measurement variance of an altimeter has to be estimated.

3.3 Slant Range Compensation

The height above ground measurement should be available with a constant frequency and a high accuracy, especially for trajectories with a small ground-clearance. The exclusion of invalid measurements or the measurement variance estimation cannot provide a benefit. While these methods are suitable to exclude erroneous measurements or estimate the measurement quality, this section introduces methods to improve the accuracy of the measurement. The reasons for slant range errors have been introduced in section 2.3. Three compensation methods are discussed suitable for different sensor classes and applications in this section. First the attitude compensation method is discussed, which compensates the deviation caused by platform attitude. This method requires a high attitude estimation accuracy of the platform. The second method is the range compensation and considers additionally the surface variations. For this method, the platform position and attitude is required with a high accuracy. Additionally, a high resolution DEM is necessary for the geometric range determination. Thirdly, the beam compensation considers furthermore the beam characteristics and signal propagation effects of the sensor.

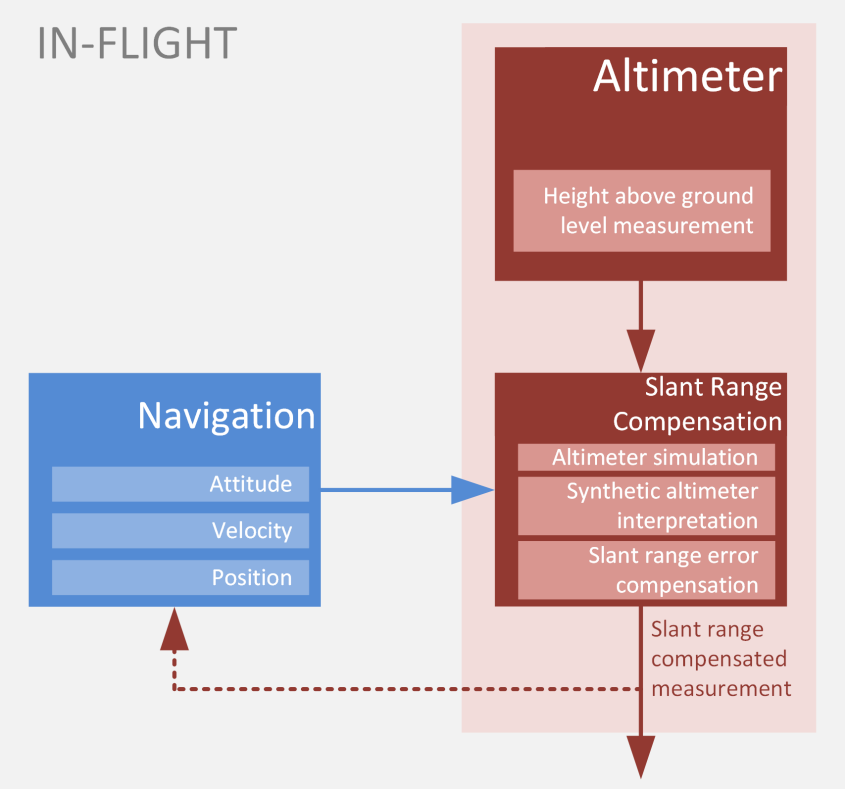

Figure 3.8: Slant range compensation with altimeter simulation model

An overview of the error coverage of the three proposed compensation methods is given in table 3.6.

The architecture of the compensation algorithm is given in figure 3.8. The altimeter measurement is preprocessed using the navigation state estimates to improve the measurement accuracy and covariance. The corrected measurement can be used as height aiding information in a central navigation filter. The three compensation methods are explained in the following three sections. Subsequently, the integration of a slant range compensated height measurement in a central navigation filter is discussed.

	Error influence		
	Platform attitude	Surface variations	Beam-shape and signal propagation
Attitude compensation	✓	✗	✗
Range compensation	✓	✓	✗
Beam compensation	✓	✓	✓

Table 3.6: Compensation method overview

3.3.1 Compensation Methods

3.3.1.1 Attitude Compensation

The attitude compensation algorithm compensates for slant range errors caused by the deflections of the measurement direction due to platform attitude angles. This approach is suitable for altimeters with narrow beam-cone shapes such as Laser altimeters. Additionally, the algorithm requires a smooth or flat surface for a good compensation performance. The calculation can be executed without high computational burden and is suitable for smaller aircraft without dedicated computational power for navigation applications. Only the roll and pitch angles are required from the aircraft navigation system for this compensation approach. The position has no influence on this method, which is another benefit. A schematic visualization of the compensation is given in figure 3.9.

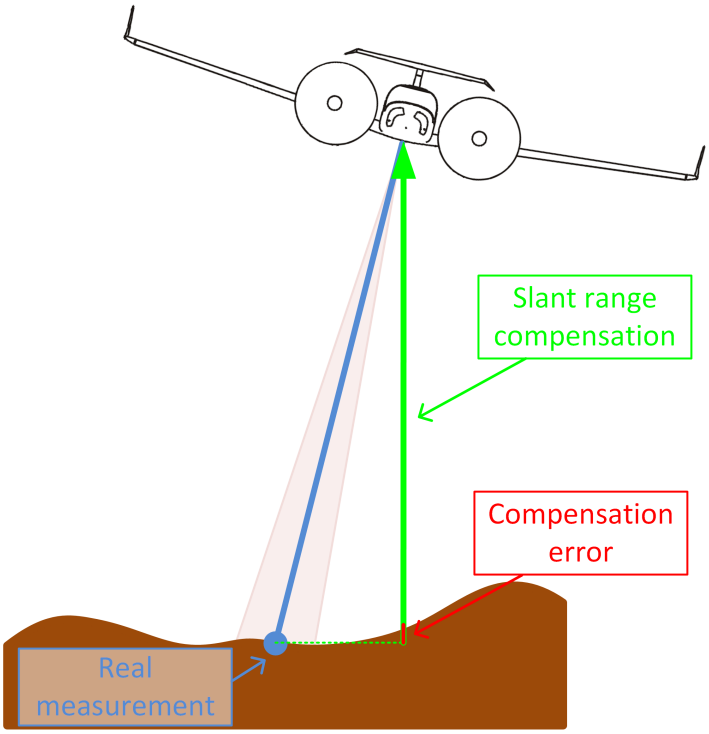

Figure 3.9: Attitude compensation - narrow beam-cone shape

The formal description of the compensation is given by equation 3.30. The measured range $\tilde{\mathbf{d}}_m$ is rotated into the s frame and compensated by the lever arm. The rotation into n frame and isolation of the height channel provides the compensated height above ground $\tilde{h}_{agl}$.

$$\tilde{h}_{agl} = \begin{pmatrix} 0 & 0 & 1 \end{pmatrix} \mathbf{R}_{\tilde{n}b} \left(\mathbf{R}_{b\tilde{s}} \tilde{\mathbf{d}}_m - \tilde{\mathbf{x}}_b(S) \right) \tag{3.30}$$

An example where the requirements on the attitude compensation algorithms are not fulfilled is given in figure 3.10. The wide beam-cone shape increases the probability of diversion of the measurement direction from the antenna center. Additionally, the hilly environment does not support the attitude compensation algorithm and causes a significant compensation error. To eliminate the surface dependent compensation errors,

the range compensation algorithm, which is going to be introduced in the following section, is a convenient method.

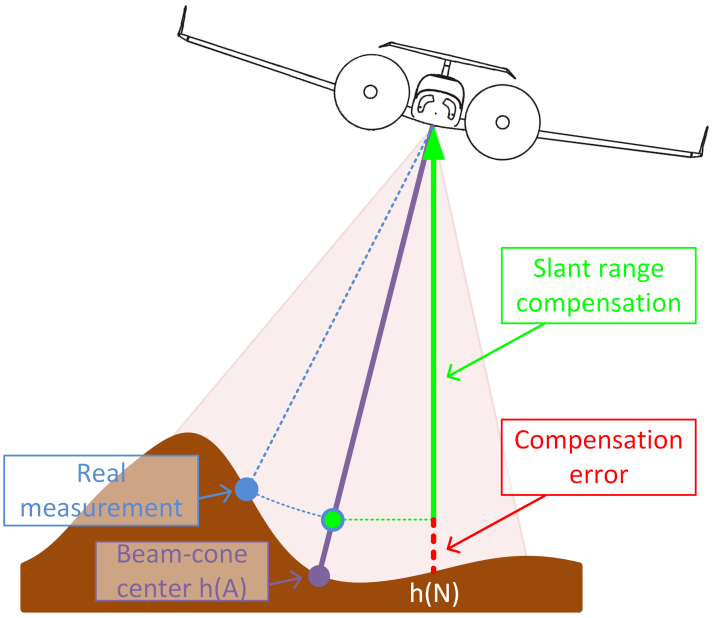

Figure 3.10: Attitude compensation - wide beam-cone shape

3.3.1.2 Range Compensation

The range compensation extends the attitude compensation algorithm to consider surface variations. Surface variation errors can be described as the difference between the topographic heights at the aircraft nadir and the beam-cone center projection on the surface. The horizontal position of the platform is required for the DEM lookup function to calculate the nadir height $h(N)$. The horizontal position has to be provided from the platform navigation system in at least the accuracy of the DEM resolution. Equation 3.31 gives the relation of the nadir height to the platform topographic height.

$$h(N) = h_{topo}(P) \tag{3.31}$$

For the in-flight compensation, the nadir height $h(N)$ is provided by a DEM as well as the beam-cone center height $h(A)$. For the determination of the horizontal position of the beam-cone center interception point, the ray tracing algorithm, introduced in chapter 2, is applied in-flight.
The compensation method is illustrated in figure 3.11. The formal two-step compensation approach is given by equation 3.32. The calculation of the slant distance $\tilde{h}_{range}$ remains identical to the attitude compensation, while the compensated height above ground $\tilde{h}_{agl}$ now consists of the slant distance and the surface variation compensation. This surface variations compensation considers the difference between the topographic height at the beam-cone center projection on the surface and the topographic height of the aircraft nadir point.

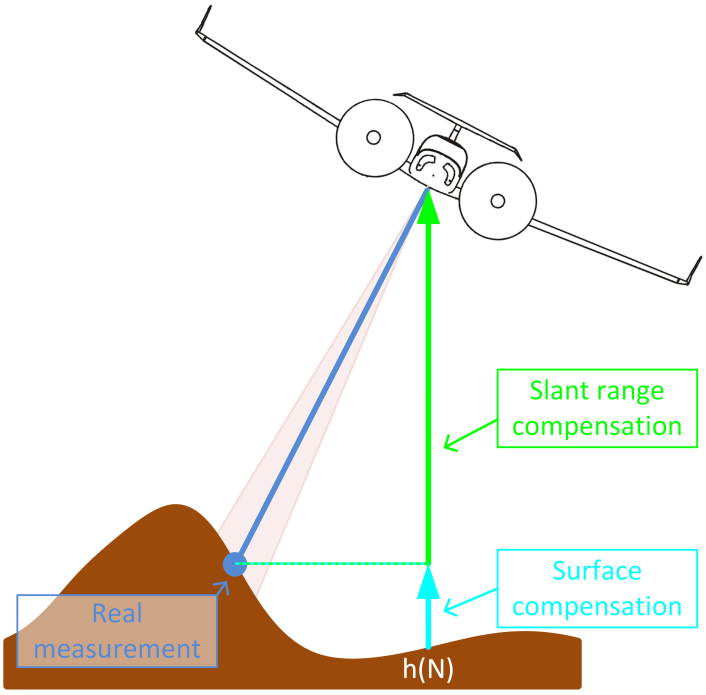

Figure 3.11: Range compensation - narrow beam-cone shape

$$\begin{aligned} \tilde{h}_{range} &= \begin{pmatrix} 0 & 0 & 1 \end{pmatrix} \mathbf{R}_{\tilde{n}b} \left(\mathbf{R}_{b\tilde{s}} \tilde{\mathbf{d}}_m - \tilde{\mathbf{x}}_b(S) \right) \\ \tilde{h}_{agl} &= \tilde{h}_{range} + h_{dem}(A) - h_{dem}(N) \end{aligned} \tag{3.32}$$

The platform attitude and the surface variations have been compensated perfectly with the distance compensation method for a narrow beam-cone shaped altimeter. This compensation method however cannot cover the measurements of a wide beam-cone altimeter. The distance compensation in a similar situation with a wide beam-cone altimeter yields a compensation error. This situation is illustrated in figure 3.12. A method which eliminates additionally the beam-cone caused errors is given in the following section.

3.3.1.3 Beam Compensation

Two methods which cover geometric slant range error sources have been introduced so far. The beam-cone shape and signal propagation effects have not been considered by the former compensation methods. The simulation model is applied in-flight to determine the required measurement direction $\boldsymbol{\psi}_{s\tilde{m}}$ additionally to the platform attitude and horizontal position. A graphical example is given in figure 3.13. Since the effects of signal propagation and signal processing cannot be modeled perfectly due to the explained reasons in chapter 2, the figure shows a small deviation between synthetic and real measurement. This deviation leads to a small compensation error which depends on the accuracy of the simulation model and the DEM. The formal description of the compensation method is given by equation 3.33. The geometric part of the compensation algorithm is supplemented by the rotation matrix from the estimated m frame to the s frame $\mathbf{R}_{s\tilde{m}}$. This rotation matrix describes the orientation of the measurement direction within the measurement frame. Assuming a wider Radar altimeter beam cone, the rotation matrix

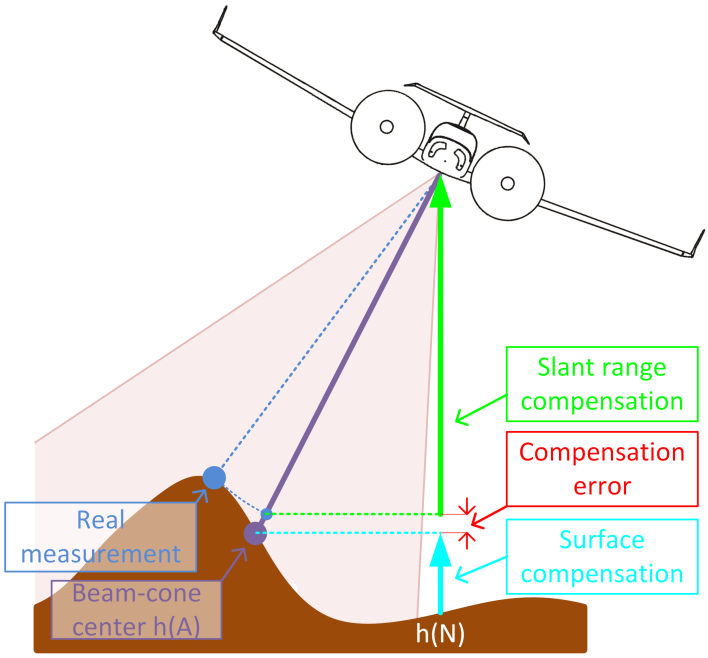

Figure 3.12: Range compensation - wide beam-cone shape

describes the deflection of the measurement direction with respect to the antenna beam-center. This direction cannot be easily determined by a generic geometric model, but can be estimated using the altimeter simulation model. The simulation model is executed in-flight with a current DEM and the current position attitude estimates. The surface share does not longer consider the topographic height of the beam-cone center, but the topographic height of the synthetic measurement $h(M)$.

$$\begin{aligned} \tilde{h}_{range} &= \begin{pmatrix} 0 & 0 & 1 \end{pmatrix} \mathbf{R}_{\tilde{n}b} \left(\mathbf{R}_{b\tilde{s}} \mathbf{R}_{s\tilde{m}} \tilde{\mathbf{d}}_m - \tilde{\mathbf{x}}_b(S) \right) \\ \tilde{h}_{agl} &= \tilde{h}_{range} + h_{dem}(M) - h_{dem}(N) \end{aligned} \tag{3.33}$$

The beam-cone compensation method promises an encouraging approach, at the price of high computational burden. To provide a highly accurate compensation, the beam-cone shape has to be modeled with a variety of rays, as shown in chapter 2. Furthermore, processing a high resolution DEM is another task which requires high computational power. As the discussion has shown, the three methods are suitable for different sensor characteristics in different environments. Table 3.7 gives an overview of the applicability, depending on the sensor and surface characteristics.

	Beam-shape		**Surface characteristic**	
	Pencil	Wide	Flat	Rough
Attitude compensation	✓	✗	✓	✗
Range compensation	✓	✗	✓	✓
Beam compensation	✓	✓	✓	✓

Table 3.7: Compensation method applications

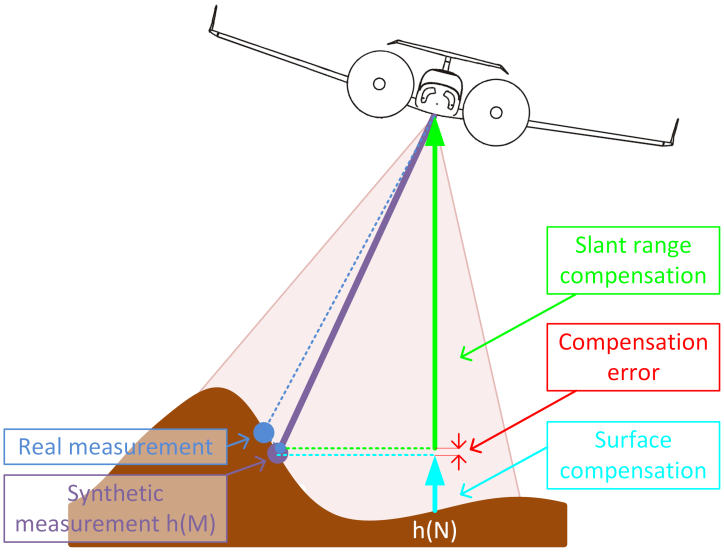

Figure 3.13: Beam compensation

3.3.2 Validation

The beam compensation algorithm, as most complex representative of the compensation methods and best suitable method for Radar altimeters, is validated on a recorded flight test trajectory in this section. The flight test setup, the trajectory and the raw altimeter measurements have been introduced in section 2.2.8. The recorded position data and the altimeter measurements are used for a post-processing compensation for this validation. For each altimeter measurement sample, the altimeter simulation model is processed with the current platform states. This includes the position, attitude and topographic elevation of the DSM. The synthetic measurement orientation $\mathbf{R}_{s\tilde{m}}$ and the elevation difference is used to compensate the real measurements.

Figure 3.14 depicts the validation results. The upper plot shows the absolute platform height and the topographic DSM elevation. The lower plot shows the height above ground error δh_{agl} of the compensated measurement in respect to the nadir height above ground. Additionally, the raw height above ground h_{ralt} measurement error is plotted in respect to the nadir height, to represent the uncompensated information.

The classical interpretation of an altimeter measurement as nadir height (blue) would lead to an erroneous measurement with errors up to 20 m. In the situations near to the forest at the time points $t_1 = 100\,\mathrm{s}$ and $t_2 = 155\,\mathrm{s}$, the missing beam compensation leads to erroneous measurements of the forest's edge, while the platform nadir is still above flat surface. The cyan line depicts the slant range compensated altimeter measurement. The erroneous measurements at the beginning and end of the forest flyover have been reduced significantly by the beam-cone compensation. The RMS error of the nadir interpretation is calculated at $\delta h_{rms} = 3.8\,\mathrm{m}$, while the compensation algorithm reduces the RMS error to $\delta h_{rms} = 1.7\,\mathrm{m}$. The introduced compensation method improves the height measurement considerably, it is however strongly depending on the accuracy and actuality of the used digital surface map, especially above vegetated areas.

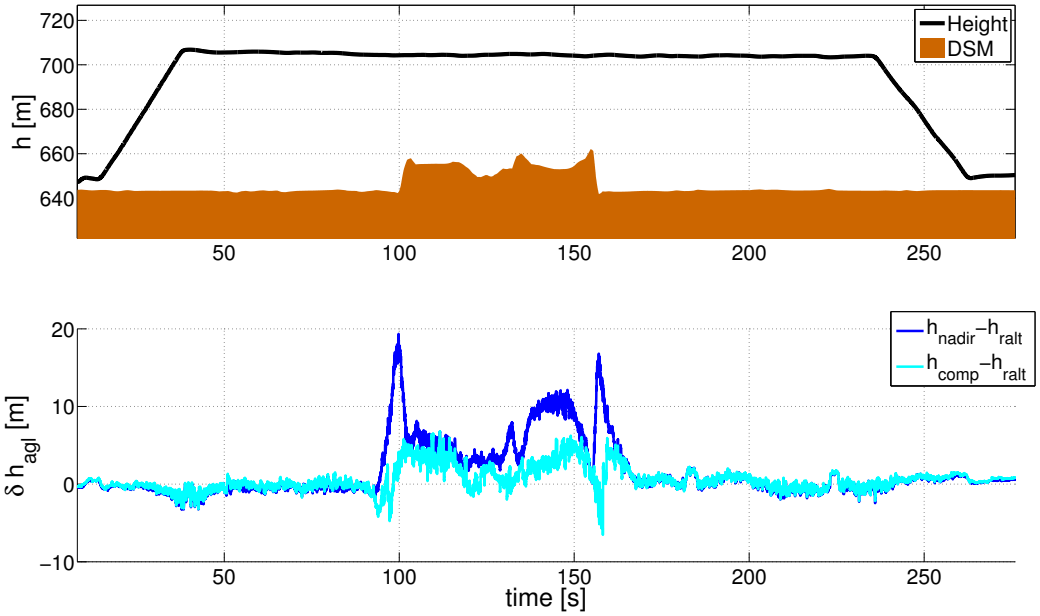

Figure 3.14: Compensation of UAV altimeter data

3.3.3 Navigation Filter Integration

This section describes the integration of a slant range measurement into an integrated navigation system. The required navigation filter basics are discussed first, followed by classical height aiding approaches and a novel approach.

3.3.3.1 Navigation Filter Update

A basic INS is based on a six-axis IMU, consisting of a three-axis gyroscope and a three-axis accelerometer. The sensor measurements are integrated with the Strapdown Algorithm (SDA) to the navigation states position, velocity and orientation. Sensor measurements are always corrupted by several error types. The influence of the error is strongly depending on the sensor class. The dominating error types of gyroscopes and accelerometers are bias-like, scale factor and noise-like errors. The integration of erroneous sensor measurements leads to position, velocity and orientation error drift. These inertial errors are usually estimated in a central navigation filter using an independent external measurement. This aiding information can be provided by GNSS or sensors like cameras, magnetometers, surface-ranging sensors, or in case of a wheel-based vehicle, odometers. Independent measurements enable the estimation of inertial navigation errors. The architecture of a conventional, aerospace typical integrated navigation system aided by a GNSS receiver is given in figure 3.15

The use of a Kalman filter has been approved for an IMU/GNSS based data fusion. Apart from the estimation of the navigation states position, velocity and orientation, an error state approach in beneficial. With this method, the position, velocity and orientation errors are estimated, which are limited in dynamic and range. The lower dynamics of the error states and the more linear behavior of the errors is the reason for this error-state-space design. The error state consists of the latitudinal position error $\delta\phi$, the longitudinal position error $\delta\lambda$, the height error δh, the velocity error $\delta\mathbf{v}_n$ and the platform orientation error $\boldsymbol{\psi}_{n\tilde{n}}$. The complete state vector is given by equation 3.34. This state error can be

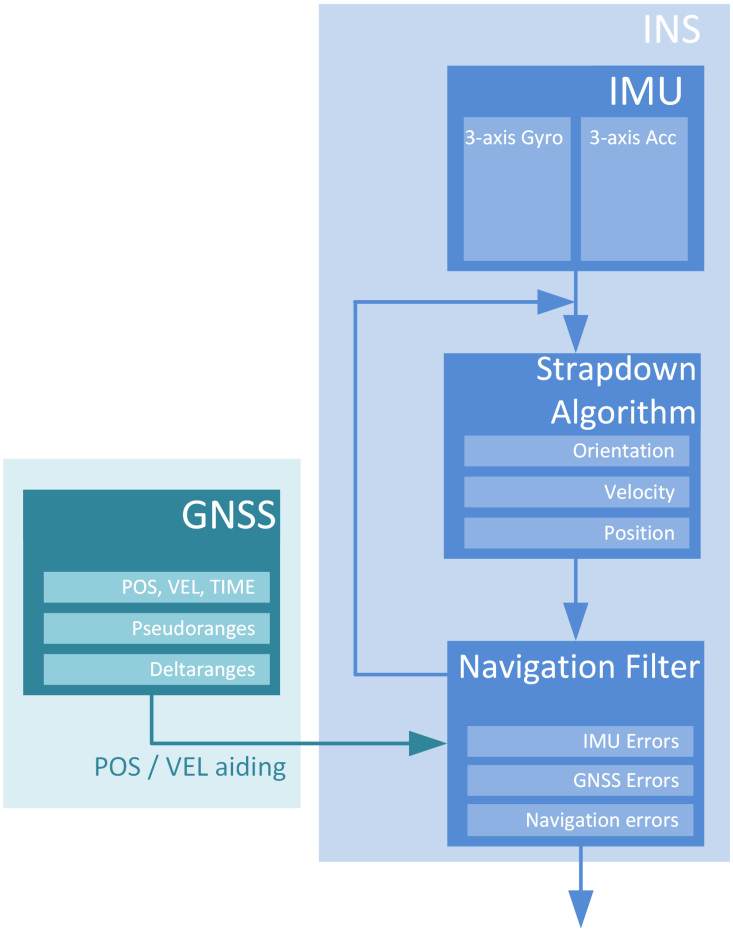

Figure 3.15: Integrated INS/GNSS navigation system

extended by inertial sensor error states to estimate for example bias or scale factor errors. For tightly coupled systems, the clock error and the clock error drift of the GNSS receiver is additionally estimated. A basic loosely coupled integrated navigation system with bias estimation of a six-axis IMU requires 15 states, a tightly coupled system requires at least 17 states. If a more detailed sensor error model is required or single satellite errors need to be estimated, the number of states increases significantly. The methods shown in this thesis are, for the sake of simplicity, independent of these additional Kalman filter states. A nine-state filter with a loosely-coupled GNSS aiding is considered further-on.

$$\delta\mathbf{z} = \begin{pmatrix} \delta\phi & \delta\lambda & \delta h & \delta\mathbf{v}_n & \boldsymbol{\psi}_{n\tilde{n}} \end{pmatrix}^T \tag{3.34}$$

For the topics discussed in this thesis, the aiding of a navigation filter is required and is explained. A more detailed consideration of navigation filters is given in [17] and [97]. The measurement matrix $\mathbf{H}$ maps the navigation filter states $\delta\mathbf{z}$ into the measurement space. For the implementation of a real navigation system, the time discrete representation of the Kalman filter is considered. A measurement $\delta\mathbf{y}_k$ is given in equation 3.35. The measurement noise requires to be zero-mean white-noise.

$$\delta\mathbf{y}_k = \mathbf{H}_k\delta\mathbf{z}_k + \delta\mathbf{h}_k, \qquad \delta\mathbf{h}_k \sim \mathcal{N}(\mathbf{0}, \mathbf{R}_k) \tag{3.35}$$

With this definition of a measurement, the first step of a Kalman filter correction begins with the calculation of the Kalman gain matrix $\mathbf{K}_k$. This matrix relates the measurement

covariance $\mathbf{R}_k$ with respect to the state covariance $\mathbf{P}_k^-$ of the last discrete time step. The Kalman gain matrix is calculated by equation 3.36.

$$\mathbf{K}_k = \mathbf{P}_k^- \mathbf{H}_k^T \left(\mathbf{H}_k \mathbf{P}_k^- \mathbf{H}_k^T + \mathbf{R}_k \right)^{-1} \tag{3.36}$$

The correction of the Kalman filter requires two steps. The navigation state is updated first (see equation 3.37), the new filter state $\delta \mathbf{z}_k^+$ thus consists of two components, the previous filter state $\delta \mathbf{z}_k^-$ and some part of the innovation. Secondly the navigation state covariance $\mathbf{P}_k^+$ is updated (see equation 3.38) using the past covariance $\mathbf{P}_k^-$.

$$\delta \mathbf{z}_k^+ = \delta \mathbf{z}_k^- + \mathbf{K}_k \left(\delta \mathbf{y}_k - \mathbf{H}_k \delta \mathbf{z}_k^- \right) \tag{3.37}$$

$$\mathbf{P}_k^+ = \left(\mathbf{I} - \mathbf{K}_k \mathbf{H}_k \right) \mathbf{P}_k^- \tag{3.38}$$

3.3.3.2 Slant Range Compensated Aiding

The conventional height aiding approach leads to the measurement matrix for a height error measurement δh given by equation 3.39.

$$\mathbf{H} = \begin{pmatrix} 0 & 0 & 1 & \mathbf{0}_{1x3} & \mathbf{0}_{1x3} \end{pmatrix} \tag{3.39}$$

The application of this measurement matrix requires an external compensation of the slant range error prior to the processing. In the sequel, a novel approach is presented which integrates the slant range compensation in the measurement equation. This section proposes an intrinsic compensation of the slant range which can be used in a navigation filter. The measurement equation is given by equation 3.40. The position errors $\delta \boldsymbol{\lambda}$ are substituted by their Cartesian counterparts $\delta \mathbf{x}$, which can be converted by $\delta \mathbf{x} = \mathbf{D} \delta \boldsymbol{\lambda}$.

$$\mathbf{d}_m = \mathbf{R}_{ms} \mathbf{R}_{sb} \left(\mathbf{R}_{bn} \mathbf{R}_{ne} \left(\mathbf{x}_e \left(L \right) - \mathbf{x}_e \left(P \right) \right) + \mathbf{x}_b \left(S \right) \right) \tag{3.40}$$

Linearization of equation 3.40 gives equation 3.41 (see appendix C.2 for derivation).

$$\begin{aligned} \delta \mathbf{d}_m \approx & \mathbf{R}_{\tilde{m}s} \mathbf{R}_{\tilde{s}b} \mathbf{R}_{b\tilde{n}} \mathbf{R}_{ne} \delta \mathbf{x}_e \left(L \right) - \mathbf{R}_{\tilde{m}s} \mathbf{R}_{\tilde{s}b} \mathbf{R}_{b\tilde{n}} \mathbf{R}_{ne} \delta \mathbf{x}_e \left(P \right) \\ & + \mathbf{R}_{\tilde{m}s} \mathbf{R}_{\tilde{s}b} \mathbf{R}_{b\tilde{n}} \boldsymbol{\Psi}_{\tilde{n}n} \mathbf{R}_{ne} \tilde{\mathbf{x}}_e \left(L \right) - \mathbf{R}_{\tilde{m}s} \mathbf{R}_{\tilde{s}b} \mathbf{R}_{b\tilde{n}} \boldsymbol{\Psi}_{\tilde{n}n} \mathbf{R}_{ne} \tilde{\mathbf{x}}_e \left(P \right) \\ & + \mathbf{R}_{\tilde{m}s} \mathbf{R}_{\tilde{s}b} \delta \mathbf{x}_b \left(S \right) + \boldsymbol{\Psi}_{m\tilde{m}} \mathbf{R}_{\tilde{m}s} \mathbf{R}_{\tilde{s}b} \mathbf{R}_{b\tilde{n}} \mathbf{R}_{ne} \tilde{\mathbf{x}}_e \left(L \right) \\ & - \boldsymbol{\Psi}_{m\tilde{m}} \mathbf{R}_{\tilde{m}s} \mathbf{R}_{\tilde{s}b} \mathbf{R}_{b\tilde{n}} \mathbf{R}_{ne} \tilde{\mathbf{x}}_e \left(P \right) + \boldsymbol{\Psi}_{m\tilde{m}} \mathbf{R}_{\tilde{m}s} \mathbf{R}_{\tilde{s}b} \tilde{\mathbf{x}}_b \left(S \right) \\ & + \mathbf{R}_{\tilde{m}s} \boldsymbol{\Psi}_{s\tilde{s}} \mathbf{R}_{\tilde{s}b} \mathbf{R}_{b\tilde{n}} \mathbf{R}_{ne} \tilde{\mathbf{x}}_e \left(L \right) - \mathbf{R}_{\tilde{m}s} \boldsymbol{\Psi}_{s\tilde{s}} \mathbf{R}_{\tilde{s}b} \mathbf{R}_{b\tilde{n}} \mathbf{R}_{ne} \tilde{\mathbf{x}}_e \left(P \right) \\ & + \mathbf{R}_{\tilde{m}s} \boldsymbol{\Psi}_{s\tilde{s}} \mathbf{R}_{\tilde{s}b} \tilde{\mathbf{x}}_b \left(S \right) \end{aligned} \tag{3.41}$$

The method assumes $\boldsymbol{\psi}_{n\tilde{n}}$ to be known with high accuracy as condition for the validity of the altimeter simulation model. If the angular orientation error cannot be neglected, this compensation method cannot be applied. Furthermore, the mechanical sensor mounting is fix and can be determined with a high accuracy, thus the s frame misalignment $\boldsymbol{\psi}_{\tilde{s}s}$ is not considered. The equation reduced by the neglectable terms is given in 3.42.

$$\begin{aligned} \delta \mathbf{d}_m \approx & \mathbf{R}_{\tilde{m}s} \mathbf{R}_{\tilde{s}b} \mathbf{R}_{b\tilde{n}} \mathbf{R}_{ne} \delta \mathbf{x}_e \left(L \right) - \mathbf{R}_{\tilde{m}s} \mathbf{R}_{\tilde{s}b} \mathbf{R}_{b\tilde{n}} \mathbf{R}_{ne} \delta \mathbf{x}_e \left(P \right) \\ & + \boldsymbol{\Psi}_{m\tilde{m}} \mathbf{R}_{\tilde{m}s} \mathbf{R}_{\tilde{s}b} \mathbf{R}_{b\tilde{n}} \mathbf{R}_{ne} \tilde{\mathbf{x}}_e \left(L \right) - \boldsymbol{\Psi}_{m\tilde{m}} \mathbf{R}_{\tilde{m}s} \mathbf{R}_{\tilde{s}b} \mathbf{R}_{b\tilde{n}} \mathbf{R}_{ne} \tilde{\mathbf{x}}_e \left(P \right) \\ & + \boldsymbol{\Psi}_{m\tilde{m}} \mathbf{R}_{\tilde{m}s} \mathbf{R}_{\tilde{s}b} \tilde{\mathbf{x}}_b \left(S \right) \end{aligned} \tag{3.42}$$

The measurement frame error $\boldsymbol{\psi}_{m\tilde{m}}$ describes the mismatch between measured and estimated measurement direction. This error is influencing the covariance matrix as derived in section 3.2. It can be neglected furthermore and the measurement equation can be reduced to 3.43. The measurement matrix is given by equation 3.44.

$$\begin{aligned}\delta\mathbf{d}_m \approx &\mathbf{R}_{\tilde{m}s}\mathbf{R}_{\tilde{s}b}\mathbf{R}_{b\tilde{n}}\mathbf{R}_{ne}\delta\mathbf{x}_e\,(L) - \mathbf{R}_{\tilde{m}s}\mathbf{R}_{\tilde{s}b}\mathbf{R}_{b\tilde{n}}\mathbf{R}_{ne}\delta\mathbf{x}_e\,(P)\\ &+ \boldsymbol{\Psi}_{m\tilde{m}}\mathbf{R}_{\tilde{m}s}\mathbf{R}_{\tilde{s}b}\tilde{\mathbf{x}}_b\,(S)\end{aligned} \tag{3.43}$$

$$\mathbf{H} = \left(-\begin{pmatrix}0\\0\\1\end{pmatrix}\mathbf{R}_{\tilde{m}s}\mathbf{R}_{\tilde{s}b}\mathbf{R}_{b\tilde{n}}\mathbf{R}_{ne} \quad \mathbf{0}_{3x3} \quad \mathbf{0}_{3x3}\right) \tag{3.44}$$

This formulation of the measurement matrix allows the processing of a raw altimeter measurement. The compensation of the slant range error is done within the measurement matrix. The height error is rotated from the e frame via the navigation frame n, the body frame b and the sensor frame s into the measurement frame m. The frame misalignment rotation matrices $\mathbf{R}_{m\tilde{m}}$, $\mathbf{R}_{s\tilde{s}}$, $\mathbf{R}_{b\tilde{b}}$ and $\mathbf{R}_{n\tilde{n}}$ are unknown and can not be considered for the compensation.
The main benefit of this formulation is the instantaneously processing of incoming measurements. While an external compensation requires a valid input measurement, the processing steps of this novel approach can be parallelized. Regarding the high computational burden of the measurement direction estimation with the altimeter simulation model, this is a benefit in terms of processing time. The measurement covariance for this novel approach has been derived in equation 3.21 in section 3.2.
The application results of the methods introduced in this chapter with simulated and real data is given in chapter 7. The results and achievements of this chapter are summarized in the following box:

Results

- Platform, sensor and environmental specific altimeter measurement validity criteria have been introduced
- Variance estimation equations for different applications (footprint, slant range and height) and sensor specifications (wide/narrow beam-shape)
- Three compensation methods presented with platform, environmental and sensor specific applications
- Method validated using recorded altimeter data
- Compensation performance is strongly depending on the currentness of the DSM (vegetation, terms, weather)
- Intrinsic slant range compensation within the measurement matrix

Chapter 4

Precise Positioning SAN

The aiding of INSs, with tactical grade performance or less, is mandatory to avoid a short-term position drift. The aiding of INSs with TAN has been a traditional approach in GNSS denied situations. TAN systems are designed to provide not only a robust height estimate, but also a horizontal position solution above sufficiently rough surface and with sufficiently low flight altitude. The application of TAN systems is complimentary to the use of GNSS in their availability. The GNSS position solution is degraded, especially in low-level flights, by poor satellite constellation geometries caused by terrain shading and vulnerable to intentional degradations like jamming or spoofing. In those situations, TAN can replace the GNSS based position aiding and can avoid position error drifts. The absolute position is determined by the comparison of the measured topographic elevation beneath the flight path with a DEM. An illustration providing the recording of the surface elevation beneath the flight path is given in figure 4.1.

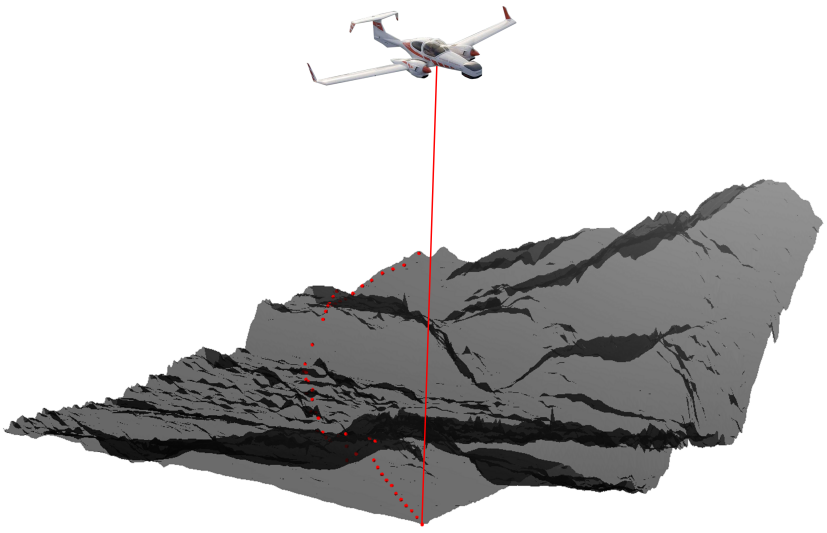

Figure 4.1: Altimeter height above ground track measurement

The surface-ranging sensor errors, discussed in 2.3, also affect TAN. The TAN algorithm is sensitive to erroneous height measurements. TAN systems have been traditionally limited by the altimeter measurement accuracy and the DEM accuracy. Classical TAN systems which do not compensate for the slant range sensor errors do not reach the GNSS position

accuracy. Therefore, these systems only serve as backup for GNSS outages rather than as alternative aiding source. Erroneous measurements can lead to position fix ambiguities, which can lead to inconsistencies of the navigation filter.
The opportunity to improve existing methods is mainly enabled by two factors: modern DSMs with high resolution and accuracy and an ever-growing computational performance of available computers. These two factors were the limitations of early TAN systems and the processing of height above ground measuring altimeters.

Motivation

- TAN is highly sensitive to surface-ranging measurement errors
- TAN accuracy cannot reach GNSS accuracy level
- Availability of computational power and high accuracy DEMs open opportunities for further improvement

In this chapter, novel methods to improve TAN based on classical matching functions are introduced. First, the knowledge of slant range measurement errors, obtained in section 2.3, is used to establish new procedures of processing height above ground measurements in TAN applications. The measurement conditioning methods of chapter 3 can only be partially applied to TAN. The aim of TAN is the estimation of a three-dimensional position, while the previously introduced methods require a precise horizontal position to improve the vertical accuracy.
New methods for improvement have to be developed. The measurement information content of surface-ranging sensors is analyzed in detail to isolate the main dominating influences and to adjust the measurement strategy. Novel methods for a robust and beneficial surface sampling are introduced. Furthermore, this knowledge is used to identify criteria for measurement exploitation to improve the position accuracy of TAN. This measurement exploitation excludes redundant information and isolates the significant information content. Not only the calculation time can be reduced with this approach, but also the shape of the matching function can be changed for a more accurate position estimate.
The knowledge of the slant range compensation algorithm is applied to TAN and adjusted to the positioning problem. With this adaption of the compensation method, the accuracy of TAN systems can further be improved. The grid-search approach is extended by a calculation time efficient method to reduce the calculation burden of the compensation.
To state the difference to classical TAN system and to highlight the application of DSM elevation databases, the term SAN is introduced in this thesis. Consequently, novel TAN systems using DSM are furthermore denoted SAN. For further improvements, approaches for multi-beam sensor measurements are discussed in section 4.6.

Solution Approach

- Measurement information content analysis & exploitation algorithm
- Improvement of matching accuracy and robustness
- Increasing the information content with multi-beam sensors

First, an overview of existing TAN and the used techniques is given. In the sequel, the information content analysis and the improvement of SAN with an information exploitation

algorithm is introduced. Furthermore, the sampling strategy of the surface elevation is analyzed. Subsequently, the influence of position error drift on the SAN is discussed. The slant range compensation approach to SAN and the benefit of reducing the probability of ambiguities is shown. The chapter is concluded with a consideration of the benefits of multi-beam surface-ranging sensors for SAN. Parts of the topics and results discussed in this chapter have first been published in [83].

4.1 Matching function-based SAN

4.1.1 Existing TAN Systems

This section gives an overview of existing TAN systems and applied technologies. The development of TAN systems began in the 1950's. Several synonyms are used for the technology of determination of a horizontal position by measuring the height above ground and comparing the height profile with a DEM. The most popular terms are given in the following list. These terms are often derived from existing systems and are regarded synonymous for the entire system category.

- Terrain Aided Navigation (TAN)
- Terrain-Referenced Navigation (TRN)
- Terrain-Contour Navigation (TCN)
- Terrain-Contour Matching (TCM)
- Terrain-Based Navigation (TBN)
- Terrain-Matching Navigation (TMN)

All of these terms include the word 'terrain' as substantial component, which is another indicator for the common use of DTM as reference in classical TAN approaches. Table 4.1 gives an overview of existing terrain navigation systems and the applied technologies. An overview of further development of TERPROM is given by [29]. The development of the Digital Terrain System (DTS) based on a TERPROM algorithm is described in [28]. A Laser scanner based SAN is promoted in [23]. A monitoring algorithm for classical TAN is introduced by [87]. The underwater application of TAN using ultrasonic sensors is explained in [66] and in [57]. A method considering the Radar beam-shape is introduced in [68]. The underwater application if TERCOM is shown in [54].
The integration of Radar altimeter measurements in a navigation system called RAPIN in shown in [56]. A method based on an interferometric synthetic aperture Radar sensor is introduced in [51]. The different use-cases of DEM in airborne platforms as navigation aiding or as display enhancement is provided in [10] and [9]. A high-level description of the development of an integrated navigation system using TAN and GPS is provided in [69].
Apart from navigation functions, surface-ranging measurements can be used to indicate critical situation to the pilots by GPWS [39].

System	Characteristics
Automatic Terrain Recognition And Navigation (ATRAN)	• Front looking scanning Radar • Analog optical correlation • Reference images stored on a film • Application: TM-76A MACE cruise missile in 1950s • Disadvantages: large and heavy
Terrain Contour Matching (TERCOM)	• Development 1960 - 1976 • Batch-correlation based method • High computational load for comparison • High memory storage for reference map • Terrain roughness dependent trajectory planning
Terrain Profile Matching (TERPROM)	• Development started in 1987 • Batch-processing mode for acquisition • Tracking mode for continuous updates • Additionally: Terrain Following and GPWS
Sandia Inertial Terrain Aided Navigation (SITAN)	• Developed around 1988 • Sequential processing approach • Extended Kalman Filter with terrain linearization • Disadvantage: Acquisition Performance due to terrain linearization
StockPot Algorithm Robust Terrain-Aided Navigation (SPARTAN)	• Reduction of altimeter measurements • Approximation (quadratic) of the comparison function • Maximum of the fitted comparison function for position estimation
Terrain Navigation System (TERNAV)	• Development started in 2001 • Non-linear recursive method based on Bayes theorem
Precise Terrain Aided Navigation (PTAN)	• Synthetic Aperture Radar • 10ft horizontal accuracy • Modular system to apply SITAN, TERCOM or TERPROM algorithms

Table 4.1: SAN systems overview ([4], [59], [45], [46], [42], [73], [47], [74], [61], [95], [78], [53])

	Batch processing	**Sequential processing**
Technology	Elevation profile matching	Stochastic filtering
Acquisition	Good performance (grid-size dependent)	Not possible, initial position required
Update frequency	Low (correlation length)	High (sensor frequency)

Table 4.2: SAN method comparison

Solutions for the indoor and urban positioning problem using horizontal Laser scanner measurements are given in [81] and [80]. A student thesis dealing with indoor navigation algorithms has been supervised ([72]).

Classical terrain navigation systems always relied on DEMs and require an on-board mass-storage, which was a limiting factor in the past. The mission trajectory had to be planned a-priori, which restricted the flexibility in-flight enormously. The DTM of the overflown path was loaded in the navigation system embedded computer, which implies that the terrain navigation was only available when the platform did not leave the defined area. Another limiting factor of terrain navigation was the calculational burden due to the high amount of table lookup function calls of the reference elevation. Additionally, the time consuming grid-search algorithms constitute a significant computational load.

The major design decision for a TAN system is whether batch processing or sequential processing algorithms shall be applied. Batch processing-based algorithm collect measurement within a certain time period and process them in batches, while a sequential approach processes each measurement separately. Both approaches provide advantages and disadvantages, they are compared on table 4.2 [95].

Batch processing based systems collect the measurements over a defined time interval and use a matching metric-based grid-search algorithm to find the best match with a reference DEM. Apart from position tracking, this method is also capable of a position acquisition.

Modern sequential TAN systems are based on Bayes' theorem and apply a nonlinear stochastic filter, like a particle or point mass filter. With this approach, nonlinear navigation problems can be covered, which is an advantage, compared to the batch processing approach. On the other hand, sequential methods cannot rely on a continuous processing of measurements and cannot be used for position acquisition.

These complementary characteristics promote the application of a comation of both approaches. For initial acquisition and re-acquisition after a loss of track, a batch-based algorithm can be used. When the initial position is fixed, the system can continue tracking with a sequential algorithm.

The further focus of this thesis will be on batch processing and matching metric based grid-search algorithms. Sequential TAN methods are not part of the problem formulation of this thesis. More details on this topic can be obtained by [11], [13], [12], [66], [59], [14] and [70].

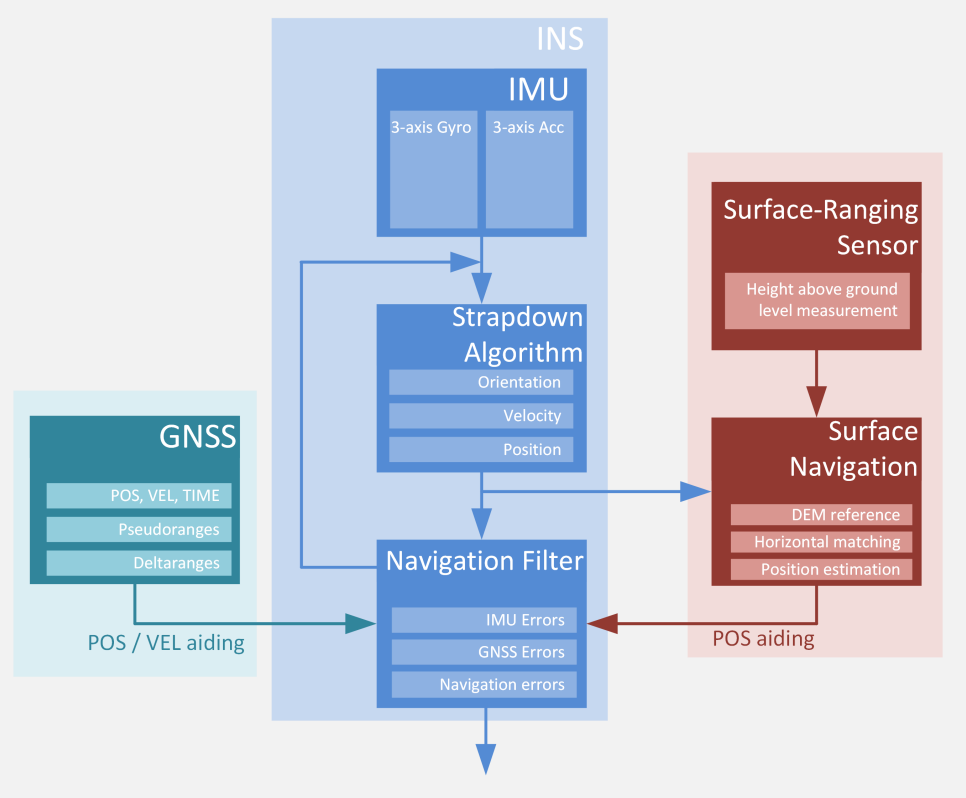

Figure 4.2: Loosely-coupled INS/GNSS/SAN (TAN)

4.1.2 TAN Methods

Comparable to GNSSs, TAN systems provide an absolute position estimate which is capable to aid an INS. TAN systems process the measured elevation profile of the overflown surface and compare it with a DEM. The architecture of a TAN system integrated in a integrated navigation system setup is given in the block diagram in figure 4.2.

4.1.2.1 Altimeter Aiding

In this section, the basic processing of a height above ground h_{agl} measurement for INS aiding is introduced. The basics of INSs are shown in [38] and [58]. Integrated navigation systems including their estimation theory and aiding sensors are explained in [37], [97], [46] and [48]. The measurement equation is given by equation 4.1.

$$h_{agl} = h(P) - h_{dem}(\phi(P), \lambda(P)) \tag{4.1}$$

The measurement has to be linearized for the use in a Kalman filter. A perturbation approach is given by equation 4.2. A first order Taylor series is applied to linearize the topographic elevation table lookup.

$$
\begin{aligned}
\tilde{h}_{agl} + \delta h_{agl} =& \tilde{h}(P) + \delta h(P) - \tilde{h}_{dem}\left(\tilde{\phi}(P) + \delta\phi(P), \tilde{\lambda}(P) + \delta\lambda(P)\right) - \delta h_{dem} \\
\tilde{h}_{agl} + \delta h_{agl} \approx& \tilde{h}(P) + \delta h(P) - \tilde{h}_{dem}\left(\tilde{\phi}(P), \tilde{\lambda}(P)\right) - \delta h_{dem} \\
&- \left.\frac{\partial h_{dem}(\phi,\lambda)}{\partial\phi}\right|_{\phi=\tilde{\phi}(P),\lambda=\tilde{\lambda}(P)} \cdot \delta\phi(P) \\
&- \left.\frac{\partial h_{dem}(\phi,\lambda)}{\partial\lambda}\right|_{\phi=\tilde{\phi}(P),\lambda=\tilde{\lambda}(P)} \cdot \delta\lambda(P)
\end{aligned}
\tag{4.2}
$$

With the basic relation of the total states in 4.3, the error equation can be isolated and is given in 4.4.

$$
\tilde{h}_{agl} = \tilde{h}(P) - \tilde{h}_{dem}\left(\tilde{\phi}(P), \tilde{\lambda}(P)\right) \tag{4.3}
$$

$$
\begin{aligned}
\delta h_{agl} \approx& \delta h(P) - \delta h_{dem} \\
&- \left.\frac{\partial h_{dem}(\phi,\lambda)}{\partial\phi}\right|_{\phi=\tilde{\phi}(P),\lambda=\tilde{\lambda}(P)} \cdot \delta\phi(P) \\
&- \left.\frac{\partial h_{dem}(\phi,\lambda)}{\partial\lambda}\right|_{\phi=\tilde{\phi}(P),\lambda=\tilde{\lambda}(P)} \cdot \delta\lambda(P)
\end{aligned}
\tag{4.4}
$$

The measurement matrix $\mathbf{H}$ for the nine states of the navigation filter, including position, velocity and orientation errors, is given by equation 4.5. The results can be compared to [59] with respect to the different definition of the n frame down channel. Apart from the height correction, this measurement matrix maps the latitudinal and longitudinal errors with the terrain gradient onto the height measurement. The use of a surface gradient for horizontal position aiding is discussed in the following section.

$$
\mathbf{H} = \begin{pmatrix} -\left.\frac{\partial h_{dem}(\phi,\lambda)}{\partial\phi}\right|_{\phi=\tilde{\phi}(P),\lambda=\tilde{\lambda}(P)} & -\left.\frac{\partial h_{dem}(\phi,\lambda)}{\partial\lambda}\right|_{\phi=\tilde{\phi}(P),\lambda=\tilde{\lambda}(P)} & 1 & \mathbf{0}_{1x3} & \mathbf{0}_{1x3} \end{pmatrix} \tag{4.5}
$$

4.1.2.2 Terrain Linearization

The validity of the terrain linearization under different conditions is discussed in this section. The gradient of the surface can be calculated with the used DEM in respect to the definitions in figure 4.3. The latitudinal gradient is given as difference quotient in equation 4.6, the longitudinal in equation 4.7.

$$
\left.\frac{\partial h_{dem}(\phi,\lambda)}{\partial\phi}\right|_{\phi=\tilde{\phi}(P),\lambda=\tilde{\lambda}(P)} = \frac{h_{dem}(R_2) - h_{dem}(R_1)}{\phi(R_2) - \phi(R_1)} \tag{4.6}
$$

$$
\left.\frac{\partial h_{dem}(\phi,\lambda)}{\partial\lambda}\right|_{\phi=\tilde{\phi}(P),\lambda=\tilde{\lambda}(P)} = \frac{h_{dem}(Q_2) - h_{dem}(Q_1)}{\phi(Q_2) - \phi(Q_1)} \tag{4.7}
$$

For the calculation of the surface gradient within the tile $(T_{11}, T_{12}, T_{21}, T_{22})$ the auxiliary point definitions in equation 4.8 are required.

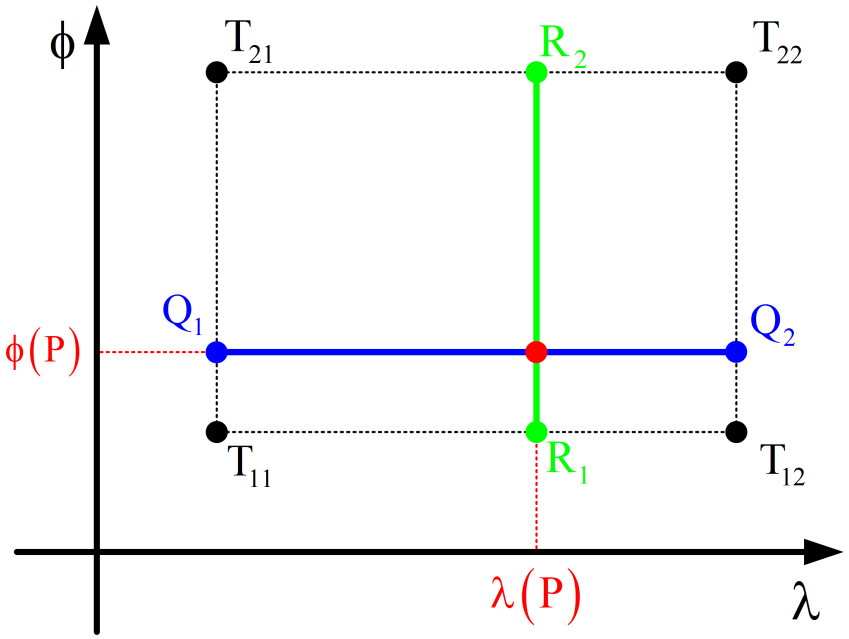

Figure 4.3: Terrain gradient

$$
\begin{aligned}
h_{dem}(R_1) &= \frac{h_{dem}(T_{12}) - h_{dem}(T_{11})}{\lambda(T_{12}) - \lambda(T_{11})}(\lambda(P) - \lambda(T_{11})) + h_{dem}(T_{11}) \\
h_{dem}(R_2) &= \frac{h_{dem}(T_{22}) - h_{dem}(T_{21})}{\lambda(T_{22}) - \lambda(T_{21})}(\lambda(P) - \lambda(T_{21})) + h_{dem}(T_{21}) \\
h_{dem}(Q_1) &= \frac{h_{dem}(T_{21}) - h_{dem}(T_{11})}{\phi(T_{21}) - \phi(T_{11})}(\phi(P) - \phi(T_{11})) + h_{dem}(T_{11}) \\
h_{dem}(Q_2) &= \frac{h_{dem}(T_{22}) - h_{dem}(T_{12})}{\phi(T_{22}) - \phi(T_{12})}(\phi(P) - \phi(T_{11})) + h_{dem}(T_{12})
\end{aligned}
\tag{4.8}
$$

Since the DEM is given as elevation raster data, the discrete elevation gradient has to be interpolated for a continuous gradient representation. A beneficial use of the linearized equations is only guaranteed if the INS position navigation error is significantly smaller than the DEM resolution. If this requirement is not fulfilled, the horizontal correction cannot compensate the estimated error and may even increase the navigation error. Two examples in the following illustration explain this aspect.
The left illustration in figure 4.4 shows the true and the estimated position of the INS. The height measurement yields a larger height measurement compared to the expected nadir height at the estimated position. The larger height of the altimeter measurement is interpreted with the surface gradient as shift towards the true position. In this example the surface gradient-based correction provides a good result due to the small relation between DEM tile size and position error.
The right part of figure 4.4 shows the same horizontal situation using a modern high-resolution DSM. The true and estimation horizontal position have not changed their position but the corresponding high-resolution DSM results in an opposing gradient compared to the first example. This opposing gradient is caused by the surface variations included in the DSM but not in the DTM.

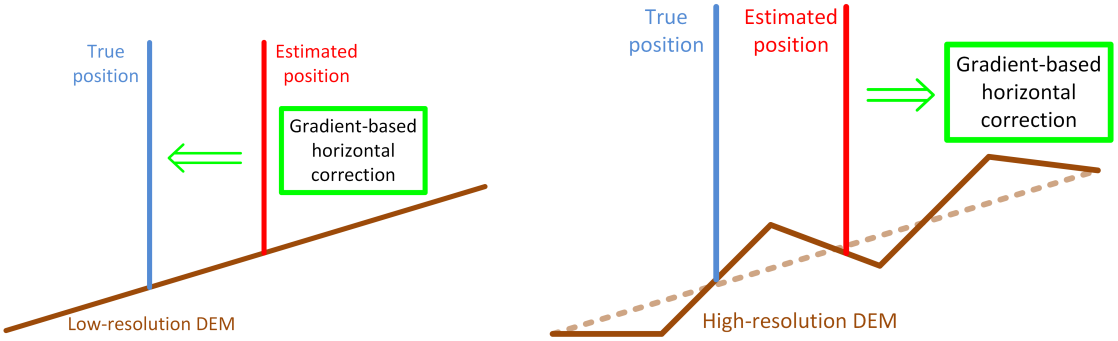

(a) Low-resolution DTM (b) High-resolution DSM

Figure 4.4: Gradient-based horizontal position correction

In this example, the correction even increases the horizontal position error. The resolution of modern DSMs is about five meters or less. The expected horizontal position error should be smaller to obtaine a suitable surface aiding.
In this thesis, the use of surface gradient based horizontal aiding is avoided due to the discussed problems. For high precise SAN DEMs with resolution up to one meter are applied and therefore gradient based horizontal aiding can not be applied.

4.1.2.3 Matching Approach

The matching metric based grid-search algorithm collects the topographic elevation measurements below the flight path and georeferences these measurements using the platform's INS position solution. By georeferencing the measurements, the navigation errors of the INS are intrinsically included in the elevation profile. This elevation profile is subsequently compared to a DEM using the matching metric.
The measured profile is shifted horizontally within the matching grid and for all grid points the matching function is repeated. The grid-resolution Δg of the grid-search can be adjusted to the available computational power, while the grid-size g has to be chosen to include the largest anticipated horizontal position error.
The matching function with the best match indicates the position error and can be used to correct the navigation system. A search-grid is given in figure 4.5, the number of matching functions calls N_{match} can be calculated with the grid-resolution Δg and the grid-size g in equation 4.9.

$$N_{match} = \left(\frac{g}{\Delta g}\right)^2 \tag{4.9}$$

The matching function of the measured height profile including the collected amount of measurements K and the DEM height h_{dem} is discussed following. For each grid-search shift i, the arithmetic mean height offset $\Delta\bar{h}_i$ of the measurement is calculated. The mean height offset is later eliminated to avoid a negative effect of an absolute platform height $\tilde{h}_k$ error. To calculate the offset, the reference elevation map is interpolated at the corresponding horizontal position of the measured samples. An illustration of the first step is given in figure 4.6, the equation to calculate the offset is given in 4.10.

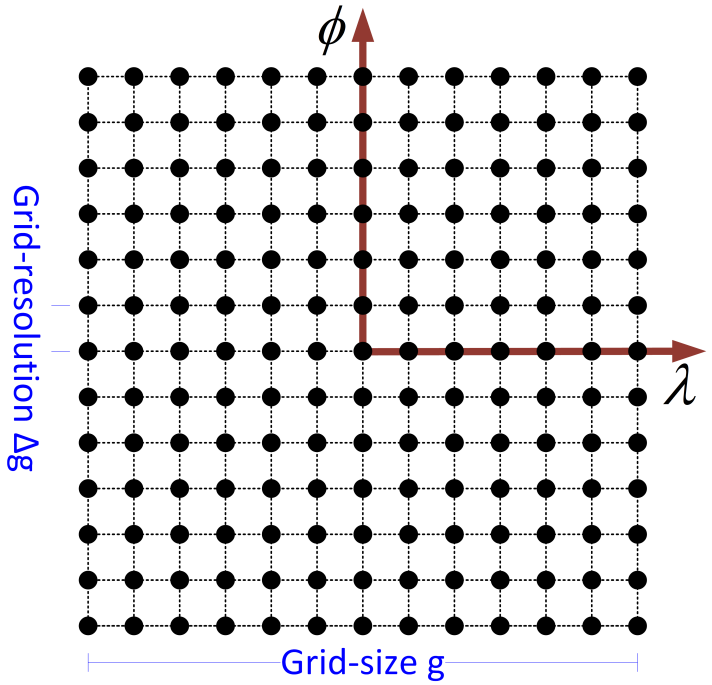

Figure 4.5: Regular grid-search

$$\Delta\bar{h}_i = \frac{1}{K}\sum_{k=1}^{K}\left(\tilde{h}_k - \tilde{h}_{agl,k} - h_{dem}\left(\tilde{\phi}_k + \Delta\phi_i, \tilde{\lambda}_k + \Delta\lambda_i\right)\right) \tag{4.10}$$

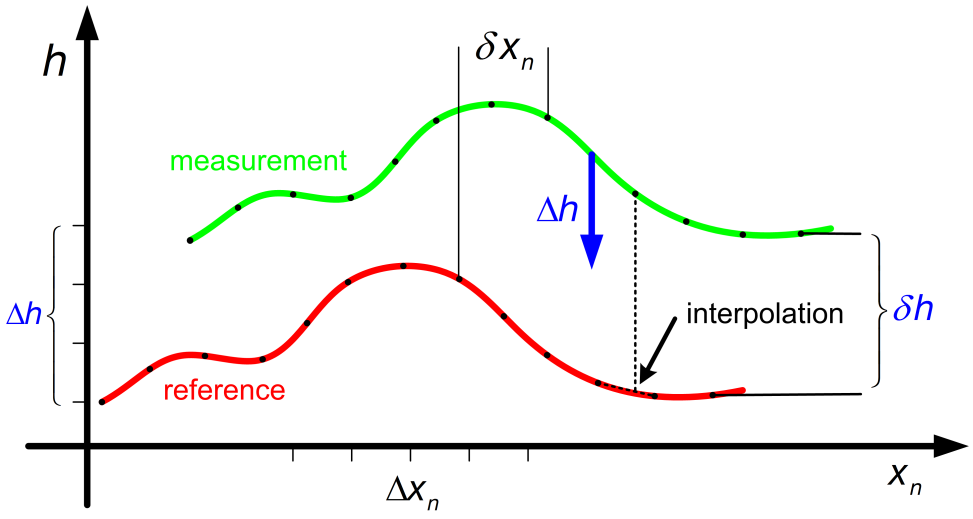

Figure 4.6: Eliminating the height offset

The elimination of the mean height offset brings the advantage that INS or barometric height error can not negatively influence the correlation result. However, the separation of two identically height profiles in different absolute heights can not be distinguished with this method. The probability of matching ambiguities can increase due to this.
The matching function compares the two elevation profiles shapes for their best match. Several matching metrics have been applied in the past, for this thesis an offset-free, non-

quadratic comparison metric has been chosen. The metric is given by equation 4.11 and is illustrated in figure 4.7.

$$M_i = \frac{1}{K}\sum_{k=1}^{K}\left|\tilde{h}_k - \tilde{h}_{agl,k} - h_{dem}\left(\tilde{\phi}_k + \Delta\phi_i, \tilde{\lambda}_k + \Delta\lambda_i\right) - \Delta\bar{h}_i\right| \tag{4.11}$$

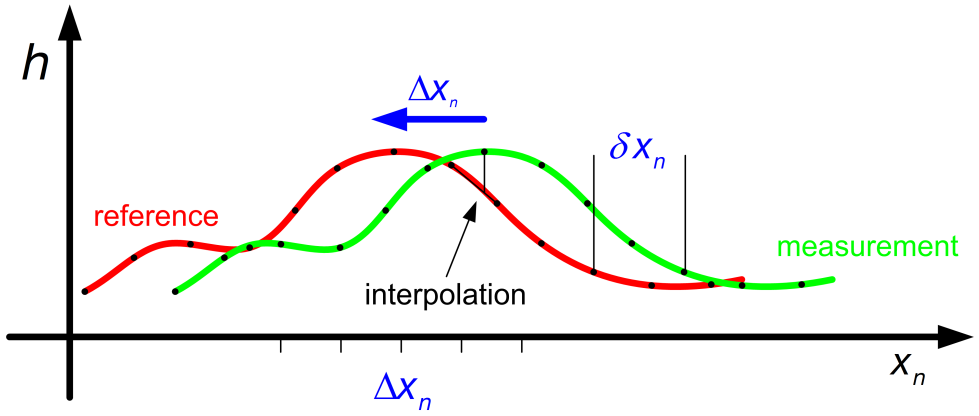

Figure 4.7: Calculating the match quality

Conclusively, the procedure of building up the entire matching matrix requires the following three steps for each grid-search shift i.

1. All elevation profile elements $\boldsymbol{\lambda}_L$ are shifted horizontally by $\Delta\phi_i, \Delta\lambda_i$

$$\boldsymbol{\lambda}_{L,i} = \boldsymbol{\lambda}_L + \Delta\boldsymbol{\lambda}_i \tag{4.12}$$

2. The mean height offset with the current shift is calculated to $\Delta\bar{h}_i$

3. The matching function M_i is calculated

The result of this grid-search algorithm is the matching matrix $\mathbf{M}$ providing the matching errors for each grid-shift. The matching function shift with the smallest error is the position with the maximum likelihood. The position error estimate can be written with the index of the minimum matching function i_{min} and the mean height offset to equation 4.13 for a non-ambiguous matching matrix.

$$\begin{aligned} i_{min} &= \arg\min\left(\mathbf{M}\right) \\ \begin{pmatrix}\delta\phi\\ \delta\lambda\\ \delta h\end{pmatrix} &= \begin{pmatrix}\Delta\phi_{i_{min}}\\ \Delta\lambda_{i_{min}}\\ \Delta\bar{h}_{i_{min}}\end{pmatrix} \end{aligned} \tag{4.13}$$

The integration of the position estimate in a Kalman Filter based nine-state navigation system with the measurement equation 4.14 is given by equation 4.15.

$$\delta\mathbf{y}_{k+1} = \mathbf{H}_{k+1}\delta\mathbf{z}_{k+1} + \nu_{k+1} \tag{4.14}$$

$$\mathbf{H} = \begin{pmatrix}\mathbf{I}_{3x3} & \mathbf{0}_{3x3} & \mathbf{0}_{3x3}\end{pmatrix} \tag{4.15}$$

The term ν_{k+1} in the measurement equation 4.14 is the measurement noise and covers the uncertainty of the measurement. The measurement noise is assumed to be zero-mean white Gaussian noise and not time correlated and the corresponding covariance of the measurement is given by equation 4.16 [30].

$$\begin{aligned} \mathsf{E}\left(\nu_k\right) &= \mathbf{0}_{3x3} \\ \mathsf{E}\left(\nu_k \nu_l^T\right) &= \begin{cases} \mathbf{R}_k & k = l \\ \mathbf{0}_{3x3} & k \neq l \end{cases} \end{aligned} \tag{4.16}$$

This assumption is fulfilled for a batch based SAN. Each update contains exclusively or mostly new measurements, which have not been used for a former navigation filter update. If the update frequency needs to be increased, the correlation length of the batch processing has to be considered in the covariance matrix. An approach for covariance estimation of a SAN system assuming uncorrelated updates is given in the following section.

4.1.2.4 Covariance Estimation

The integration of TAN into an existing Kalman Filter based navigation system requires not only a position observation, but also the corresponding covariance matrix $\mathbf{R}$ of the measurement. The covariance of a measurement indicates the accuracy quality and is used in the discrete Kalman filter for the calculation of the Kalman filter gain matrix $\mathbf{K}$ (see equation 4.17).

$$\mathbf{K}_{k+1} = \mathbf{P}_{k+1}^{-} \mathbf{H}_{k+1}^T \left(\mathbf{H}_{k+1} \mathbf{P}_{k+1}^{-} \mathbf{H}_{k+1}^T + \mathbf{R}_{k+1}\right)^{-1} \tag{4.17}$$

The measurement covariance required for the central navigation filter has to represent the current measurement quality. TAN strongly depends on external factors like the surface characteristics and the range measurement quality, which influence the measurement quality and should hence be covered in the covariance estimation. With a static approach, well shaped matching functions would be downgraded in their impact on the total navigation performance and inaccurate matching functions would be overrated, which could result in an inconsistent navigation solution. Hence, a static covariance estimation must be avoided.
While a sequential TAN system delivers an intrinsic covariance based on the measurement input variances, the covariance of a matching function-based system has to be calculated separately. A particle-based approach for covariance estimation of a block processing TAN system is given e. g. in [59], a covariance estimation based on the input variances is given in [60]. A method for covariance calculation based on the application of a recursive least square estimator is given in [102].
In this thesis, an appropriate approach using the matching function shape to derive the covariance is applied, which has been first introduced in [11]. The following covariance estimation is divided into two parts, first the covariance of the horizontal position estimate is derived using the matching function shape, then the covariance of the height is included to cover a three-dimensional position covariance. The basic idea of this approach is the interpretation of the matching matrix $\mathbf{M}$, which is a quality value for the matching of the measured height profile to the DEM reference, as probability density function.

This approach requires that the most unlikely position estimate provides the smallest value within the matching matrix and the most likely provides the maximum value. The matching metric in equation 4.11 is defined as matching function error and provides the smallest value for the most probable position estimate and the largest error for the most unlikely. For the covariance estimation, the matching metric is transformed from an error indication into a matching quality indication value with the relation in equation 4.18. The operation $\max(\mathbf{M})$ yields the largest value of the matching matrix $\mathbf{M}$.

$$\mathbf{M}^{+} = \max(\mathbf{M}) - \mathbf{M} \tag{4.18}$$

For the calculation of the covariance, the matching function will be interpreted as probability density function and thus has to be normalized. The normalized matching metric is given by equation 4.19.

$$\bar{\mathbf{M}}^{+}(\Delta\phi, \Delta\lambda) = \frac{\mathbf{M}^{+}(\Delta\phi, \Delta\lambda)}{\int\int \mathbf{M}^{+}(\Delta\phi, \Delta\lambda)\, d\phi d\lambda} \tag{4.19}$$

This normalized matching function fulfills the requirements on a probability distribution and can be used to calculate the expectation value vector. This expectation can be used as alternative to the minimum matching function error as position estimate. The calculation of the expectation value vector of the matching matrix is given by equation 4.20.

$$E(\boldsymbol{\lambda}) = \begin{bmatrix} E(\phi) \\ E(\lambda) \end{bmatrix} = \begin{bmatrix} \int_{-\infty}^{\infty}\int_{-\infty}^{\infty} \phi_i \bar{\mathbf{M}}^{+}(\phi_i, \lambda_i)\, d\phi d\lambda \\ \int_{-\infty}^{\infty}\int_{-\infty}^{\infty} \lambda_i \bar{\mathbf{M}}^{+}(\phi_i, \lambda_i)\, d\phi d\lambda \end{bmatrix} \tag{4.20}$$

The covariance of the matching matrix can be calculated with equation 4.21 using the expectation vector. This approach is analog to the covariance determination of a point mass filter [2].

$$Cov(\boldsymbol{\lambda}) = E\left[(\boldsymbol{\lambda} - E(\boldsymbol{\lambda}))(\boldsymbol{\lambda} - E(\boldsymbol{\lambda}))^{T}\right] \tag{4.21}$$

In figure 4.8 the covariance estimation algorithm is applied to a Gaussian surface with the variances $\sigma_{x_e} = 25\,\mathrm{m}$ and $\sigma_{x_n} = 15\,\mathrm{m}$. The Gaussian function, which represents the matching metric results in this example is fed into the covariance estimation algorithm described above. The result affirms perfectly the inputs of the Gaussian function variances parameters which proves the analytical correctness of the estimation approach.
To demonstrate that the approximation is also valid for non-Gaussian unimodal matching matrices, two generic matching matrices, with a characteristic shape for matching metrics are fed into the covariance estimation algorithm. The illustration is reduced to a two-dimensional representation to simplify the visualization, however the calculation are performed in three dimensions. The variances of the two examples were parametrized to $\sigma_1 = 2.5\,\mathrm{m}$ and $\sigma_2 = 0.6\,\mathrm{m}$. Figure 4.9 shows two examples with their matching function peaks and the corresponding Gaussian distribution with the estimated variances.

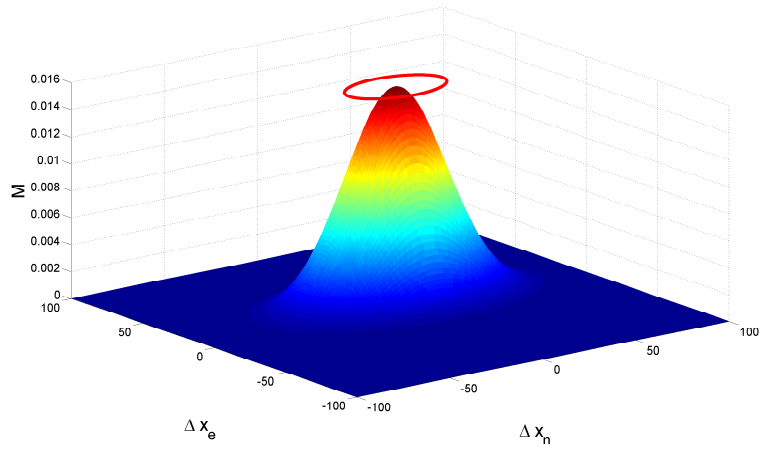

Figure 4.8: Gaussian covariance estimation

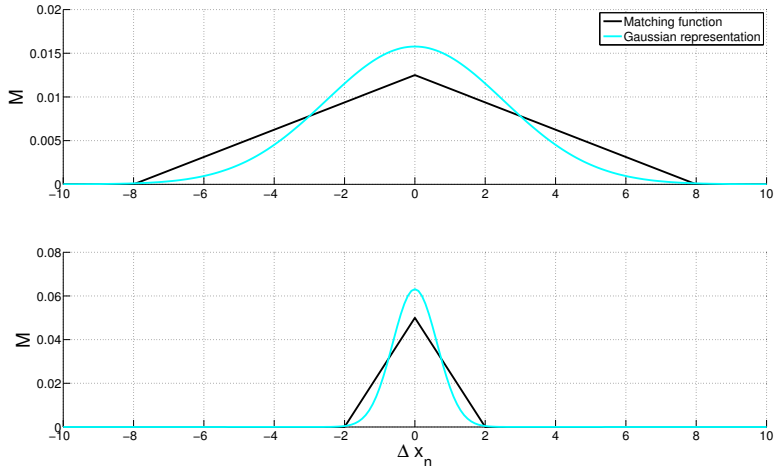

Figure 4.9: Matching function peak covariance estimation

4.2 Information Exploitation

The influencing factors on the horizontal matching quality are analyzed in this section. As already shown with the validity assessment in section 3.1, the elimination of erroneous or invalid measurements can provide advantages. In this section, a similar approach is targeted, which aims at the improvement of the matching metric. Not only erroneous measurements are eliminated, but additionally measurements containing no information are excluded from further processing. The following approach assumes that the impact on the matching function depends on the information content of the single measurements. The elimination of unimportant samples will improve the matching function. Not only the calculation burden can be reduced with this approach, but also the matching function shape will be improved at the same time. For single-beam or fixed-mounted multi-beam setups, the selection of measurements can be post-processed. For range-scanning sensors, the measurement direction has to be defined a priori. The altimeter simulation model can be used to select the most beneficial measurements depending on the flight situation and surface characteristics. This approach is explained in more detail in section 4.6.

The determination of the matching matrix has already been discussed in section 4.1. First, the matching function of an analytic stair function is analyzed to show the effects

of different sampling methods. Figure 4.10 shows the stair function and the sampling of the function at a high and low frequency in the upper plot. The matching function is considered to be one dimensional in the sequel for visualizing the principle. The effect get by principle more prominent in the two-dimensional case [83].

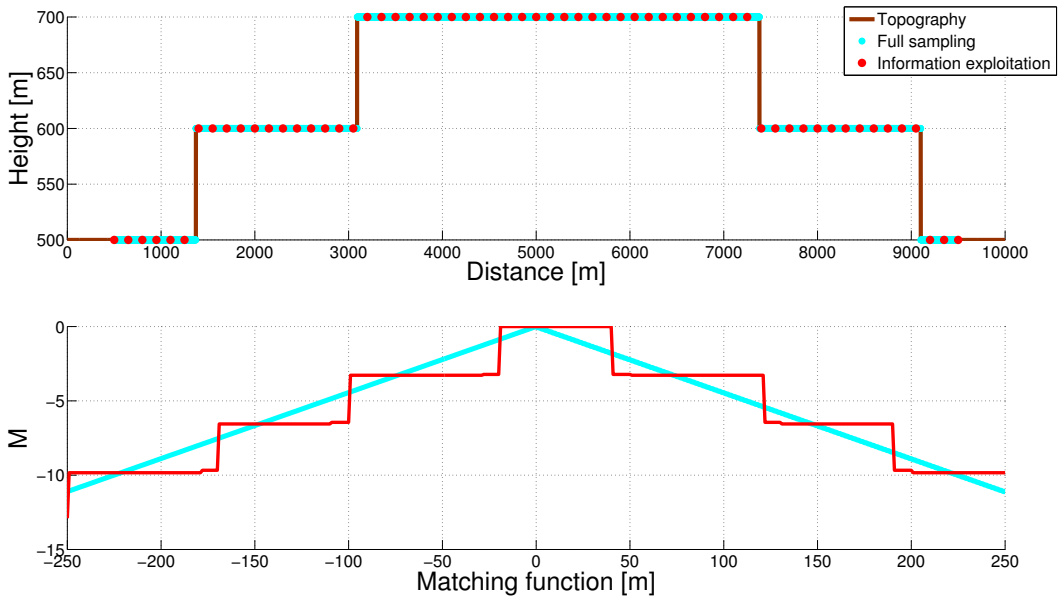

Figure 4.10: Analytic matching function with arbitrary sampled measurements

The matching function based on the high frequency samples, shows a continuous shape with a linear behavior. The sampling of the low frequency method has been chosen equidistant. The matching shape of the low frequency sampling results in a stair function with wide ambiguities. The ambiguities are caused by an inaccurate sampling of the important surface gradients. For localization, the shape of the matching function is important and is desired to be sharp and unambiguous. The contained surface gradients in the measurement samples have the major influence for the matching function shape.
To proof this, the same analysis is repeated with an algorithm searching for high gradients in the samples. The algorithm detects pairs of samples with high elevation gradients. For this example, the flanks of the rectangular obstacle are selected. Additionally, the beginning and the end sampling measurement is fed into the matching algorithm to increase the matching length. The sampling and the corresponding matching function is demonstrated in figure 4.11.
With this method the matching function shape can be changed to be much sharper, compared to previous approaches. Thus the shape of the matching function has been improved significantly while reducing the number of samples.
This gradient-based selection rule for measurements is now applied on a real DEM to show the performance in a non-synthetic environment. The matching value based on a high sampling frequency is compared to the matching value at a low sampling frequency. The matching function is illustrated in figure 4.12.
Both matching functions show a similar shape and accuracy. The oversampling of the surface does not provide any advantage compared to a low frequency sampling.
The gradient-based information exploitation algorithm is further applied on this topographic profile. The sampling and matching function is illustrated in figure 4.13.

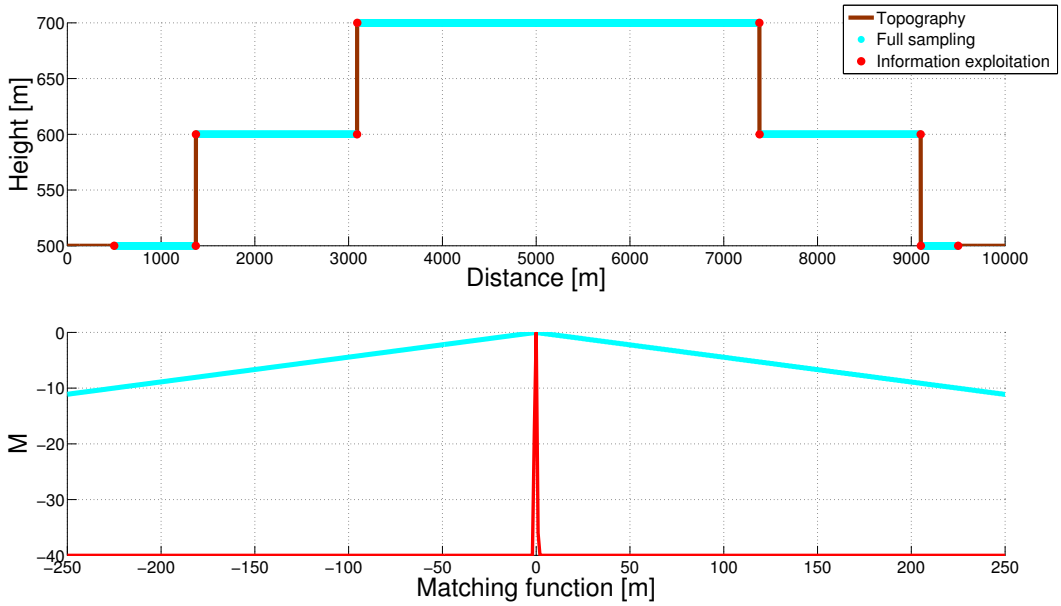

Figure 4.11: Analytic matching function with selected reduction

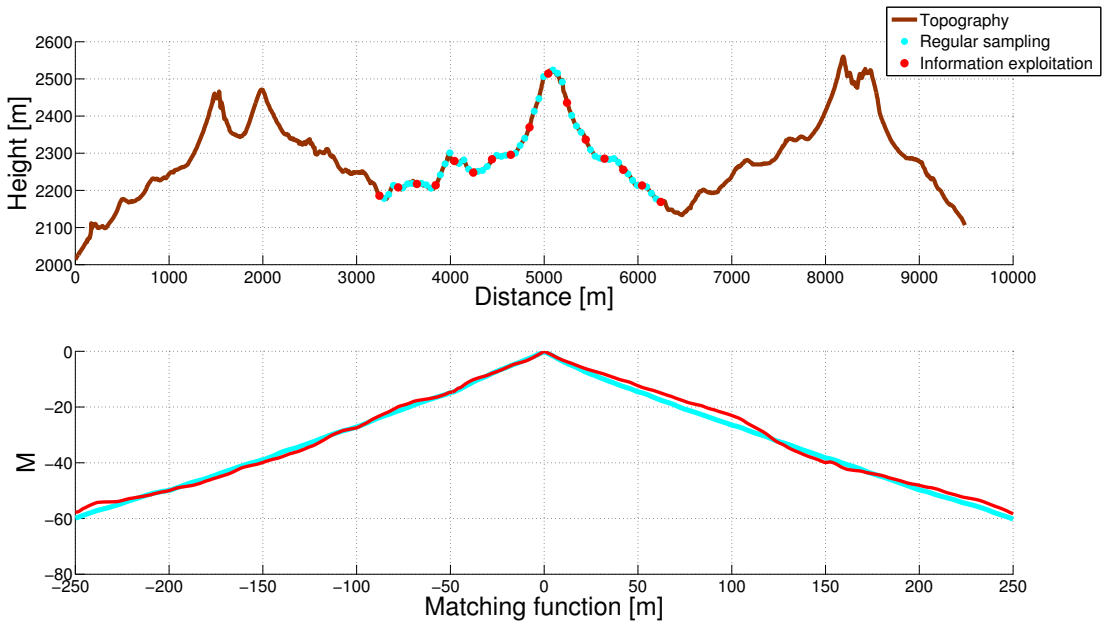

Figure 4.12: Topographic matching function with arbitrary sampled measurements

The algorithm selects the hilly surface in the middle of the surface with the most significant gradients and a smaller obstacle in the left side due to contained higher gradients compared to the smoother behavior of the other parts. The algorithm is tuned to select the best 10% of the measurement samples in this example. The information exploitation method improves the matching function significantly.
For a better understanding of this effect, a graphical processing of a matching matrix is illustrated in figure 4.14. The example features a profile including low gradients (blue) and a profile including high gradients (cyan). The exemplary calculation of a two-dimensional matching function, with five grid-search points are described in the following list according to the illustration. The illustration shows the surface shape in the upper subplots and the matching function in the lower subplots.

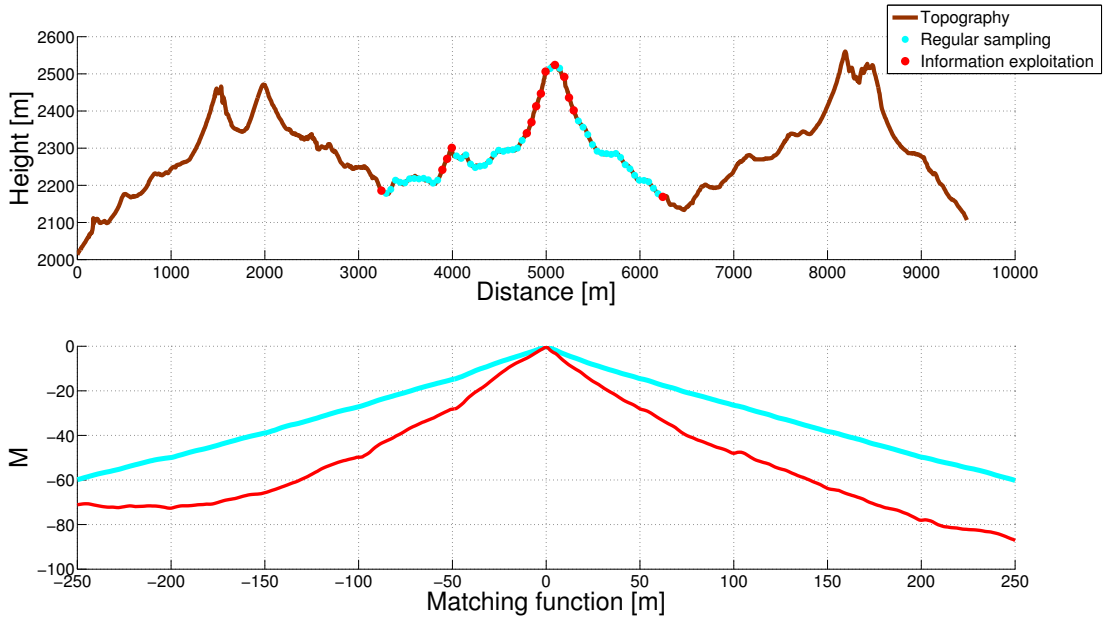

Figure 4.13: Topographic matching function with selected reduction

1. Without navigation error, the center matching function produces no errors for both profiles.

2. A shift to the left results in a small error for the flat samples, while the comparison with the high gradient samples produces a larger error.

3. The matching function to the right brings errors to both results in the same magnitude

4. The fourth matching function distinguishes the results clearly due to the high gradient.

5. The shift to the right brings also a clear difference between both methods, however the difference in the left direction is clearer

Not only the appearance of surface gradients in the overflown surface is important, but also the correct sampling of them. The sampling of a surface gradient with a high and low sampling frequency is illustrated in figure 4.15.
It is important to sample the surface with a high resolution to avoid sampling errors of the surface gradients due to undersampling. It is important to choose the sensor sampling frequency at least twice as high as the maximum expected surface variation frequency.
A disadvantage of the introduced method is the increasing influence of measurement errors by reducing the number of processed measurements, i.e. the error on a single measurement has a larger impact on the result. To avoid an increasing influence of the sensor measurement errors, the validity assessment is mandatory to avoid a degradation of the matching algorithm result. However, the reduction of samples reduces the processing time of the matching algorithm, whereas the selection of the measurements itself requires computational power. Thus, a part of the saved calculation time has to be invested for the mandatory validity assessment and inherent selection algorithms.

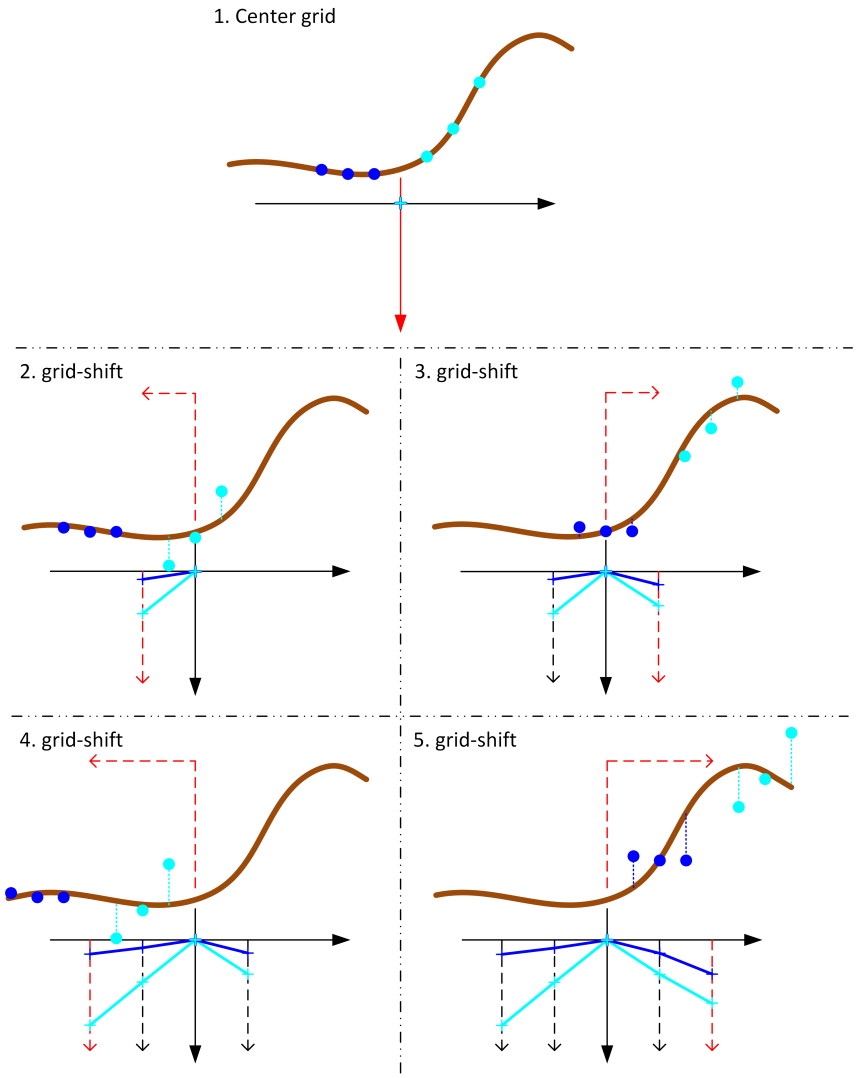

Figure 4.14: Gradient impact on matching function

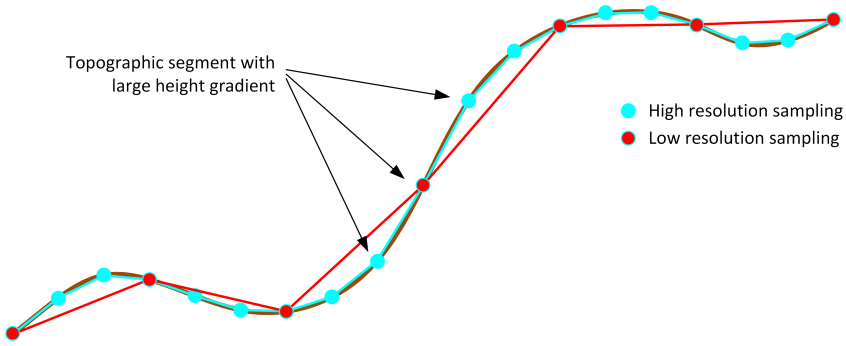

Figure 4.15: High gradient selection

The performance of the reduced matching function compared to a matching function with the full number of measurements is demonstrated with a simulation example. The scenario with the measurements (red) and the gradient-selected samples (white) is given in figure 4.16.
Figure 4.17 shows the matching function results of the full sampling and the information exploitation algorithm.

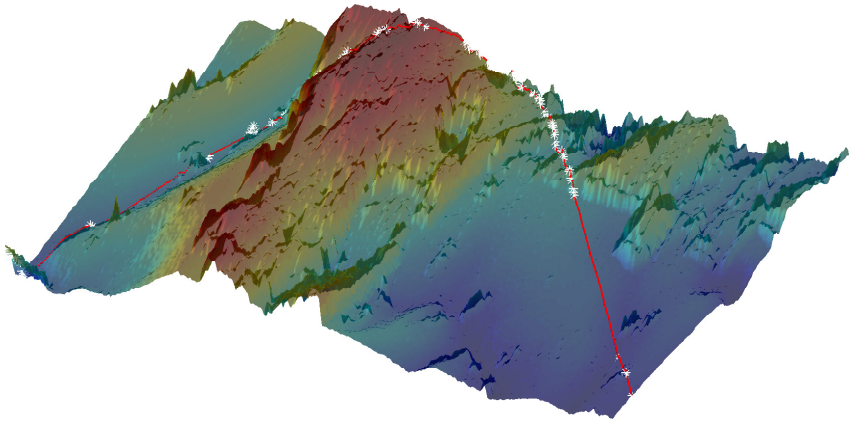

Figure 4.16: 3D measurement

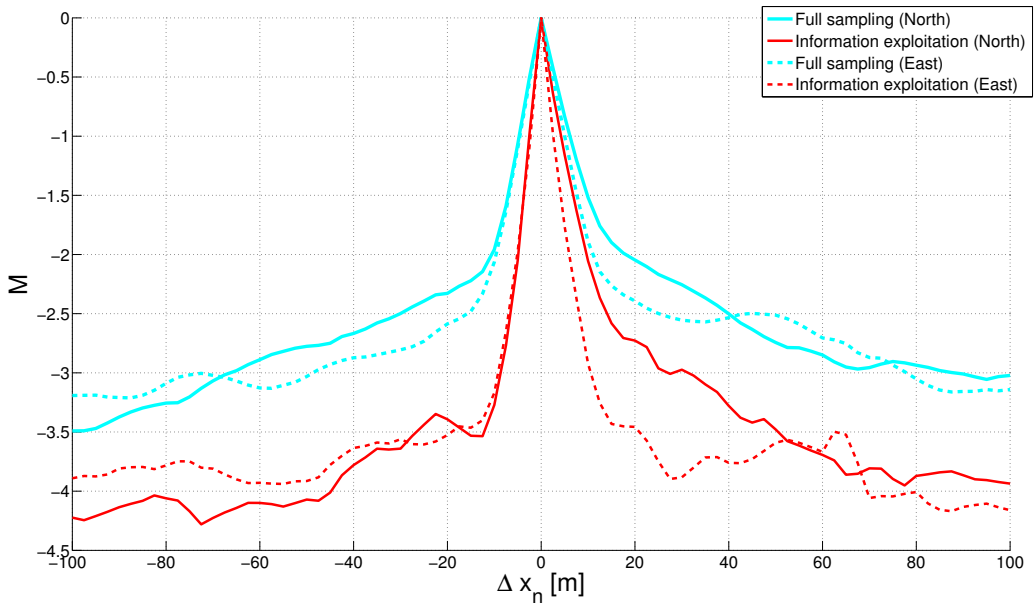

Figure 4.17: Reduced samples matching function comparison

The matching function shape is improved by the information exploitation, the number of samples is reduced to 10 percent of the measurements and the calculation burden is therefore decreased. Not only the shape of the matching function peak is sharpened, but also the noise floor level is decreased. These characteristics provide a more unique appearance of the matching function peak and a smaller covariance value.

4.3 Surface Sampling Analysis

In this section, the information content of the altimeter height above ground measurement is analyzed. This knowledge is used to improve the performance of matching function-based SAN. The information contained in the Earth's surface elevation is analyzed in the spatial and frequency domain to derive requirements on the surface sampling. A similar analysis to improve SAN systems can be found in [5] or [67].

4.3.1 Spatial Domain

Several aspects and methods to improve the matching function accuracy and shape have been introduced in the previous sections and the previous chapter. These methods aim either to estimate the measurement validity or variance value, to obtain a quality estimate of the measurement or to reduce the measurement error with a compensation algorithm. This results in a more accurate and reliable matching matrix and reduces the risk of ambiguities and the need for non-linear filter methods. These filter methods require high computational burden which is disadvantageous. Another benefit of an unimodal matching matrix is the interpretation of the matching function as Gaussian distribution, which enables the direct processing in a central navigation Kalman-Filter (KF).

Often, matching function ambiguities are the result of surface sampling effects and not caused by real surface ambiguities. Not only measurement errors, but also too low surface sampling frequencies, lead to a worse representation of the overflown surface. This sampling issue propagates into the comparison results and is responsible for a degradation. With the methods introduced earlier, the measured surface representation becomes more accurate, detailed and unique. Normally, matching function ambiguities are not caused by surface ambiguities, but by some combination of sampling and measurement errors. If real surface ambiguities appear in the measurement, the explained methods will have the same problems as the traditional approaches, but real surface ambiguities within the matching function grid do often just occur in quite special landscapes and are hence nor very likely for many applications.

For a graphical explanation of the relation between sampling, measurement error and matching quality, two examples will be shown. The first example features an elevation profile with two unique obstacles, one rectangular shaped and one triangular shaped (upper part of figure 4.18). Both shapes can be found in real surfaces, for example produced by houses or trees. A traditional low frequency surface sampling is compared to a high frequency sampling method in the sequel. Additionally, the information exploitation method is compared to the classical method. The upper plot in figure 4.18 also shows choice of the three different sampling methods, while the lower plot gives the matching function of the three different methods. The analysis is provided in a one-dimensional representation to isolate the main influences more obvious. The low-frequency sampling in the following examples is intentionally representing the worst case sampling to show the effects on the matching function.

The low frequency sampling method just measures the middle of the rectangular obstacle and both flanks. With the higher frequency, the rectangular obstacle is resolved in more detail and the flank gradients are sampled more accurately. The information exploitation algorithm can reduce the significant samples to the rising and falling edge of the rectangular obstacle. In the matching function result in figure 4.18, the true position on the left is detected perfectly with all three methods, but with different sharpnesses of the matching functions. However, the triangle leads to an ambiguity for the low frequency sampling method. While the high frequency sampling method shows a local maximum at the triangle position, whereas the information exploitation method suppresses this peak.

A second example, given in figure 4.19, illustrates a situation with two almost similar rectangular obstacles, but slightly different dimensions. A surface elevation with these characteristics can e.g. be found in urban surroundings.

Compared to the first example, the rectangular shape of the obstacle is sampled better

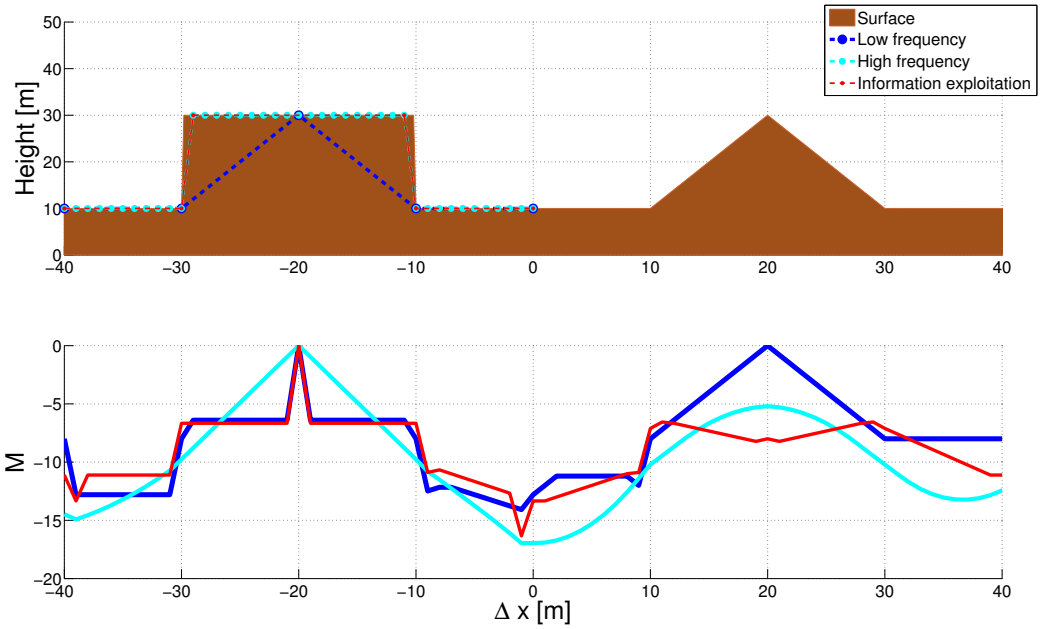

Figure 4.18: Different shaped obstacle with matching function

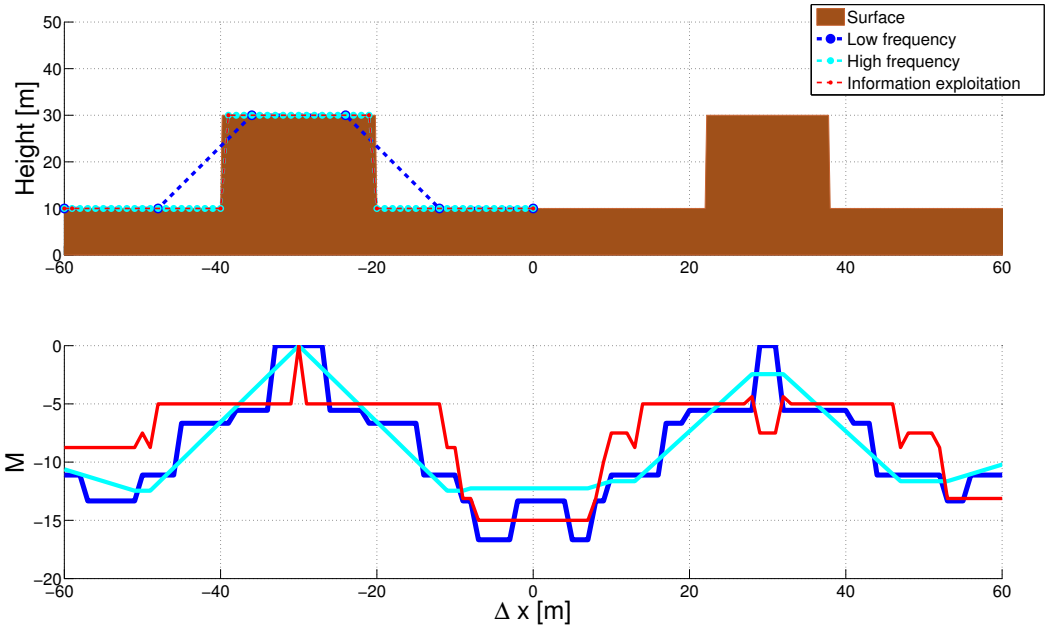

Figure 4.19: Similar shaped obstacles with matching function

with the low-frequency method, however the object dimensions are not covered perfectly. The high frequency sampling gives a good representation of the surface, as well as the information exploitation method does. The matching function result is illustrated in the lower plot showing again a good position detection performance of all three methods. While the low frequency sampling approach yields a small ambiguity, the two other methods provide a sharp matching function peak. Once again, the information exploitation method outperforms the other two methods concerning the peak sharpness. The obstacle on the right hand side leads again to matching ambiguities with the low frequency sampling approach. The methods using a high sampling frequency can resolve the dimension differences of the two shapes and are advantageous in this situation, too. The local maximum of the high frequency sampling can be suppressed with the information exploitation method again.
Consequently, the sampling with a higher frequency provides a more detailed model of the surface and describes the situation in a more unique way. The reduction of erroneous measurements and the intrinsic compensation of slant-range errors are additionally beneficial, as shown earlier. To increase the amount of measurements with the aim to reduce the likelihood of matching function ambiguities, the extension of the SAN algorithm using multi-beam sensors is explained at the end of this chapter.

4.3.2 Frequency Domain

The topographic surface of the Earth can be spatially Fourier analyzed similar to a frequency analysis of a time-series signal. The spatial Fourier transformation gives the surface spectrum, which influences the required sampling frequency of the surface measuring sensors which transform via the maximum allowed velocity into a sensor update frequency. The spatial (lateral ϕ and longitudinal λ) Fourier transformation is given in 4.22, the result in units of $1/m$.

$$\begin{aligned} H(f) &= \mathcal{F}\{h_{topo}(\phi,\lambda)\} \\ &= \int_{-\infty}^{\infty}\int_{-\infty}^{\infty}\left(h_{topo}(\phi,\lambda)\, e^{-j2\pi f\phi} e^{-j2\pi f\lambda}\right) d\phi d\lambda \end{aligned} \tag{4.22}$$

The Nyquist-Shannon sampling theorem can be directly transferred from time to spatial domain. The sampling frequency has to be at least twice the maximum spatial surface frequency of the signal to avoid information loss. The requirement is given by equation 4.23. An example showing an analytic topographic model based on superposed trigonometric functions is given in spatial domain in the upper plot of figure 4.20. The plot shows the superposed function as well as the samples, the lower plot illustrates the frequency domain of the reference and the sampled surface calculated with a sampling frequency of $f_s = 3 \cdot f_{max}$.

$$f_{sample} \geq 2 \cdot f_{max} \tag{4.23}$$

The maximum frequency contained in this surface example is $f_{max} = 0.5\,\mathrm{km}^{-1}$. For sampling frequencies, which do not meet the Shannon-Nyquist requirement, the spatial spectrum cannot be covered completely. The following examples illustrates an undersampling with a sampling frequency of $f_s = 1.8 \cdot f_{max}$ of the same surface. An additional peak due to aliasing effects appears in the plot in figure 4.21.

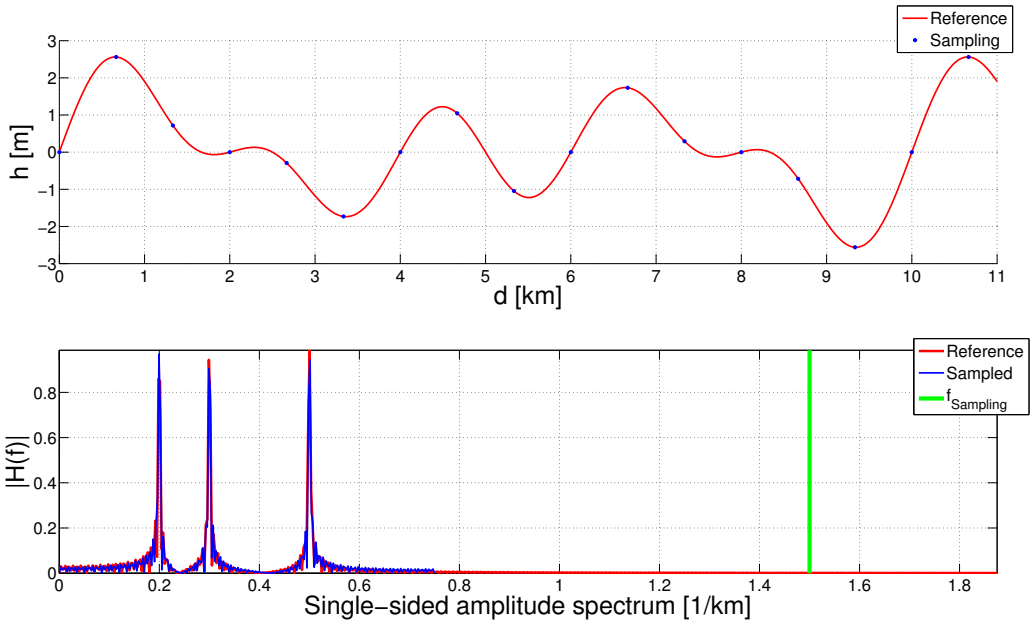

Figure 4.20: Spatial Fourier analysis of a synthetic surface

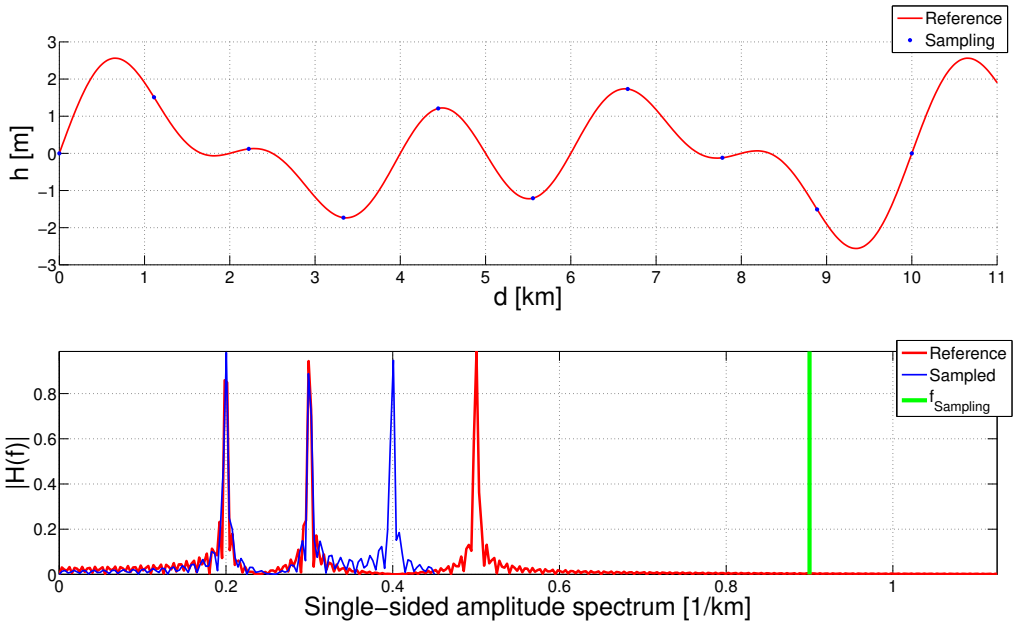

Figure 4.21: Spatial Fourier analysis of a synthetic surface with $f_{Sampling} < f_{Nyquist}$

Next, the spatial Fourier analysis is applied on a real DEM. Figure 4.22 follows the same plot order as the previous example, just the frequency plot uses a logarithmic scale. The Fourier analysis shows that 90 % of the information is within a frequency of $f_{topo,max} \approx 92\,\mathrm{km}^{-1}$. The minimum required sampling frequency is given by equation 4.24.

$$\begin{aligned} f_{sample} &\geq 2 \cdot f_{topo,max} \\ &\geq 0.18\,\mathrm{m}^{-1} \end{aligned} \tag{4.24}$$

In this example, the recommended sensor update frequency for a medium velocity platform with an along track speed of $v_x \approx 50\,\mathrm{m\,s}^{-1}$ is calculated by equation 4.25. The required

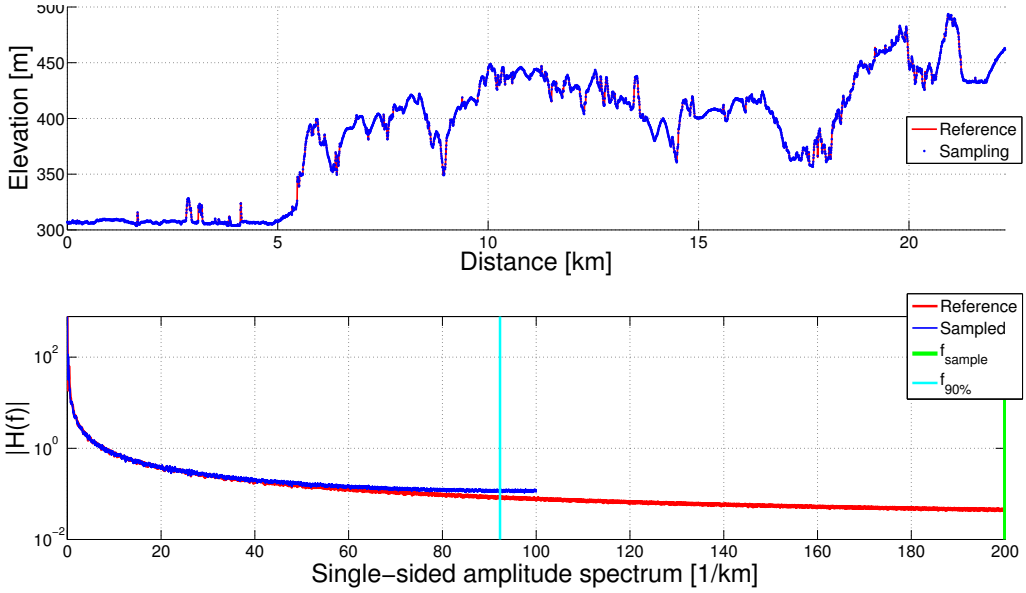

Figure 4.22: Spatial Fourier analysis of a topographic surface

sensor update frequency, depending on the platform along track velocity, is given in figure 4.23.

$$\begin{aligned} f_{update} &\geq v_x \cdot f_{sample} \\ &\geq 9\,\mathrm{Hz} \end{aligned} \tag{4.25}$$

Obviously, this result strongly depends on the applied digital elevation model. It is important whether a surface or terrain model is used and which resolution of the elevation database is applied. The second major influencing factor is the specific local surface characteristics. Urban scenarios or rough shaped surfaces will inhibit more details and more high-frequency elements. For this example, a high resolution DSM with a resolution of about 2 m has been used. The platform velocity dependent sampling frequency of the surface ranging sensor is given in figure 4.23.

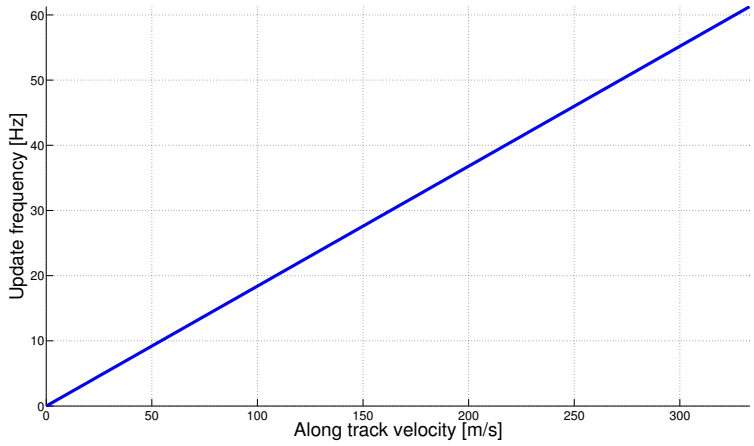

Figure 4.23: Required along track update frequencies

The upper sampling limitation is given by the applied digital elevation model. It is useless to sample details of the surface, which are not covered in the reference map. To avoid a

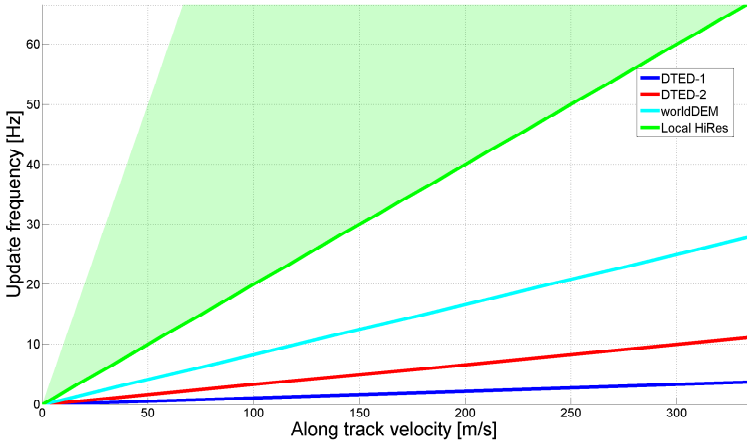

Figure 4.24: Along track update frequencies limitations

oversampling of the surface, the maximum sampling frequency of the surface is given in dependence of the along track velocity v_x for four different types of DEMs. The resolutions of the used elevation models are given in table 4.3, the update frequencies are illustrated in figure 4.24.

DEM Label	**Resolution**
DTED Level 1	90 m
DTED Level 2	30 m
WorldDEM	12 m
Local High Resolution	1 m-5 m

Table 4.3: DEM resolutions

4.3.3 Sampling Length

The contained frequencies of a surface elevation profile have been analyzed in the previous section. The most significant spatial frequencies have been determined to be between $f_{topo} = 0.1^1/_{km}$ and $f_{topo} = 1^1/_{km}$. Obviously, this result is strongly dependent on the considered area. Even though this value is not representative for the entire Earth's surface, the calculation can be applied in general. It is recommended to evaluate the surface in the particular application region. With this analysis, the ideal sampling length for the matching function can be determined. For the given example it can be determined to be between $1km < \Delta s_{cor} < 10km$.

4.4 Translational Drift Estimation

The traditional matching function approach determines the best three-dimensional matching offset between the reference elevation model and the measured surface elevation profile. This approach implies a constant position offset of all measured samples within the matching function interval. This assumption is fulfilled for high class INSs, while the position

error drift becomes the more important to be considered the lower accurate the used INSs are.
The position error drift behavior within the recording time interval is illustrated in figure 4.25. The left illustration shows a linear position error drift, while the right image shows a non-linear behavior, both within the selected matching length.

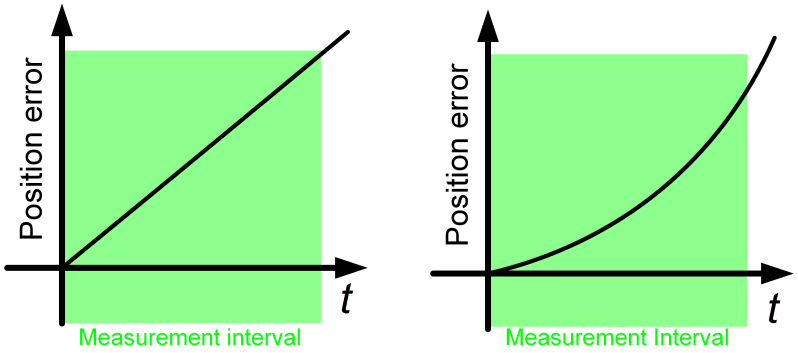

(a) Linear Behaviour (b) Non-Linear Behaviour

Figure 4.25: Position error drift behavior

Normally, SAN is applied when other aiding systems are not available and is used for a closed loop correction of the estimated position error.
A linear behavior of the position error can be assumed due to the continuous correction of the position error in the main navigation filter. The non-linear consideration is relevant if the system is unaided for a longer time interval.
A realization if the position error drift of a tactical grade INS is plotted in horizontal and vertical direction in figure 4.26. The plot additionally shows a linear approximation of the position error growth.

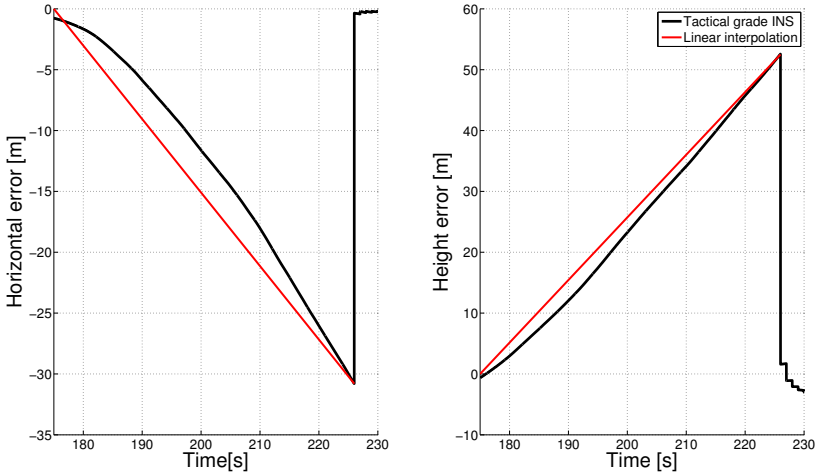

Figure 4.26: Tactical grade INS linear drift interpolation

This linear approximation can be applied as drift correction in the matching algorithm to improve the matching accuracy. The matching function procedure, which has been described in the enumeration in section 4.1.2.3, has to be extended by the drift consideration. The horizontal shift of the i-th grid search step $\Delta\boldsymbol{\lambda}_i$ of all measured samples

$\boldsymbol{\lambda}_L(t_k)$ is replaced by a time depending relative shift of the measured samples, it is given by equation 4.26.

$$\boldsymbol{\lambda}_{L,i}(t_k) = \boldsymbol{\lambda}_L(t_k) + \frac{t_k - t_{min}}{\Delta t_{cor}} \Delta\boldsymbol{\lambda}_i \tag{4.26}$$

Obviously, this approach assumes that surface samples, recorded at the beginning of the matching interval Δt_{cor}, are influenced less from a position error compared to the ones recorded at the end of the matching interval. To show the improvement of this approach, a conventional matching algorithm, which assumes a constant position error within the matching interval is compared to the position drift corrected algorithm. The horizontal position error in North direction has been chosen to $\delta x_n = 10\,\mathrm{m}$, the position error in East direction to $\delta x_e = 15\,\mathrm{m}$ in this example. The results for both directions are given in figure 4.27.

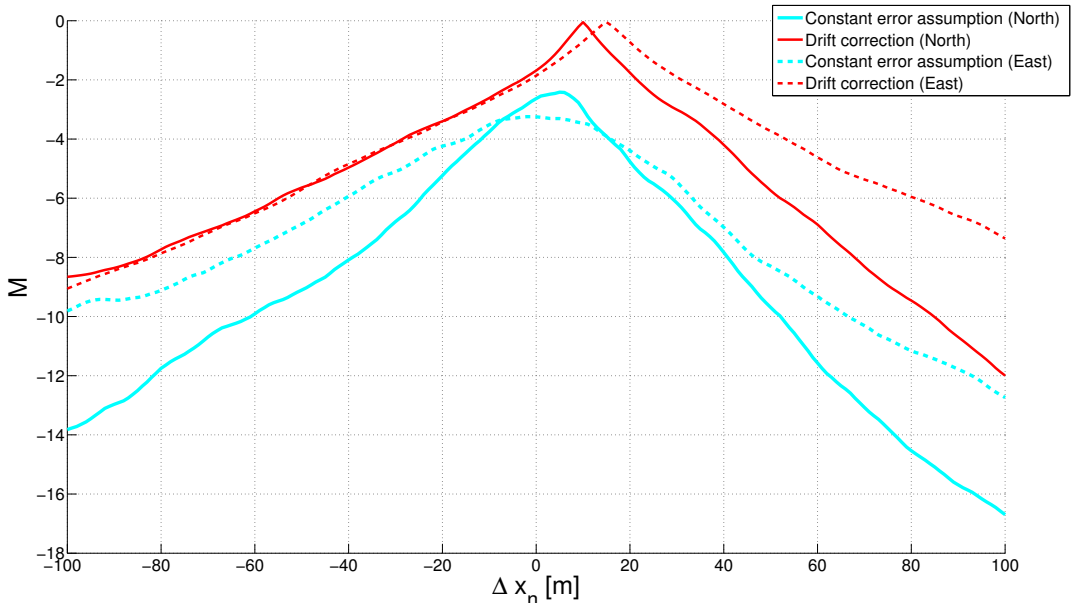

Figure 4.27: Constant error assumption vs. drift correction

As mentioned above, the linear position error drift assumption is only valid for high precision IMU sensors and for a closed loop correction. While the position error drift provides a linear short period behavior, the medium- and long-term characteristics can include quadratic and even cubic terms. While an compensation of a quadratic or cubic drift characteristics is a theoretical opportunity, it is not applicable for practical solutions. The number of drift coefficients would blast the matching problem and the calculation time would increase dramatically. Furthermore, an application using a low-class IMU in combination with a SAN is inappropriate.

4.5 Closed-Loop Slant Range Compensation

The selection of the most beneficial measurements improves the matching function, which has been discussed at the beginning of this chapter. However, the altimeter measurements are still affected by slant range errors. SAN algorithms are often applied in platforms with high dynamics and are vulnerable to attitude depending error effects. Erroneous height

measurements lead to weak and ambiguous matching functions and as a consequence to inaccurate position estimates. The slant range compensation methods of section 3.3 can be a means to improve the position matching function.

As a proof of concept, the compensation algorithm is applied to the matching problem. For this example, the horizontal position of the platform is assumed to be known. While this assumption cannot be fulfilled in later applications, in this analysis only the improvements of the compensation are focused. The matching functions are compared in figure 4.28. The red line illustrates the matching function, when the measured distance is interpreted as nadir height above ground, while the results illustrated with the cyan colored line uses the slant range compensated height measurements.

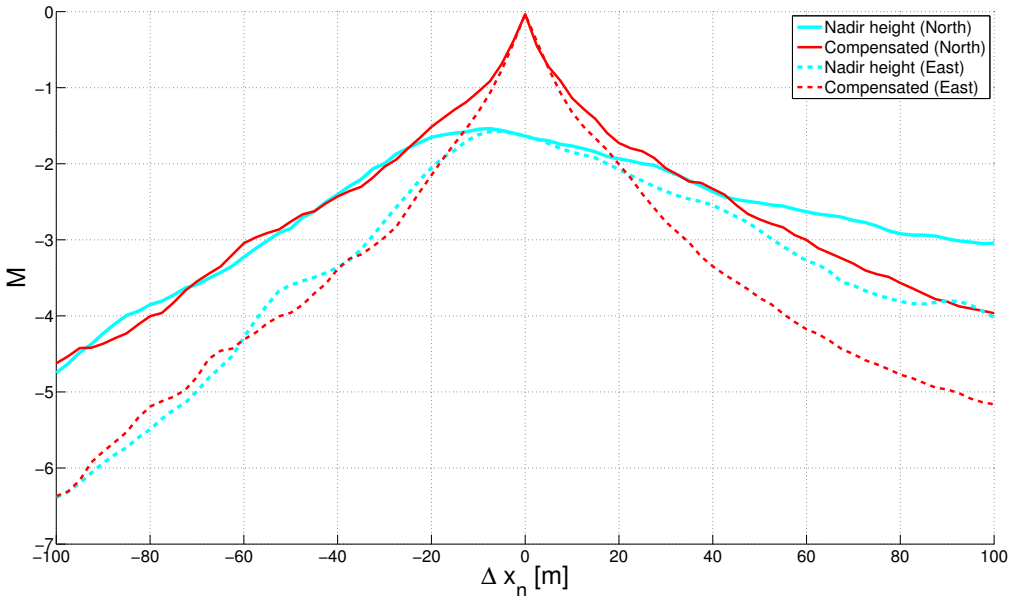

Figure 4.28: Nadir height and slant range matching comparison

The application of the slant range compensated measurement improves the matching function significantly. Especially, the characteristics of the matching function peak is improved in its shape and correspondingly in its accuracy. The expected matching function shift for both directions is equal to zero for this example. However, even when the slant range compensation algorithm may be an adequate approach for the solution of this problem, it does require a precise horizontal position estimate. This requirement is fulfilled in the height aiding application, where only the degraded vertical position channel is aided, while the horizontal position is available with a sufficient precision. For SAN applications, which require a three dimensional position estimate, the uncertainty in the horizontal position must be additionally considered.

Therefore, the compensation algorithm is integrated into the matching metric and processed for each matching function shift. The grid points of the search algorithm are considered as input to the compensation algorithm. The matching function not only includes the measurement errors but also the compensation errors. The modification on the matching metric is discussed in the following section.

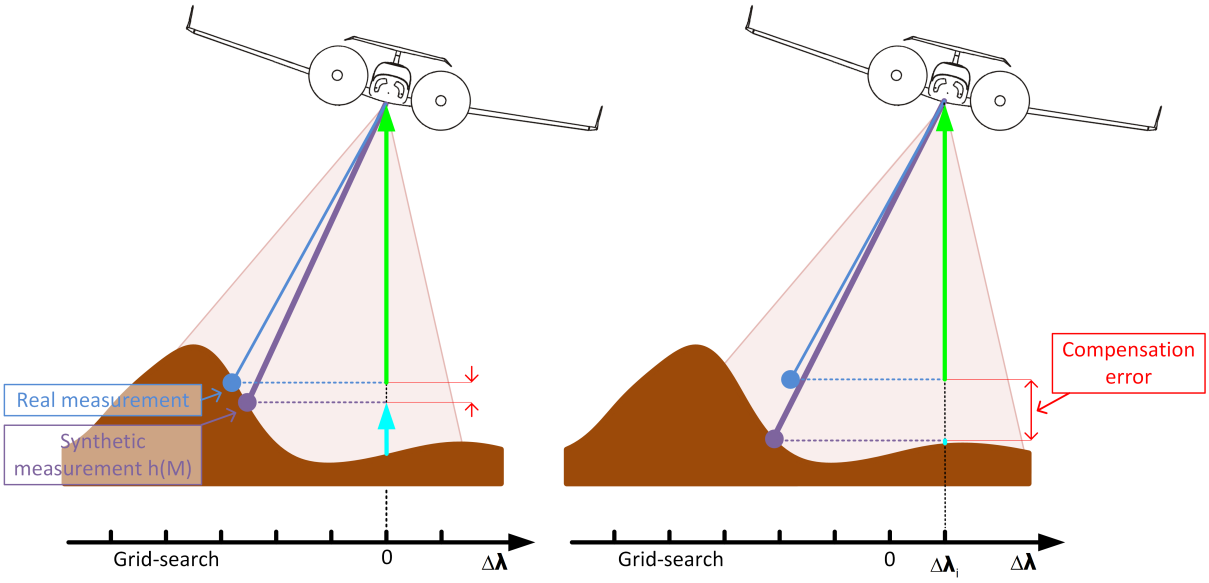

Figure 4.29: Slant range compensated SAN

4.5.1 Slant Range Compensated Matching Metric

The basic principle of the matching algorithm including the slant range compensation is illustrated in figure 4.29. The left image shows the slant range compensation algorithm in the position error-free situation. The synthetic measurement has a small deviation due to errors of the simulation model. The estimated matching function shift for the best match is zero. In this situation, the compensation algorithm can improve the matching function by reducing the slant range measurement error.
The right image shows the effects of a horizontal position shift on the compensation algorithm. While the real measurement is not influenced by the matching function shift, the synthetic measurement from the altimeter simulation model provides a modified result. This synthetic measurement does not fit well the real measurement and benefits the matching function.
Furthermore, the calculation of the mean height offset includes the dependency of the compensated height measurement on the matching function shift. The same relation is covered in the matching function. The mean height offset is given by equation 4.27, the matching function calculation in equation 4.28.

$$\Delta\bar{h}_i = \frac{1}{K}\sum_{k=1}^{K}\left(\tilde{h}_k - \tilde{h}_{agl,comp,k}\left(\tilde{\phi}_k + \Delta\phi_i, \tilde{\lambda}_k + \Delta\lambda_i\right) - h_{dem}\left(\tilde{\phi}_k + \Delta\phi_i, \tilde{\lambda}_k + \Delta\lambda_i\right)\right) \tag{4.27}$$

$$\mathbf{M}_i = \frac{1}{K}\sum_{k=1}^{K}\left|\tilde{h}_k - \tilde{h}_{agl,comp,k}\left(\tilde{\phi}_k + \Delta\phi_i, \tilde{\lambda}_k + \Delta\lambda_i\right) - h_{dem}\left(\tilde{\phi}_k + \Delta\phi_i, \tilde{\lambda}_k + \Delta\lambda_i\right) - \Delta\bar{h}_i\right| \tag{4.28}$$

The compensation of the height above ground $\tilde{h}_{agl,comp,k}$ has to be calculated for each grid-search shift and for all measurements K. The compensation is repeated for convenience in equation 4.29.

$$\tilde{h}_{agl,comp,k}\left(\tilde{\phi}_k + \Delta\phi_i, \tilde{\lambda}_k + \Delta\lambda_i\right) = \tilde{h}_k + h_{dem}\left(M_k\right) - h_{dem}\left(N_k\right) - \begin{pmatrix}0\\0\\1\end{pmatrix} \mathbf{R}_{nb}\mathbf{R}_{bs}\mathbf{R}_{sm} \begin{pmatrix}0\\0\\\tilde{d}_{m,k}\end{pmatrix} \tag{4.29}$$

The determination of the topographic height of the synthetic measurements $h_{dem}\left(M_k\right)$ and the rotation of the s frame into the m frame $\mathbf{R}_{sm}$ require the execution of the altimeter simulation model. The model has to be executed for all samples within the matching length and for all matching function shifts of the grid-search.
Even with the calculation power of today's processors, this exceeds the technical capabilities. An approach to reduce the measured samples was introduced earlier and is one step to solve this problem. Unfortunately, this method implies a selection of measurements before compensation. Without compensation, the selection algorithm would degrade. Another approach to reduce the calculation burden is the reduction of the number of matching function shifts. Modern matching function grid concepts with reduced grid points are therefore introduced in the following section.

4.5.2 Grid-Search Optimization

A conventional matching function grid with the grid-size g and the grid-resolution Δg has been introduced earlier in this chapter and is illustrated in figure 4.5.
The computational burden for the slant range compensated matching algorithm is huge. Means to reduce the computational effort are to reduce the number of samples or the number of grid-points. In this section, the reduction of grid-search shifts with modern grid concepts is introduced.
Obvious approaches to reduce the amount of grid-points are an increase of the grid-resolution or the reduction of the grid-size. While the enlargement of the grid-resolution results in a degradation of the matching function accuracy, the reduction of the grid-size reduces the operating area of the SAN system. The grid-size should cover the maximum expected horizontal position error. A coupling of the grid-size on the covariance information of the navigation filter is an option to reduce calculation effort, but is not promising as a general solution of the problem. In this thesis, an iterative grid-search is used for a significant reduction of the number of matching functions.
The iterative matching grid-search concept has first been introduced in [91]. It is based on a five-point grid-search algorithm, four corner and one central grid point, with an variable grid-resolution for each iterative step. For the first step, the distance between the corner grid points is equal to the grid-size and is halved in each step. Whenever the central matching function does not provide the best matching result, the center is shifted onto the best corner point without reducing the grid-resolution. This algorithm is repeated until the grid-resolution is smaller or equal to the required resolution.
This algorithm can only replace a regular grid search is the result is assumed to be unimodal. Therefore the surface has to be rough enough and sampled with a high frequency [66]. If these requirements are not fulfilled a conventional algorithm has to be executed instead. A horizontal illustration of the grid-search is given in figure 4.30.
While the number of grid corners is reduced with this method, the resolution in the target area can be increased. This feature is advantageous especially if the expected results

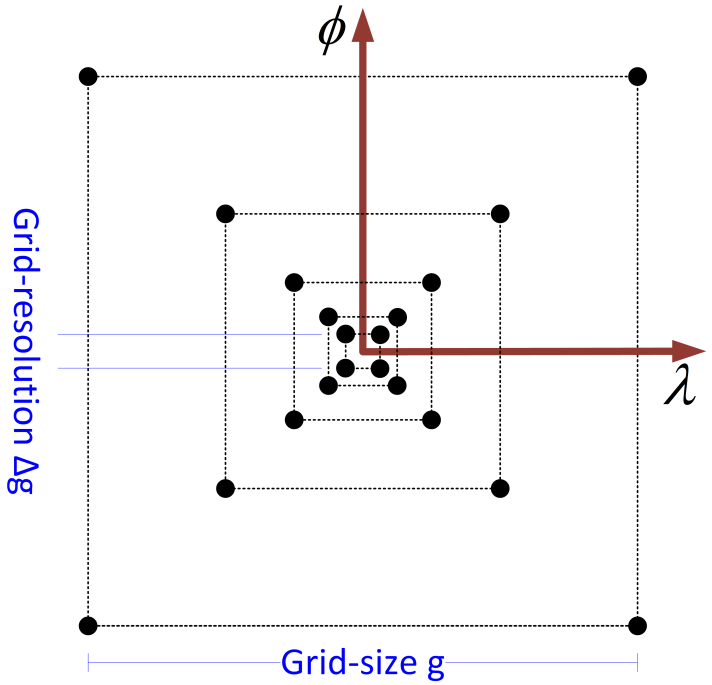

Figure 4.30: Five-point grid-search

provide a linear behavior, i.e. the surface in the considered are is sufficiently smooth. A diagram of the calculation procedure is given in figure 4.31.

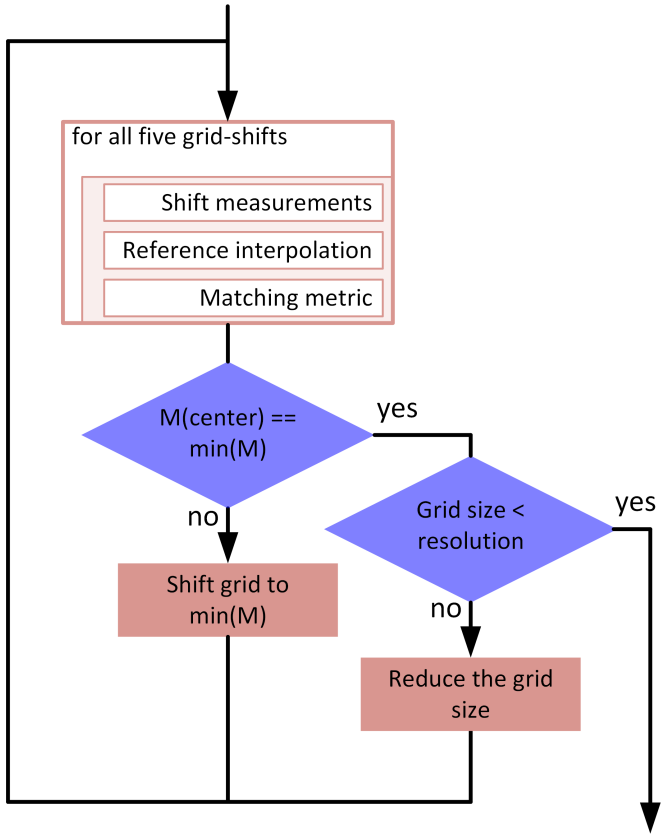

Figure 4.31: Five-point grid-search block diagram

The number of iterations N_{iter} of the five-point grid-search algorithm can be calculated depending on the required resolution Δg and the grid-size g. The result is given by equation 4.30 with a variable factor s, which describes the reduction of the grid-resolution in each step.

$$\begin{aligned} \Delta g &\geq g s^{N_{iter}} \\ s^{N_{iter}} &\leq \frac{\Delta g}{g} \\ N_{iter} &\geq \frac{log_{10}\left(\frac{\Delta g}{g}\right)}{log_{10}(s)} \end{aligned} \tag{4.30}$$

Whenever the center grid-search matching result is the best and a re-centering of the five-point grid is not required, the number of matching functions is $N_{match} = 4N_{iter} + 1$. This is a significant reduction of the number of matching function calls $(g/\Delta g)^2$ of a regular grid. A comparison is given in logarithmic scale in figure 4.32, which illustrates the number of matching function calls depending on the grid-resolution of the two approaches.

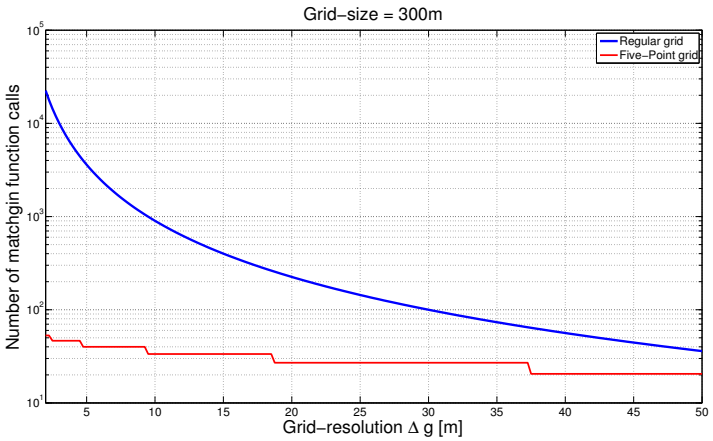

Figure 4.32: Number of grid-search corners

An example of the five-point grid-search algorithm applied on a real three dimensional matching function is given in figure 4.33.

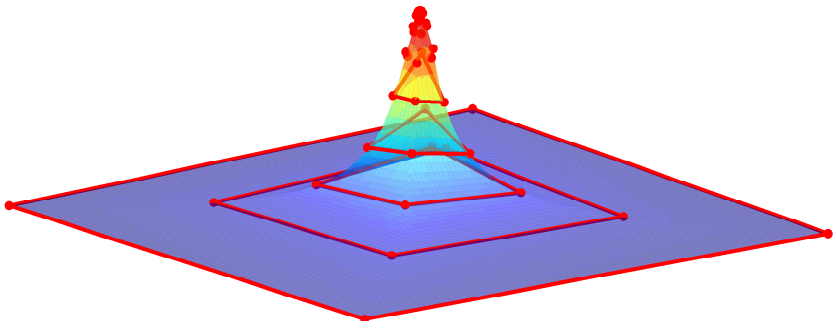

Figure 4.33: Five-point grid-search example

To illustrate the compensation within the process of matching function grid shifting, the process diagram of the five-point grid-search is extended by the execution of the synthetic altimeter simulation model.

An additional benefit of the five-point grid-search, compared to a regular grid-search, is the ability to extend the grid size limit. This can be an advantage whenever the navigation system is degraded and is operating outside its specifications. The five-point grid-search algorithm, including the slant-range compensation is illustrated as block diagram in figure 4.34.

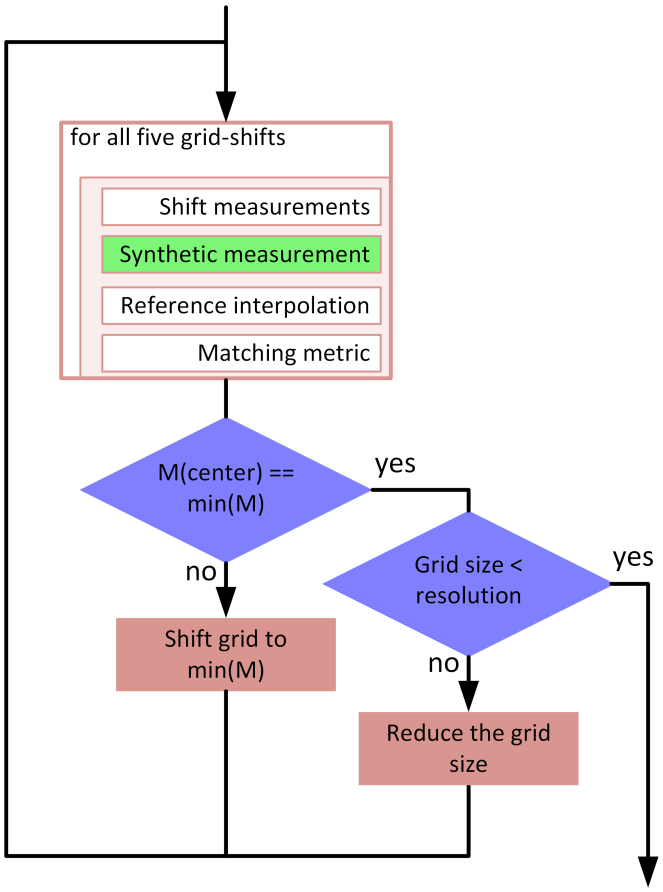

Figure 4.34: Slant range compensation matching algorithm expansion

When the five-point grid-search is applied, the represented area of the specific corner grid points is not anymore equally distributed. The specific corner points have to be weighted depending on their corresponding influence. A Delaunay triangulation is applied to calculate the representation area of the single grid points. Figure 4.35 shows such a triangulation. This method is only partially suitable to multimodal matching function results.

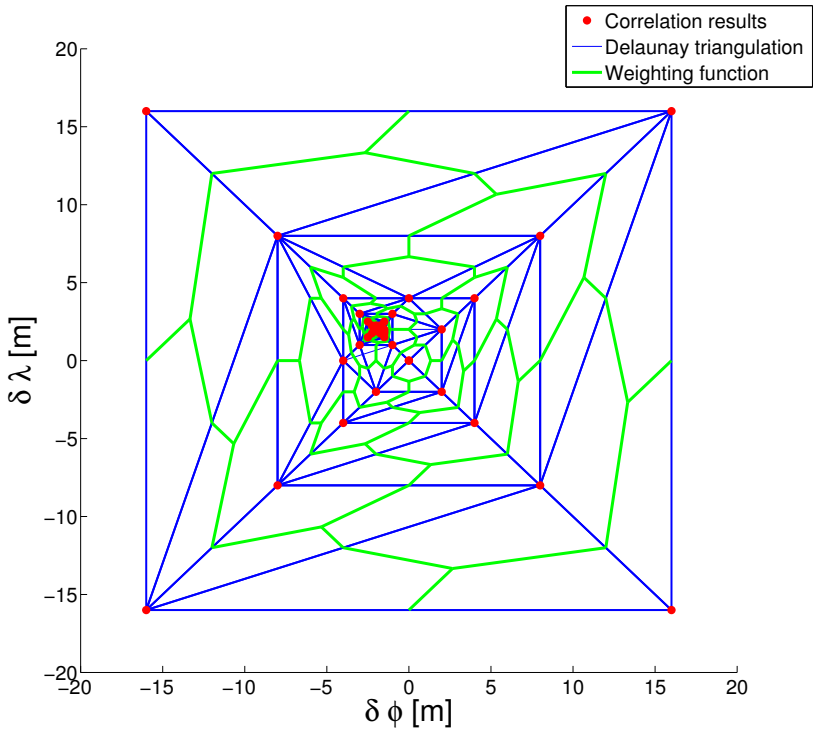

Figure 4.35: Five-point grid-search weighting

4.5.3 Matching Function Comparison

As already shown, a narrow beam-shaped altimeter provides advantages for the matching function shape of a SAN system. If either the platform, application or mission profile does not allow a narrow-beam shaped surface-ranging sensor, a synthetic compensation of the slant rage errors can improve the matching function. In this section, the results of the slant range compensated matching function are compared with the conventional approach. The matching function is calculated using the five-point grid-search, due to the high computational burden of a regular grid. A comparison of the performance of both matching metrics is given in figure 4.36.

Due to the high calculation effort of the compensation algorithm in each grid shift, the combination of the classical matching function grid approach, using a regular grid, and the five-point grid-search is beneficial. The combination of both methods aims to reduce the compensated matching function calls without reducing the grid-size.

First, the matching function is calculated using the regular grid without compensation. The most probable position shift is used as the initial value for the compensated five-point grid-search. The five-point grid-size can be reduced for the fine search of the most probable position. The result of the combined method promises a large grid-size, as well as a high resolution by combining the advantages of the both method for sufficiently smooth areas. The result of the combined approach is given for the same situation in figure 4.37.

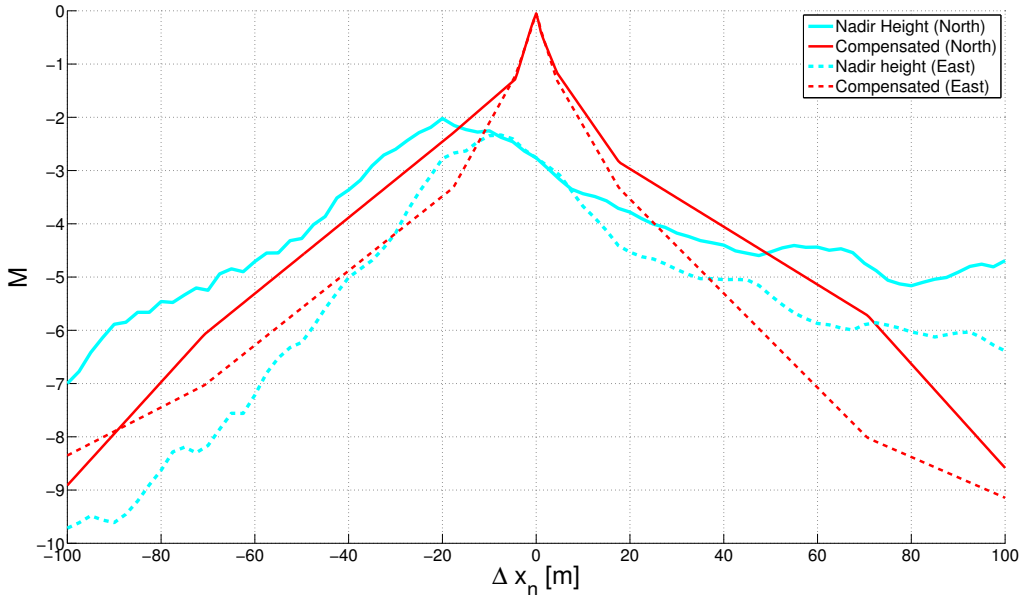

Figure 4.36: Comparison of classical and slant range compensated matching algorithm

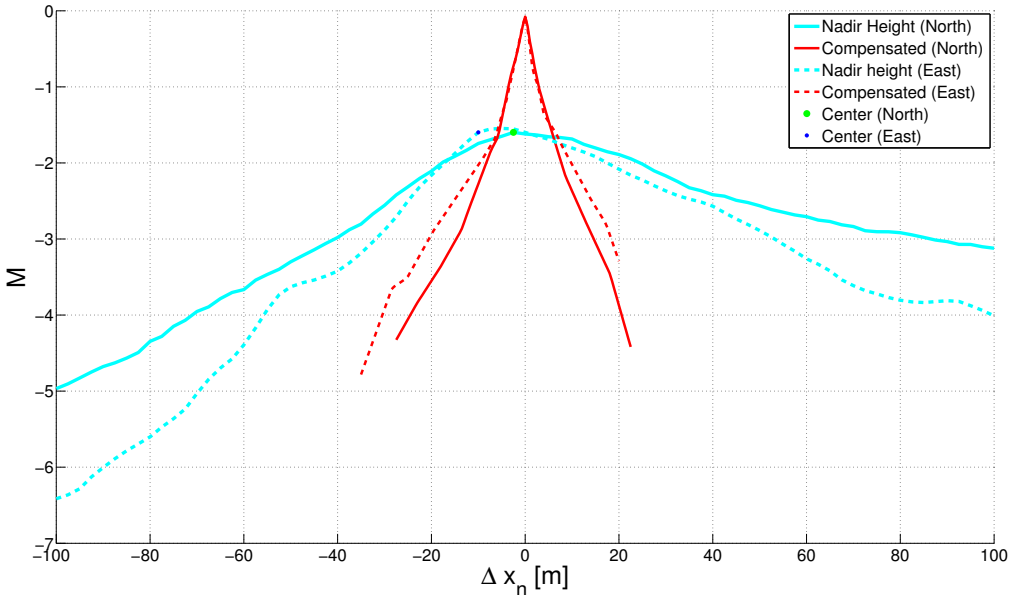

Figure 4.37: Combination of classical and slant range compensated matching algorithm

4.6 Multi-beam SAN

In the previous section, the requirements on a high precision SAN system have been considered. The measurement of high surface gradients, which guarantee a sharp and unambiguous matching function, require a flight trajectory above hill-tops and other significant obstacles. A trajectory which fulfills this requirement is on the other site quite exposed which. For civil aviation, the restrictions of the ATC do not allow to adjust the trajectory to the needs of the SAN system. The joint usage of some prominent landmarks would significantly rise the risk of an in air collision. The performance of SAN systems can be increased without adjustments of the trajectory by using multi-beam surface ranging sensors. The term multi-beam covers sensor class with multiple parallel measuring beams, as well as sequential measuring sensors with a variable beam direction. Sensors providing these characteristics can be Laser-scanners, phased array Radars or multi-antenna altimeters. As example, the measurement of the Earth's surface with a sequential Laser-scanner is illustrated in figure 4.38. Several SAN systems based on multi-beam sensors have been introduced in [31], [34], [27], [26], [24], [25].

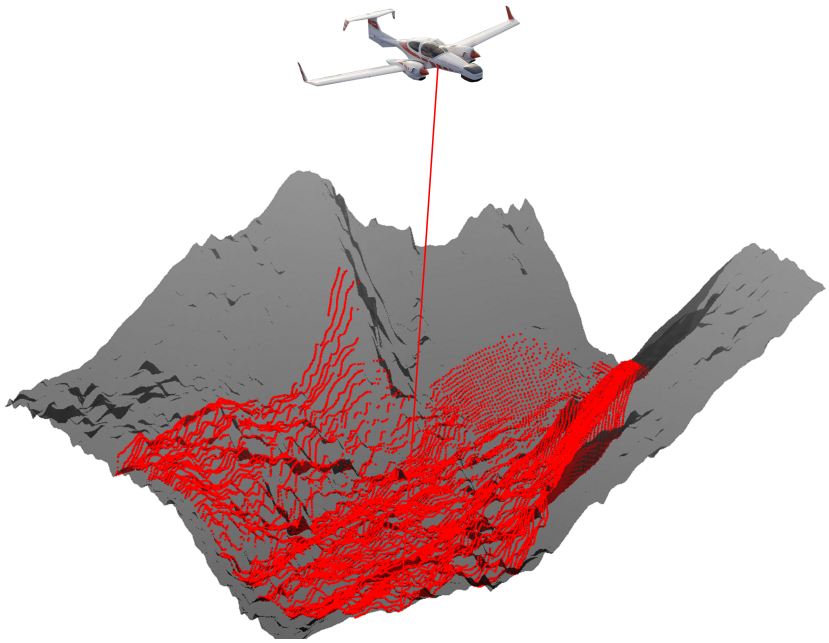

Figure 4.38: Airborne Laser scanner

In this section, the beneficial application of multi-beam sensors in SAN systems is discussed. The benefits of the introduced information exploitation method is used for multi-beam measurements with fixed-antenna sensors. A gradient-based beam prediction for maximization of the matching function accuracy is introduced for variable beam sensors. This algorithm can also be applied for sensors with variable beam directions and is based on the previously introduced altimeter simulation model.

4.6.1 Architectures

In this section, three different multi-beam measurement setups and processing methods will be explained. The first measurement setup uses three fixed-beam altimeters, one in platform normal direction and two side-looking beams, one left and one right of the

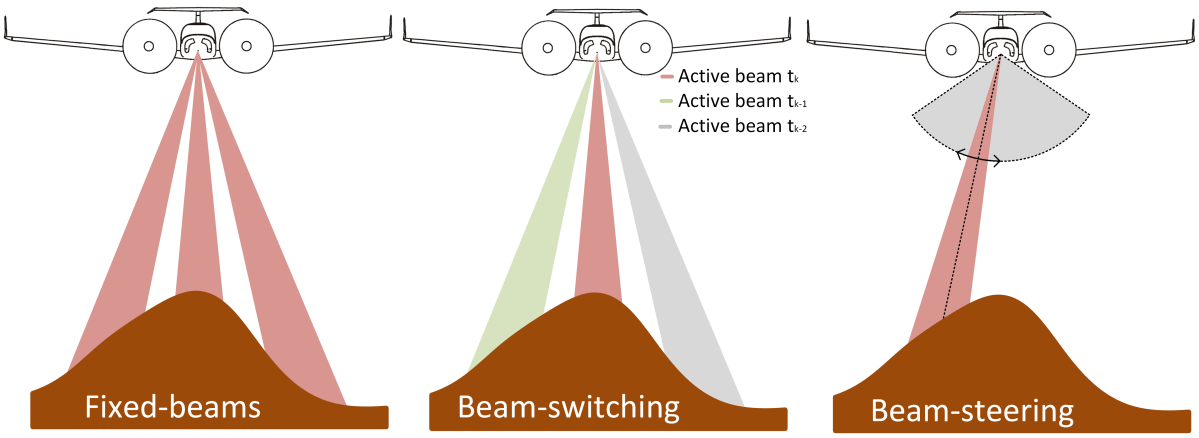

Figure 4.39: Multi-beam setup

center beam in across track direction. Whereas the antenna positions and directions of the second method called beam-switching are similar to the fixed-beam approach, they share one single receiver. This setup is not suitable to provide parallel measurements, but may be preferred due to the reduced hardware costs. A beam-switching sensor setup has the advantage of requiring only one receiver, while a parallel measurement requires one for each antenna. The third setup is based on a variable pivoted beam which can be used for the beam-steering approach. A schematic illustration of the three methods is given in figure 4.39.

The information exploitation of the fixed-beam measurement method can be applied in the post-processing, while the beam-switching and beam-steering method require the a-priori information about the measurement direction. The information exploitation algorithm is similar to a single beam approach in case of a fixed-beam measurement apart from the modification to a multi-beam measurement.

Apart from the center altimeter, which provides similar information as in a single-beam setup, the two side-looking sensors from the fixed-beam setup provide additional across track information. The additional information content can improve the matching function in the weak across track direction. The measurements of the three fixed-beams in a bank-to-turn flight situation are illustrated above a digital elevation model in figure 4.40.

The information exploitation algorithm is now applied on the beam-switching measurements and is shown in figure 4.41. The algorithm selects the measurements with the highest impact by a gradient analysis, which has been shown in the previous chapter. In case of a parallel measurement of three independent surface distances, the selection of measurement can be done in the post-processing in-flight. If the antennas share one receiver and only one measurement can be made simultaneously, the introduced altimeter simulation model is applied to calculate a measurement forecast. Based on the simulated measurement, the beam-switching command can be derived. The sampling result of the beam-switching method is given in figure 4.41. The samples with high gradients are selected (red samples), the other samples are ignored (gray samples). In this example, the algorithm is tuned to select the best measurement in each time step. The information exploitation algorithm will reduce the samples further when it is applied on the samples within on matching function length.

When a multi-beam surface measuring sensor is applied, such as a Laser scanner or a

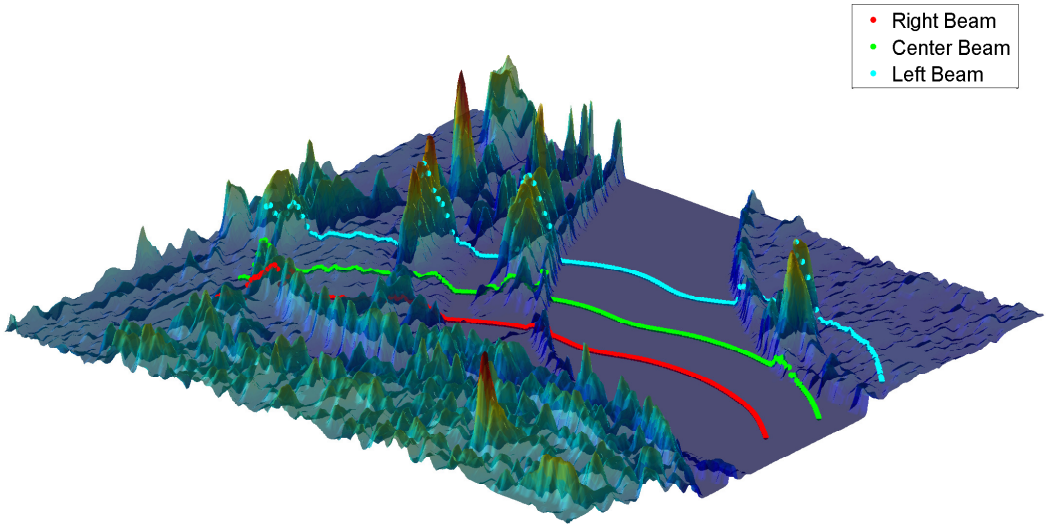

Figure 4.40: Fixed-beam measurement

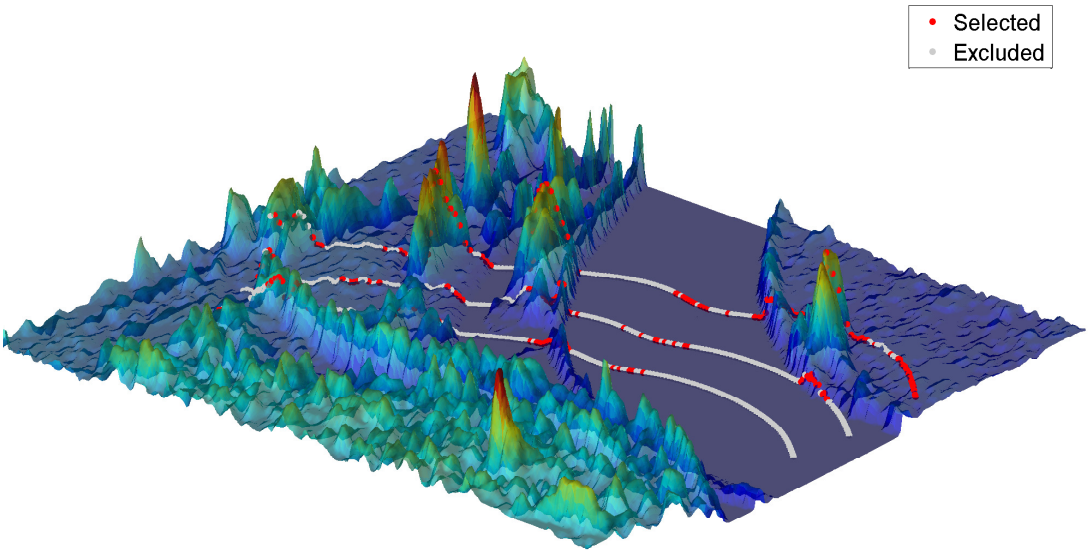

Figure 4.41: Beam-switching measurement

phased array Radar, the measurement direction can be chosen freely within the sensor boundaries. This gives two degrees of freedom, which allows to maximize the information content of the collected measurements.
The simulation model is used for an in-flight terrain gradient analysis. The model predicts the measurement direction which features the most beneficial measurement. The beam-steering command for the sensor, for example the lateral deviation of a Laser scanner is derived from the measurement direction to ensure the sampling of this area. The measurement representations obtained by this method are given in figure 4.42.
The chapter is concluded by a comparison of the matching functions of the three multi-beam approaches in a two-dimensional intersection of the three-dimensional matching matrix. The result is given in figure 4.43.
The multi-beam approach using three fixed-beams improves the matching function slightly, compared to a single-beam setup. The beam-switching method improves the matching function significantly, the beam-steering method shows the expected additional benefits

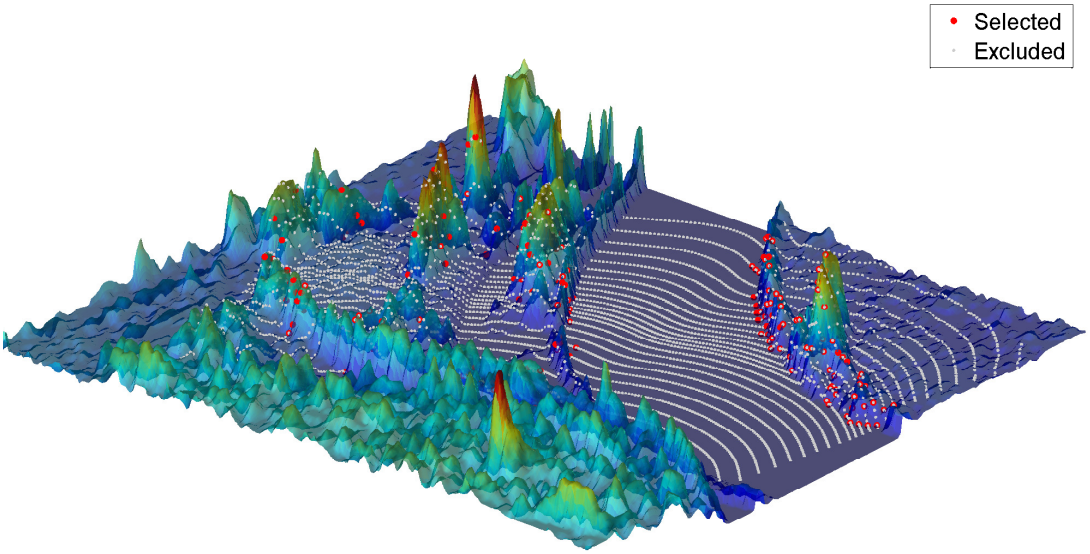

Figure 4.42: Beam-steering measurement

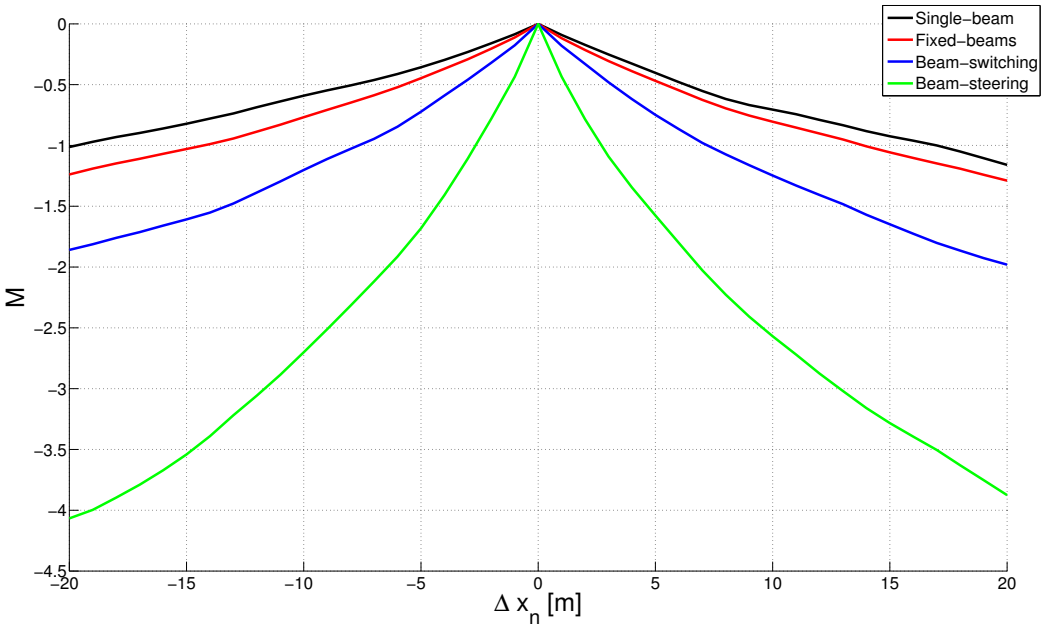

Figure 4.43: Comparison of the multi-beam matching function

to the matching function. In this example, the information exploitation is not applied, and thereby, the fixed-beam method processed $3N$ measurements, while the others process only N measurements.

The results of the multi-beam measurements using the information exploitation is illustrated in figure 4.44. The information exploitation brings the expected improvements. The matching function shape of all methods profits from the selection of the measurements. The fixed-beam method can catch up the performance of the beam-switching method and in some situations even improve the result. When the beam-switching method has not measured the surface information with the best impact on the matching function, the fixed-beam method is beneficial.

SAN systems can be improved by this method, but the achievable increase is limited by

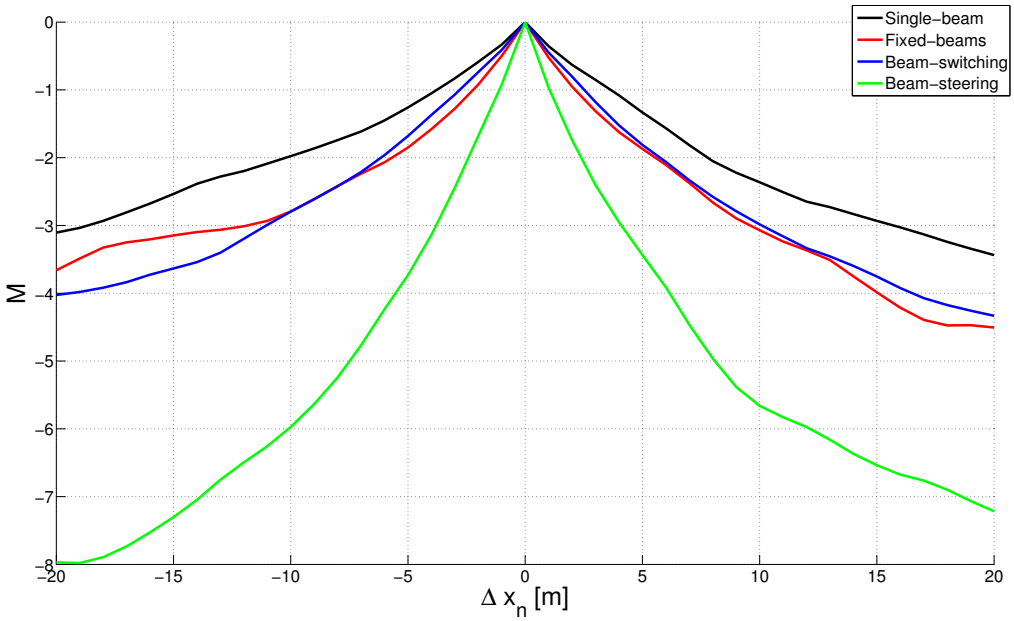

Figure 4.44: Comparison of the multi-beam matching function using the information exploitation method

the resolution of the DEM used. To calculate the maximum across track resolution of the sensor, an maximum view-angle of $\theta_{sm} = 60°$ is assumed as an example. The limitation concerning the number of beams, dependent on the DEM resolution and the platform height above ground, is illustrated in figure 4.45.

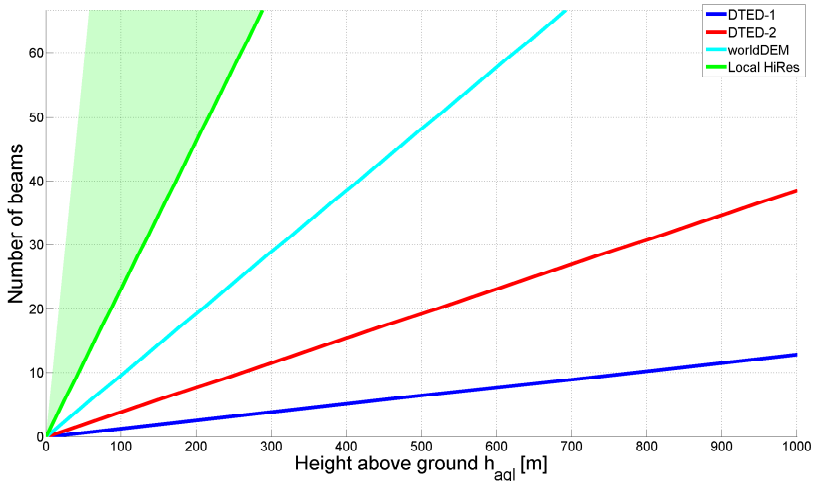

Figure 4.45: Number of beams - across track

Generally, if the application of a SAN system is proposed, the nominal trajectory of the aircraft should be adjusted to the needs of SAN. Especially the following three requirements have to be fulfilled:

- Flight path within surface-ranging sensor range
- Significant and rough surface characteristics
- Corresponding DSM available in the required detail level.

As additional benefit, SAN systems can support the platform guidance in case of degradation of the main navigation system by adjusting the flight path to the needs of the SAN systems. Comparable to an in-flight alignment bank-to-turn maneuver for INS, a sweep motion above a characteristic surface helps improve the SAN accuracy.
This method can also provide a solution for asymmetrically shaped matching functions, which means that the position is estimated with a high accuracy in one and with a low accuracy in the opposite direction. The prediction of the most beneficial measurement area can be used to identify measurements to particularly aid the weak matching function direction. In [101], a method to determine the update area of a SAN depending on the surface roughness is introduced.
The improvements of this chapter are summarized in following box. The methods introduced in this chapter are applied in simulations in chapter 7.

Results

- Information exploitation method increases the processed information content and sharpens the correlation shape
- Sampling requirements derived from surface characteristics in time and spatial frequency domain reduce the probability of ambiguities
- Consideration of the translational position drift by the matching function improves positioning accuracy
- Closed-loop slant range compensation improves the position accuracy for unimodal matching functions
- Multi-beam methods can increase the measured information content, reduce the probability of ambiguities and increase the position accuracy

Chapter 5

Dead Reckoning SAN

The so far introduced methods for SAN relied on an a-priori available DEM. There are several DEMs which cover the Earth's surface world wide, an overview of available DEMs and their resolution has been given in table 2.6. For high precision SAN, DEMs with high resolution, accuracy and currentness are required. DEM providing these feature are not available with a global coverage or an adequate currentness. Especially fast changing environments, like urban surroundings or dune-like surfaces in deserts are difficult to capture in DEMs. Seasonal differences of forests, vegetation and agricultural fields also complicate the comparison with the DEM. Tidal differences of the water level of coast, rivers or floods are another fast changing surface characteristics. Furthermore, in winter term, snow- or ice-covered surfaces are also changing the surface range measurements, compared to the reference DEM.
Another issue with the application of SAN systems is the in-flight availability of the entire DEM, which is required for the upcoming mission. The Earth surface covers an area of about $150\,000\,000\,\mathrm{km}^2$ (without water surfaces). Especially for long-endurance missions or missions with unplanned or dynamically adapted trajectories, a DEM independent SAN would be beneficial. In this section, a dead-reckoning approach for SAN is therefore introduced in order to overcome the DEM dependency.

Motivation

- DEMs not applicable for SAN above:
  - fast changing environments (urban/dunes)
  - seasonal differences (forests/vegetation/agricultural fields)
  - water level fluctuation (tidal/rivers/floods)
- Huge memory storage for unknown/unplanned/changeable flight paths

The dead-reckoning approach to SAN follows the basic idea of a temporal triangulation of the overflown surface. The comparison of the earlier and later recorded surface elevations indicate the position error, which was accumulated before and after the overflight. The INS position estimation of the platform is used to create the elevation map by georeferencing the measured distance and direction to the surface. Using the platform navigation system to create the elevation model, the position errors are intrinsically contained in the model and can be estimated by a classical matching approach. Even though no absolute position aiding to the integrated navigation system can be provided with this method, the error of the estimated position increment can be reduced. This linear position drift

measurement can be used to aid the navigation filter and to reduce the quadratic and cubic drift of the INS, for example for the bridging of GNSS outages. The basic concept of this approach is based on the following publications: [94], [90], [89], [92], [91], [88], [33], [32]. A student thesis dealing with this topic has been supervised ([75]).

Solution Approach

- Dead-reckoning as DEM independent approach to SAN
- Overlapping measurements of the surface elevation before and after overflight
- Multi-beam sensors to increase the measured information content
- Estimation of the platform position error drift to be used in the navigation filter for position error drift limitation

While reference-based SAN methods can be applied using single-beam altimeters as well as multi-beam sensors, the dead-reckoning approach requires multi-beam measurements. Not only the larger information content of the multi-beam sensors, but also the independence of platform maneuvers require a wider across track sampling. The range accuracy and measurement density must be very high in order to cover prominent features sufficiently well. The small footprint of a single-beam altimeter would disable the probability of measuring the same area twice with two sensors within high dynamic platform maneuvers. In this thesis, dead-reckoning SAN methods using range-scanning and range-imaging sensors are discussed. For a better overview, table 5.1 brings this chapter in context to the earlier discussed approaches.

	Reference DEM	Without DEM
Single-beam	✓	
Multi-beam	✓	✓

Table 5.1: SAN methods

The architecture of a dead-reckoning SAN system is given in the diagram in figure 5.1. While the integrated navigation system part is unchanged compared to the classical SAN approach, the dead-reckoning approach requires strongly redundant surface-ranging measurements and provides a position increment aiding to the navigation system. The next sections discus the range-scanning and range-imaging measurements followed by the analysis of the position drift estimation. The determination of the measurement time period and the integration of the measurement in the central navigation filter complete this section.

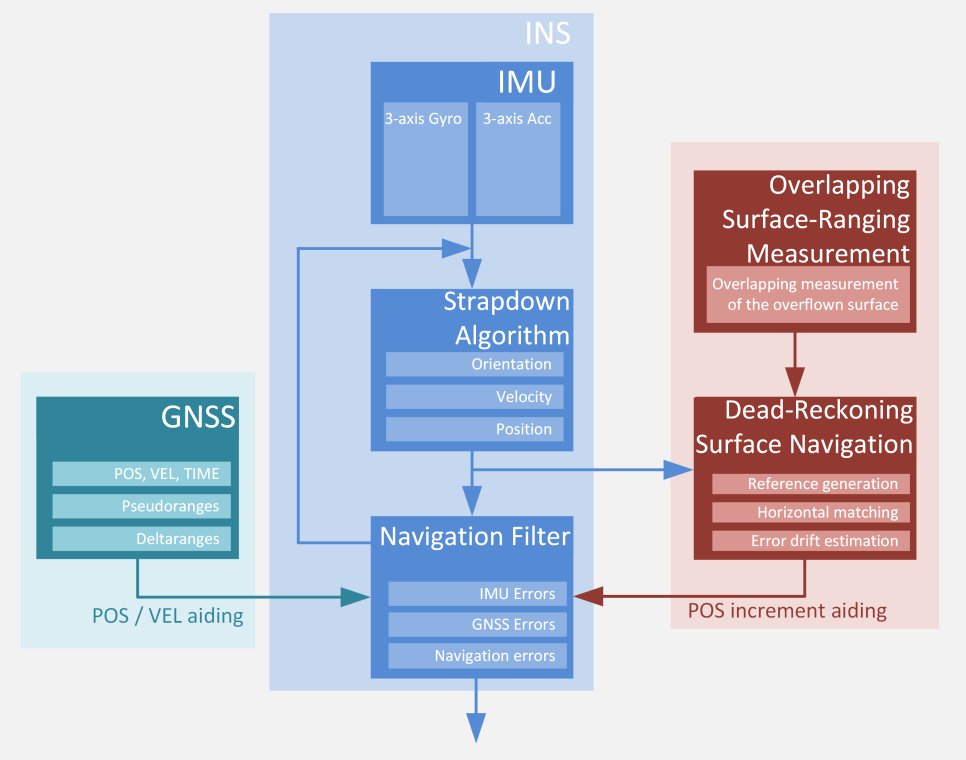

Figure 5.1: INS/dead-reckoning SAN

5.1 Range-Scanning Measurements

A dual range-scanning sensor configuration is the basic setup for a overlapping measurement of the surface. To measure the same surface with both sensors at two different points in time, the mounting angle or the mounting position or both have to be chosen differently for each sensor. It is important to ensure different angles of view for both range-scanning sensors in along track direction, to enable the measurement of the same surface are at different points in time.

An example for a dual range-scanning sensor configuration with a forward (red) and a backwards (green) looking Laser scanner is given in figure 5.2.

Furthermore, the surface elevation measured with the forward looking range-scanning sensor is interpreted as reference, the data provided by the backwards looking sensor as measurement. To record the reference elevation map and the measurement elevation map, range-scanning sensors are sampling the surface sequentially in different directions. A schematic top-view of the expected measurements is given in figure 5.3.

In this example, the forward looking range-scanning sensor is parametrized with a wider angle-of-view compared to the back looking sensor. This allows small platform roll maneuvers without loosing the required overlap. For the further system engineering calculations, the Earth's surface variations are neglected to find a solution without local dependencies. Laser scanner data sheets often state the lines-per-second n_l as indication of the radial velocity of the rotation mirror and the sampling frequency f_s. The angular sampling resolution $\Delta\alpha$ is calculated with the scanning beam-width α in equation 5.1.

$$\Delta\alpha = \alpha \cdot \frac{n_l}{f_s} \tag{5.1}$$

The functional principle of range-scanning sensors has been discussed in chapter 2. To achieve the sampling of a squared surface grid, which provides an ideal resolution of the overflown surface, the distances of points in-line and the distance between the scanned lines have to be equal. The mean point distance $\Delta\bar{s}_y$ of the scanned line is considered. It is calculated with the across track scanning range s_y, the scanning beam-width α and the sensor mounting angle θ_{sm} in equation 5.2 depending on the height above ground.

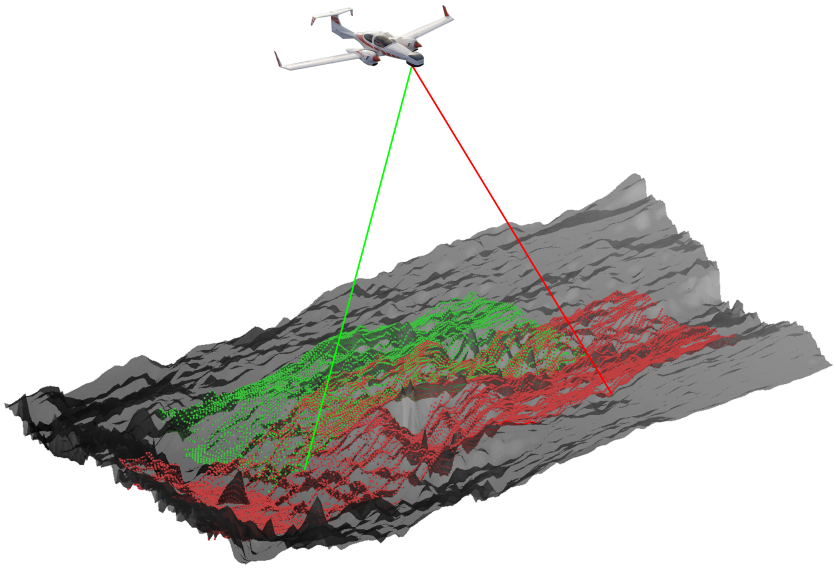

Figure 5.2: Dual airborne Laser scanning simulation scenery

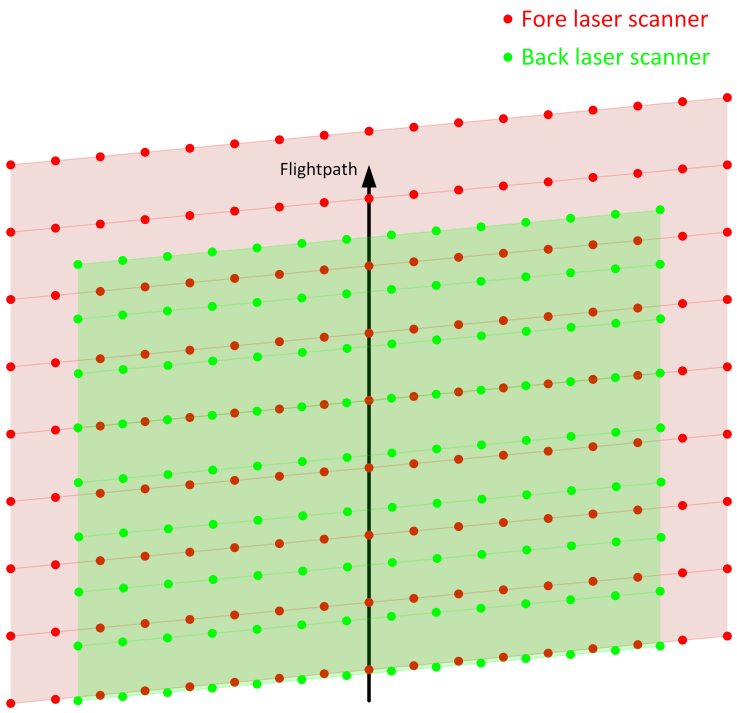

Figure 5.3: Laser scanner - overlap measurement concept

$$\begin{aligned}\Delta\bar{s}_y &= s_y \cdot \frac{n_l}{f_s} \\ &= 2\tan\left(\frac{\alpha}{2}\right)\frac{h_{agl}}{\cos\left(\theta_{sm}\right)} \cdot \frac{n_l}{f_s}\end{aligned} \tag{5.2}$$

The along track displacement of the point has been neglected due to the small along track movement between the high frequency sampling intervals. Additionally, this displacement affects all measurements in the same way. The distance between the scanned lines exclusively depends on the platform along track velocity v_x and the scanned lines per second. The corresponding relation is given by equation 5.3.

$$\Delta s_x = \frac{v_x}{n_l} \tag{5.3}$$

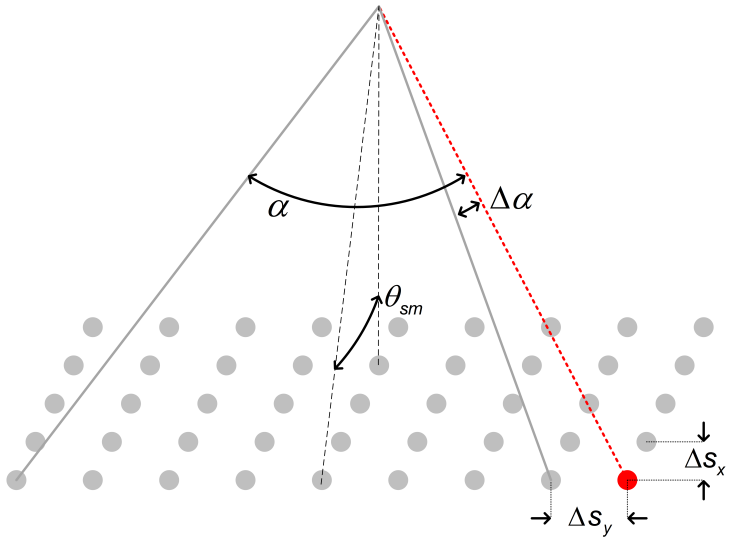

Figure 5.4: Sensor angle and point distances sketch

The along and across track point distances as well as the sensor view angle and the angular sensor resolution are illustrated in figure 5.4. By equalizing the across track Δs_y and the along track Δs_x distances, the nominal lines-per-second for a squared sampling grid can be determined (equation 5.4).

$$\frac{v_x}{n_l} = 2\tan\left(\frac{\alpha}{2}\right)\frac{h_{agl}}{\cos\left(\theta_{sm}\right)} \cdot \frac{n_l}{f_s} \tag{5.4}$$

Rearranging the relation to isolate the sensor mirror velocity leads to equation 5.5.

$$n_l = \left|\sqrt{\frac{f_s v_x \cos\left(\theta_{sm}\right)}{2\tan\left(\frac{\alpha}{2}\right) h_{agl}}}\right| \tag{5.5}$$

Figure 5.5 exemplifies equation 5.5 for a down-looking Laser scanner with an angular field-of-view of $\alpha = 80°$ and a measurement frequency of $f_l = 10\,\text{kHz}$. The lines-per-second n_l are illustrated depending on the along track velocity v_x and for different heights above ground h_{agl}.

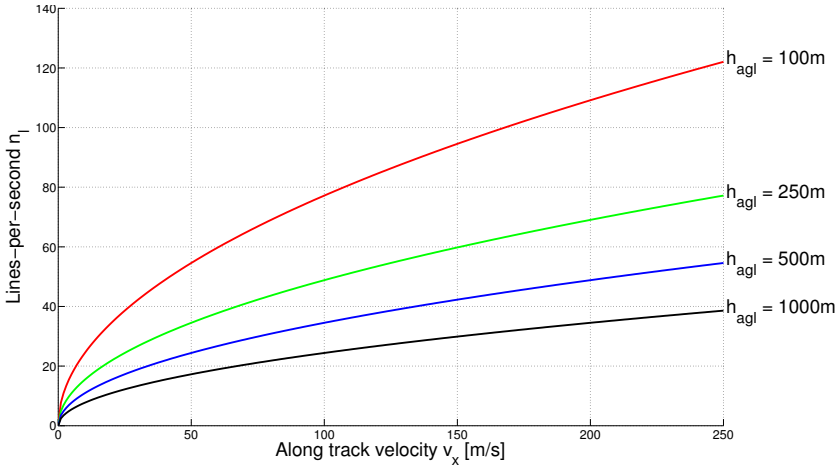

Figure 5.5: Regular grid tuning

To maintain an almost squared grid an increased along track velocity must be compensated by an increased line-per-second scan speed. An increased height above ground requires the reduction of the lines-per-second scan speed.
Another design criterion for a dual Laser scanner sensor configuration are the mounting angles θ_{sm} of both sensors. The tilted installation of at least one of the sensors enables the capability to provide an overlapping scan of the same area at different points in time. The angle between both sensors' viewing direction determines the time-to-overlap between both measured point clouds. In figure 5.6 the time-to-overlap for a configuration with a forward looking scanner mounted with $\theta_{sm} = 20°$ pitch and a down-looking scanner is calculated for four heights above ground.
The plot shows that an increase of velocity reduces the time-to-overlap t_o, while the increase of the height above ground h_{agl} increases the time-to-overlap.
While the lines-per-second can be adjusted, the mounting angles of the dual scanner configuration are fix. It is important to consider the mission profile of the platform, especially the expected height above ground and the along track velocity for a sustainable SAN system design. Apart from the surface sampling, the time-to-overlap is the other main dominating parameter. On the one hand, the time-to-overlap is desired to be large

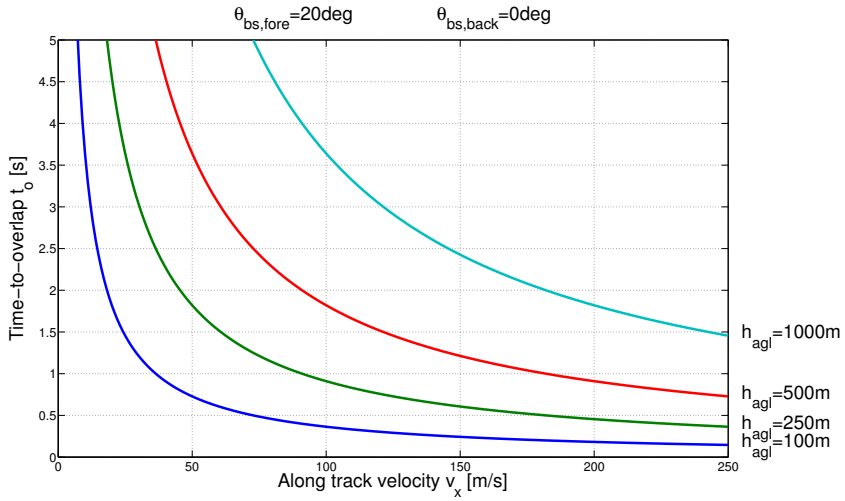

Figure 5.6: Time-to-overlap parameters

enough to allow a considerable position drift and on the other hand it shall be small enough to enable overlapping measurements despite from platform movements and rotations. The roll dynamic is thereby the most important factor, as high roll can prevent an overlapping of both surface maps. A small mounting angle between both sensors is therefore preferable for platforms with high roll dynamics.

5.2 Range-Imaging Measurements

Another measurement method which can provide overlapping surface measurements is based on snapshot measurements with a range-imaging sensor. Sensors which provide a range-matrix measurement are for example a Ladar, PMD Camera or ToF-camera. Figure 5.7 gives an example for a range-imaging sensor.

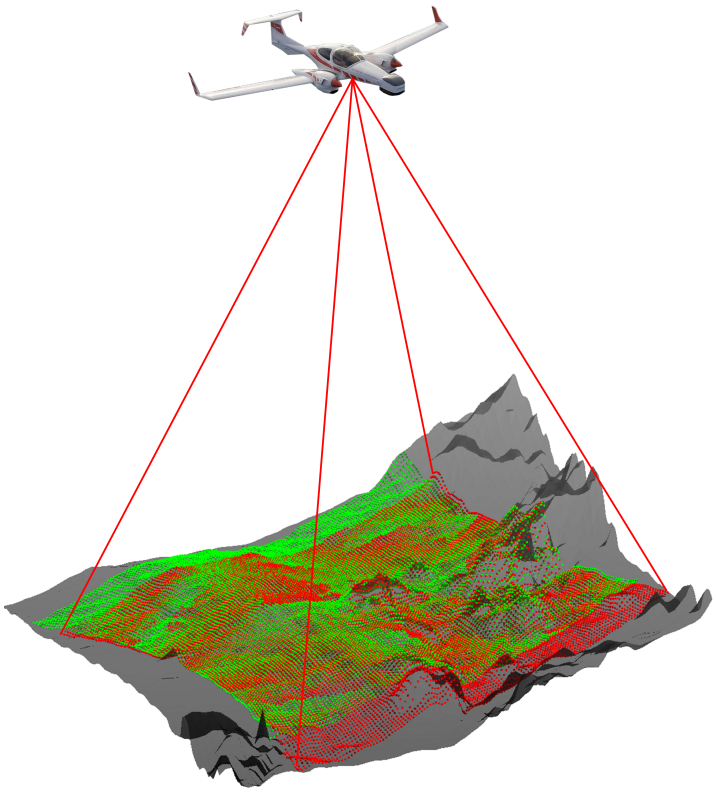

Figure 5.7: Range-imaging simulation scenery

These types of sensors output measurements which can be seen as photographic image with an additional ranging information attached to each pixel. This sensor type provides several advantages. First, the measured samples on the surface are almost equidistant, when assuming a flat surface. Second, range-imaging sensors provide a range-matrix recorded at one point in time. Third, this method only requires one sensor and hence allows an easier integration in the platform.
Table 5.2 gives a comparison of a range-scanning and a range-imaging measurement with a resolution of p_x to p_y pixels for comparison reasons.

	Time stamp	Measurement Quantity	Range	Direction
Range-scanning	t_k	1	$d_{m,k}$	$\Phi_{sm,k}$
Range-imaging	t_k	$N_k = p_x \cdot p_y$	$\mathbf{d}_{m,1..N}$	$\mathbf{\Phi}_{sm,1..N}$

Table 5.2: Range-imaging measurement

The footprint of an overlapping recording with a range-imaging sensor is illustrated for an exemplary flat surface in figure 5.8.

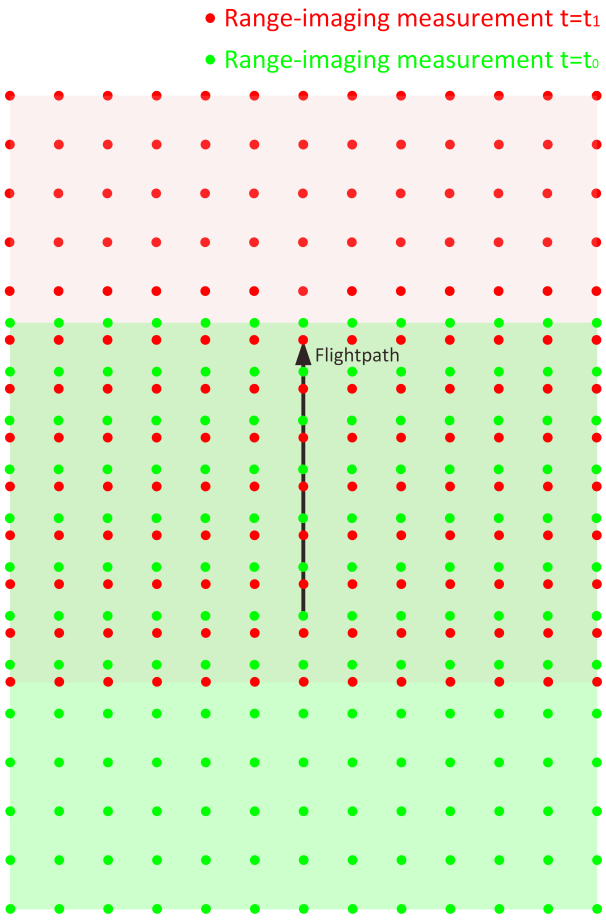

Figure 5.8: Overlap measurement concept

The array measurement structure of a range-imaging sensor implies an almost regular surface measurement grid. While the footprint is intrinsically regular, the update frequency is important to guarantee an overlapping measurement. As a rule of thumb, an overlapping of at minimum $s_o \geq 50\,\%$ of the measured area should expected (see figure 5.9).

The time duration between two measurements Δt_s to fulfill the requirement is given by equation 5.6 with the along track velocity v_x and the along track angle-of-view β.

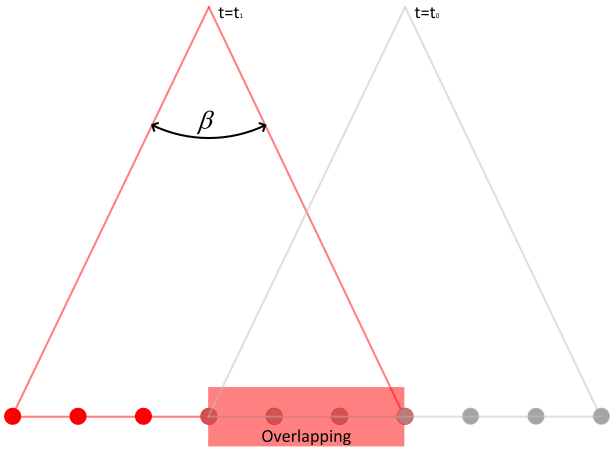

Figure 5.9: Range-imaging overlapping area sketch

$$\begin{aligned} \Delta t_s &\leq \frac{s_o}{v_x} \\ &\leq \frac{h_{agl}}{v_x} \tan\left(\frac{\beta}{2}\right) \end{aligned} \tag{5.6}$$

Figure 5.10 illustrates the resulting requirements on the sensor update frequency and the sampling time Δt_s. For the illustration the sensor angle-of-view of the range-imaging sensor is set to $\alpha = 80°$. The illustration gives the relation of the sampling time and the along track velocity v_x for different heights above ground.

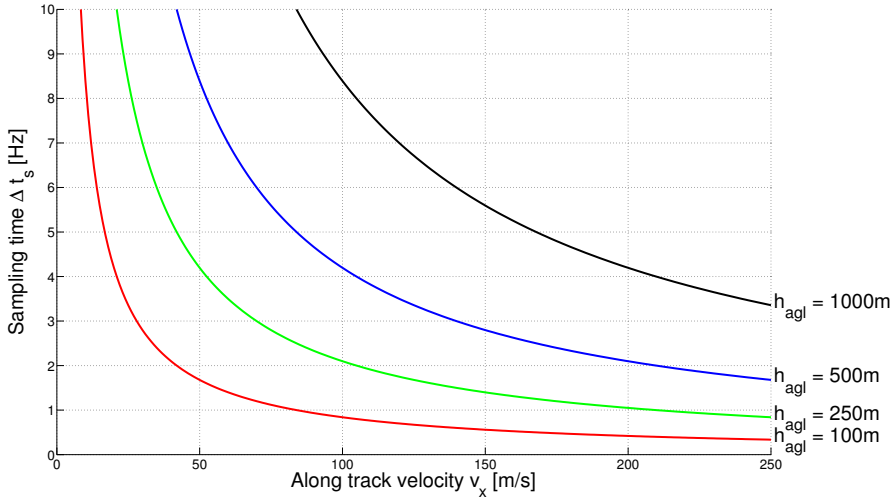

Figure 5.10: Range-imaging update frequency requirements

Obviously, the increase of the along track velocity leads to a reduction of the sampling time and an increase of the sensor update frequency. By increasing the height above ground, the sensor update frequency can be reduced.

5.3 Position Drift Calculation

The calculation of the position error drift follows a similar approach compare to reference-based SAN systems. The main difference of the dead-reckoning approach is the application of an in-flight recorded point cloud as reference. Due to this fact, a dead-reckoning SAN system measures the position drift of the INS within the measurement time interval. A benefit, compared to a reference-based approach, regarding the information processing, is the reduction of the grid-search size. Due to the fact, that the position drift is limited by the measurement time interval, the grid-size can be reduced to the corresponding maximum expected position error as given by the INS specifications. The computational burden can be reduced by limiting the grid-search size and the number of matching calculations. Furthermore, dead-reckoning SAN systems have no need for a time consuming acquisition mode. The time drift statistics of the INS can be used to determine the matching result grid-size. The main difference regarding the signal processing is in the use of an in-flight recorded irregular point cloud as reference. The processing of irregular point clouds as reference map requires additional calculation (see figure 5.11).

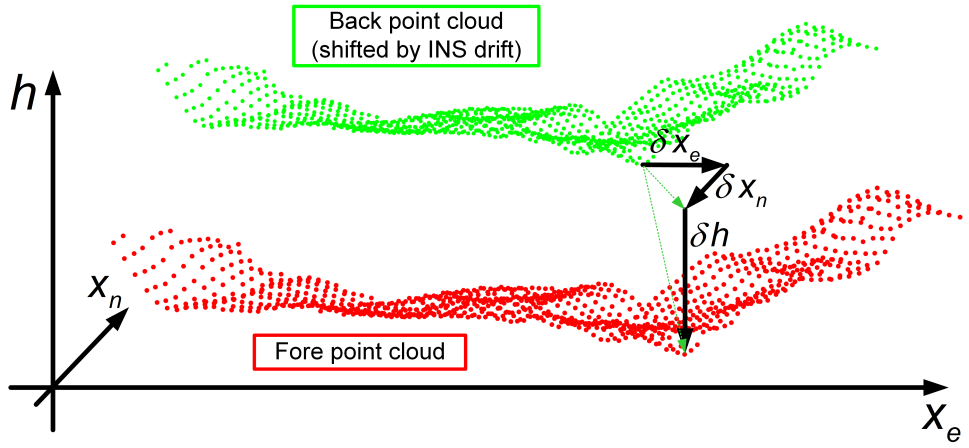

Figure 5.11: Matching algorithm applied on point cloud measurement

For regular grids, the interpolation of the reference elevation of the DEM can be processed using the bilinear interpolation as shown in chapter 2. One way to handle irregular grids is to transform the point cloud into a regular grid before processing. This approach may eliminate essential information and is therefore not recommended. In this thesis a triangulation is used to interpolate the irregular point cloud. The interpolation of the reference height at the measured horizontal position is a sequential process consisting of the following steps:

1. Find a triangle including/surrounding the measurement point
2. Prove the validity of the triangle geometry
3. Calculate the height of the reference triangle at the horizontal position.

Especially the first two items on the list are computationally challenging. First, the triangle which includes the measured horizontal position, has to be identified. The distances to the reference points (fore measurement) are calculated in the near surrounding. When

the corresponding reference points are identified, the triangles are checked whether the measured point is inside or outside the triangle. For a better interpretation, this situation is illustration in figure 5.12.

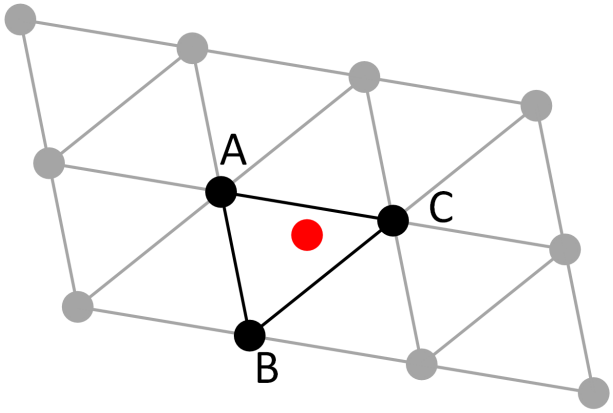

Figure 5.12: Triangle search

The search for a matching triangle is enormously time consuming for an unclustered and unsorted reference point cloud. As alternative to the approach in this thesis, a management of the point cloud with an intelligent tree data structure would reduce the computational effort. However, clustering can enable a faster triangulation search, but the clustering itself requires computational power. The identified triangles are checked whether they include the searched measurement point or not.
As second step, the chosen triangle is checked for its geometry. Before interpolating, it has to be ensured, that the triangle is representing the specific measurement point in a good way. Simulations have shown, that triangles with pointy edge angles or corners with excessive distance are not suitable for an interpolation. These assignments are identified and excluded for further processing. These situations often appear at the edges of the measurement width. If the requirements on the surface sampling are fulfilled, the consideration of this situation can be neglected. Figure 5.13 gives examples for valid and invalid geometries for interpolation purposes.

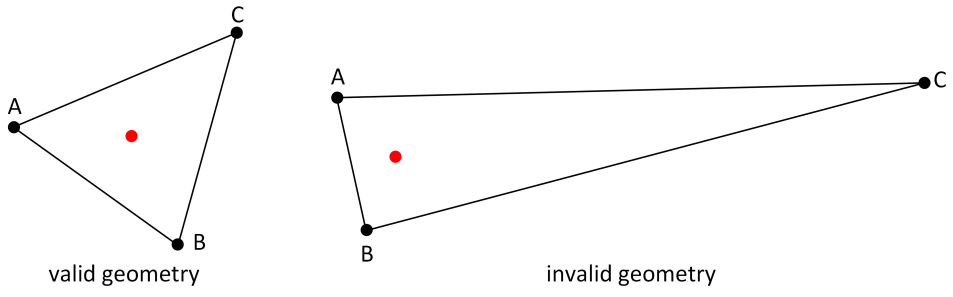

Figure 5.13: Examples for valid and invalid triangle geometry

The high computational effort of the triangulation, interpolation and matching function requires a fast grid-search algorithm. Therefore, the already introduced five-point grid-search is used. The entire process is illustrated in figure 5.14.
The algorithms developed as part of this thesis are modularly designed and can handle regular gridded as well as irregular gridded elevation models. Figure 5.15 shows an

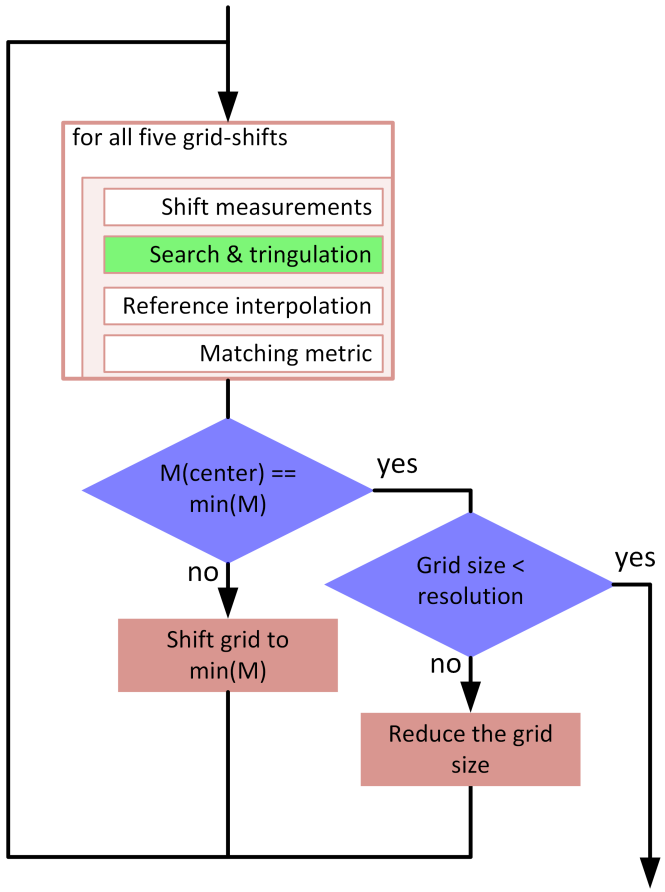

Figure 5.14: Five-point dead-reckoning grid-search block diagram

exemplary triangulation of Laser scanner measurements above a smooth surface.

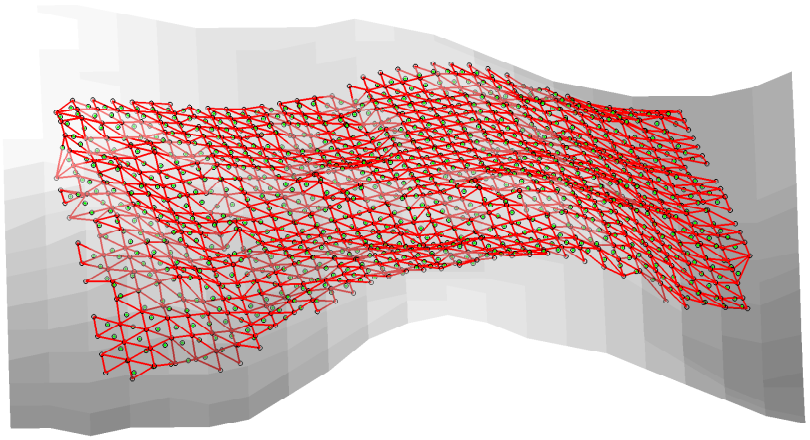

Figure 5.15: Triangulated point cloud example

The rest of this section deals with the difference and effects on the matching function between an overlapping range-imaging measurement and a dual Laser scanner measurement setup. While range-imaging sensors provide two measurements with a direct assignment to two points in time, range-scanning sensors measure sequentially over time. The aim of the matching algorithm is the isolation of the position error drift of the INS. Figure 5.16 depicts the situation for a range-imaging measurement recorded with a range-imaging

sensor.

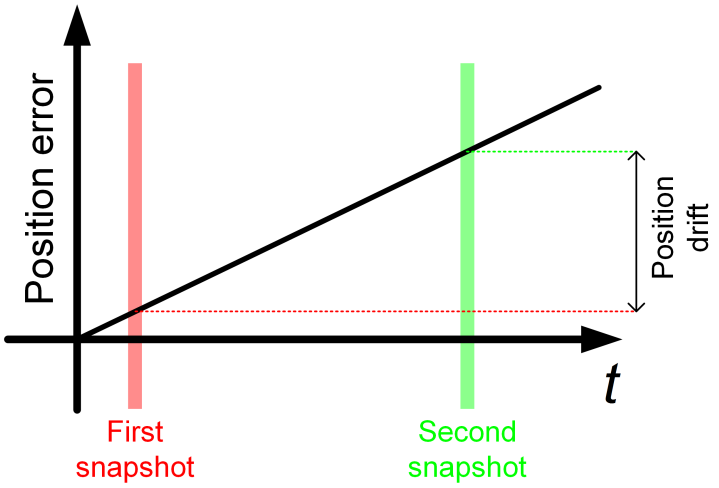

Figure 5.16: Time sequence for a range-imaging measurement

For sequential range-scanning measurements the time variant position error is assigned to each single measurement. A growing position error will affect later recorded measurements more strongly than older measurements. As long as the position error has a linear growth within the measurement time period, the error will be compensated with the matching function intrinsically. This situation is illustrated in the left illustration of figure 5.17.

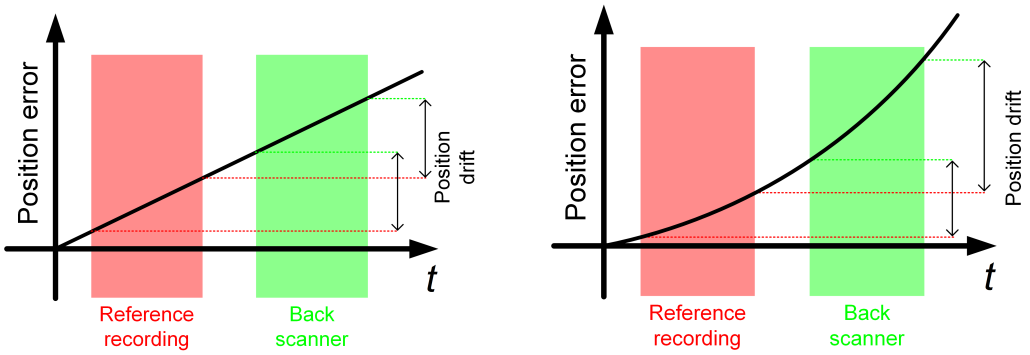

(a) Linear position error growth

(b) Non-linear position error growth

Figure 5.17: Time sequence for a range-scanning measurement

Depending on the grade of the inertial sensor characteristics, the position error drift may also be non-linear. This non-linear error growth can influence the measurement and cannot be compensated by the matching metric. This situation is illustrated in the right part of figure 5.17. The application boundary conditions for a high precise surface measurement do not allow a low-grade INS due to the required georeferencing precision. Obviously, the processing of the range-imaging sensor measurements is beneficial considering this effect.

5.4 Time-to-Overlap

The position error drift estimation is not the sole measurement for a dead-reckoning SAN system. The time-to-overlap Δt_o, which describes the time period between both mea-

surements, has to be determined exactly. For a range-imaging based dead-reckoning SAN system, the time-to-overlap can easily be determined as difference of the measurement time stamps. Using a range-scanning sensor setup, the determination of the time-to-overlap is more complicated due to the fact that each measurement sample has a different time stamp. The basic idea for the time-to-overlap estimation is illustrated in figure 5.18.

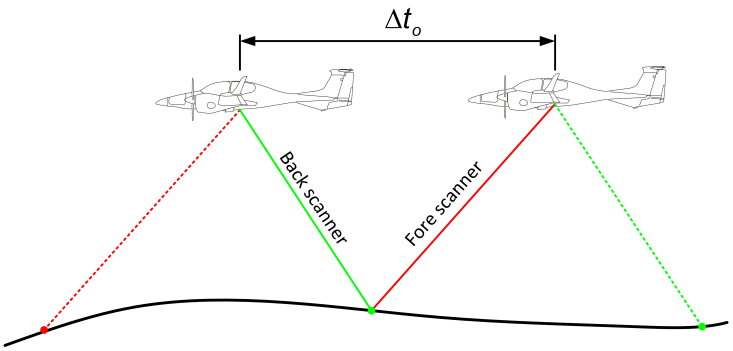

Figure 5.18: Time-to-overlap

When it comes to the interpolation of the measurement on the recorded reference, not only the height of the horizontal measurement position, but also the time stamp has to be interpolated. Using a range-imaging sensor, the time stamps within one snapshot are the same, but for a range-scanning measurements, they are recorded sequentially. For the interpolation of the measured height with a reference triangle, the time stamp assignment is important. Figure 5.19 describes this problem on a simplified example. The left part of the figure illustrates a footprint of a range-scanning sensor mounted on a platform in a bank-to-turn maneuver. Due to the maneuver, the footprint scanning lines are distorted. Hence, in the lower left area measurements m_k with significant different time stamps are neighboring.

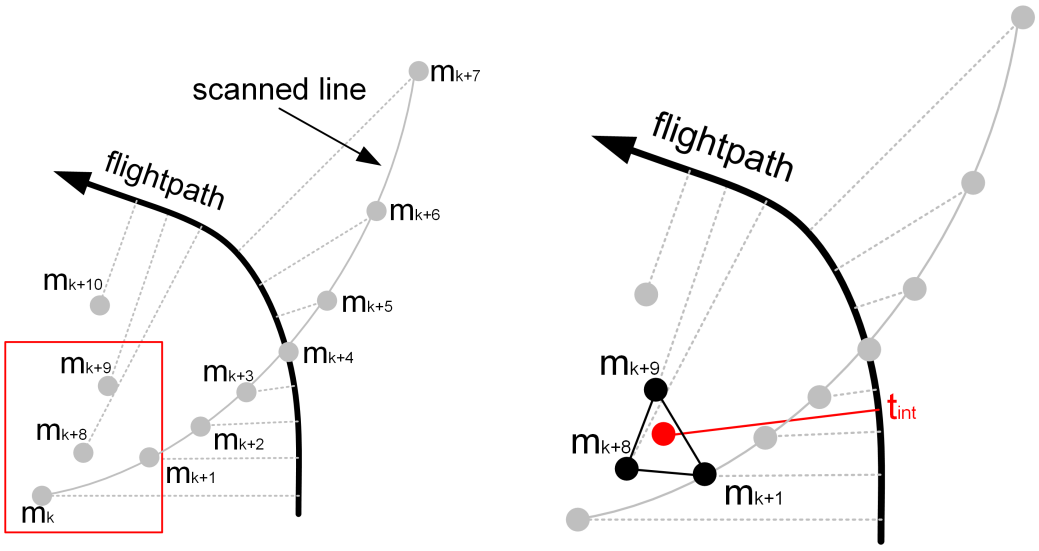

(a) Corresponding interpolation area (b) Interpolation triangle

Figure 5.19: Time-to-overlap non-linearities

The non-linear assignment of the mission time onto the sampling time is caused by the runtime measurement principle. The right part of figure 5.19 illustrates an interpolation

triangle with corner point from significant different points in time. In this simplified example the triangle consists of one corner point of the first scanned line and two corner point of the second scanned line. The recording time of the corner point of one triangle used for interpolation has to be as near as possible to provide a representative position error drift estimation. The different influence of the position error growth on the sampled measurement causes this effect.
While the position error drift affects the measurement linearly over time, in this situation a linear behavior cannot be guaranteed anymore. Triangulations with corner measurements from strong varying time-points are detected with the triangulation algorithm and excluded from further processing.
For interpolation with a valid triangle, the time-to-overlap can be calculated with a linear interpolation. For the entire position error drift estimation, the time to overlap is given by equation 5.7.

$$\Delta t_o = \frac{1}{N} \sum_{n}^{N} t_{fore,n} - t_{int,n} \tag{5.7}$$

5.5 Navigation Filter Integration

The fusion of a position error drift estimate, as provided by a dead-reckoning SAN system is not comparable to the integration of a height or position aiding information. The estimated position error drift within the estimated time period cannot directly be fed into a standard nine-state navigation filter. A simple approach is the interpretation of the measurement as velocity error, which is a navigation filter state. This measurement could then be used directly as aiding information.
The calculation of the mean velocity error uses the measured position drift $\delta\tilde{\mathbf{x}}_n$ and the time-to-overlap Δt_o (see equation 5.8). The measurement matrix for a mean velocity error for an error state space filter with the state introduced by equation 3.34 is given by equation 5.9.

$$\delta\bar{\mathbf{v}}_{en} = \frac{\delta\tilde{\mathbf{x}}_n}{\Delta t_o} \tag{5.8}$$

$$\mathbf{H} = \begin{pmatrix} \mathbf{0}_{3x3} & \mathbf{I}_{3x3} & \mathbf{0}_{3x3} \end{pmatrix} \tag{5.9}$$

A more advanced processing of the dead-reckoning SAN measurement, considering the platform motion, is introduced following. Instead of interpreting the measurement as mean velocity error, the position error estimate $\delta\mathbf{x}_n$ can be interpreted as position error increment. The relation can be written as an integral as shown by equation 5.10.

$$\delta\tilde{\mathbf{x}}_{n,k} = \int_{t_k - \Delta t_o}^{t_k} \delta\mathbf{v}_{en}(t)\, dt \tag{5.10}$$

Using this approach, the velocity measurement matrix, given in 5.9 can be applied again. The measurement can be rewritten with the navigation filter state vector $\mathbf{z}$ to equation 5.11.

$$\delta\tilde{\mathbf{x}}_{n,k} = \int_{t_k-\Delta t_o}^{t_k} \mathbf{H}\delta\mathbf{z}\,(t)\,dt \tag{5.11}$$

The transition to a discrete measurement is given with the relation in equation 5.12 using the propagation matrices of the navigation filter history $\mathbf{\Phi}_{t_k,t_{k-1}}$ in equation 5.13.

$$\delta\mathbf{z}\,(t) = \mathbf{\Phi}_{t,t_k-\Delta t_o} \cdot \mathbf{\Phi}_{t_k-\Delta t_o,t_k} \cdot \delta\mathbf{z}_k \tag{5.12}$$

$$\begin{aligned}\delta\tilde{\mathbf{x}}_n &= \int_{t_k-\Delta t_o}^{t_k} \mathbf{H}\mathbf{\Phi}_{t,t_k-\Delta t_o} \cdot \mathbf{\Phi}_{t_k-\Delta t_o,t_k} \cdot \delta\mathbf{z}_k dt \\ &= \underbrace{\mathbf{H} \int_{t_k-\Delta t_o}^{t_k} \mathbf{\Phi}_{t,t_k-\Delta t_o} dt\ \mathbf{\Phi}_{t_k-\Delta t_o,t_k}}_{\mathbf{H}'} \cdot \delta\mathbf{z}_k\end{aligned} \tag{5.13}$$

The new measurement matrix $\mathbf{H}'$ maps the the position error increment onto the measurement values [98]. This method is applied in simulations in chapter 7.
The results of this chapter are shortly summarized in the following box.

- The lines-per-second, along track velocity and the height above ground are influencing the range-scanning sampling grid
- The time-to-overlap is dependent on the mounting angles
- Range-imaging sensors provide a squared grid (flat surface) with a beneficial instant range-matrix measurement
- Position error drift matching algorithm follows the reference-based SAN method with an additional triangulation
- The platform dynamics can distort the range-scanning footprint and has to be considered for triangulation
- The position increment aiding can be achieved with the transition matrix including the platform motion history

Chapter 6

Flight Test Instrumentation

The Institute of Flight System Dynamics owns a twin-engine, four-seated aircraft research platform. The research aircraft, a Diamond Aircraft DA42 MPP (see figure 6.1), was modified to a fly-by-wire research testbed and supplemented by a reference sensors suite. In the context of this thesis, the sensor related aspects of the research aircraft are discussed, to explain the steps beginning with the sensor selection, the integration into the aircraft, to finally record and evaluate real-data. The work packages are summarized as follows:

Work packages

- Selection and integration of a suitable reference sensor suite
- Development of a modular and extendable data recording infrastructure
- Development of an in-flight sensor data visualization.

The first section gives an overview of the sensors, which have been integrated into the research aircraft. The second section presents the interface architecture including the sensors, connection cables and the Flight Test Instrumentation (FTI) setup. The data logging concept is explained in the third section followed by the flight test engineer monitoring system. The chapter ends with a short introduction to the FTI Hardware in the Loop (HIL) environment.

Figure 6.1: Diamond Aircraft DA42 MPP research platform

6.1 Sensor Suite Integration

The research aircraft features a high precision integrated navigation system using Ring Laser Gyroscopes (RLGs) as reference. The device provides a free inertial position accuracy of 0.8 nautical miles per hour. The unit is integrated in the nose baggage compartment of the aircraft and is connected to the Flight Control Computer (FCC) and FTI via a RS232 connection. It is additionally connected to the Ethernet hub for service applications and high frequency data logging. An image of the device installed in the aircraft nose compartment is given in figure 6.2.
While the integrated navigation represents the core navigation reference system using GNSS aiding information, a standalone GNSS solution is additionally provided with an independent connection to the FTI. Apart from position and velocity information, the connection to the GNSS receiver is used to record additional data like satellite constellations, clock errors and raw measurements. The GNSS setup also includes three optional antennas, one on the roof and one on each wingtip for a future GNSS attitude estimation using two additional receivers. Air data measurements, such as static and dynamic pressure, the temperature or the differential dynamic pressure for the angle of attack and the angle of side-slip, are provided by a SIMTEC air data system. While the Air Data Computer (ADC) is mounted in the rear baggage compartment, the airdata sensor boom can optionally be mounted on the wing tips or the aircraft's nose. The height above ground is measured with a Radar altimeter and a Laser altimeter. The Laser altimeter unit and the Radar altimeter antennas are integrated in the fuselage, near to the center of gravity, and are connected to the FTI. An illustration of the mounted Laser altimeter is given in figure 6.3.
The integration of the Radar altimeter provides several challenges concerning the installation location. The requirements on the antenna mounting, concerning their relative position to each other, the distance to other HF antennas and the obstacle clearance in the near surrounding are given in [43]. Following list gives a brief overview of the major requirements on the antenna mounting.

- Mounted parallel to the ground within an angle of 6°
- Angle between both antennas should not exceed 6°
- Obstacle clearance within a 120° cone around both antennas

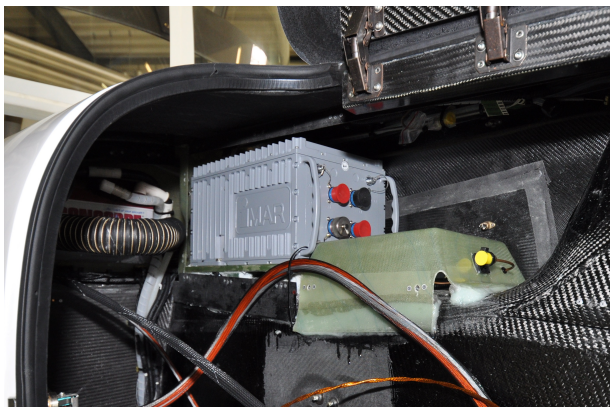

Figure 6.2: Integration of the RQH1003 in the nose baggage compartment

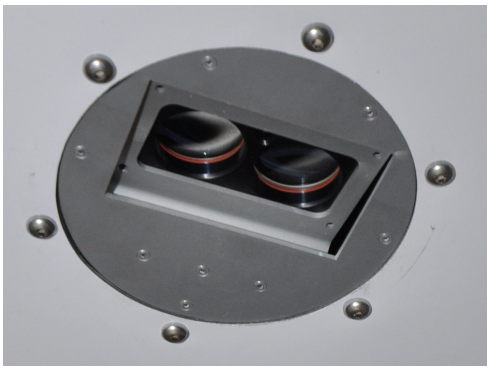

Figure 6.3: Integration of the Laser altimeter ILM500 in the fuselage

- Distance between both antennas $0.45\,\mathrm{m} < d < 1.0\,\mathrm{m}$
- Mounting close to the aerodynamic center of the aircraft
- Distance between Radar and DME, ADF, VHF or other HF antennas $d > 0.9\,\mathrm{m}$

These requirements are challenging for the integration of the antennas in a small aircraft. Especially in approach situations in which the Radar altimeter is normally used, the extracted gear has to be considered, when the antenna position is specified.
A magnetometer has additionally been integrated in the left wing for an independent orientation measurement. A tabular overview of the included navigation sensors with the used interfaces and update frequency settings is given in table 6.1
The research aircraft's sensor setup provides measurements of the deflection of the control surfaces and pilot control inputs additionally to the classical navigation sensors. Therefore, analog Laser position pickup distance sensors are mounted near to the corresponding control surface to measure the deflection. The analog sensor measurement is processed in a local micro-controller, which is connected to the Controller Area Network (CAN) bus. This micro-controller has the capability to digitize the analog measurements and transform the raw measurements into physical surface deflections by a stored calibration table. Each micro-controller can host up to four analog sensors, and therefore the surface deflection sensors are clustered into groups dependent on their location. The five micro-controllers are connected via CAN to the FTI. The aircraft features two independent sensor CAN buses, sensor bus 1 covering the left wing to the nose compartment and

Sensor class	**Sensor label**	**Interface**	**Frequency**
Integrated navigation system	iMAR RQH1003	RS232 UDP	100 Hz 300 Hz
GNSS receiver	Novatel ProPack OEM638	RS232	10 Hz
Airdata computer	Simtec RTMC	CAN	10 Hz
Laser altimeter	ILM 500 R/R	RS232	9 Hz
Radar altimeter	FreeFlight RA4500	RS232	25 Hz
Magnetometer	Honeywell HMR2300	RS485	20 Hz

Table 6.1: Sensor suite overview

Micro computer	**CAN interface**	**Laser position pickup**
Tail	Sensor bus 2	Elevator surface deflection Rudder surface deflection Rudder trim pad
Left wing	Sensor bus 1	Left aileron
Right wing	Sensor bus 2	Right aileron
Flaps	Sensor bus 1	Flap position
Pilot controls	Sensor bus 1	Aileron - stick position Elevator - stick position Rudder - pedal position Elevator - trim pad

Table 6.2: Laser position pickup overview

sensor bus 2 covering the tail to the right wing area. Table 6.2 gives an overview of the measured deflections and the connections to the aircraft CAN buses. A top-view on the research aircraft is given in figure 6.4.

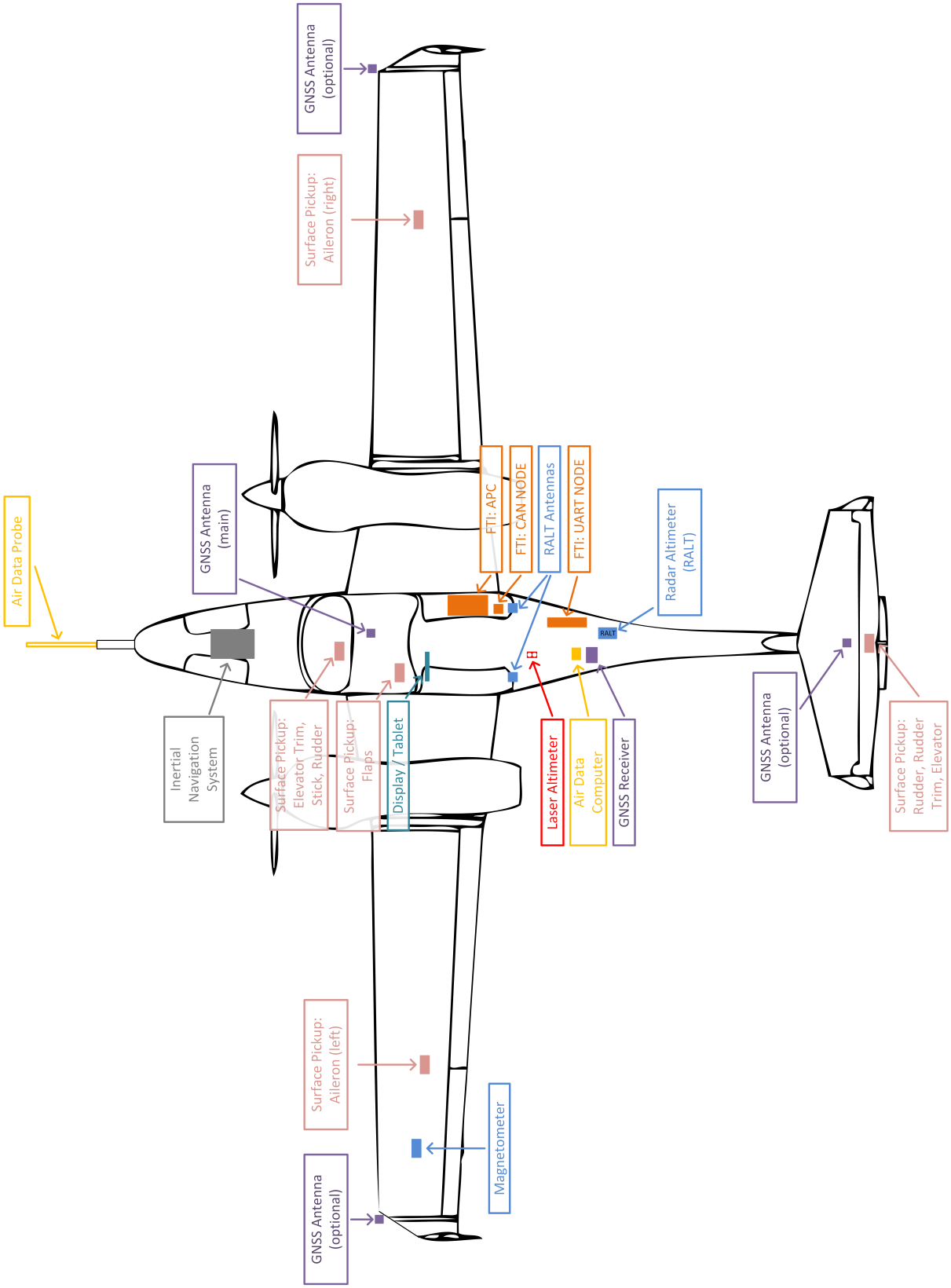

Figure 6.4: Research aircraft sensor suite

6.2 Architecture

All devices related to the research infrastructure like sensors, experimental flight controls and telemetry, are connected to the FTI computer. The primary task of the FTI is the recording of all incoming sensor measurements on all interfaces for later evaluations and analyses. The in-flight evaluation and visualization of the data, operated by the pilots and flight test engineers, is the secondary task. Based on the opportunity to pursue a flexible number and type of supported interfaces, an Automation PC (APC) has been chosen as FTI hardware. Furthermore, the modular concept of the chosen Bernecker & Rainer (B&R) APC 910 allows an easy extension or replacement of interfaces. The installed FTI setup consist of the APC with two powerlink interfaces, one used for the three powerlink nodes, responsible for Universal Asynchronous Receiver Transmitter (UART) (RS232, RS422, RS485) modules, the other one is used for CAN bus transmission. Therefore, the CAN transmit modules are connected directly via powerlink node to the APC, while the CAN receive nodes are connected via an additional B&R X20CP3586 programmable logic controller as Intelligent Controlled Node (ICN) due to internal processing reasons. Figure 6.5 shows an overview of the installed system as displayed in the B&R Automation Studio System Designer tool.
The APC provides a VxWorks based real-time operating system and can be programmed with the B&R Automation Studio software. Several computer languages (i.e. ANSI C, ANSI C++, Structured Text, Basic, diagram-based programming) are supported and can be combined within one project. The scheduling of the different subprograms is done, by assigning each program to one of eight task classes with definable cyclic time. All programs and library have been realized in ANSI C and a modular submodule structure for this project.
All tasks have been categorized into groups with different cyclic frequencies to establish a computational burden efficient project. The interface handling, responsible for receiving and transmitting data, is assigned to the task with the lowest cyclic time. The post-processing of the data for visualization purposes can be done at a medium frequency. This medium frequency corresponds to the update frequency of the visualization. While the collection of the data to an internal buffer is done at a high frequency, the file writing is established with a reduced frequency, due to the high computational burden of file access operations. Table 6.3 gives an overview of the used submodule categories, the

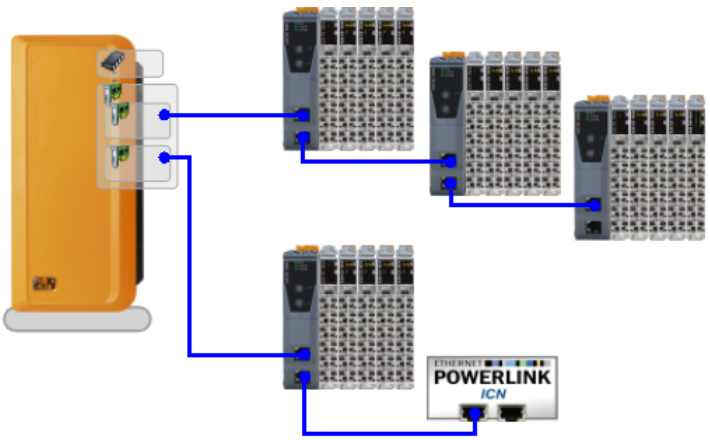

Figure 6.5: B&R Automation Studio system designer

Submodule	Category	Description	Frequency
_tx	I/O handling	transmit	high
_rx		receive	
_trx		bidirectional	
_interpret	data processing	protocol unpack	medium
_convert		physical value conversion	
_pack		protocol pack	
_ctrl	device control	sensor setting modifications	startup/on request
_datalog	file I/O	file write	low

Table 6.3: Submodule categories

nomenclature and the frequency association.
The total number of interface handling routines is given in table 6.4.

	RS232	RS485/RS422	CAN (tx)	CAN (tx)	UDP
Number of modules	7	4	4	6	>30

Table 6.4: Number of interface handling functions

The UART and CAN connections are mainly used for sensor measurements and communication with the experimental control system. The high amount of User Datagram Protocol (UDP) connections is used by the communication to the in-flight visualization. All incoming messages are time stamped and written to a data logging file. The messages which are important for the in-flight visualization are unpacked, Cyclic Redundancy Check (CRC) checked and interpreted, too.

6.3 Data Logging Concept

For data logging, a robust time stamp is the most important meta information for the later data synchronization with other sensor data. Each incoming data stream segment is time stamped immediately after reception. For sensors without an internal time, like the Laser altimeters or the air data computers, this time stamp is the only association to the other sensors. For sensors with internal clocks, like GNSS receivers, this time stamp is the association with the FTI time. The time stamping of the incoming data stream is coded as a relative time, beginning with the FTI start up. The FTI time stamp can be transformed into a global time for an absolute time-precise post-processing of the recorded data. Therefore, the GNSS receiver clock is used to compensate a possible time drift of the internal FTI clock.
The requirements on the time stamp are a resolution of minimum 50 µs and an unambiguous time assignment of at least one week, especially for HIL simulation. An unsigned

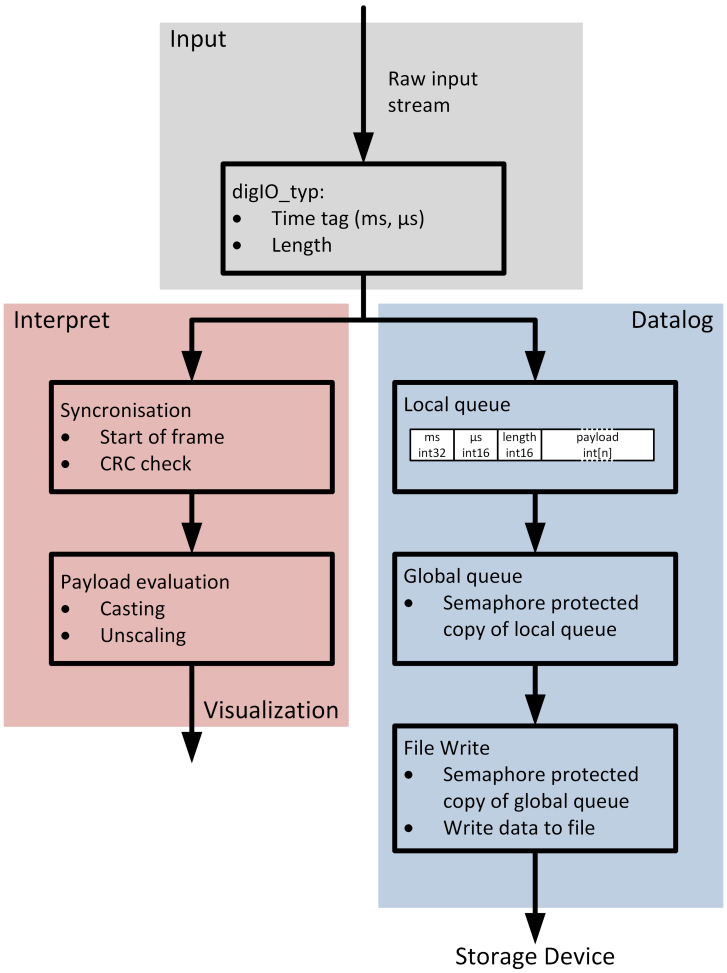

Figure 6.6: Message interpretation and data logging stream division

32-bit integer with a bit resolution of 50 µs can cover the time maximum period $T_{FTI,max}$ given by equation 6.1.

$$T_{FTI,max} = \left(2^{32} - 1\right) \cdot 50\,\mu\text{s} = 2.49\,\text{d} \tag{6.1}$$

As an alternative, the time stamp is divided into two variables, one unsigned 32-bit integer representing the milliseconds, with a range up to $T_{FTI,max} = 49.7\,\text{d}$ and a unsigned 16-bit integer representing the μ seconds with a range up to 999 µs.
To avoid interdependencies, the data logging task is completely independent of the data interpretation and data visualization tasks. The input data streams are separated into a logging stream and an interpretation stream, immediately after reception. This design is required to ensure a completely independent logging and avoid a potential blocking of the the recording procedure.
If the design had included the logging of unpacked and converted sensor data, a failed CRC check for example would have lead to the exclusion of the data packet and to the interruption of the logging process. Such a data stream would have not been logged and the error source could not be identified in the post processing. The schematics of the receive stream division is given in figure 6.6.
After time stamping the incoming data stream, it is copied immediately into a local, semaphore protected queue. This semaphore prevents the concurrent access to the queue

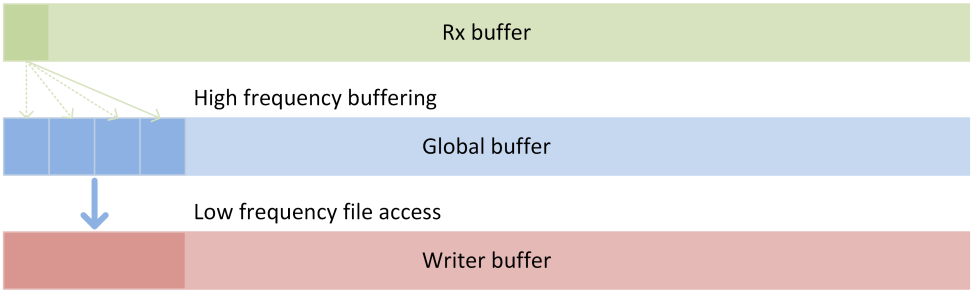

Figure 6.7: Data logging buffer concept

which could lead to potential corruption of the data stream. Immediately after reception, the local queue tries to copy its information in a global queue. The purpose of the global queue is the data transmission to the file writer module. This operation is again semaphore protected. In case of a locked global buffer, the data is collected in the local stream until the global buffer is available again. The global buffer collects the data from the local buffer over a larger period of time. The low frequent file writer task is executed when the global buffer size has reached a minimum write threshold. This limitation avoids high computational costs due to the file access routines. If the file writer buffer is locked, the routine is executed at the next availability. The three buffer types and their interaction are illustrated in figure 6.7.

The data logging algorithm requires several cycles to save the data on the storage medium, depending on the amount of data and the general system load. To avoid exhausting file sizes, new files are generated in defined time intervals, typically every five minutes. A time sequence of the queue copy process is given in figure 6.8.

The filenames of the generated files include the logged device identification and a date and time stamp for an unambiguous assignment. The amount of data is not the only influencing factor for the file writer process runtime. This process is realized in the data logging function of the fsdDatalog library using a state machine and the B&R FileIO library. This manufacturer library offers several functions to open, close and write data to a file. The rudiment FileIO functions are managed with a state machine for an automatic flow. Additionally, the device hot plug functionality is managed in this function to allow changes of the storage device during the runtime. The state diagram of the data logging function is depicted in figure 6.9.

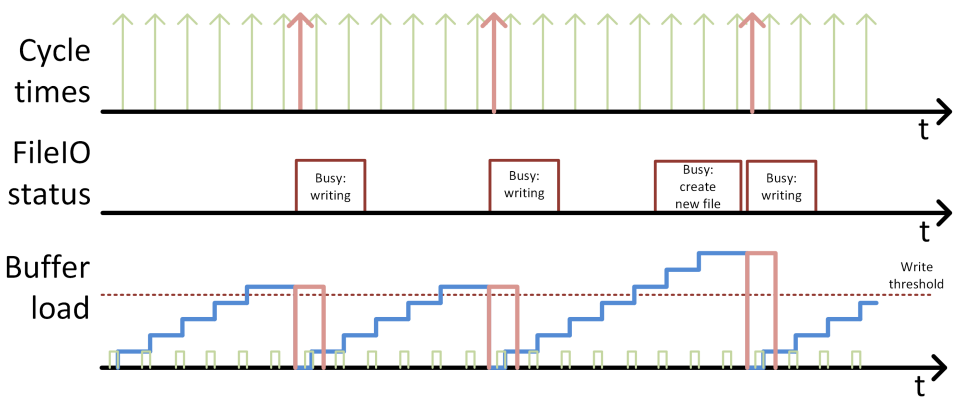

Figure 6.8: Data logging timing concept

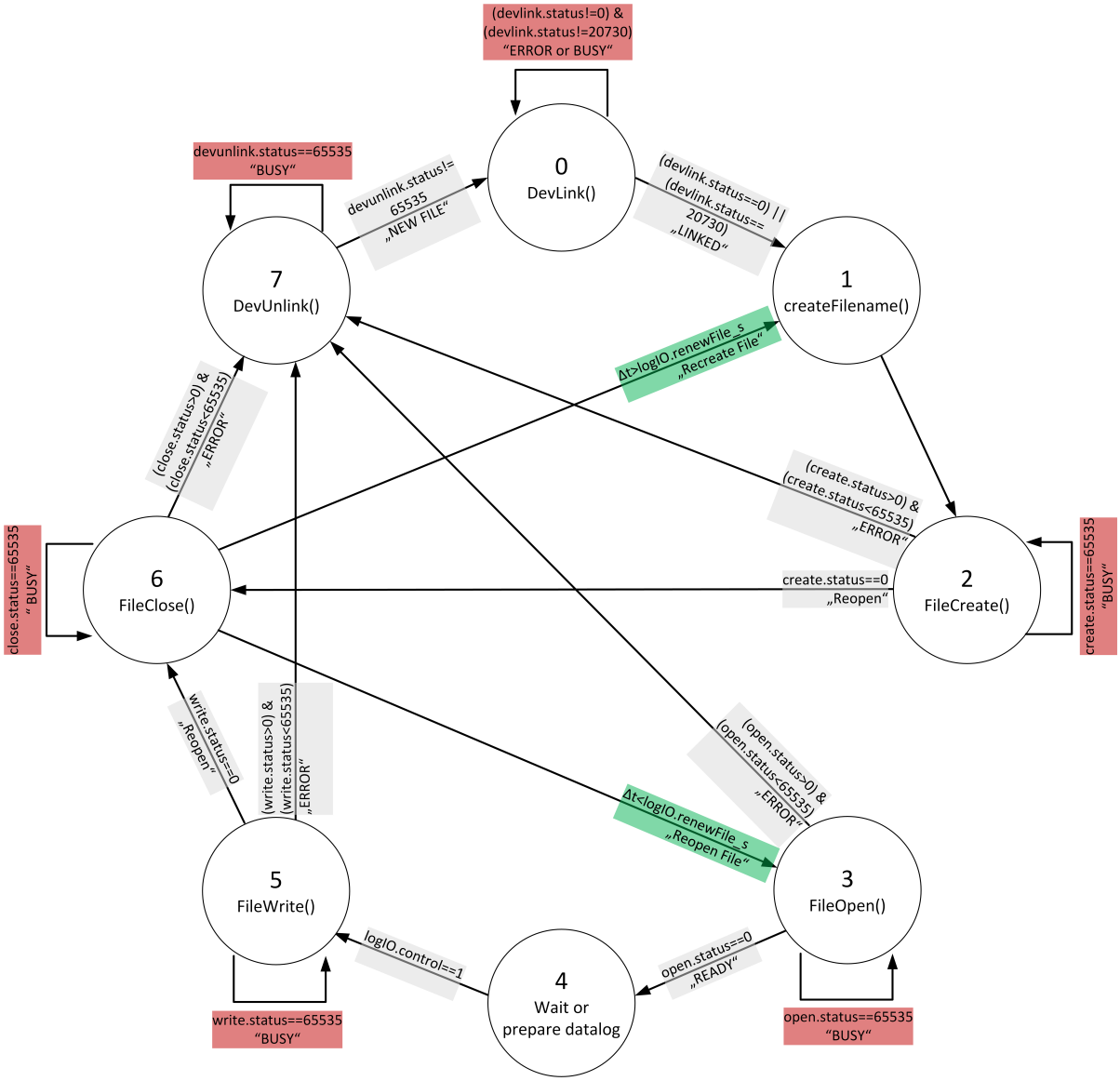

Figure 6.9: fsdDatalog library - state diagram

The queue size of the three buffers (receive, global, write) for each sensor are designed to be $s_{buffer} = 2^{19} = 524\,288\,\mathrm{B}$, which adds up to a total buffer for all 23 data-log channels of about 35 MB of disk space. In the event that the required recording storage medium is not responding (busy), a controlled global buffer overflow is enforced if the global buffer load is at $l_{global} = 100\,\%$ and the receive buffer load is at $load_{rx} \geq 90\,\%$. The receive buffer is not completely utilized to provide a minimum memory space for future incoming messages, for a possible reconnection to the storage medium. The queues are continuously shifted to delete older messages and keep the current ones. This methods enables a continuous logging as long a the outage time $\Delta t_{overflow}$ is not exceeded.
Considering a sensor with the frequency f_1, a message length of s_{msg} and the factor c_{msg} describing the number of time cycles needed to receive one message, the total storage medium overflow time $\Delta t_{overflow}$ is calculated by equation 6.2. Assuming a message with a frequency of $f_1 = 100\,\mathrm{Hz}$ and a message length of $s_{msg} = 66\,\mathrm{Byte}$ and a mean number of message receptions of $c_{msg} = 2$, the time span the storage medium is not responding should not exceed the overflow time $\Delta t_{overflow} \approx 2\,\mathrm{min}$ to prevent a buffer overflow.

$$\Delta t_{overflow} = \frac{1.9 \cdot s_{buffer}}{f_1 \cdot (s_{msg} + 8 \cdot c_{msg})}. \tag{6.2}$$

An important aspect for the post-processing of the recorded data is the time drift behavior. While sensors without an internal clock rely on the FTI clock, the integrated navigation system or the GNSS receiver provide an internal clock. The logged time tag sequence of the GNSS receiver does not only provide the Seconds-of-Week (SoW) of the highly precise Position-Velocity-Time (PVT) solution, but also the FTI time stamp. These time stamps enable the absolute synchronization from the relative FTI time t_{rx} to the absolute GNSS time t_{SoW} in the post-processing. The time drift behavior for a flight test with a duration of $T \approx 60\,\mathrm{min}$ is shown in figure 6.10. A drift of $\delta t_{rx} \approx 4\,\mathrm{ms}$ between FTI time stamp and the t_{SoW} over a period of one hour can be identified.

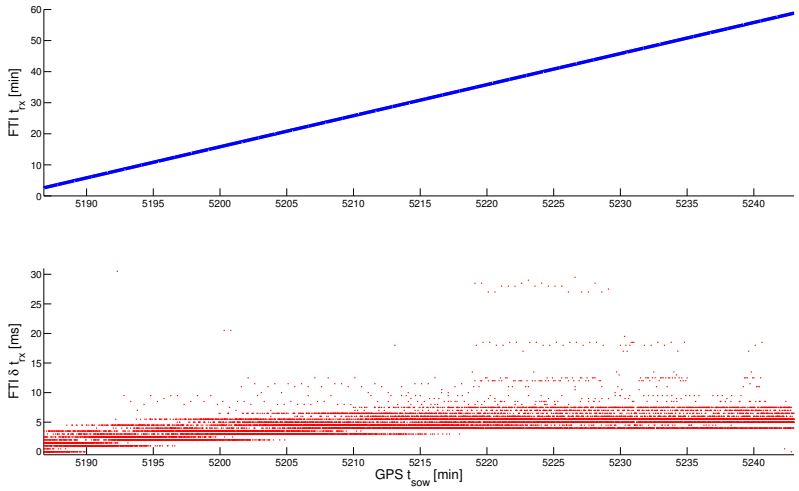

Figure 6.10: FTI time drift

The outages of up to $\delta t_{rx} \approx 25\,\mathrm{ms}$ are not indicating a timing problem of the recording device, but are a sensor specific characteristic. In this example, the timing of the GNSS receiver was analysed in detail. The GNSS receiver does not only provide position and velocity information at a constant data rate, but also gives meta information like satellite

constellation information or clock error model parameters. This information are provided with a delay and without constant data rate. However, the data contains the time stamp of their validity time, which explains the higher time stamp discrepancy.

6.4 In-flight Visualization

The in-flight visualization displays all important information to the Flight Test Engineer (FTE). The amount of expensive flight test hours can be minimized by indicating malfunctions directly. The most important functions have been indicated and grouped for visualization onto eight subpages. The eight subpages and a brief overview of the contained information are given in table 6.5.

Page	Content	Controls
Overview	Primary Flight Display (PFD), position, height above ground, Experimental Flight Control System (EFCS), surface deflections	-
EFCS	detailed drive train information, internal error list	-
RQH	navigation states, covariances, device status	trigger alignment, trigger UDP stream
PFD	PFD, detailed air data information, Radar and Laser altimeter	Pressure Settings
GPS	GNSS position and velocity, device Status	log, unlog and reset, toggle antenna power
POS Pickups	raw and calibrate surface deflections	modify calibrations and update frequencies
Logmonitor	USB device indication, buffer load, file-age	reset buffer overflow
Flight Control	autopilot modes, direct law, moving map, error list, software versions	set flight test number, toggle flight test, toggle waypoints

Table 6.5: FTI display pages

An indication of the state of the buffers and the storage device is avaiable to monitor the data logging. The load of the three buffers and the age of the file indicates the health of the data logging channels. Additionally, a red frame around the corrupted buffer would indicate a potential buffer overflow. This information can be reset by clicking onto the symbol of the corrupted buffer if the FTE is aware of the malfunction (see figure 6.11).
The information of each page is transmitted to the visualization device by a separate UDP package. Short time variant information can be transmitted at a higher data rate (e.g. PFD) than information with low variance in time (waypoint list). The computational effort of the FTI and the display computer as well as the network load is reduced this way. The FTE workstation including the FTI and the display is shown in figure 6.12. The left

Figure 6.11: Data logging monitoring

image displays the EFCS safety system, the FCC, the Power Distribution Unit (PDU) and actuators. The UART powerlink knot of the FTI is installed in the rear baggage compartment of the research aircraft. The FTI consists of the APC, the interface boxes for CAN and UART and the display. The right image gives a more detailed view on the FTI display with the selected overview page. While the aircraft is on ground in this situation, the FTI inputs are fed by the Aircraft-in-the-Loop (AIL) system. This additional HIL environment can be used for testing specific in-air situations on ground.

The display information is rigorously checked for their currentness. Therefore, each sensor protocol package type is assigned a maximum outage time threshold. If no update is received at the FTI within this time interval, the outdated sensor information is crossed out from the display to indicate the sensor outage. If a complete UDP package is lost over a specific time interval, the display itself indicates the loss of the Ethernet connection by a red display overlay.

While the information content of the eight subpages are transmitted simultaneously, there

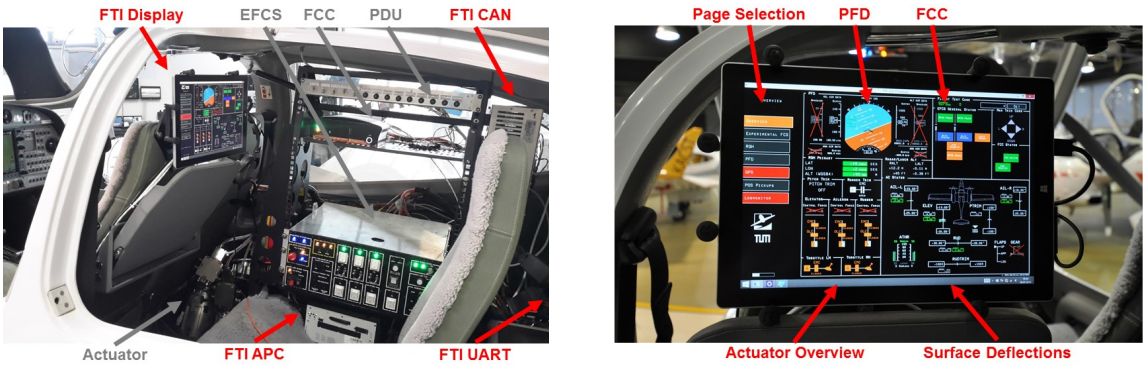

(a) Flight test engineer workstation

(b) FTI display

Figure 6.12: FTI setup

are contents which have to be requested by the user. For example, the calibrations table of the surface deflection pickups is only provided for the selected sensor. Transmitting the calibration table for each sensor would exhaust the UDP protocol structure and would increase the network traffic load. The request of the sensor and generally, the operation of a display button requires a handshake protocol for debouncing. The main reason for this approach is the asynchronous timing of the display and the FTI and the indeterminism of the UDP protocol. Additionally, the timing of the FTI has to be considered. A button request for example can be received multiple times before the FTI reacts. Therefore, all bi-directional message streams with the display are debounced. The implemented debouncing method is illustrated in figure 6.13.

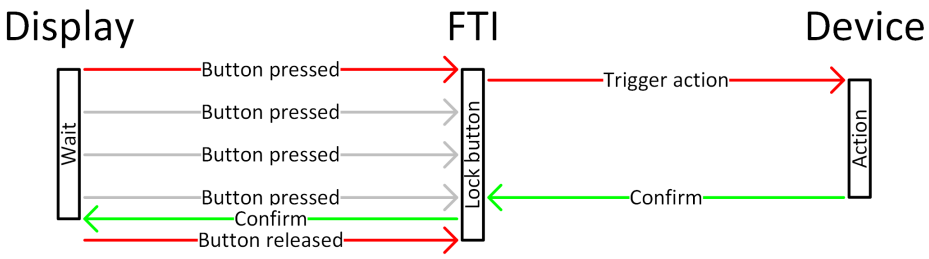

Figure 6.13: Display button debouncing

As example, the control of a device via FTI display is described in detail. The modification of a calibration sampling point on a surface deflection sensor is chosen to show the procedure. While the calibration commands are provided via UDP to the FTI, the sensors have to be configured via CAN bus. To insert, modify or delete a sampling point of the calibration curve, which maps the raw sensor measurements onto physical surface deflections, several steps have to be realized. The control of this sensor via display is illustrated as sequence diagram in figure 6.14. The debouncing of the several buttons is omitted in the diagram for convenience.

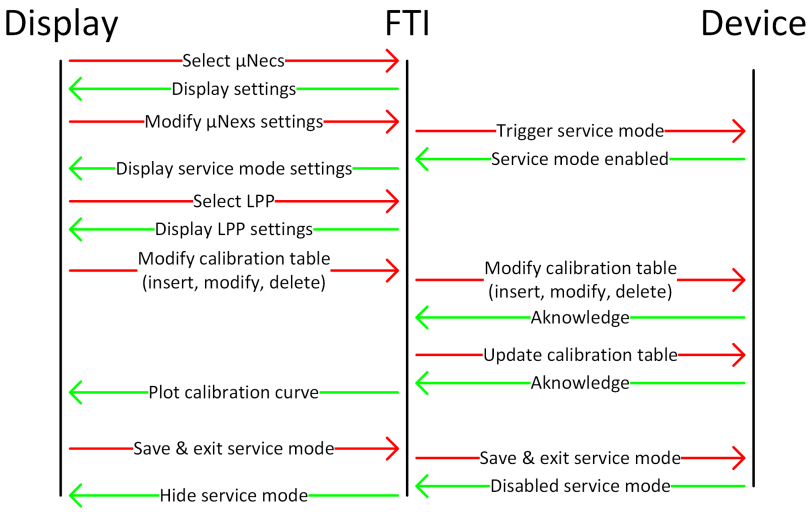

Figure 6.14: Modify the calibration table

Figure 6.15 depicts the rendered calibration curve of one Laser Position Pickup (LPP), in this case the deflection indicator of the landing flaps.

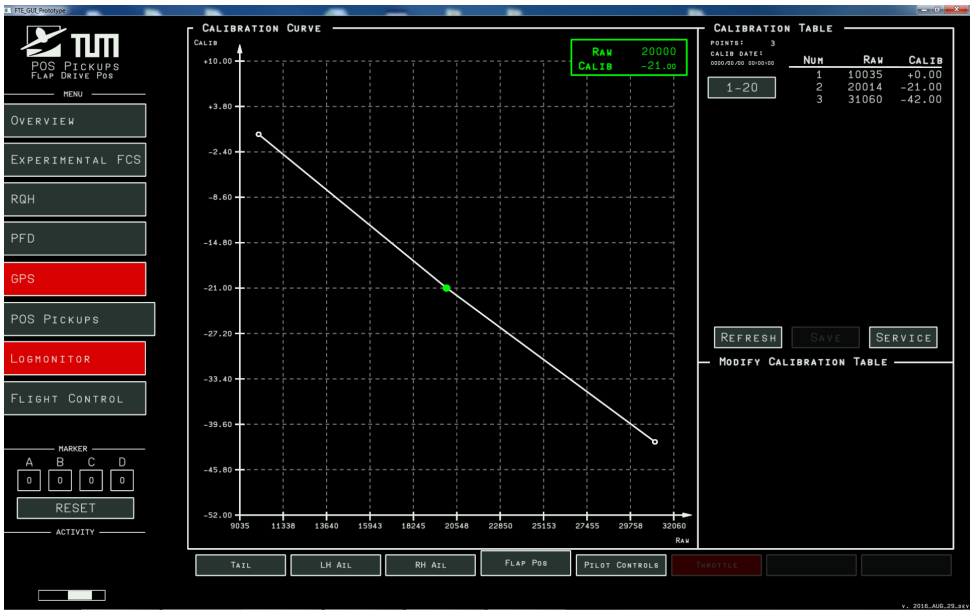

Figure 6.15: LPP calibration table

6.5 Hardware-in-the-Loop Setup

The development of such a complex system as the FTI was realized sequentially and separately for each single sensor. The integration procedure was similar for all sensors and started with a laboratory setup with the laboratory FTI. The laboratory FTI is equal to the aircraft FTI in its interface setup and software. With an established electrical interface and an implemented software protocol interface, the sensor was basically tested for its functionality. A HIL environment was required due to physical limitations of sensor testing in the laboratory and the need for sensor integration in the aircraft. The FTI HIL consists of a Total System Simulation (TSS) containing a Flight Dynamic Model (FDM), sensor simulation models and the sensor interface simulation. With this HIL environment, the FTI interface and protocol interpretation can be tested more comfortably. The processing of nominal sensor values can be tested in the HIL environment as well as extreme values near or out of the measurement range of the sensor. With this stepwise testing approach, the integration in the aircraft could be dramatically accelerated and the hard- and software development can be parallelized. Furthermore, the TSS is used for debugging purposes of flight tests, if a sensor or FTI shows an abnormal behavior. The HIL setup with the TSS and the laboratory FTI is illustrated in figure 6.16.
The architecture of HIL sensor models providing the inputs for the FTI can be divided into following three main layers:

- Electrical Layer,
- Functional Layer,
- Interface and Protocol Layer.

The aim of the electrical layer of the TSS is the interaction of the HIL with the PDU simulator, where circuit breakers control the power for each connected sensor. Specific sensors can be switched on and off with a hardware interface similar to the aircraft PDU.

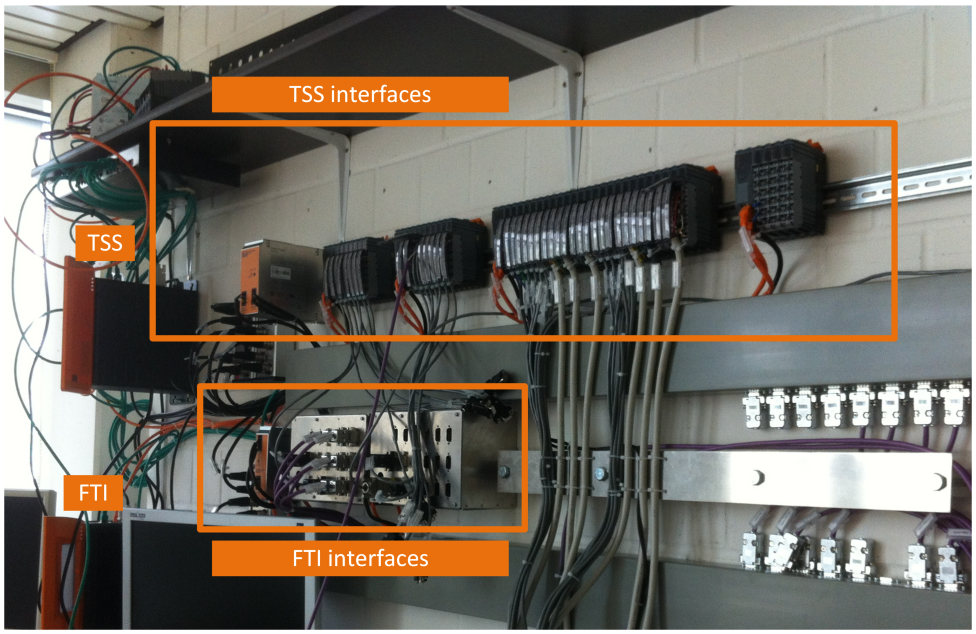

Figure 6.16: FTI and TSS in HIL environment

The specific sensor output for each sensor is calculated in the functional layer, which requires the FDM states as input. Therefore, simple generic sensor behavior models can be implemented up to highly detailed specific sensor models. As the main purpose of the facility is protocol and interface testing, generic sensor models have been implemented so far. For the further integration of a high detail sensor model, the real-time framework of the APC is designed to include a model-based functional sensor model created with MATLAB/SIMULINK. The protocol layer takes care of the conversion of the physical sensor measurements into the specific sensor transmission protocol. HIL benefits of the modular setup based on industrial components, which provide all established interface types are available. The implementation of the sensor protocol has to be identical to the real sensor for replicability and comparability. Therefore, especially the protocol headers, checksums and protocol peculiarities, like stuff bytes, have to be implemented carefully.
A special feature of the research aircraft FTI HIL is the capability of simulating asynchronous sensor measurements within a real-time system on any integer time interval. One requirement on the HIL is to simulate time shifts and time drifts for each sensor and interface and to individually test the performance of the device, not only under laboratory timing conditions. The simulation of any integer time interval is realized with a high-frequent sensor management function, which coordinates the submodules of the electrical, functional, protocol and interface layers.
The achievements introduced in this chapter are summarized in the following box:

Achievements

- Modular FTI setup with industrial automation components
- Completely independent data logging and sensor protocol interpretation
- In-flight visualization and device control
- HIL environment for development and testing purposes

Chapter 7

Flight Emulation and Simulation

The methods and algorithms introduced in the chapters 3, 4 and 5 are applied in this chapter. Laser and Radar altimeter data of a real flight campaign have been recorded to demonstrate the algorithms. Due to air traffic regulations, low-level flights could not be realized however, hence real altimeter data for SAN algorithms are not available. Since the research aircraft currently does not feature range-scanning or range-imaging sensors, the applications using these sensors are demonstrated in simulations featuring a high-detailed sensor data simulation. An overview of the three applications applied in this chapter is given in figure 7.1. The three corners of the triangle represent, as already explained in the introduction, the different aiding orders.

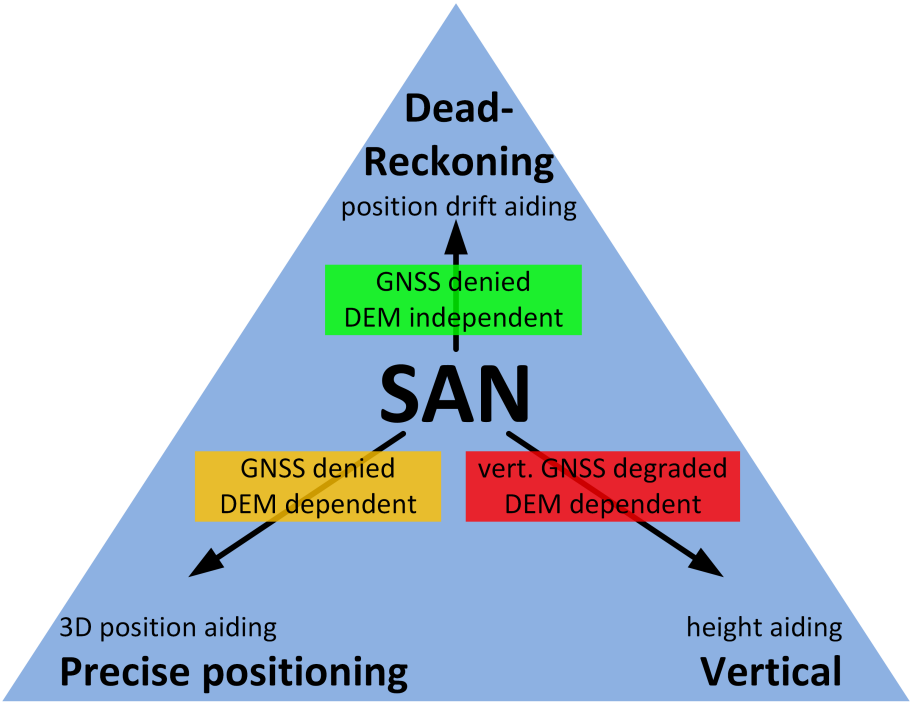

Figure 7.1: SAN Applications

The Vertical Surface Aided Navigation (VSAN) provides an absolute height information in situations with degraded vertical GNSS performance. In GNSS denied situations, the Precise Positioning Surface Aided Navigation (PPSAN) can provide an absolute three-dimensional position aiding. However, both algorithms rely on a reference DEM. In

contrast, the Dead-Reckoning Surface Aided Navigation (DRSAN) cannot provide an absolute positioning information, but a relative position drift estimation without the need of a reference DEM.
The first section of this chapter gives an introduction of the infrastructure used for the simulations. The slant range compensated height aiding is demonstrated for a general aviation airfield approach in simulation in the second section. As alternative the ground-clearance integrity monitor is shown for smaller platforms. As a second application, PPSAN applied on a simulated fighter aircraft trajectory with single and multi-beam sensors is investigated. The results are compared to traditional TAN approaches. The performance of the DRSAN concept is shown in the following section. The chapter is completed with the application of the validity assessment and the slant range compensation on recorded flight test data.

7.1 Simulation Environment

The evaluation of SAN requires the analysis of platform, sensor and environmental characteristics. The institute's research aircraft features only the existing altimeters which are integrated in the platform. This limits the available real data to the available sensor types and to only one platform dynamics profile. Especially SAN algorithms have applications in military aircraft with high dynamics. Therefore a simulation environment has been developed to simulate a wide range of surface-ranging sensors and SAN algorithms with different platforms. The simulation environment is based on Mathworks MATLAB and is divided into three layers. The input trajectory data is pre-processed to provide an analytic representation of the trajectory. The analytic trajectory representation is fed into a generic sensor data generation for several implemented sensor types. Finally, the generated sensor simulation can be applied to the SAN algorithms. In this section, the trajectory generation and the sensor data generation are discussed.

7.1.1 Trajectory Generation

The trajectory generation is designed to provide a wide interface spectrum for all kinds of simulated or recorded flight data. It is not important whether the data is available with a defined frequency or with a specified accuracy. Apart from a time stamp, the trajectory generation only requires a position and an attitude input. The outcome of the trajectory generation tool is an analytic representation of the trajectory for the later calculation of highly consistent inertial measurement data.
The trajectory is represented by splines fitted to the input position coordinates and attitude angles. The tool contains an additional filtering option to eliminate quantization errors in the input data. This option is not mandatory, but can be helpful when dealing with recorded data with insufficient data type resolution. For example, the accuracy of the geodetic position in radians stored in a float variable with single precision can lead to quantization errors.
The quantization error of the longitudinal position (in radians) at the equator is given by equation 7.1 assuming a single precision data type with the quantization $q_{single} = 0.0000001$.

$$\begin{aligned} q_\lambda &= q_{single} \cdot N(\phi) \\ &= 0.64\,\mathrm{m} \end{aligned} \tag{7.1}$$

Single precision variables with a resolution of $q_\lambda = 0.64\,\mathrm{m}$ are not sufficient for a high precision simulation and have to be avoided. The filtering of the input data to suppress the quantization effects is a trade-off between closeness to the input data and smoothness. For the spline fitting approach, quintic splines for position coordinates and attitude angles have been chosen. The quintic splines feature the opportunity of an analytic differentiation of the acceleration measurement with a continuously differentiable behavior. An example showing the position and attitude of a departure trajectory as spline representation and the raw input data is given in figure 7.2.

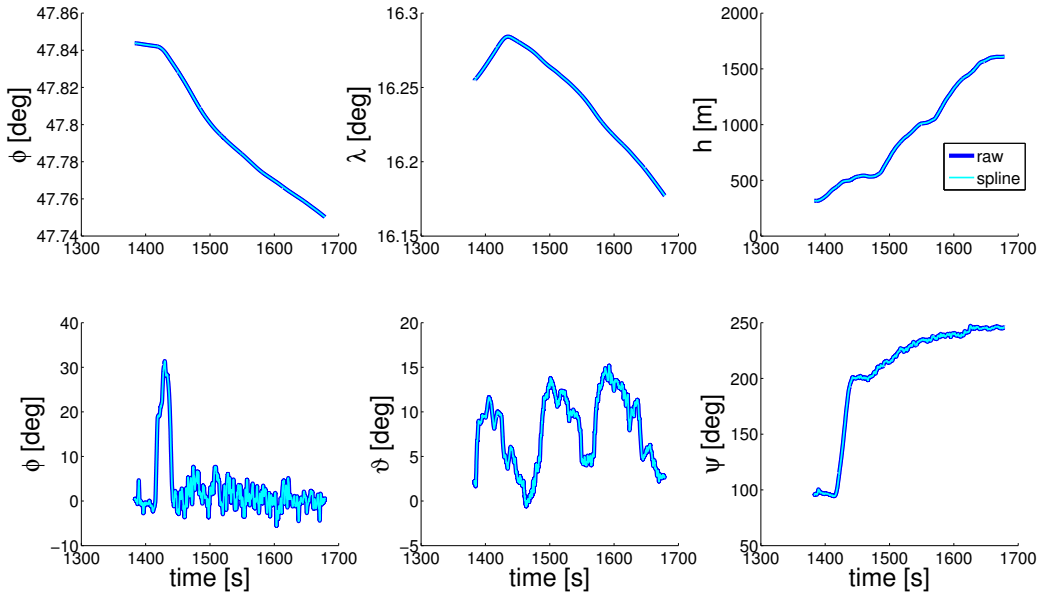

Figure 7.2: Spline fitting of trajectory

The plot shows a good match between the input data and the spline approximation. For a detailed performance analysis, the absolute differences between input data and the spline representation are considered. The result in figure 7.3 is split in two components, the red plot indicates the errors of the filtered signal with respect to the input data. The cyan plot indicates the errors of the spline signal with respect to the filtered signal.

The deviations caused by the filtering can be led back to the quantization errors of the input data and are welcome to provide a smooth input signal in prior to the spline fitting. The error values are within a few decimeters in position and about two-hundredth of a degree for the attitude angles.

The spline fitting errors of the position are within several millimeters, while the attitude spline fitting errors are about a factor two smaller than the attitude filtering errors. Summarized, the deviations from the input data are within a quite tolerable range and acceptable in order to generate highly consistent data for this high precision simulation.

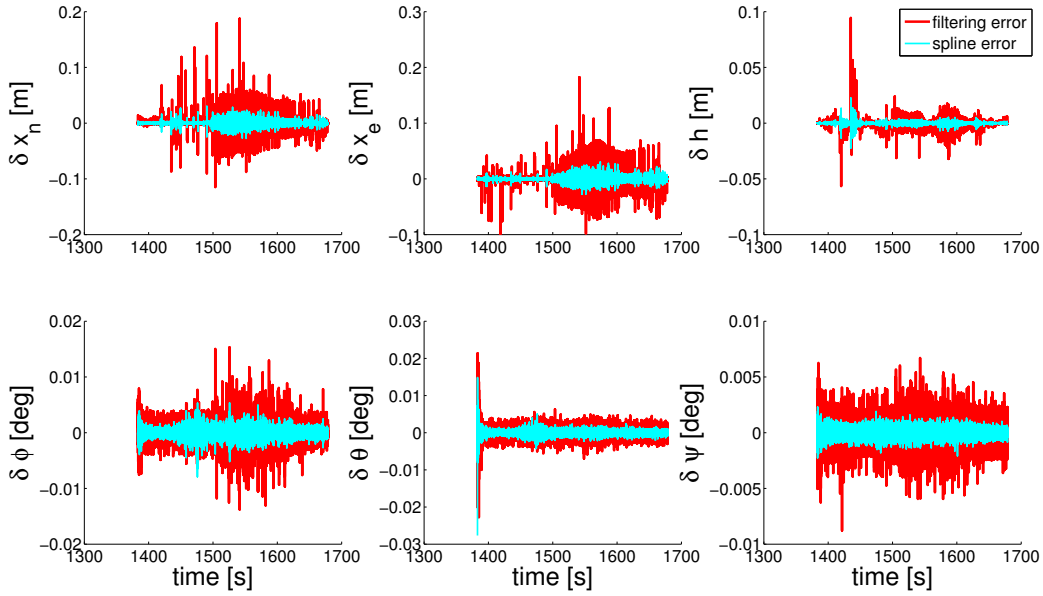

Figure 7.3: Spline fitting errors

7.1.2 Sensor Data Generation and Validation

The output created by the trajectory generation tool is stored in a generic spline file. The advantage of processing an analytic trajectory spline is not only the continuous differentiability, but also the continuous availability of position and attitude without any sample time restrictions. The sensor data generation tool offers the possibility to simulation the following sensors type:

- Inertial Measurement Units
- GNSS Receivers
- Altimeters (Radar and Laser)
- Range-scanning sensors (f.i. Laser scanners)
- Range-imaging sensors (f.i. ToF cameras)
- Barometers
- Magnetometers

The focus of the following example is on the generation of IMU measurements. The simulation models for altimeters, range-scanning and range-imaging sensors have been discussed in chapter 2.
The specific force $\mathbf{f}_b$ can be obtained by resolving the velocity navigation frame differential equation, the derivation is given by equation 7.2. The angular rate $\boldsymbol{\omega}_{nb}$ is superposed by the transportation rate $\boldsymbol{\omega}_{en}$ and the Earth rotation rate $\boldsymbol{\omega}_{ie}$ to obtain the inertial angular rate measurement by equation 7.3.

$$\begin{aligned} \dot{\mathbf{v}}_n &= \mathbf{R}_{nb}\mathbf{f}_b + \boldsymbol{\gamma}_n - (2\mathbf{R}_{ne}\boldsymbol{\omega}_{ie} + \boldsymbol{\omega}_{en}) \times \mathbf{v}_n \\ \mathbf{f}_b &= \mathbf{R}_{bn}\left(\dot{\mathbf{v}}_n + (2\mathbf{R}_{ne}\boldsymbol{\omega}_{ie} + \boldsymbol{\omega}_{en}) \times \mathbf{v}_n - \boldsymbol{\gamma}_n\right) \end{aligned} \tag{7.2}$$

$$\boldsymbol{\omega}_{ib} = \mathbf{R}_{bn}\left(\mathbf{R}_{ne}\boldsymbol{\omega}_{ie} + \boldsymbol{\omega}_{en}\right) + \boldsymbol{\omega}_{nb} \tag{7.3}$$

This approach enables the calculation of highly consistent inertial sensor measurements with a freely selectable frequency. The trajectory and sensor data generation tool chain is verified by a numerical integration of the derived inertial measurements. The continuously available inertial measurements are sampled at a common frequency for inertial measurement, in this example $f_s = 100\,\mathrm{Hz}$. The sampled measurements are integrated to velocity, attitude and position with the SDA, and finally compared to the input trajectory.

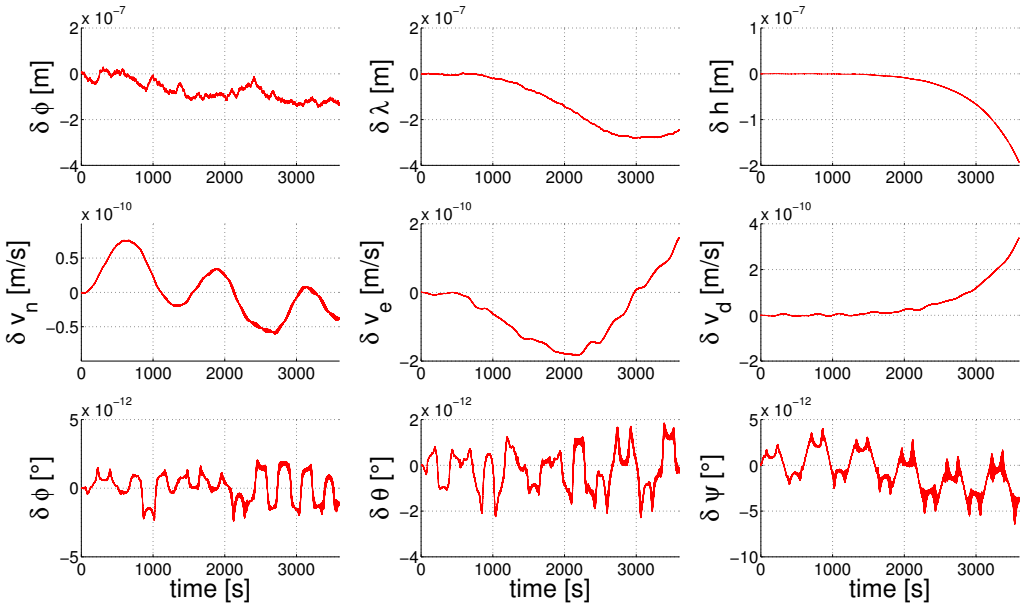

Figure 7.4: Sensor data integration error

The errors in position, velocity and attitude of the simulated one hour trajectory are given in figure 7.4. The position integration error does not exceed $\delta\mathbf{x}_n < 1\,\mu\mathrm{m}$. Due to the central gravity field of the Earth, the height channel shows an instable behavior. The velocity error do not exceed $\delta\mathbf{n}_n < 1\,\mathrm{nm\,s^{-1}}$ and the attitude errors do not exceed $\delta\boldsymbol{\psi} < 5\,\mathrm{pdeg}$. These errors result from the discrete measurement sampling and the numerical strapdown integration and are totally tolerable for the error free, inertial-only integration.

7.2 Simulation Study - Vertical SAN

The methods discussed in chapter 3 are now applied in an approach scenario with a general aviation aircraft. This section considers two different approach applications. First, a slant range compensated height aiding of an INS is demonstrated. The scenario and the simulation results are introduced in the first subsection.
The second example considers an Unmanned Aerial Vehicle (UAV) or small aircraft without the capability of an in-flight slant-range compensation in an approach situation. Therefore, an alternative method with a-priori processed altimeter measurement expectations is discussed. The application description is given in the following box:

Application Description

- Height aiding for approach guidance
- In-flight slant range compensation
- Ground-clearance integrity monitor for small platforms.

7.2.1 Compensated Height Aiding

Airfields used for general aviation aircraft are often significantly smaller than international commercial airports. On these airfields, ground-based navigation aiding systems like ILS or GBAS are not offered. The airfields are limited to a small area around the runway and hence do not feature a RAOA. The exemplary airfield discussed in this section is located in Vilshofen (identification EDMV), it lies in the Danube river valley surrounded by a hilly environment.

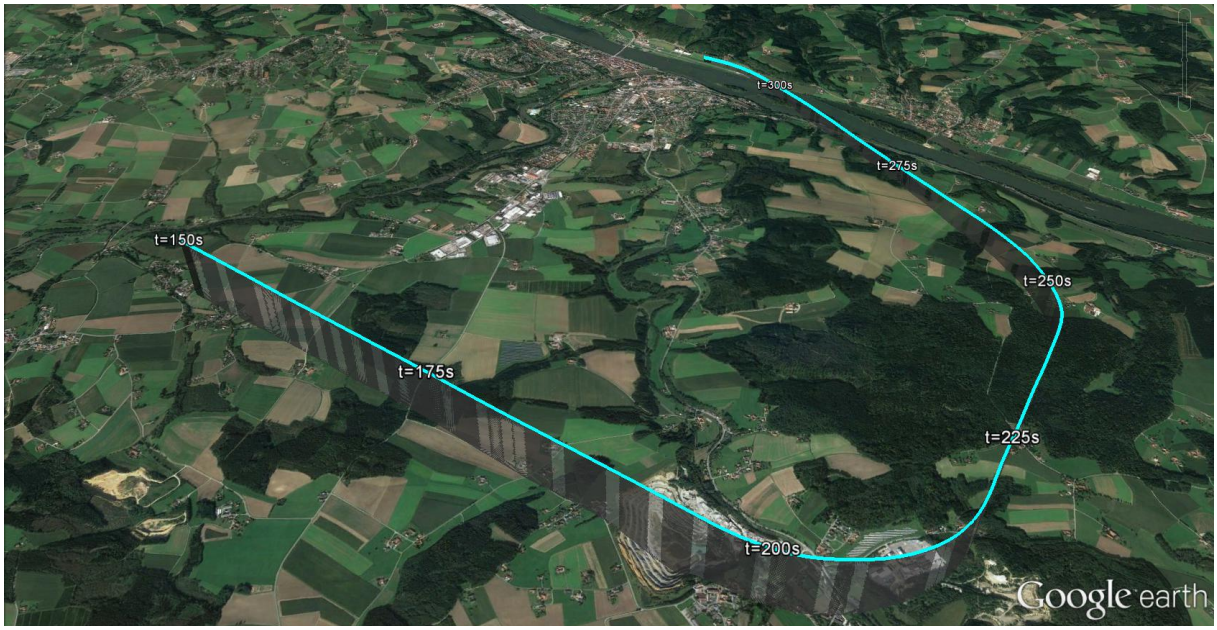

Figure 7.5: Google Earth visualization of the EDMV approach trajectory

An additional peculiarity of this airport is the traffic pattern path, which does not allow a direct approach into the centerline direction. Due to the shape of the river and the mountains on both sides, a direct approach is not possible. As alternative, an approach with

an angular offset is mandatory. The simulated trajectory in the described surrounding is depicted in figure 7.5.
The trajectory starts with the downwind sector at a constant height. The final sector is approximately 30 degrees tilted to the runway center line axis, the heading is compensated near to the runway threshold. This pattern provides rough surface variations, including vegetation, forests, hilly surface and the river valley. The simulation of the approach is started in the mid downwind sector at $t_0 = 150\,\mathrm{s}$ and covers the complete approach. The vertical profile including the overflown surface is given in the upper plot of figure 7.6. The simulated height above ground measurement of the Radar is depicted in the middle plot of the figure together with the nadir height above ground. The lower plot illustrates the simulated measurement errors with respect to the nadir height above ground.

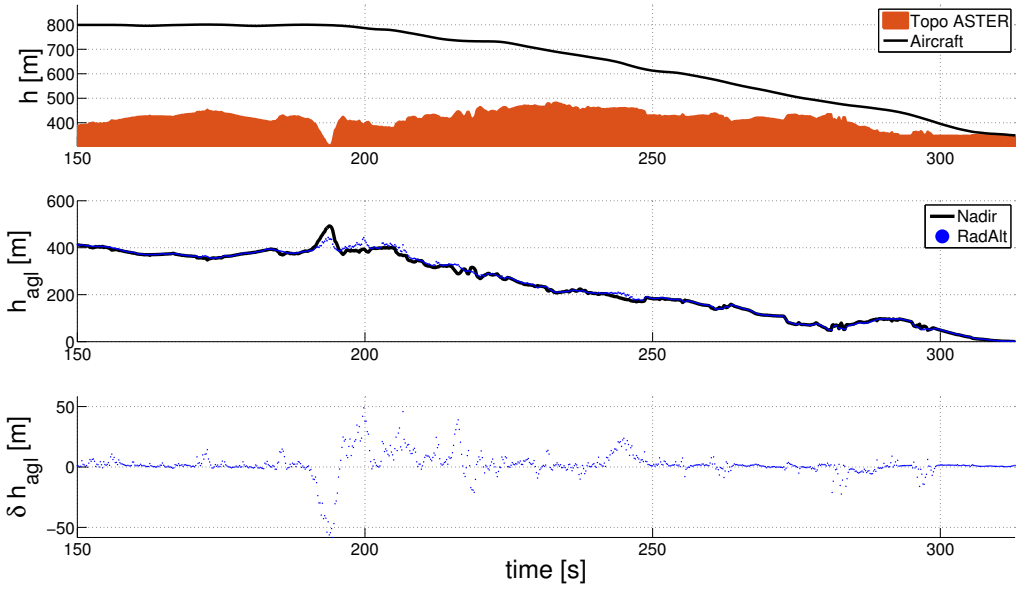

Figure 7.6: Radar altimeter raw measurement

The RMS error of the simulated Radar altimeter measurements is calculated to $\delta h_{rms} = 10.3\,\mathrm{m}$. Applying the slant range compensation algorithm to the measurements reduce the error to $\delta h_{rms} = 0.97\,\mathrm{m}$. The results are illustrated in figure 7.7.
Finally, a INS/GNSS integrated navigation solution is compared to a raw Radar altimeter aiding and to a compensated altimeter aiding. The height channel of the three methods are depicted in figure 7.8.
As expected, the covariance of the height channel of the INS/GNSS is constant. While this method is recommendable for trajectories which can guarantee a good GNSS constellation and a large ground-clearance, it cannot be used for real-world landing applications.
The direct aiding with the Radar altimeter reduces the height variance. The errors of the raw altimeter measurements however are to large to provide a height accuracy ensuring a save guidance for small ground-clearances.
The application of the compensated measurement reduces the covariance and coincidentally increases the accuracy of the height channel, especially with decreasing ground distance. The results are summarized in the following box:

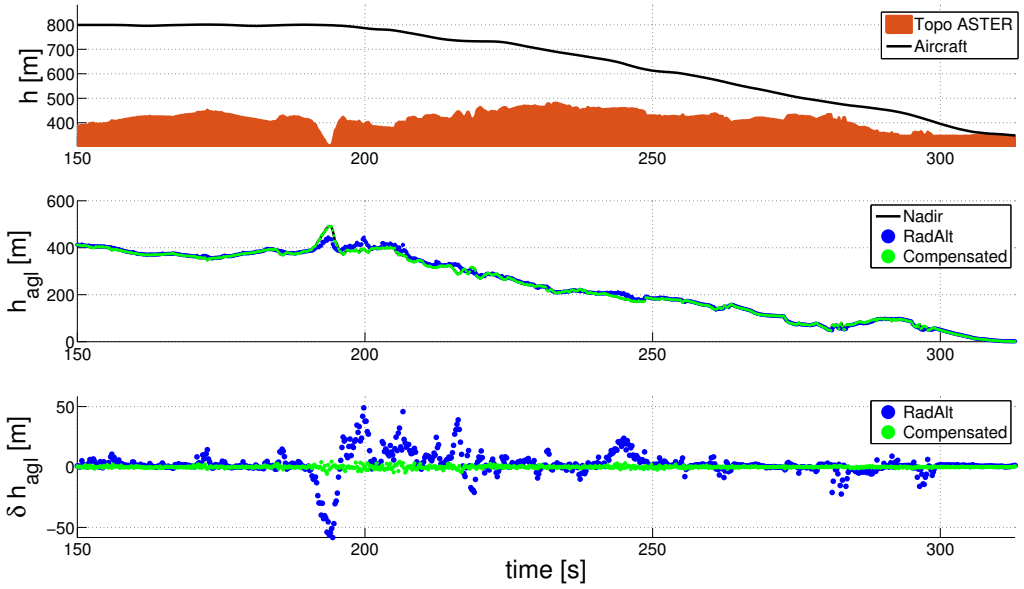

Figure 7.7: Radar altimeter slant range compensation

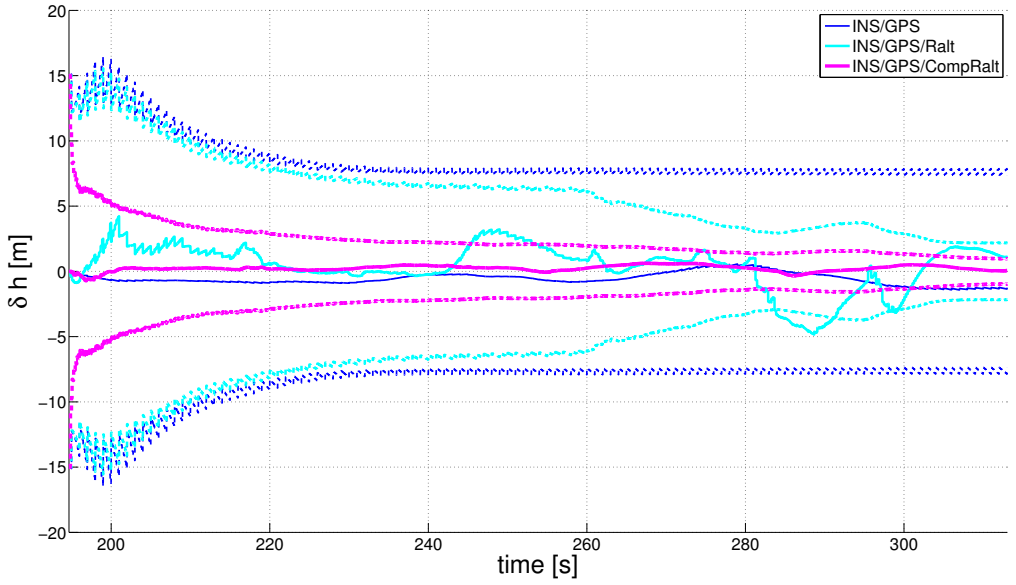

Figure 7.8: Integrated altimeter height aiding comparison

Results

- GNSS only aiding is not suitable for approach guidance
- GNSS + Radar (raw) cannot provide the required height accuracy
- GNSS + Radar (compensated) increases the height accuracy and reduces the covariance

7.2.2 Ground-Clearance Integrity Monitoring

Processing a DEM and the slant range compensation algorithm in-flight requires a powerful computer. While this requirement is fulfilled for military and commercial aircraft, the computational power may not be available on-board of smaller platforms. An altime-

ter application as ground-clearance integrity monitoring without the need for complex in-flight calculations is introduced in the sequel. The method is based on pre-processed altimeter measurement expectation values along a common flight path profile. The live measurements are compared to the expected altimeter measurements and are checked for accordance to ensure a correct measurement behavior, as long as the preplanned expectations are met.
For this approach, either the introduced Radar simulation model is used to process the synthetic altimeter measurements of a standard approach pattern of a specific airfield or representative altimeter measurements are recorded directly. The pre-processed, synthetic height expectation is provided digitally a-priori for storage in the platforms.
This step has to be iterated whenever the airfield surrounding (vegetations, buildings, etc.) or the approach path itself changes. Therefore, a current DSM has to be created, representative altimeter measurements have to be recorded or the altimeter measurement recording flight has to be repeated.
Whenever the platform is on the defined path, for example guided by GNSS way-points, the synthetic altimeter measurement can be compared to the live altimeter measurements. While the height above ground measurement contains the discussed errors, the comparison of two altimeter measurements is advantageous. A generic example of this application is illustrated in figure 7.9.

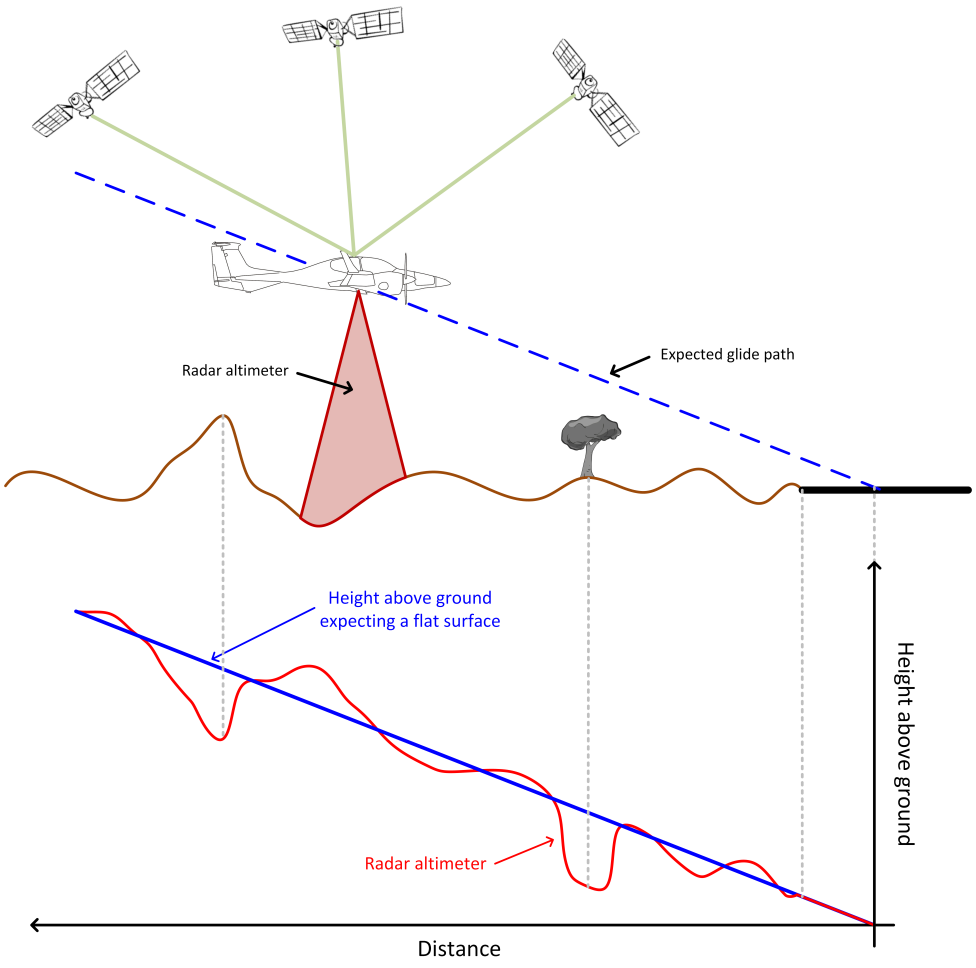

Figure 7.9: Ground-clearance integrity monitor concept

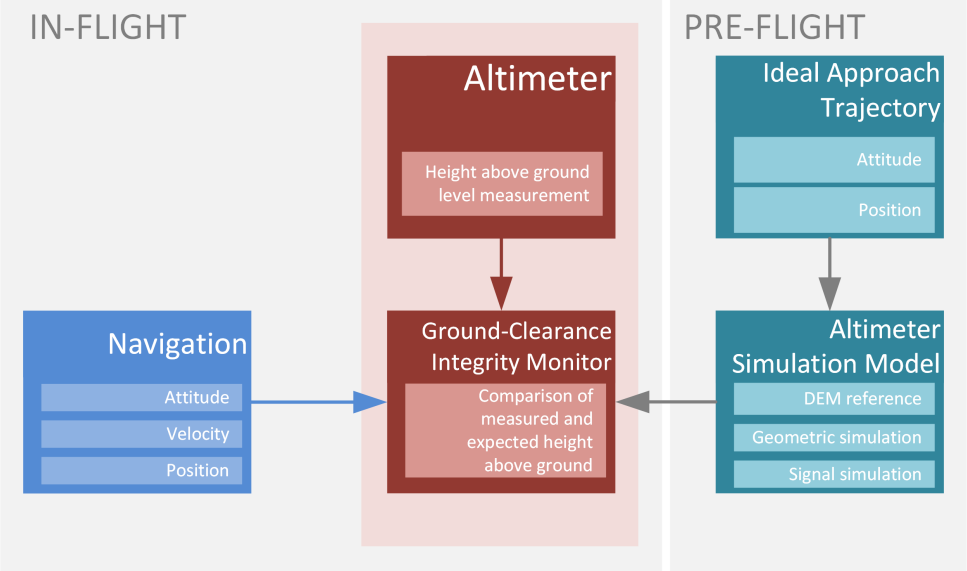

Figure 7.10: Ground-clearance monitoring - architecture

The upper sketch shows the approach situation above varying and vegetated surface. The lower sketch gives the altimeter measurement (red) and the expected measurement assuming a flat surface. Comparing the altimeter measurement with the expected linear progress of the height above ground due to the aircraft sink rate, will result in huge differences of the both signals. The difference of both signals can provide an integrity information concerning the glide slope, which will be more robust compared to the use of the height above ground in combination with the airfield height. A block diagram of the navigation architecture with the preflight processing of the expected altimeter measurements and the in-flight integrity check is given in figure 7.10. The computational burden of the in-flight calculation is comparably small and the method is therefore suitable also for small aircraft or UAVs.
The integrity of the glide path can be calculated by evaluating the history of altimeter measurements, as it is done in the SAN approach. In contrast to comparing the measurements to a DEM, the a-priori processed Radar altimeter expectations are used, including all the specific surface features below the glide path. Those features are used to identify the correct horizontal position.
As integrity feature, different criteria obtained from a reduced, two-dimensional comparison algorithms can be used. The comparison metric used for the integrity determination is similar to the metrics used for SAN (see section 4). It requires the distance to the airfield as argument instead of the horizontal position coordinates. The matching metric and the height offset calculation thereby simplifies to equation 7.4 with the reference altimeter measurements denoted by $h_{agl,ref}$, the matching result vector M_i and the distance to the runway touchdown point d_{rwy}.

$$\begin{aligned} \Delta\bar{h}_i &= \frac{1}{K}\sum_{k=1}^{K}\left(\tilde{h}_k - \tilde{h}_{agl,k} - h_{agl,ref}\left(d_{rwy}\right)\right) \\ M_i &= \frac{1}{K}\sum_{k=1}^{K}\left|\tilde{h}_k - \tilde{h}_{agl,k} - h_{agl,ref}\left(d_{rwy}\right) - \Delta\bar{h}_i\right| \end{aligned} \tag{7.4}$$

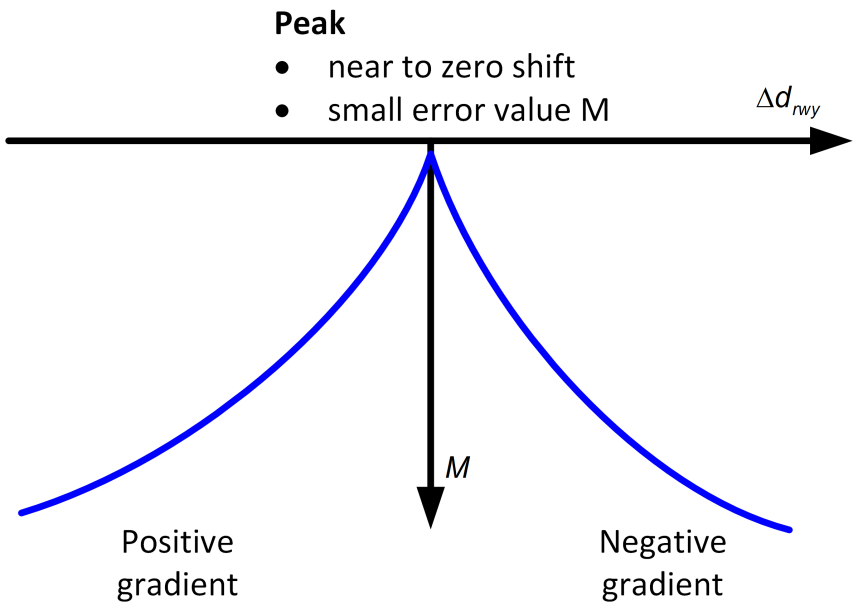

Figure 7.11: Integrity matching criteria

The glide path integrity can be indicated by the characteristics of the matching output. There are several criteria which define a robust and accurate matching function if the true position fits the expected position, they are summed up in the following list:

1. The peak value of the matching function is small, approximately in the quality of the sensor errors.
2. The peak of the matching function is near to the zero matching algorithm shift.
3. The gradient on the left side of the peak is positive.
4. The gradient on the right side of the peak is negative.

An illustration of a matching function fulfilling all the criteria for a positive integrity is given in figure 7.11. The requirement 1 on the matching result ensures that the minimum matching result provides a good absolute match quality which is important for the integrity monitoring. Relative matches, often caused by local surface similarities, can be avoided with this requirement. Requirement 2 ensures a small drift of the distance to the runways touchdown point and thereby confirms the estimated position solution. The demands on the gradients 3 and 4 on both sides of the peak ensure a sharp and unambiguous peak.
The application of the integrity monitor is demonstrated on two examples. The first example in figure 7.12 shows an approach trajectory over a rough surface. The absolute height, the height above ground h_{agl} and the integrity error value are plotted over the distance to the runway touchdown point d_{rwy}. The upper plot shows the ideal and true three degree approach on the runway with exact match. This visualization only provides the height in dependence of the runway distance d_{rwy}, the aim of the integrity algorithm is to ensure that the expected topographic surface below the approach path is actually measured.

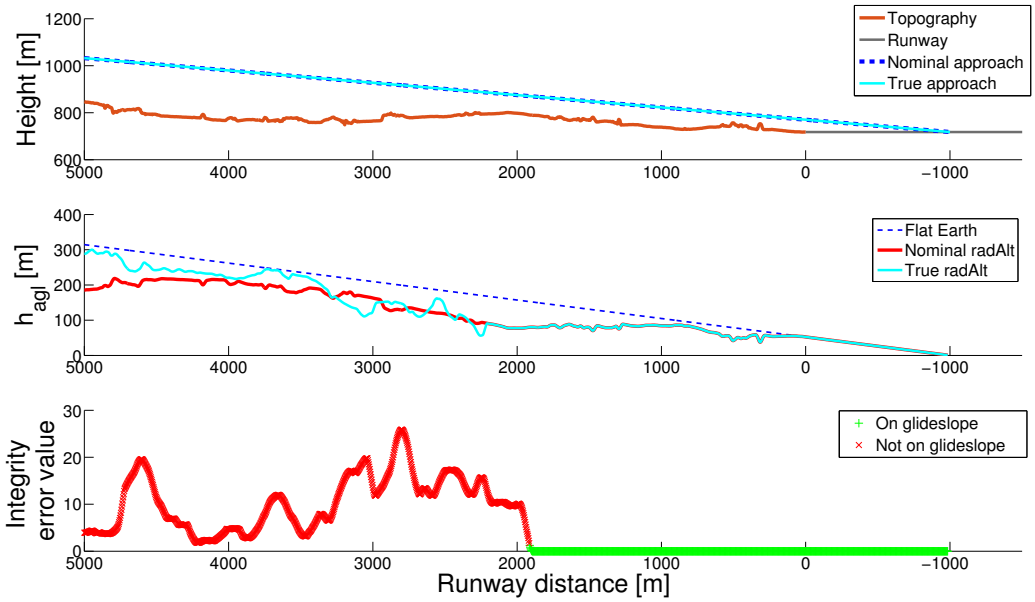

Figure 7.12: Approach integrity signal with mismatch indication

However, the height and the distance to the runway in the upper plot shows a perfect match, the pilot is flying another approach path on the runway as the standardized approach pattern. This information is obtained by the height above ground measurements, where the ideal and true measurement deviate until a distance of $d_{rwy} \approx 2200\,\mathrm{m}$. At this distance, the aircraft is back on the standard approach pattern and the reference altimeter measurement fits the actual measurement. The lower plot shows the corresponding integrity error value and a colored integrity assessment. While the integrity error indicates the deviations in the height above ground above unknown topographic surface, the integrity error value decrease when flying back on the assumed track. The integrity value provides a low-pass behavior due to its dependency on the measurement history. The algorithm requires a sufficient number of correct matches before showing a good integrity result, which is not only an algorithmic dependency, but also a robust behavior which can eliminate outages. To show the performance of the algorithm without a deviation of the approach track, the second example is given in figure 7.13. The trajectory provides a flight path above the expected surface. The good match leads to a perfect integrity error value and hence to a perfect integrity assessment.
An additional information can be obtained by this algorithm in form of a glide slope deviation, which is similar to the signal provided by ILS. This deviation signal is calculated as the ratio between expected and measured altimeter height in dependence of the distance to the runway landing threshold, the equation is given in 7.5.

$$\delta\gamma = \tan^{-1}\left(\frac{h_{agl} - h_{agl,ref}}{d}\right) \tag{7.5}$$

An example showing the relation between a deviation of the glide path, the measured height above ground and the glide slope deviation signal, is illustrated in figure 7.14.
The upper plot shows the absolute height with the ideal glide path, the true glide path, the topographic height and the runway. The height above ground over a flat earth is given in the middle plot as well as the expected Radar altimeter measurement and the true Radar

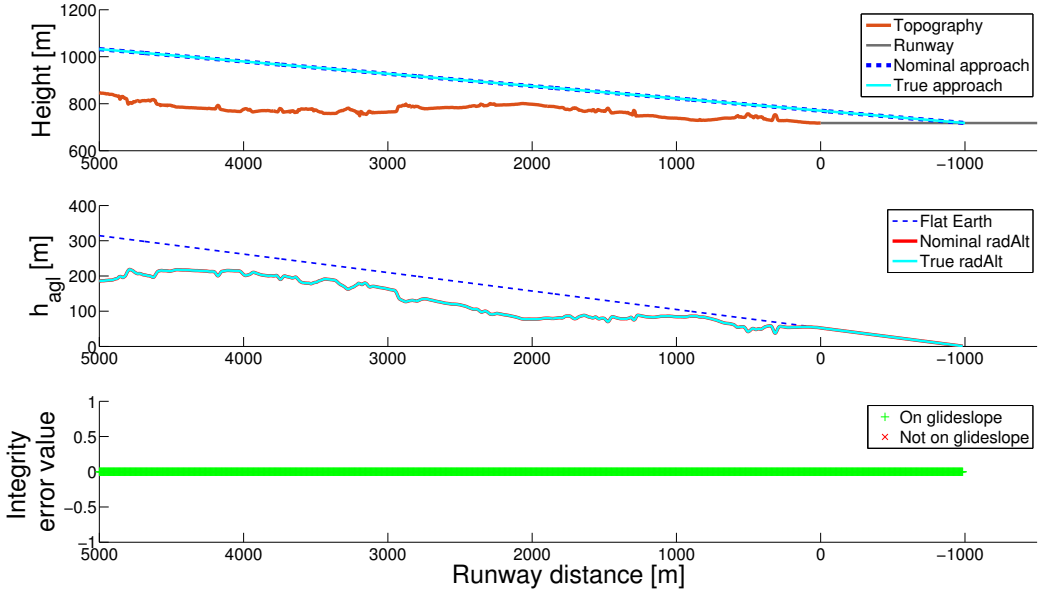

Figure 7.13: Approach integrity signal with positive indication

altimeter measurement. The expected radar altimeter measurements are obtained with an a-priori processed synthetic estimation of the height above ground, assuming an ideal glide path. For this demonstration, the true measurements are forced to deviate from the expected measurements to show the performance of the glide slope indication in the lower subplot.

Comparable to an ILS receiver, the dashed line indicates a one degree height deviation from the glide path relative to the runway distance. This depiction has been chosen due to its similarity to the ILS glide slope indication. Especially for a landing application, a relative error indication depending on the distance to the threshold is beneficial.

This method can be used as an alternative approach guidance if a standardized approach pattern and the corresponding altimeter reference measurements are available. The performance of this method in combination with the integrity monitor is in the following demonstrated by two examples. First, the integrity indication and glide slope deviation is simulated for a nominal trajectory. The approach result is given in figure 7.15.

The integrity monitor acknowledge the altimeter measurements for the entire trajectory, after a short transient at the beginning of the simulation due to the measurement history dependency. The deviations of the standard approach glide slope are indicated in the lower plot, with increasing deviations towards the runway threshold. These deviations are caused by an in-precise true flight path height and the relative formulation of the deviations with respect to the runway distance.

The same simulation is repeated to show the integrity indication for the occurrence of an unexpected obstacle beneath the approach path. The results are depicted in figure 7.16. At d_{rwy} =3000 m an obstacle with a height of about $h_{obstacle}$ =150 m is measured from the altimeter, while the expected altimeter measurement does not include this object. The integrity monitor instantaneously indicates the mismatch and the monitoring will first be available again, when the false measurements are eliminated in the measurement history. This example demonstrates the performance of the algorithm with unknown obstacles very well. In this special case, a novel reference measurement of the approach path or the

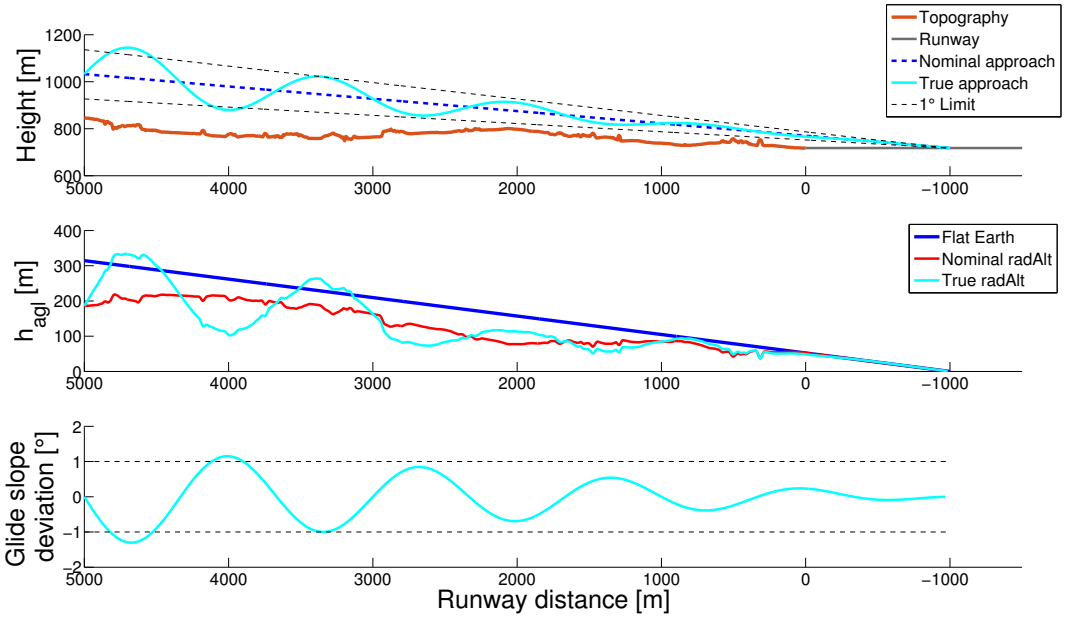

Figure 7.14: Glide slope signal

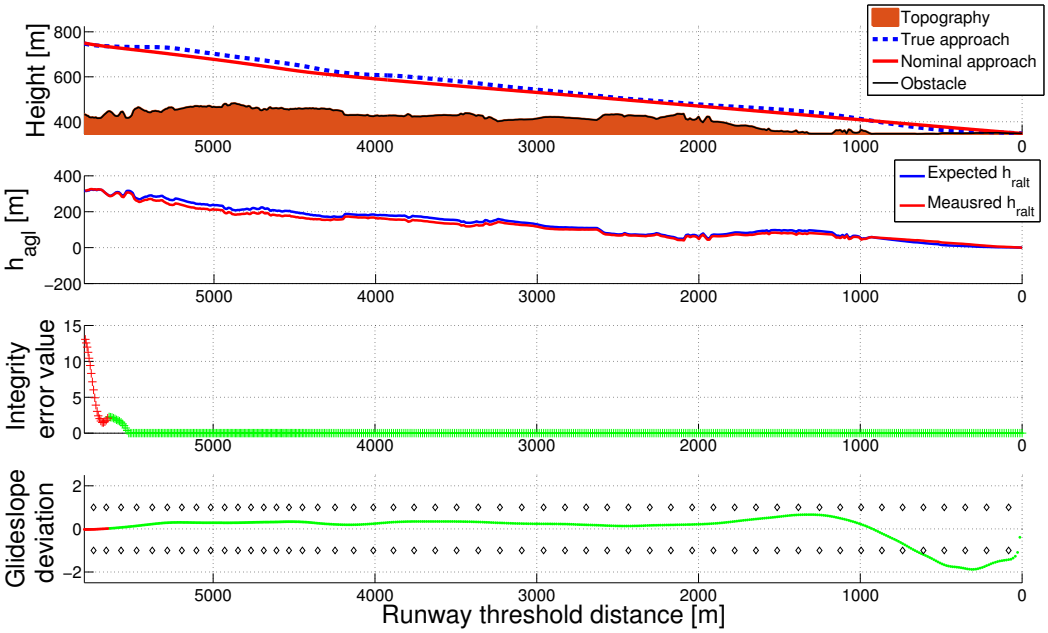

Figure 7.15: Ground-clearance monitoring with glide-slope indication

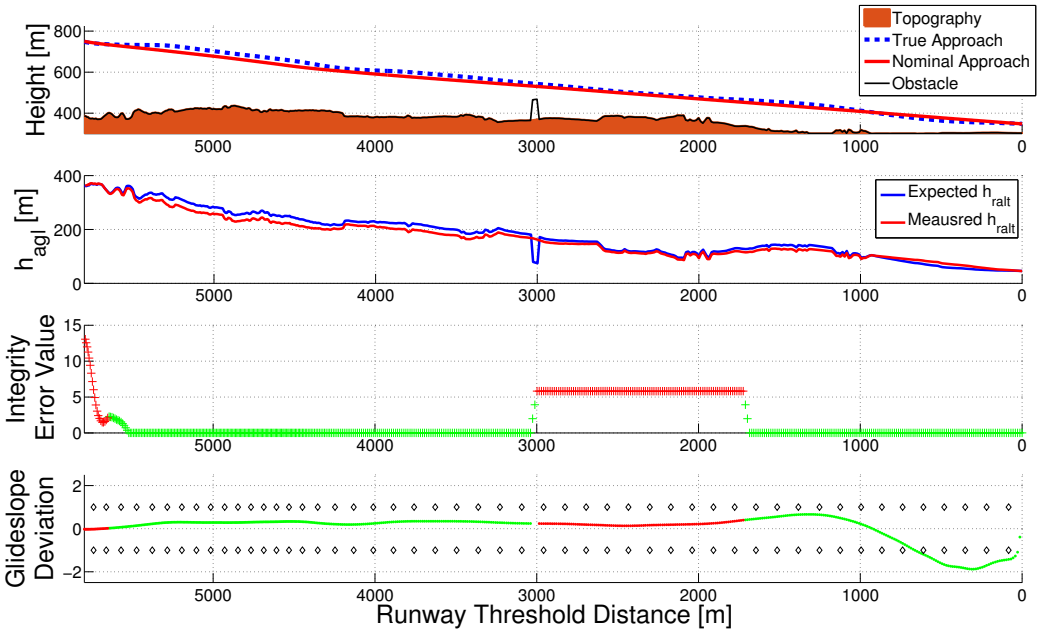

Figure 7.16: Ground-clearance monitoring with unexpected obstacle

removal of the obstacle is mandatory.
The results of this chapter including the vertical aiding of an INS and the ground-clearance monitoring is summarized in the following box:

Results

- Ground-clearance monitor for platforms with weak computational power
- Enabling the reliable usage of altimeter measurements above rough surface on a standardized trajectory
- Glide slope deviation as additional information

7.3 Simulation Study - Precise Positioning SAN

The performance of modern SAN methods introduced in chapter 4 is compared to classical TAN approaches in this section. The modern SAN methods are applied to a fighter aircraft-like, highly dynamic trajectory with small ground-clearance. This trajectory profile is the most representative for SAN applications due to the complementary characteristics of the two aiding system GNSS and SAN. While GNSS performs well and cannot be jammed or spoofed easily in situations with sufficient height above ground, a low-level flight is a challenge due the high probability of satellite line-of-sight loss caused by terrain shadowing or the high roll dynamics. Additionally, the risk of jamming and spoofing increases with a low-level flight. In this application, SAN can be used as aiding alternative. Obviously, SAN depends on a surface-ranging information and is only applicable to terrain-following trajectories.

Application Description

- Position aiding during temporal GNSS degradations
- Position aiding during temporal GNSS outages
- Long-term position aiding during GNSS outages

Apart from a low ground clearance, the trajectory selected for the performance demonstration features high roll dynamics and a high along track velocity. The trajectory starts with a take-off in East direction followed by a bank-to-turn maneuver into North-West direction. The flight path ends with a valley flight heading North-East. The surface below the flight path can be described as hilly and rough in the mountainous area and moderate in the valley. The surface roughness in the valleys can be described as moderate. The complete trajectory is visualized in a Google Earth environment in figure 7.17.

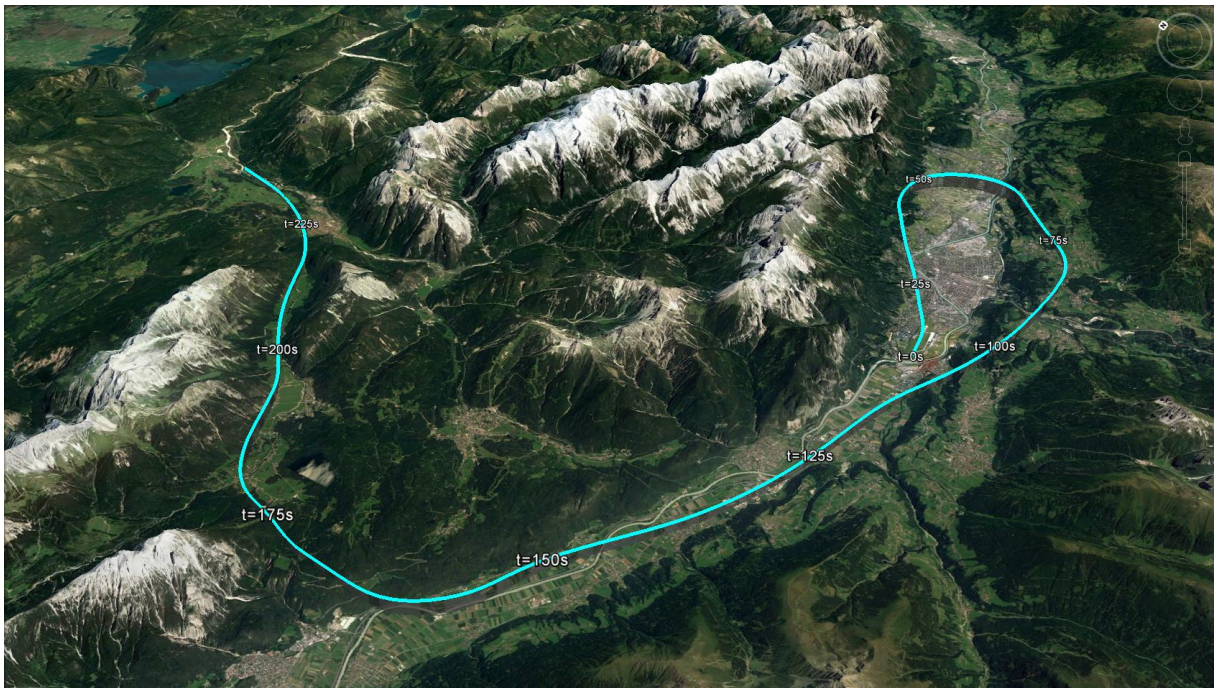

Figure 7.17: High dynamic trajectory above rough surface

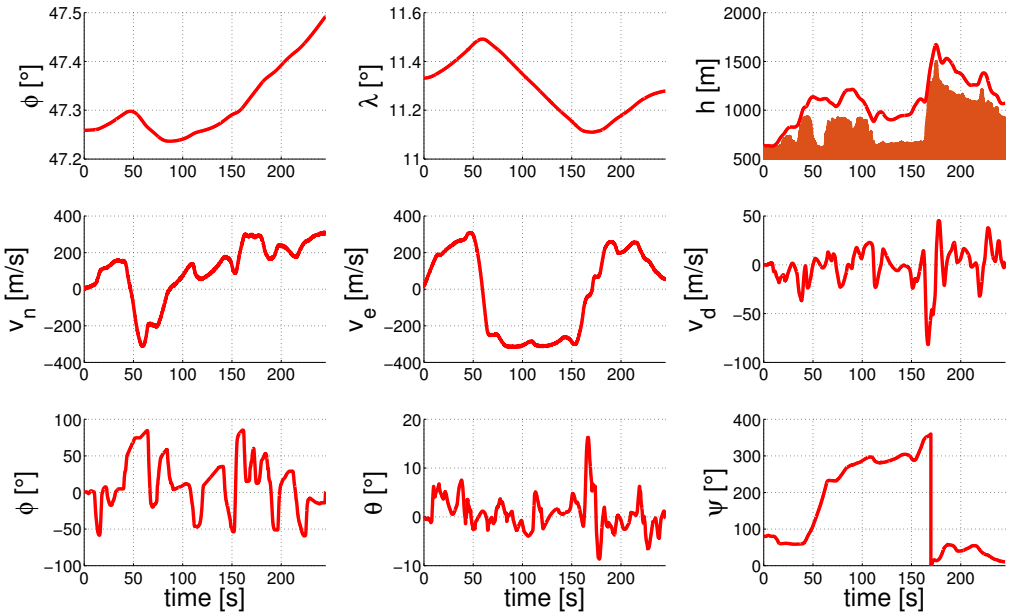

Figure 7.18: Reference navigation states

The trajectory is flown with ground clearances between $100\,\mathrm{m} < h_{agl} < 500\,\mathrm{m}$, the along track velocity is near to the speed of sound. The maximum simulated roll angle is about $\phi \approx 90°$. The absolute aircraft position, velocity and attitude states are given in figure 7.18.
For the simulation, a tactical grade navigation system is simulated as basic system using loosely coupled GNSS aiding information. Even though a tightly coupled system is beneficial in this scenario, this thesis aims to highlight the benefits of modern SAN. These benefits can be shown equally with a loosely coupled system. The estimation of IMU biases is also not discussed in this section in order to highlight the pros and cons of the SAN system.

7.3.1 Measurement

For the single beam SAN, a Radar altimeter with a narrow beam-width is applied. The considerations of the beam width and their effects on the measurements have been discussed in section 2.3. The antenna characteristics are given in figure 7.19. The antenna provides a maximum gain of $G = 10\,\mathrm{dBi}$ at the beam center, while the HPBW is reached for the symmetric antenna for $az = el = 15°$. In military application, narrow shaped altimeter antennas are common due to a decreased detectability. The Radar altimeter simulation parameters which are used for the simulation are given in table 7.1.
With this settings, the altimeter measurements have been created along the entire trajectory with their detailed error characteristics. The vertical situation of the trajectory is illustrated in figure 7.20.
The upper plot shows the absolute height with the surface height including several mountain tops and valleys. The second plot gives the height above ground measurement and the nadir height for comparison reasons. Especially in the two flight phases beginning at $t_1 = 50\,\mathrm{s}$ and $t_2 = 150\,\mathrm{s}$, the altimeter measurement differs from the nadir height. This difference is plotted as height above ground error δh_{agl} in detail in the third row. The last

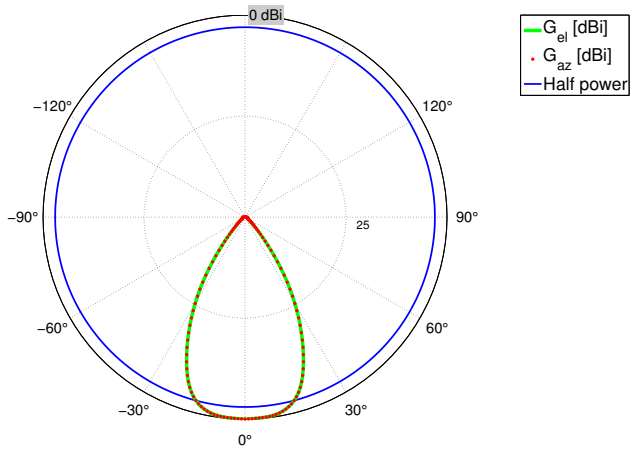

Figure 7.19: Narrow beam characteristics

Parameter	**Value**
DEM source	NEXTMAP DSM
DEM resolution	$\Delta x_n \times \Delta x_e = 5\,\mathrm{m} \times 5\,\mathrm{m}$
DEM vertical accuracy	$\delta h_{topo} < 1.5\,\mathrm{m}$
Number of rays	$N_{ray} = 2000$
Center frequency	$f_c = 4.3\,\mathrm{GHz}$
Update frequency	$f_s = 10\,\mathrm{Hz}$

Table 7.1: Altimeter simulation model settings

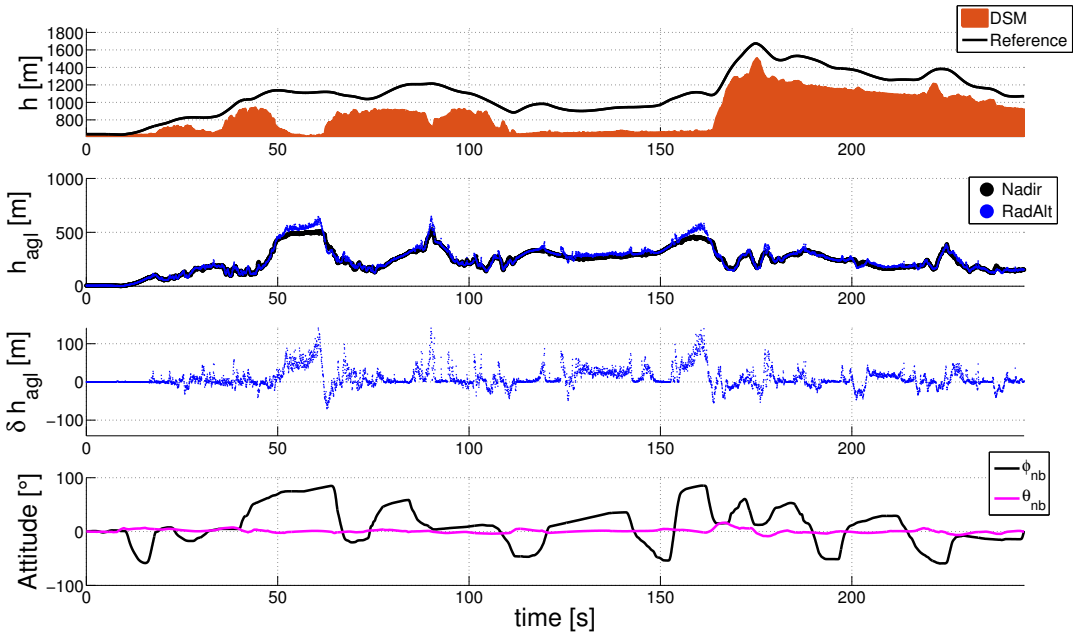

Figure 7.20: Vertical situation and measurement

row offers the platform roll ϕ_{nb} and pitch θ_{nb} attitude angles for a better identification of the flight situations. Obviously, the platform attitude influences the altimeter measure-

ment enormously, as already discussed in section 2.3. While the high platform attitude angle at $t = 12\,\mathrm{s}$ has minor influence on the measurement due to the small height above ground, the errors at t_1 and t_2 can be explained by the large roll angle of the platform in these situations.

7.3.2 Conditioning

Table 7.2 gives an overview of the four different SAN approaches with increasing complexity which are used in the sequel. The first system processes the altimeter measurement directly in the grid-search comparison algorithm with the information exploitation and position drift consideration algorithm as introduced in chapter 4. The second SAN approach adds the validity assessment to remove invalid measurements before processing the comparison algorithm (see section 3). In the third algorithm, the platform attitude compensation is added. Finally, the beam-cone shape and the signal processing of the altimeter is additionally compensated by the fourth approach.

Method No.	Information exploitation	Translational drift estimation	Validity assessment	Attitude compensation	Closed-loop slant range compensation
1	✓	✓	x	x	x
2	✓	✓	✓	x	x
3	✓	✓	✓	✓	x
4	✓	✓	✓	✓	✓

Table 7.2: PPSAN methods overview

To show the effects of the validity assessment on the measurements, the raw and compensated height above ground measurements are plotted in the following. First, the raw altimeter measurements are illustrated with the results of the validity detection algorithm in figure 7.21.
The validity assessment eliminates the most erroneous measurements with the decreased SAN availability as disadvantage. The trade-off for this consideration is to eliminate erroneous measurements and thereby reducing the availability or to accept erroneous measurement and thereby decreasing the SAN accuracy. This trade-off has to be decided depending on the platform, application and on the mission profile. The raw measurement without any invalidity removal are fed into the first algorithm, while the second algorithm only processes the valid measurements.
Figure 7.22 shows the attitude compensated measurements and the corresponding validity assessment. Obviously, the attitude compensation exhibits huge compensation errors due to the high roll dynamics of this trajectory. This compensation method is therefore not suitable for high attitude dynamics above a rough surface. These huge errors are detected by the validity assessment and are identified to be invalid. In this example, the availability of the SAN decreases further.

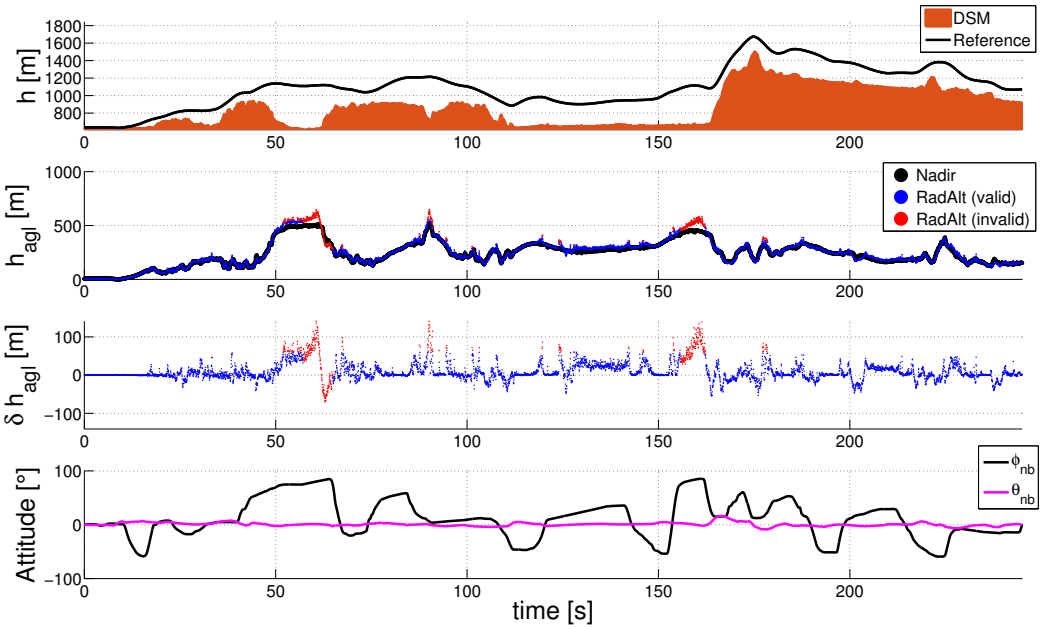

Figure 7.21: Validity check for raw measurements

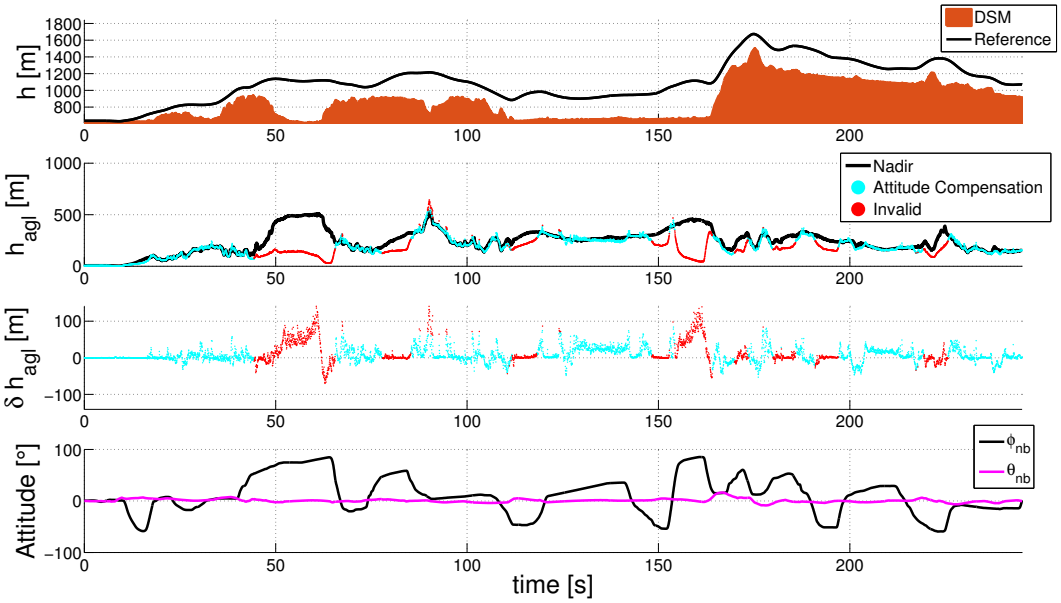

Figure 7.22: Validity check for attitude compensation

Finally, figure 7.23 provides the beam-cone compensated measurements with the corresponding validity assessment. Due to the well performing compensation algorithm, the validity assessment identifies only a small number of measurements to be invalid.
This analysis has been simulated with a perfect navigation solution and is thereby not exactly representing the SAN method. The validity assessment as well as the information selection and beam-cone compensation depends on the navigation solution. If the navigation system is already degraded, these methods won't work.

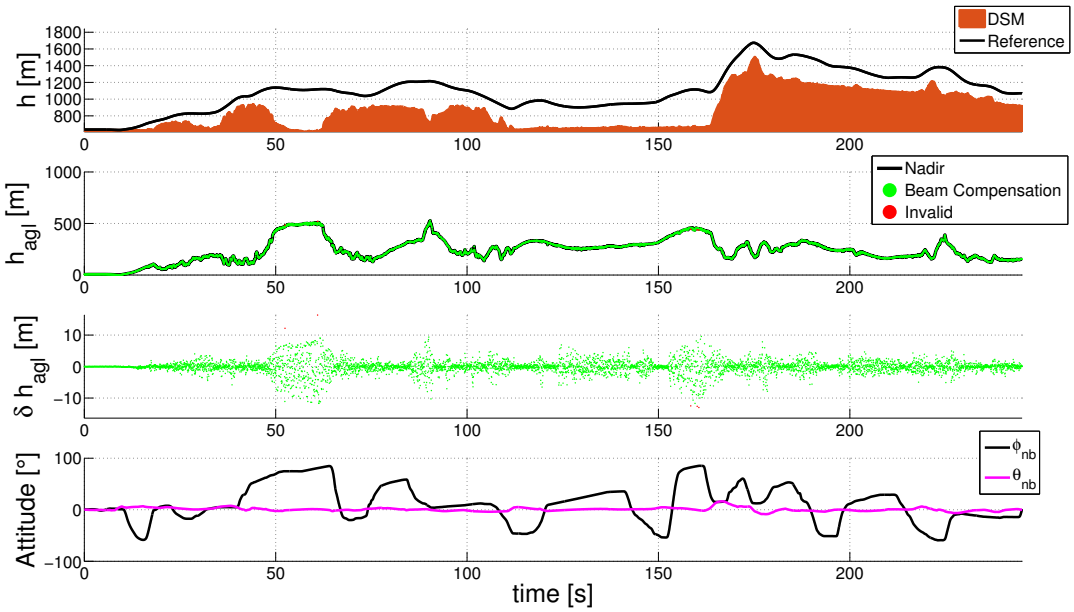

Figure 7.23: Validity check for beam compensated measurements

7.3.3 Positioning

The settings for the grid-search and comparison algorithm are summarized in table 7.3. While the matching length and the number of measurements are the same for all four methods, the method number four differs in the grid-resolution and grid-size from the other three methods. The grid-resolution and size have been reduced for the fourth method due to the expected higher accuracy of this approach according to the input measurement accuracy.

Parameter	**No. 1**	**No. 2**	**No. 3**	**No. 4**
Correlation length	$t_{cor} = 5\,\mathrm{s}$			
Number of measurements	$N_s = 125$			
Grid resolutions	$\Delta g = 5\,\mathrm{m}$			$\Delta g = 0.2\,\mathrm{m}$
Grid size	$g = 100\,\mathrm{m}$			$g = 10\,\mathrm{m}$

Table 7.3: PPSAN comparison grid-search settings

The SAN performances of the four methods are first compared to each other in a scenario with a perfect reference navigation (see figure 7.24).
Obviously, the errors of the first and second method are clipping the grid-size in several situations. This indicates an invalid solution and reduces the availability of the SAN system. This horizontal inaccuracy of up to $\delta x = 100\,\mathrm{m}$ leads to height errors up to $\delta h > 30\,\mathrm{m}$. The attitude compensation method three leads, because of the erroneous input, to errors in a comparable scale of the other methods. Only the beam compensation method (four) performs at a quality which is sufficient for aiding a high precision navigation system. Therefore, a more detailed insight into the accuracy of the beam compensation method is given in figure 7.25.
Method four, which includes the validity check, the information exploitation and the

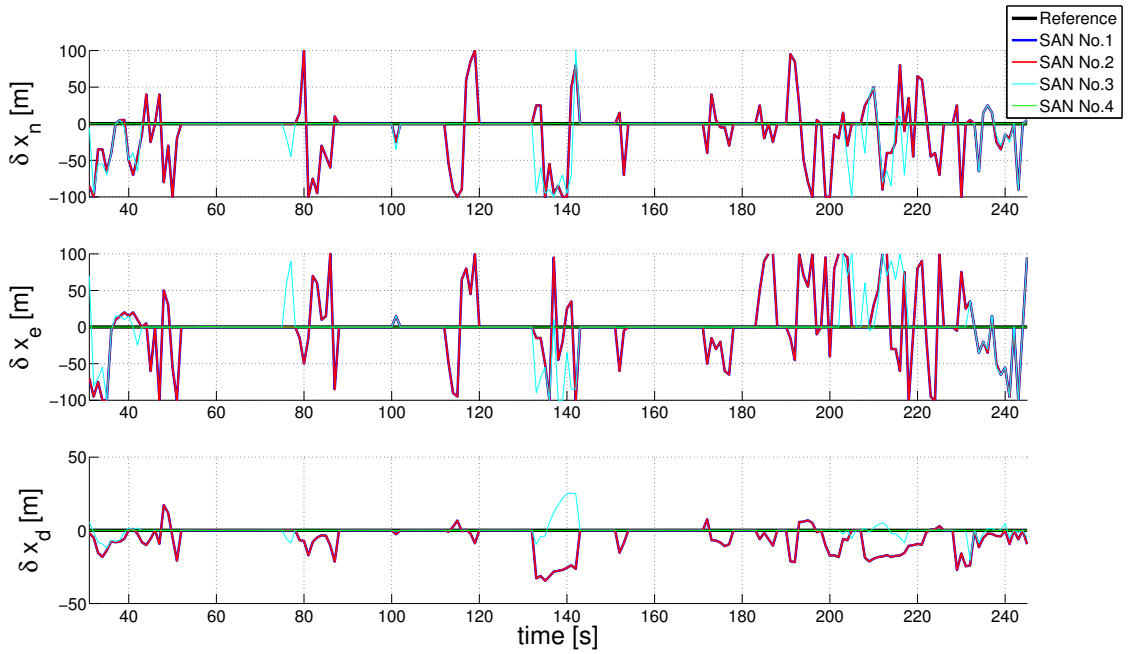

Figure 7.24: PPSAN positioning method comparison

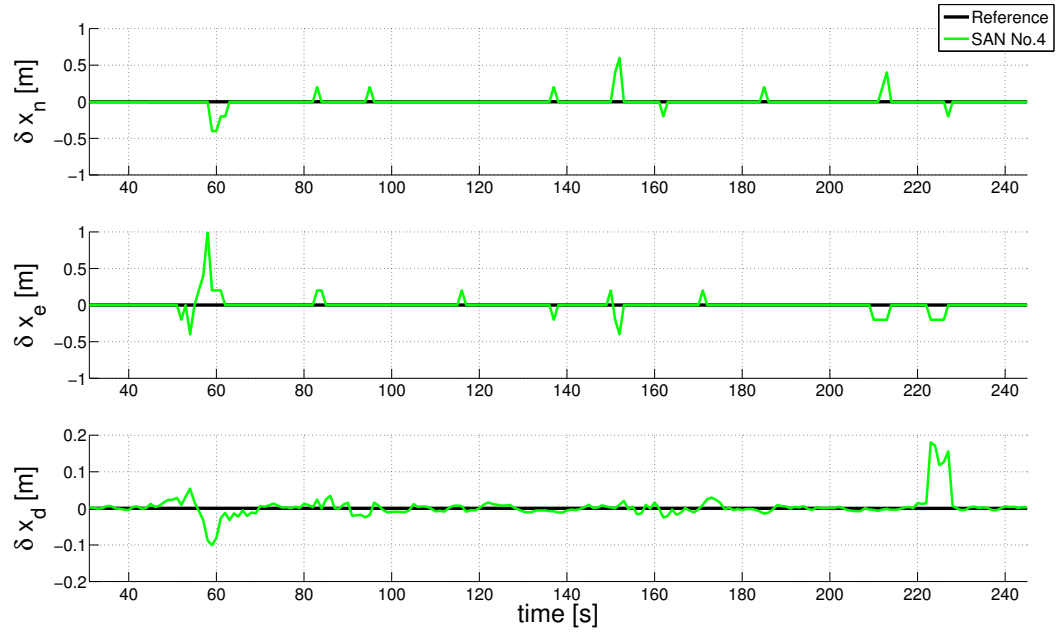

Figure 7.25: Slant range compensated PPSAN

beam-cone compensation provides a high accuracy during the entire trajectory. The horizontal errors of the SAN system with a perfect INS navigation estimation are limited in this perfect navigation environment to $\delta x \leq 1\,\mathrm{m}$ and the vertical error to $\delta h \leq 0.2\,\mathrm{m}$.

7.3.4 Aiding

The single beam SAN performance of the fourth method is now demonstrated with non-ideal navigation solutions in three application scenarios. First, SAN is applied as aiding support for the established INS/GNSS system to provide an additional information source.

Second, the performance of the inertial/GNSS/SAN system is analyzed for three different time periods with degraded GNSS accuracy. Finally, SAN is applied to replace GNSS in three flight phases with GNSS outages.
The additional aiding of an INS/GNSS system with a redundant, complementary system like SAN provides several advantages. While the covariance will reduce slightly, the system becomes more robust against local disturbances or GNSS constellation changes, for example. While the benefit in a nominal situation is slightly noticeable, in case of a degradation or outage of the GNSS, the SAN gains impact. The results of a redundant SAN are provided in figure 7.26.

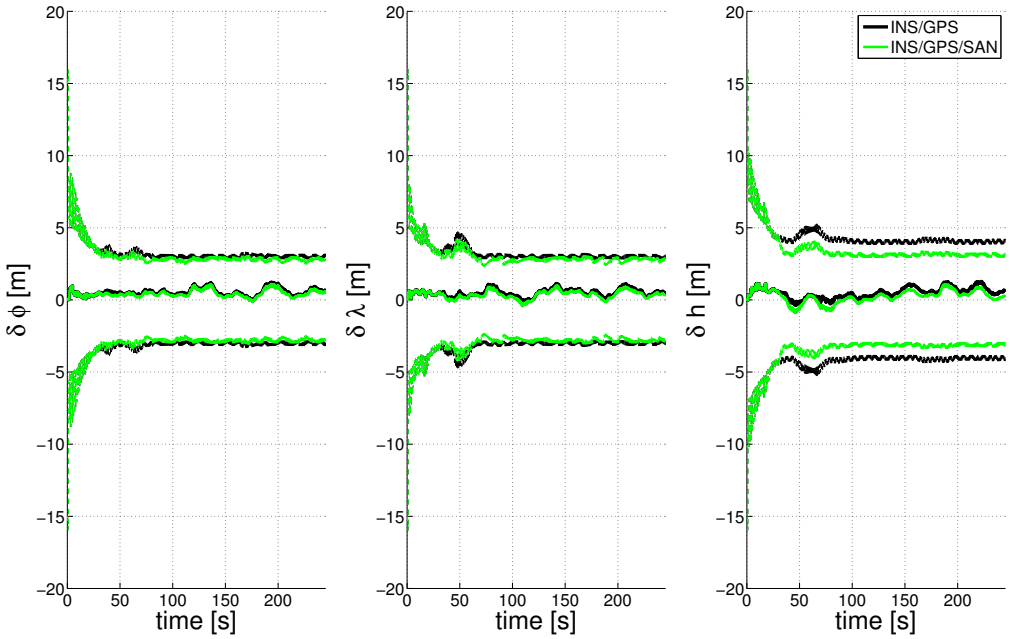

Figure 7.26: INS/GNSS/PPSAN

For this consideration, only the three position channels are shown including their standard deviations. The SAN aided system is compared to the INS/GNSS system. The variances of all three channels can slightly be decreased when the SAN aiding is activated at $t = 30\,\mathrm{s}$. The nominal GNSS standard deviation is set to $\sigma_{hor} = 2\,\mathrm{m}$ and $\sigma_{vert} = 3\,\mathrm{m}$. Especially the height channel benefits of the SAN aiding.
The second scenario simulates a degradation of the GNSS aiding concerning the position accuracy. The SAN aiding is continuously available after the take-off beginning at $t = 30\,\mathrm{s}$. While the nominal GNSS standard deviation is set to $\sigma_{hor} = 2\,\mathrm{m}$ and $\sigma_{vert} = 3\,\mathrm{m}$, the standard deviation is varied in three situations with different lengths to simulate the degradation. The degradation can be caused by all kinds of GNSS error sources like satellite constellation changes, loss of satellite line of sight due to the platform dynamic or terrain shading. The degradation sequence is given in table 7.4.
The standard deviation of the GNSS measurements increase stepwise as well as the time period of the degraded phases. The main focus of this simulation is the behavior of the integrated navigation system within the GNSS degraded phases. The position channels of the simulation results with their corresponding covariances (3σ) are given in figure 7.27. It shows the reduction of position errors in the three phases of GNSS degradation by SAN aiding. The position accuracy can significantly be improved in the three phases $t = 40\,\mathrm{s}$,

Time [s]	GPS standard deviation	
	horizontal [m]	vertical [m]
0-30	2	3
30-40	4	6
40-80	2	3
80-100	5	7
100-170	2	3
170-200	6	8
200-250	2	3

Table 7.4: Degraded GNSS standard deviations

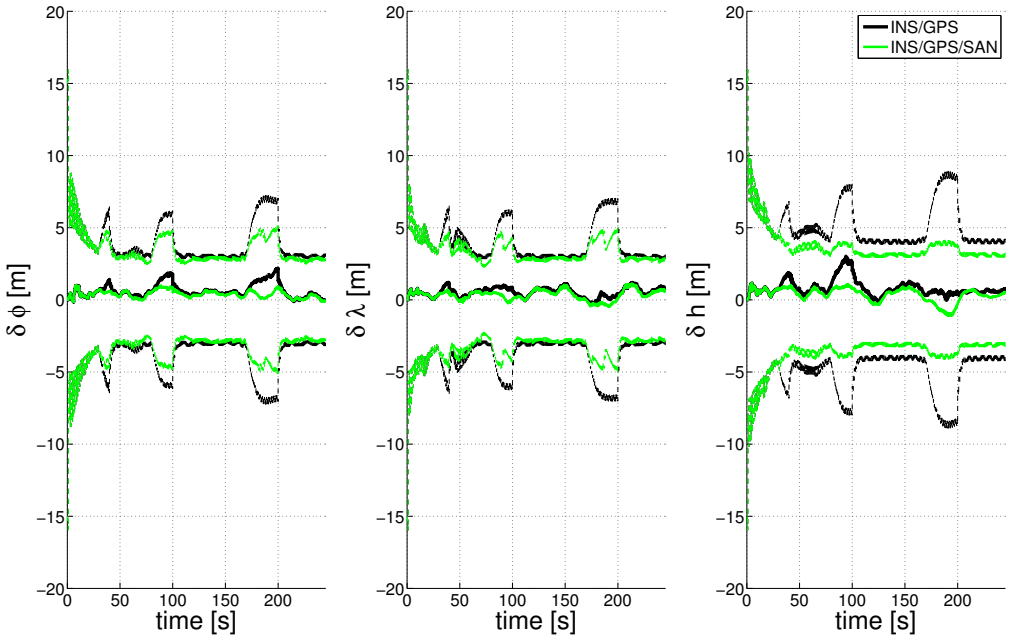

Figure 7.27: INS/PPSAN with degraded GNSS

$t = 100\,\mathrm{s}$ and $t = 200\,\mathrm{s}$. The application of SAN impacts the integrated navigation system by reducing the level of covariance degradation and replaces the GNSS as main aiding source. While the variances and accuracies of the horizontal channels still degrade due to the GNSS outages, the vertical channel is only marginally affected, since SAN is dominating it instead of GNSS.
The final example simulates a total outage of the GNSS aiding for the three time periods. This example stands for a jamming or spoofing scenario or a total GNSS outage due to the loss of the satellite tracking and a subsequent reacquisition. The sequence of outages and the availabilities of both aiding systems are given in table 7.5. The simulation results are depicted in figure 7.28.
The phases with GNSS outages are compensated by the SAN aiding at a high accuracy. The position errors and variances are reduced and thereby, the system can provide a stable, non-drifting position information. The results of a long-endurance SAN-only aiding is given in section 7.3.6.

Time [s]	Aiding availability	
	GNSS	SAN
0-30	✓	x
30-40	x	✓
40-80	✓	✓
80-100	x	✓
100-170	✓	✓
170-200	x	✓
200-250	✓	✓

Table 7.5: Aiding availability

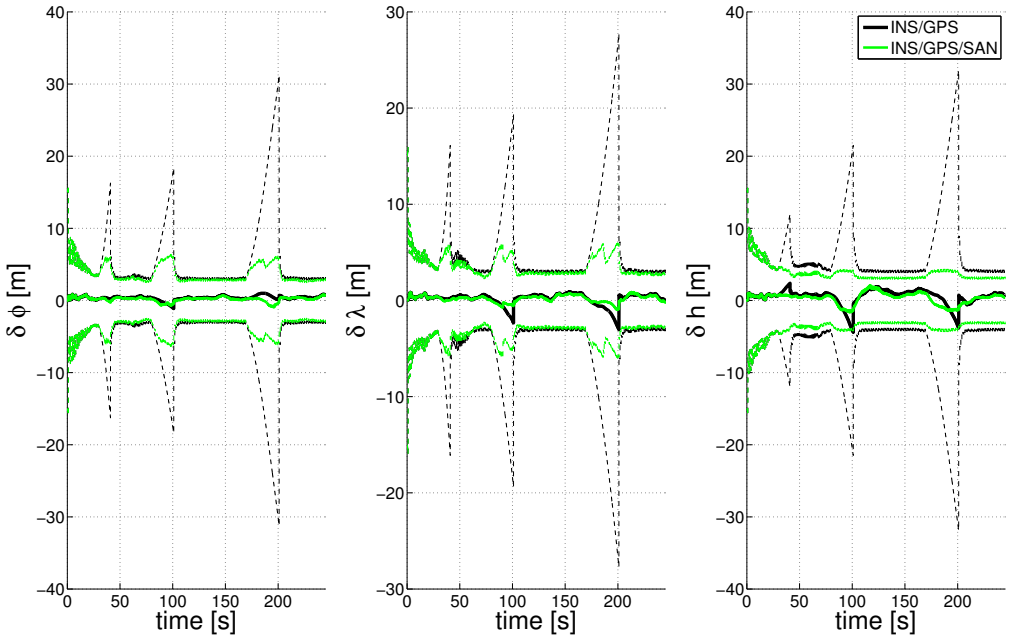

Figure 7.28: INS/PPSAN with GNSS outages

7.3.5 Multi-Beam Extension

The benefits of a multi-beam extension for SAN have already been explained and are now quantified in simulation in comparison to the single-beam approach. Several beam arrangements are applied to indicate the advantages and disadvantages. Apart from the single-beam approach, four systems with $N = 3$, $N = 5$, $N = 7$ and $N = 9$ beams are investigated. Each setup is configured with equidistant beam separations and different absolute angles-of-view. The beam setups are depicted in figure 7.29, a tabular overview is given in table 7.6.

The benefit of using multiple beams for SAN is the increased information content of the additional measurements. Not only the number of measurements, but mainly the different directions provide additional information. Therefore, the introduced five beam setups are compared along a trajectory. This simulation provides the position variances as quality index of the different systems. The simulation is given in figure 7.30.

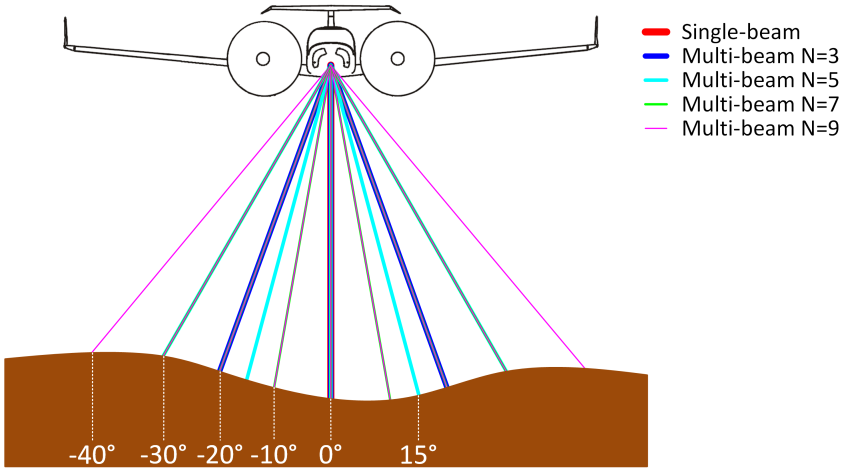

Figure 7.29: Simulated number of beams

	0°	±10°	±15°	±20°	±30°	±40°
N=1	✓					
N=3	✓			✓		
N=5	✓		✓		✓	
N=7	✓	✓		✓	✓	
N=9	✓	✓		✓	✓	✓

Table 7.6: Multi-beam directions

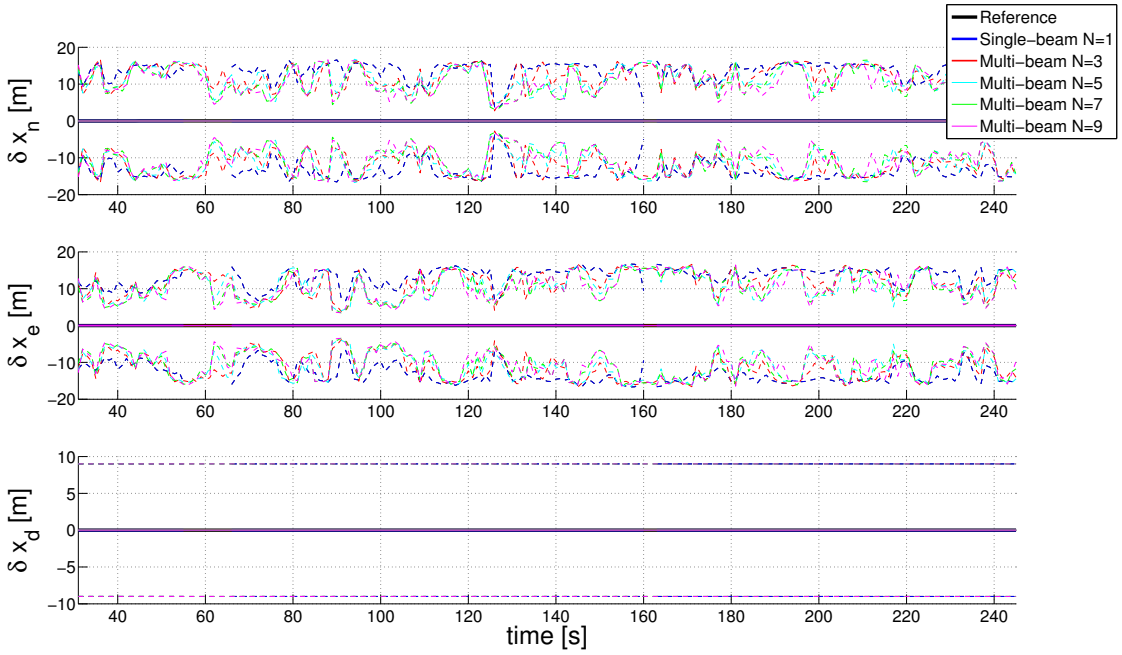

Figure 7.30: Multi-beam PPSAN method comparison

As expected, the multi-beam approaches provide a sharper matching function shape than the single-beam approach does whenever additional features become visible. This behavior

can be observed for example at $t = 90\,\mathrm{s}$, $t = 105\,\mathrm{s}$ and $t = 200\,\mathrm{s}$. If a feature is measured with one of the additional beams, the result can be improved. If the information with the most beneficial impact is measured with the central beam, the covariance of all measurement setups is equal. A good example for variance improvement is given at $t = 150\,\mathrm{s}$. While the covariance decreases with increasing number of beams, the last two setups provide the same result. That implies that the information content is distributed within the first seven beams, but the additional two side-beams do not provide any additional important information. An example, where the main information is measured with the central beam is given at $t \approx 60\,\mathrm{s}$.
In the next paragraph, the scenarios with degraded GNSS performance and GNSS outages are repeated using the multi-beam measurement approach. The first result is given in figure 7.31.

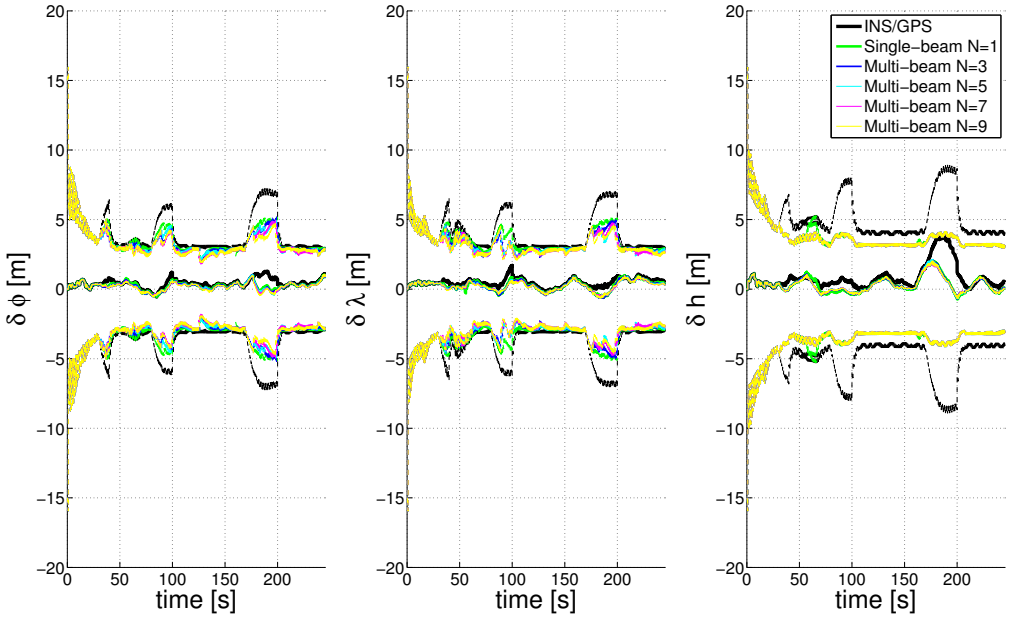

Figure 7.31: INS/Multi-beam PPSAN with degraded GNSS

The three phases with degraded GNSS accuracy are significantly complemented by SAN. The four multi-beam SAN methods are compared to the single-beam approach. The plots affirm the results obtained in the previous error-free simulation. The multi-beam methods improve the performance significantly in situations in which additional surface features can be measured.
The performance during GNSS outages is demonstrated in figure 7.32. The behavior of the different multi-beam setup is equal to the previous simulations.
The application of multi-beam sensor configurations is recommendable to increase the measurement accuracy, whenever additional information content is provided by the over-flown surface. Especially in feature-less environments like flat surface with rare variations the probability of measuring additional signification variations increases by applying a multi-beam approach.

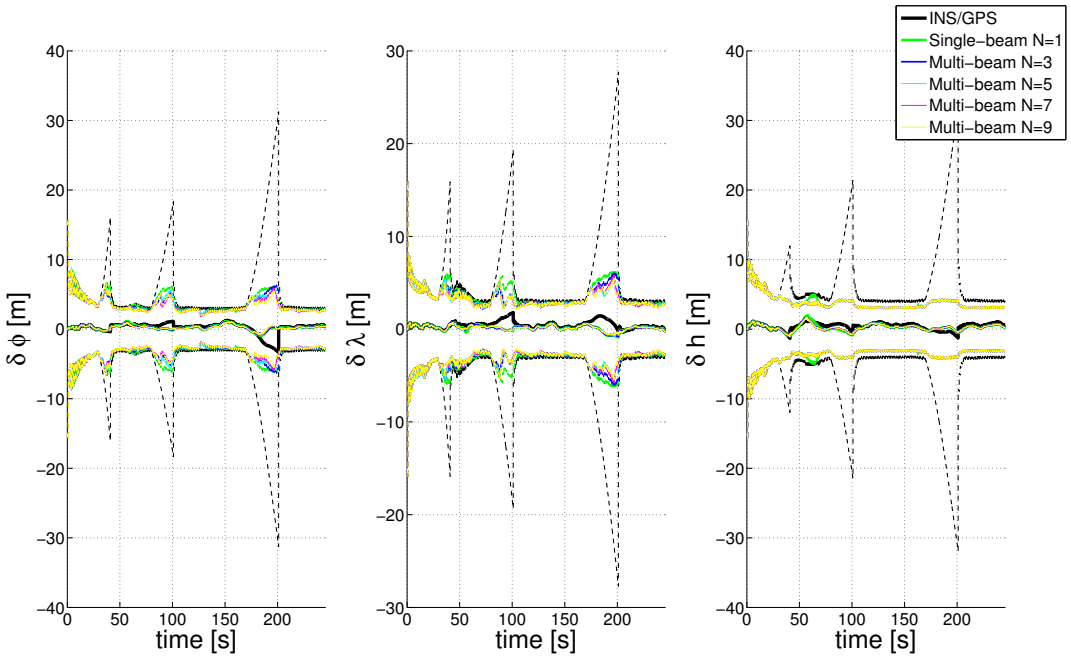

Figure 7.32: INS/Multi-beam PPSAN with GNSS outages

7.3.6 Long-Endurance Results

The long-term behavior of a single-beam and a $N = 9$ beam SAN is analyzed and compared against the INS only solution in this section. Therefore, a new trajectory is simulated with medium dynamics, which additionally can be used for the later dead-reckoning SAN comparisons. The trajectory represents a flight with a duration of $T \approx 1000\,\mathrm{s}$, which contains GNSS outages between $t = 250\,\mathrm{s}$ and $t = 750\,\mathrm{s}$. The three-dimensional trajectory is shown in figure 7.33.
The trajectory features and the sensor settings are summarized in table 7.7. The height above ground plot in figure 7.34 shows the low-ground clearance and the terrain following flight path characteristics.

Trajectory	
Along track velocity	$v_x \approx 170\,\mathrm{m\,s^{-1}}$
Mean ground clearance	$h_{agl} \approx 300\,\mathrm{m}$
Single-beam altimeter	
Update frequency	$f_s = 25\,\mathrm{Hz}$
Beam-shape	Narrow
Multi-beam altimeter	
Number of beams	$N = 9$
Update frequency	$f_s = 25\,\mathrm{Hz}$
Measurement direction	$\phi_{sm} = [-40 : 10 : 40]$
Beam-shape	Narrow

Table 7.7: PPSAN simulation setup

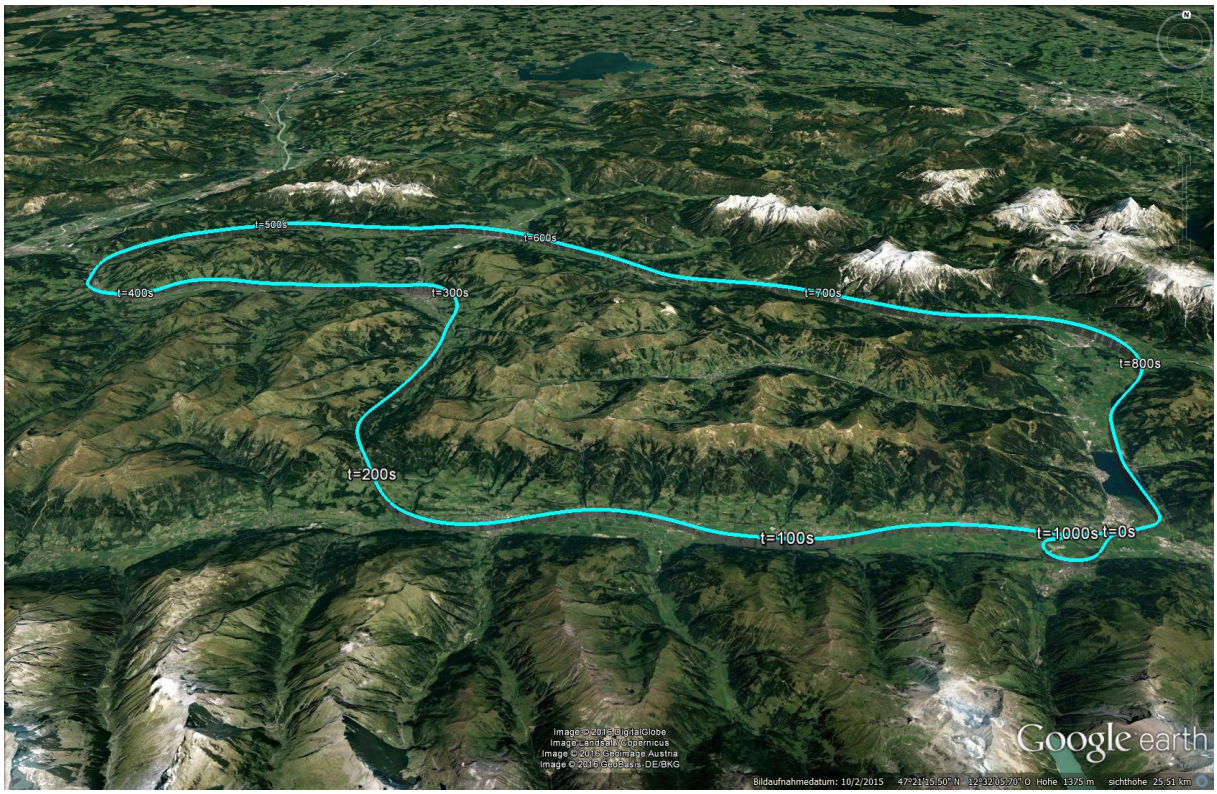

Figure 7.33: Medium dynamic trajectory above rough surface

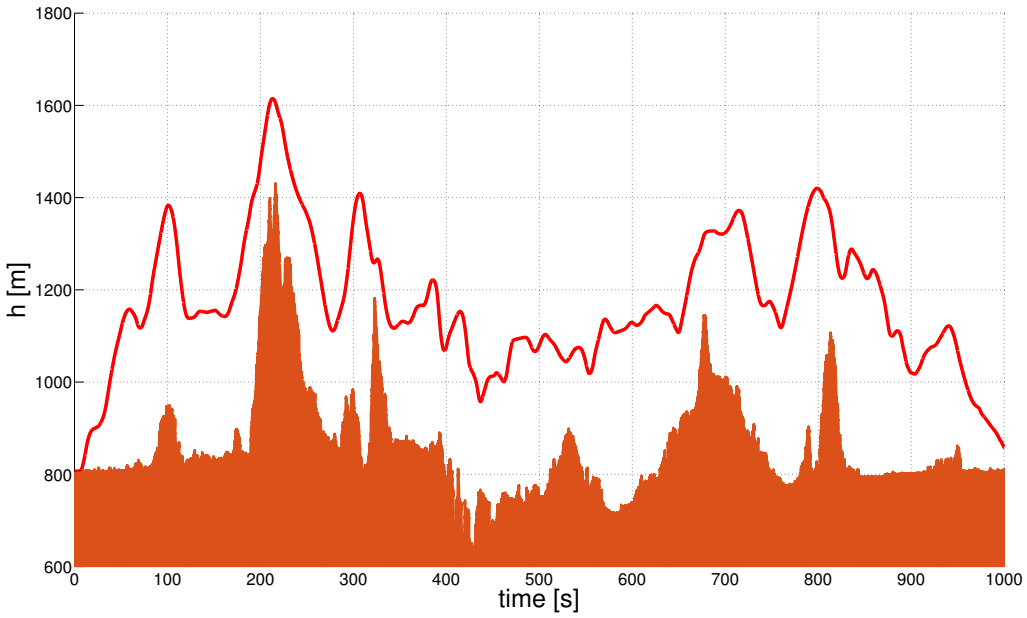

Figure 7.34: Vertical situation

The position estimation errors in figure 7.35 show the position error drift of the unaided inertial navigation solution during the GNSS outage period between $t = 250\,\mathrm{s}$ and $t = 750\,\mathrm{s}$. The horizontal position error raises to several hundred meters, while in this realization the height position error is limited to about $14\,\mathrm{m}$. The SAN estimations provide a stable and accurate estimate.
Figure 7.36 depicts an zoomed plot of the position errors including the 3σ standard devi-

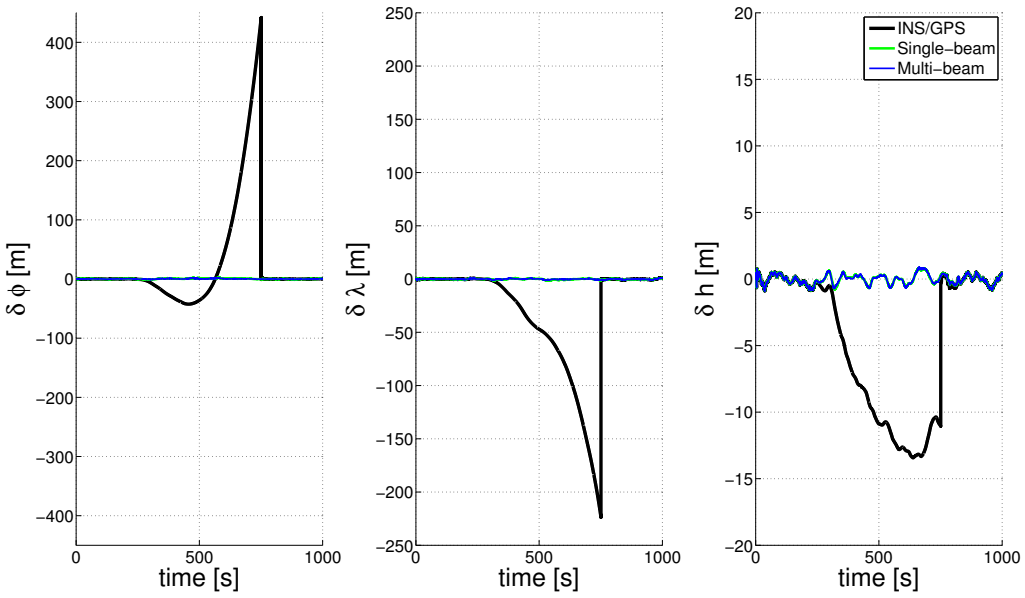

Figure 7.35: Long-endurance position error

ations. Both SAN aided position solutions show long-term stable results with a slightly better horizontal position accuracy and standard deviation for the multi-beam approach. As explained in the earlier analysis, this depends on the occurrence of features measured by the additional sensors. The multi-beam benefit can be observed, for example, between $t = 500\,\mathrm{s}$ and $t = 600\,\mathrm{s}$. The high redundancy of the height information results in a highly stable vertical channel for both systems.

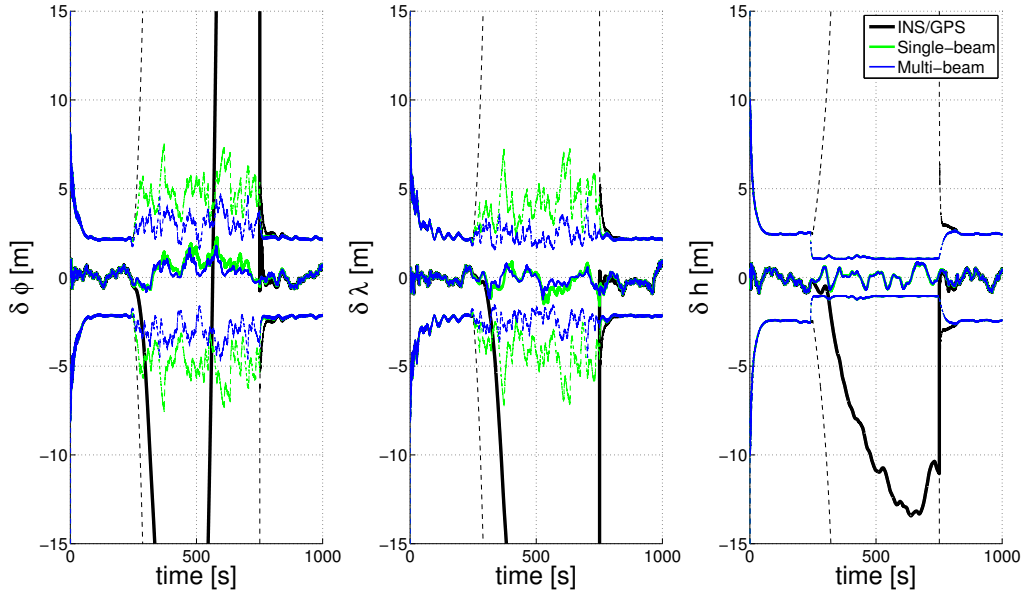

Figure 7.36: Long-endurance position error zoom

Results

- GNSS degradations and outages can be compensated with SAN
- SAN can provide an accuracy in the same magnitude as GNSS (depending on the surface)
- Multi-beam sensors improve SAN if additional surface information is available
- SAN is also capable of compensating long-term GNSS outages.

7.4 Dead-Reckoning Surface Aided Navigation

The simulation study is completed with the results of the dead-reckoning surface aided navigation. The trajectory introduced in the previous chapter is used to demonstrate the performance without the use of a DEM reference. The trajectory is illustrated in figure 7.33, the characteristics are given in table 7.8. In this scenario, the surface is assumed to be fast changing or unknown and therefore, an overlapping measurement of the same surface has to be guaranteed. This simulation study analyses the performance of a dead-reckoning SAN using range-imaging sensors.

Application Description
- Flight above unknown / fast-changing surface
- DRSAN approach using range-imaging sensor
- Position increment aiding during long-term GNSS outages

Assuming a sensor with a given angle-of-view, the update frequency of the sensor measurements has to be adjusted a-priori to the trajectory characteristics. Two factors influence the requirements on the sensor update frequency, the height above ground and the along track velocity. Equation 5.6 of chapter 5 poses a condition for the update frequency which needs to be fulfilled to guarantee an 50 % overlap of the two measurements. The sampling interval is calculated for the parameters of this trajectory by equation 7.6.

$$\begin{aligned} \Delta t_s &\leq \frac{h_{agl}}{v_x} \tan\left(\frac{\alpha}{2}\right) \\ &\leq \frac{300m}{170\frac{m}{s}} \tan\left(30°\right) \\ &\leq 1.02\,\mathrm{s} \end{aligned} \tag{7.6}$$

The sampling interval is set to $\Delta t_s = 0.5\,\mathrm{s}$ to ensure a margin for velocity and height variations. This also allows the selection of the best range-imaging snapshot. The product of the area of overlap and the time duration has been identified as valid selection criterion. In figure 7.37, the upper plot shows the overlapping area of two snapshots above the time interval between the measurements. Obviously, the overlapping area is decreasing over time. The lower plot provides the product of time delay and overlapping area.

Trajectory	
Along track velocity	$v_x \approx 170\,\mathrm{m\,s^{-1}}$
Mean ground-clearance	$h_{agl} \approx 300\,\mathrm{m}$
Range-imaging sensor	
Update frequency	$f_s = 2\,\mathrm{Hz}$
Pixel	$p_x = 75 \times p_y = 75$
Angle-of-view	$\phi_{sm} = 60° \times \theta_{sm} = 60°$

Table 7.8: DRSAN simulation setup

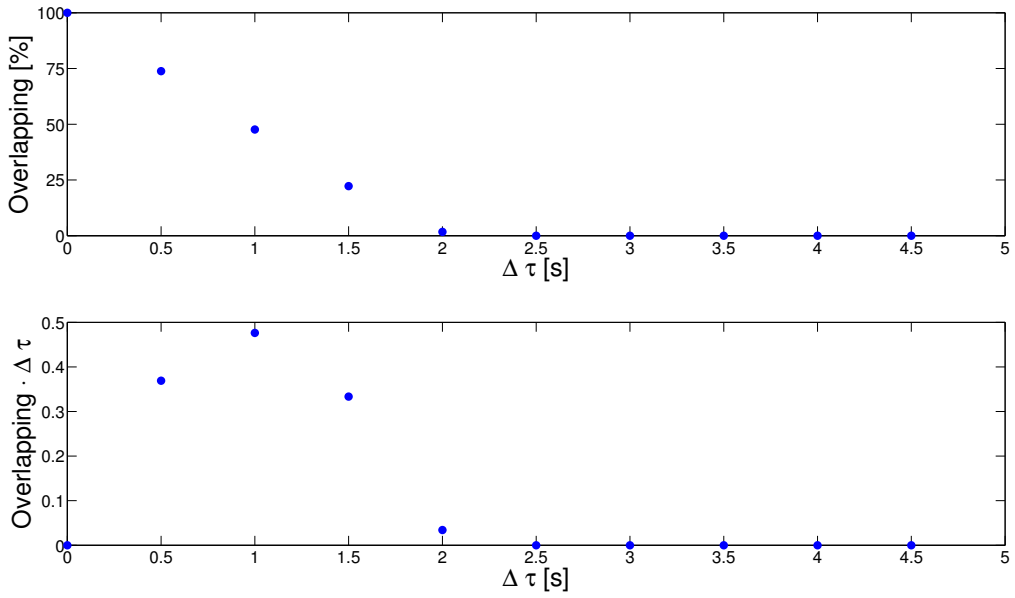

Figure 7.37: Overlapping area and time delay

The snapshot measured at $\Delta\tau = 1\,\mathrm{s}$ provides the maximum product, hence the position drift determination is based on this two snapshots. If a measurement concept provides less information content, or the position drift error is increasing fast, the time duration between the snapshot can be reduced. For this simulation it is important that a possible position drift increases to a relevant and detectable value for the comparison algorithm.

To give an impression of the characteristics of the overflown surface and the surface sampling, the situation at $t = 300\,\mathrm{s}$ is illustrated in figure 7.38. The aircraft is in a bank-to-turn maneuver while measuring the range-imaging snapshots. The maneuver is indicated by the contour distortion of the two measurements. The overlapping area in the middle of the illustration includes several features, like the small valley and some hills, which provide the necessary horizontal information to calculate the position drift.

The simulation results of the three position channels are plotted in figure 7.39. The simulation demonstrates the behavior of the dead-reckoning SAN/INS. While GNSS aiding

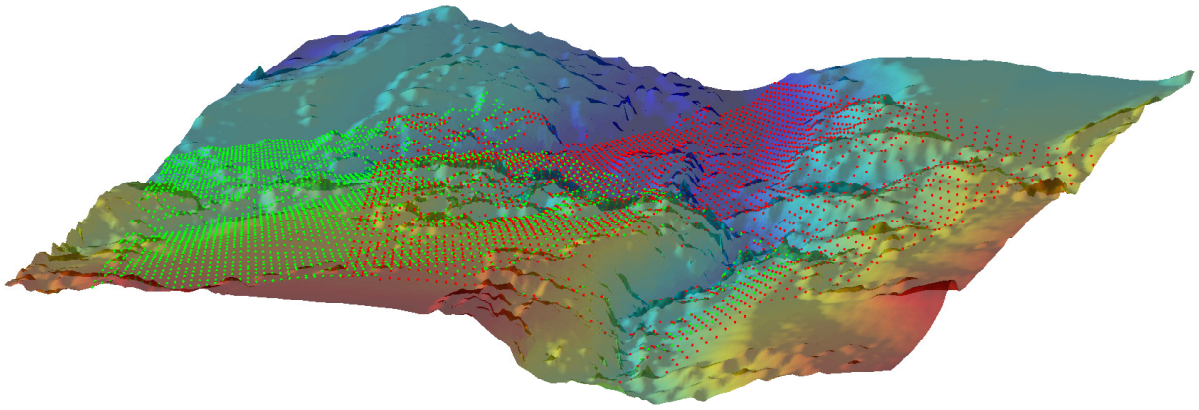

Figure 7.38: Range-imaging surface sampling

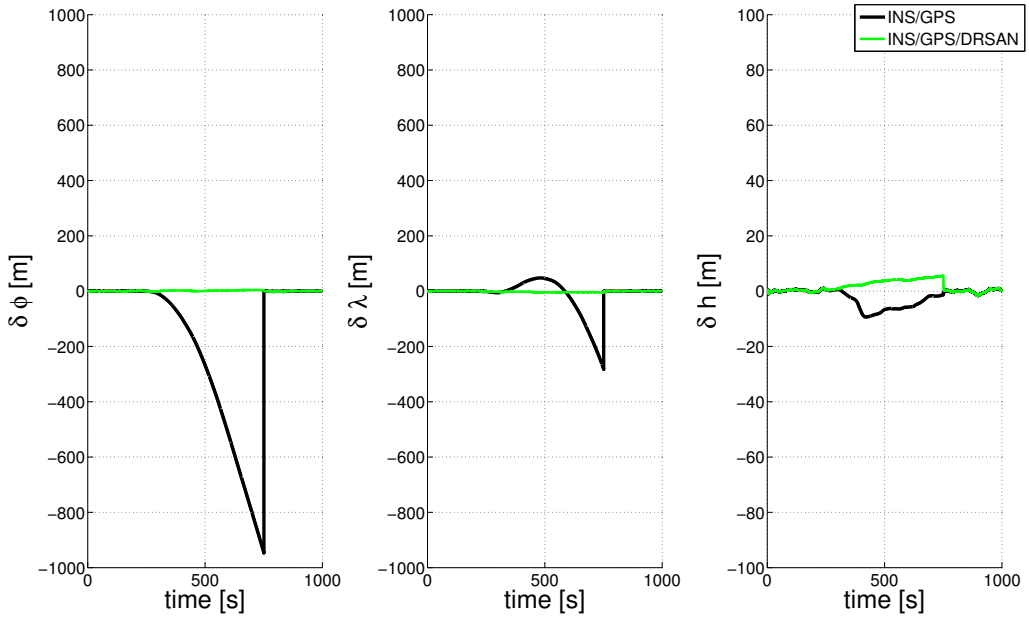

Figure 7.39: Long-endurance dead-reckoning position error

is available before $t = 250s$ and after $t = 750s$, it is switched off in between.
The simulation results show the expected behavior of the inertial-only navigation system. The position error uncertainty grows with time until the GNSS aiding is available again. The dead-reckoning SAN system provides a good positioning performance (see figure 7.40 for a zoomed plot).

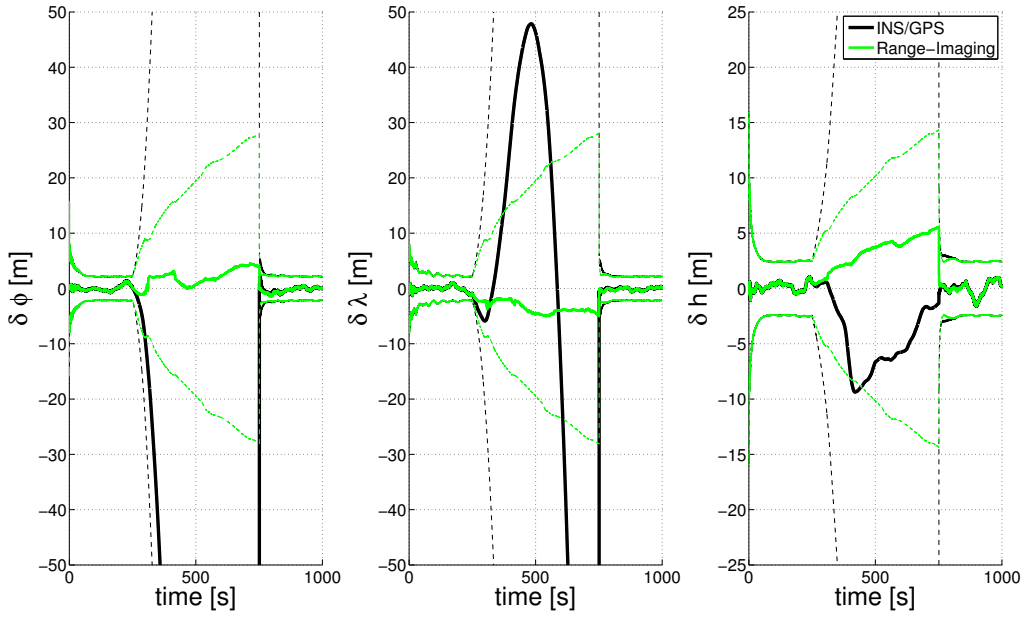

Figure 7.40: Long-endurance dead-reckoning position error zoom

The zoomed view manifests the reduction of position drift of the dead-reckoning SAN. While the expectation value only represents the current realization of IMU errors, the covariance of the DRSAN aided position indicates the growing uncertainty. The growth of position uncertainty cannot be fully compensated with the incremental measurement

equation. Whenever an absolute position aiding is required, this system cannot be applied. However, this approach provides a fully self-contained system to reduce the position drift when no other aiding system is available. At last, the mission time duration and mission profile decides whether a DRSAN is applicable. Whenever no surface elevation model is available and GNSS outages are probable, dead-reckoning SAN is a suitable extension of an INS/GNSS/SAN system.

Results

- Fully autarchically position error drift limitation
- Recommendable solution if no DEM for PPSAN is available

7.5 Real Data Evaluation

The methods of chapter 3 are now applied to recorded real data. In this section, three recorded trajectories and the corresponding Laser and Radar altimeter measurements are discussed. The aircraft and the FTI which was used for this campaign has been introduced in chapter 6. This section is organized in four subsections. The first subsection introduces the three trajectories and the corresponding altimeter raw measurements. The second subsection compares the recorded altimeter measurements with the altimeter simulation model results of chapter 2. The validity assessment of chapter 3 is applied in the third subsection. This section is concluded by the application of the slant range compensation algorithm of section 3.3 in the fourth subsection. Some results and explanations of this section have been prepublished in [83].

Applications Description

- Simulation model comparison with recorded real data
- Validity assessment on real data
- Slant range compensation of real data

7.5.1 Trajectories and Measurements

7.5.1.1 Flight Test 1

The first flight test trajectory start South of LOAN (Wiener Neustadt) with an low-pass approach on runway 09. The low pass overfly is initiated by two bank-to-turn maneuvers to the right. The low pass over runway 09 is flown at a ground clearance of about seven meters. The flight test ends with a traffic pattern flown counterclockwise and the final landing again on runway 09. The three dimensional trajectory is illustrated in figure 7.41.

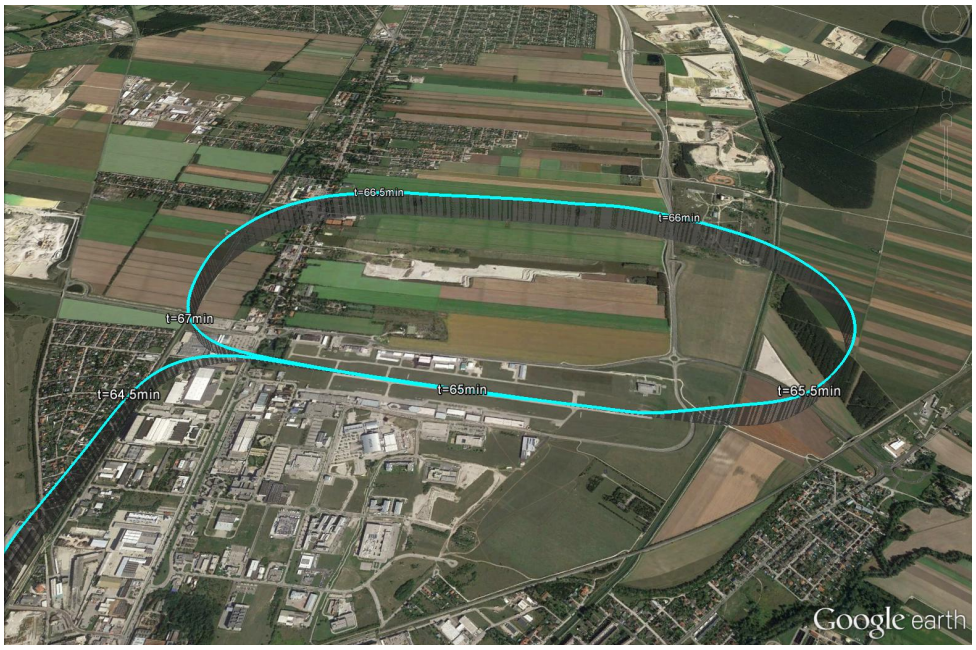

Figure 7.41: Flight test 1 - 3D situation

Two digital elevation models are applied as surface height reference. In the near airfield surrounding and below the approach paths in both directions, a high resolution DSM obtained from Laser scanner measurement data is available. The outer regions are covered by an ASTER tile with a lower resolution and accuracy.

The trajectory and the height above ground measurements are shown in figure 7.42. The upper plot gives the absolute height with respect to WGS84 including the INS/GNSS height and the DSM height. The second row shows the raw height above ground measurements of the Laser and Radar altimeters. To show the causal relations between the platform attitude and the altimeter measurements, the figure gives the roll and pitch angle of the aircraft in the lower row.

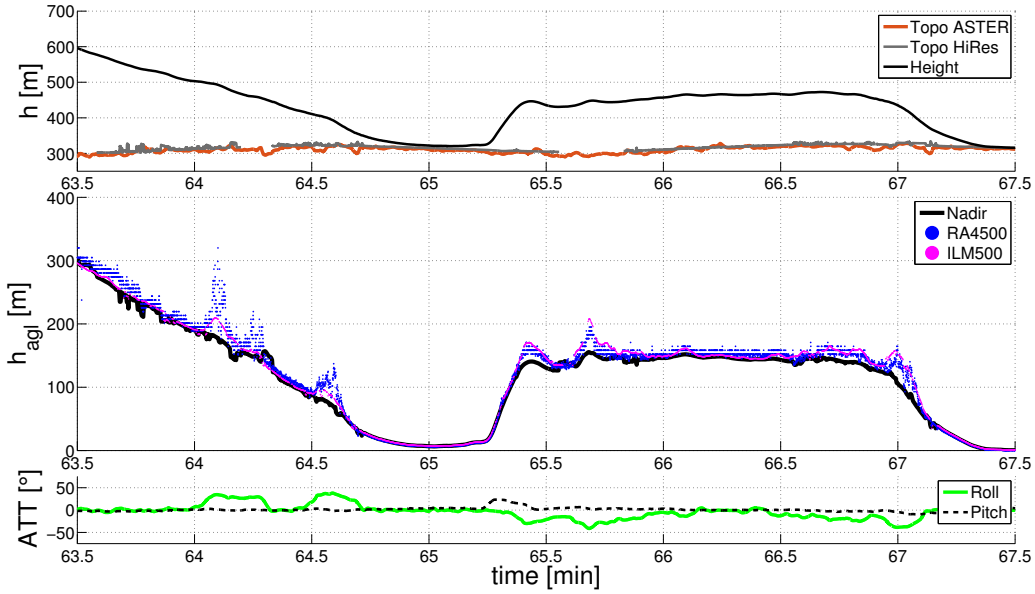

Figure 7.42: Flight test 1 - altimeter measurements

The error characteristics of both altimeters exhibit a similar behavior with respect to their attitude dependency. The height above ground overshoots in figure 7.42 show some coincidence with the roll and pitch angles displayed in the lower plot. The wide beam-cone of the Radar however is designed to compensate platform roll and pitch angles, the beam-cone divergence leads to a dispersion of the signal and thereby to an erroneous measurement. This topic has already been discussed in section 2.3. Especially the bank-to-turn maneuver at $t = 64.1\,\text{min}$ causes large height measurement errors, while the Laser altimeter measurement errors are limited to $\delta h_{agl} \approx 50\,\text{m}$, the Radar altimeter errors grow up to $\delta h_{agl} \approx 100\,\text{m}$. In this situation with a height above ground of $h_{agl} \approx 200\,\text{m}$, this is an error of 50% of the measurement value. Another remarkable property of both sensors is the predicted scale factor error dependency. While the measurement errors are minimized in the runway overfly phase around $t = 65.0\,\text{min}$ with a minimal sensor noise characteristic, the errors increase in the leveled flight phase between $t = 66.0\,\text{min}$ and $t = 66.5\,\text{min}$. Especially the Radar altimeter is sensitive to surface variations in this situation, while the Laser altimeter provides a better measurement result.

7.5.1.2 Flight Test 2

The second trajectory visualized in figure 7.43 includes two three-degree-approaches on runway 27 with subsequent go-around maneuvers, the first one aborted at $h_{agl} \approx 8\,\mathrm{m}$, the second one aborted at $h_{agl} \approx 4\,\mathrm{m}$. The flight test is finished with a $180\,^\circ$ turn and the final landing on runway 09.

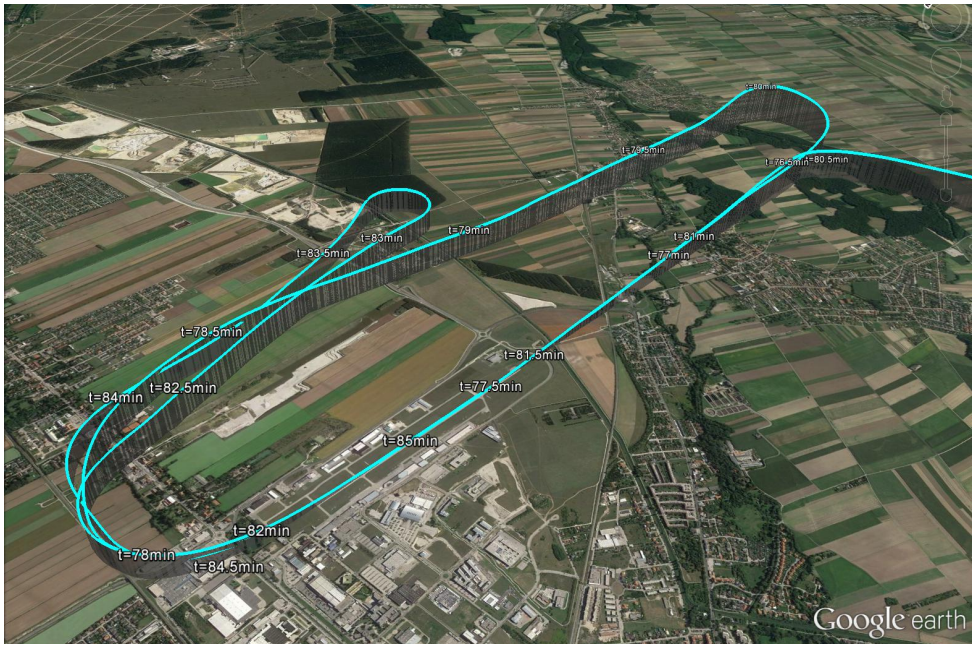

Figure 7.43: Flight test 2 - 3D situation

The measurement results given in figure 7.44 show the same error characteristic as in the first flight test. The main influencing factors are the aircraft attitude and the height above ground. Especially the four situations with high roll angles up to $\varphi \geq 50^\circ$ at $t_1 \approx 78.0\,\mathrm{min}$, $t_2 \approx 80\,\mathrm{min}$, $t_3 \approx 82.2\,\mathrm{min}$ and $t \approx 83.2\,\mathrm{min}$ are remarkable.
While the measurement errors of both sensors are comparable to the results of the first flight test, at the time points t_2 and t_4 the platform angles cause the exceed of the Laser altimeter's maximum measurement range. The Laser altimeter cannot measure a feasible distance and provides an invalid indication in this situation. Another noticeable effect occurs at time t_2 where the Radar altimeter keeps tracking the height above ground but reduces the measurement resolution. This effect is caused by quantization error effects due to the rounding function of the used Radar altimeter. The quantization interval is increased by the Radar altimeter software above $h_{agl} > 1000\,\mathrm{ft}$ from at least $h_{quant} = 20\,\mathrm{ft}$ to $h_{quant} = 50\,\mathrm{ft}$, which explains this effect in the situation with $h_{agl} > 304.8\,\mathrm{m} = 1000\,\mathrm{ft}$. The quantization steps of the used Radar altimeter RA4500 are given in table 7.9 [43].

Height (ft)	≤199	120-199	200-499	500-999	1000-2099	≥2100
Quantization (ft)	1	2	5	20	50	100

Table 7.9: Freeflight RA4500 measurement quantization

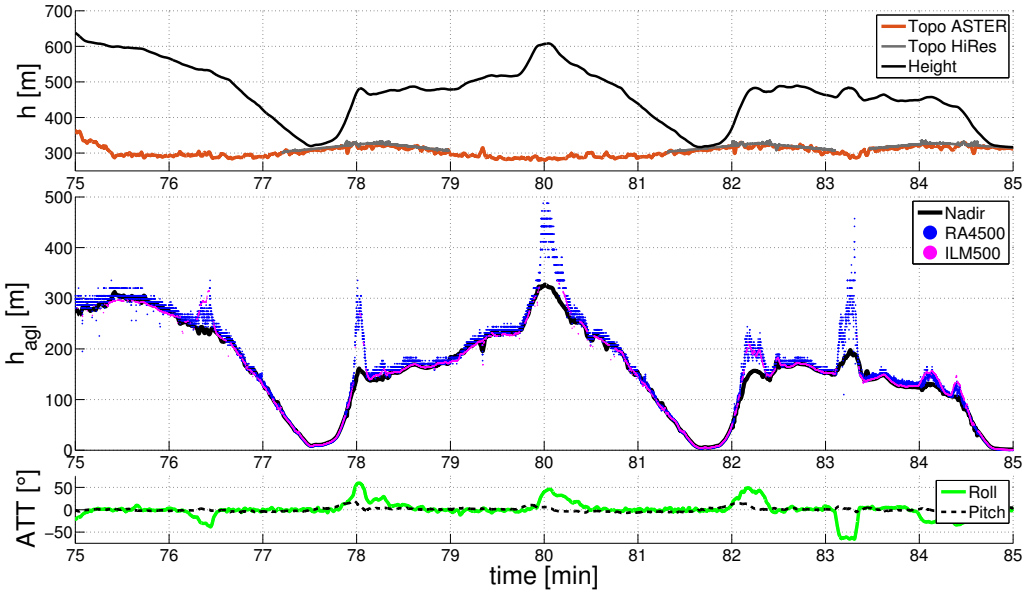

Figure 7.44: Flight test 2 - altimeter measurements

7.5.1.3 Flight Test 3

While the other trajectories provide dedicated test trajectories including several approaches in both runway directions, this trajectory defines only one approach with an inconspicuous flightpath. The approach is flown on runway 27 after a continuous descend with one medium bank-to-turn maneuver at $t = 47.5\,\text{min}$. While this trajectory does not provide a special flight path, the weather conditions of this recorded flight test contain a short flight through foggy environment. The three dimensional illustration of this trajectory is shown in figure 7.45.

Figure 7.45: Flight test 3 - 3D situation

The Radar altimeter outputs inconspicuous measurements (see figure 7.46). The quan-

tization effects can be observed above $h_{agl} \approx 300\,\text{m}$. The bank-to-turn maneuver at $t = 47.45\,\text{min}$ causes a slant range error of $\delta h_{agl} \approx 50\,\text{m}$. The scale factor like errors above $h_{agl} > 300\,\text{m}$ are also influenced by the quantization algorithm and could be reduced with a more detailed measurement resolution. The Laser altimeter measurements are error-prone during the flight through the foggy area. Beginning at $t = 47.25\,\text{min}$ the Laser altimeter start outputting measurements which result from reflections in a distance of $h_{agl} \approx 75\,\text{m}$ to $h_{agl} \approx 5\,\text{m}$ at $t = 47.75\,\text{min}$. This effect remains until the aircraft descends below $h_{agl} < 100\,\text{m}$ where the Laser altimeter starts operating nominally. The missing invalid indication in the erroneous measurement phase is remarkable. As mentioned in the trajectory description, this flight test was recorded under poor visibility conditions, and therefore the explanation for the Laser altimeter behavior is caused by the weather conditions.
A detailed analysis reveals that the most probable explanation is the Laser altimeter detection of a cloud reflection at $47.25\,\text{min} < t < 48.8\,\text{min}$. The Laser altimeter initially starts operating nominally as the weather conditions recover and the height above ground decreased below $h_{agl} < 100\,\text{m}$.

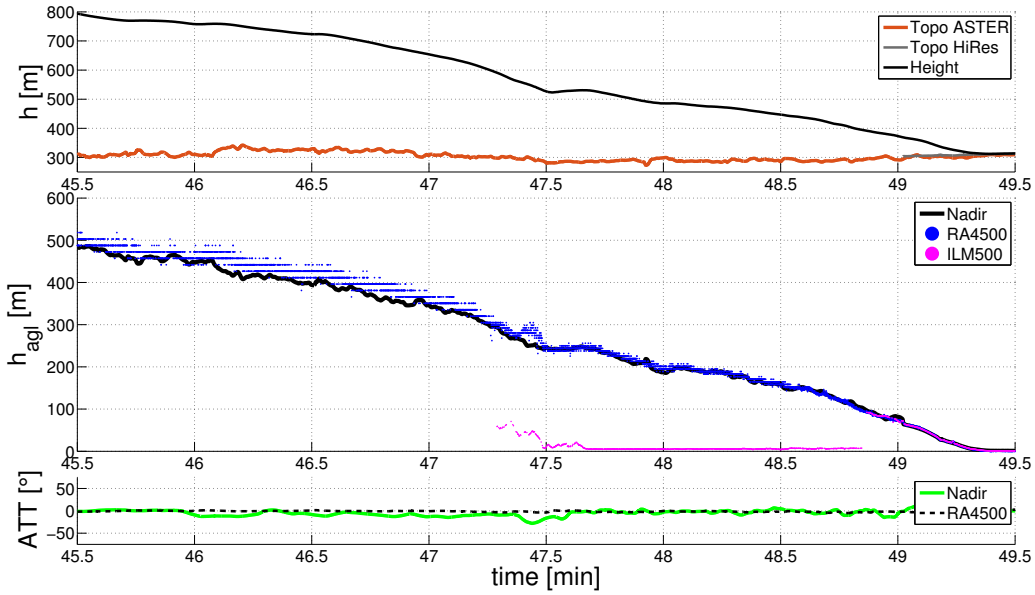

Figure 7.46: Flight test 3 - height measurement

These three trajectory examples show the performance of a Radar and a Laser altimeter in realistic approach scenarios. The strength and weaknesses of both measurement principles are identified and the similarities of both principles have been shown. The attitude dependency of wide beam-cone Radar altimeter has been identified as issue, as well as the quantization and scale factor errors. While the Laser altimeter causes slant range errors for larger attitude angles, the visibility conditions are limiting its performance significantly. Especially in situations with poor visibility, altimeter are required as support for the pilot, and therefore the applied Laser altimeter is not usable in approach applications.

7.5.2 Altimeter Simulation Model Comparison

The recorded flight test data is compared to the simulation model in this subsection. First the simulation model, parametrized as a pencil beam, is compared to the Laser altimeter

measurement of the three trajectories. Then, the Radar altimeter measurements are compared to a Radar simulation model.

7.5.2.1 Laser Altimeter

The comparison of the simulation results and the measurements of the first trajectory is given in figure 7.47. The upper plot shows the absolute height, followed by the height above ground and the height above ground errors with respect to the nadir height above ground. The lower plot provides the platform roll and pitch angles.

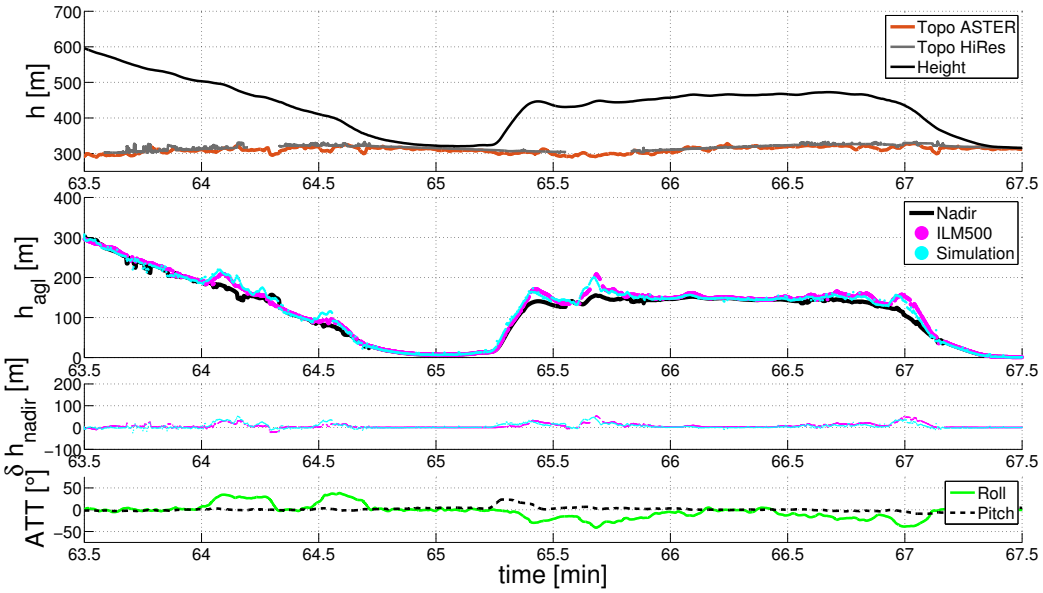

Figure 7.47: Flight test 1 - Laser altimeter simulation

Naturally, the simulation model performs better for lower heights above ground. The platform attitude, surface characteristics, signal propagation and environmental effects are additionally influencing the match of the simulation results to the measurements. To quantify the matching quality, table 7.10 provides the according RMS errors between simulated and measured height above ground. The table distinguishes the RMS error of the entire trajectory and sequences above the lower resolved DTM and above the high-resolution DSM. This partitioning indicates the dependency of the simulation model quality on the DEM resolution and accuracy.
However, for the height plot, the DEM type dependent on the platform nadir is plotted, for the distinction of the simulation model results the platform normal is required. In certain situations, the platform nadir DEM could provide a high resolution, while the simulation model uses the low-resolution DEM due to the high slant range angle.

	Total	**DTM**	**DSM**
RMS error	$\delta_{rms} = 5.5\,\mathrm{m}$	$\delta_{rms} = 5.9\,\mathrm{m}$	$\delta_{rms} = 3.0\,\mathrm{m}$

Table 7.10: Flight test 1 - Laser altimeter simulation error

As expected, the simulation quality increases with the quality (resolution and accuracy) of the DEM. While the results for the entire trajectory and the DTM applied situations provides results significantly below the guaranteed DEM accuracy the application of the DSM in the simulation model outperforms the remaining situations. The comparison however is slightly biased due to the fact that the DSM is only available in the near surrounding of the airfield, where the aircraft is flying with low ground clearance.
The interpretation of the measurement and simulation results of the second trajectory is given in 7.48.

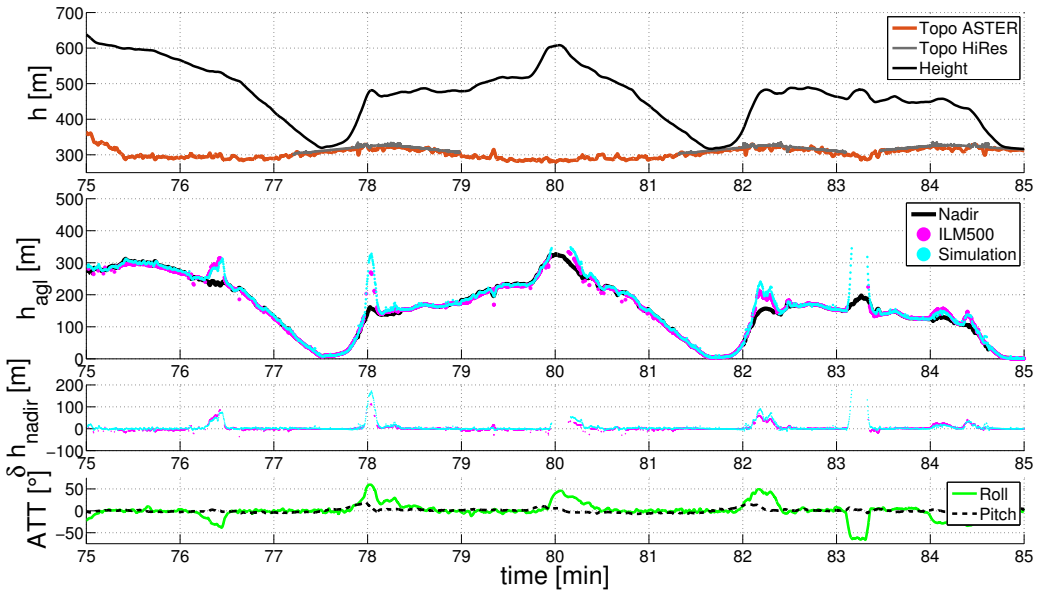

Figure 7.48: Flight test 2 - Laser altimeter simulation

While the results show similar characteristics, the measurement outages at $t = 80.0\,\text{min}$ and at $t = 83.2\,\text{min}$ influence the comparability of the DEM dependency. Especially the behavior of the simulation model during the bank-to-turn maneuvers at $t = 76.3\,\text{min}$, $t = 78.0\,\text{min}$ and $t = 82.2\,\text{min}$ matches the real data well. To quantify this results, the RMS errors are given in table 7.11.

	Total	**DTM**	**DSM**
RMS error	$\delta_{rms} = 6.8\,\text{m}$	$\delta_{rms} = 7.2\,\text{m}$	$\delta_{rms} = 4.1\,\text{m}$

Table 7.11: Flight test 2 - Laser altimeter simulation error

While the results are slightly worse compared to the results of the first trajectory, a significant improvement by using a DSM as simulation model reference is observable. The degradation of the simulation model fit is caused by the increased number of roll maneuvers. Additionally, these maneuvers are realized with higher platform dynamics.
For the third trajectory, the comparison of simulation model with the real data is not representative. Environmental conditions like fog and rain are not covered by the simulation model, and thereby the erroneous measurements of the Laser altimeter cause a huge difference to the simulation model. This trajectory however is a good demonstration of

the limitation of the developed altimeter simulation model. The vertical situation of the third trajectory is plotted in figure 7.49.

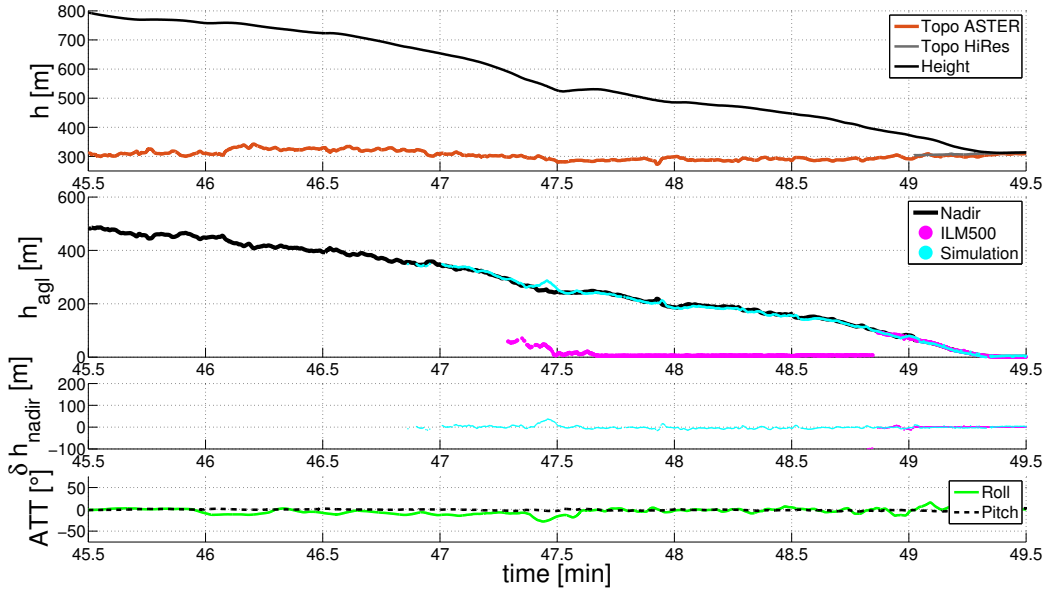

Figure 7.49: Flight test 3 - Laser altimeter simulation

For completeness reasons, the RMS evaluation is executed for this trajectory, too. The results are given in table 7.12.

	Total	**DTM**	**DSM**
RMS error	$\delta_{rms} = 147.8\,\mathrm{m}$	$\delta_{rms} = 153.6\,\mathrm{m}$	$\delta_{rms} = 3.0\,\mathrm{m}$

Table 7.12: Flight test 3 - Laser altimeter simulation error

The RMS value for the entire trajectory and for the DTM parts rise to above 100m. Only the error indication of the DSM parts, where the Laser altimeter is working nominal again, is representative and is in the same magnitude as the earlier results.

7.5.2.2 Radar Altimeter

The same analysis as performed for the Laser altimeter is subsequently done for the Radar altimeter. While the simulation model performance for the Laser altimeter is only based on the platform normal range, and thereby, due to the pencil beam-shape, on one surface point on the applied DEM, the Radar altimeter model simulates the complete beam-shape. For a better understanding of the effects of the beam shape and to explain effects of the simulation model in comparison to the measurements, figure 7.50 provides the HPBW footprint of the trajectory.
The figure shows the HPBW footprint of the simulated Radar altimeter of the recorded trajectory as red area. As mentioned earlier, the real data evaluation is based on two different DEM types. While the gray area is covered by the ASTER database with a resolution of about 30 m, for the colored area, a local hi-resolution DSM is available with

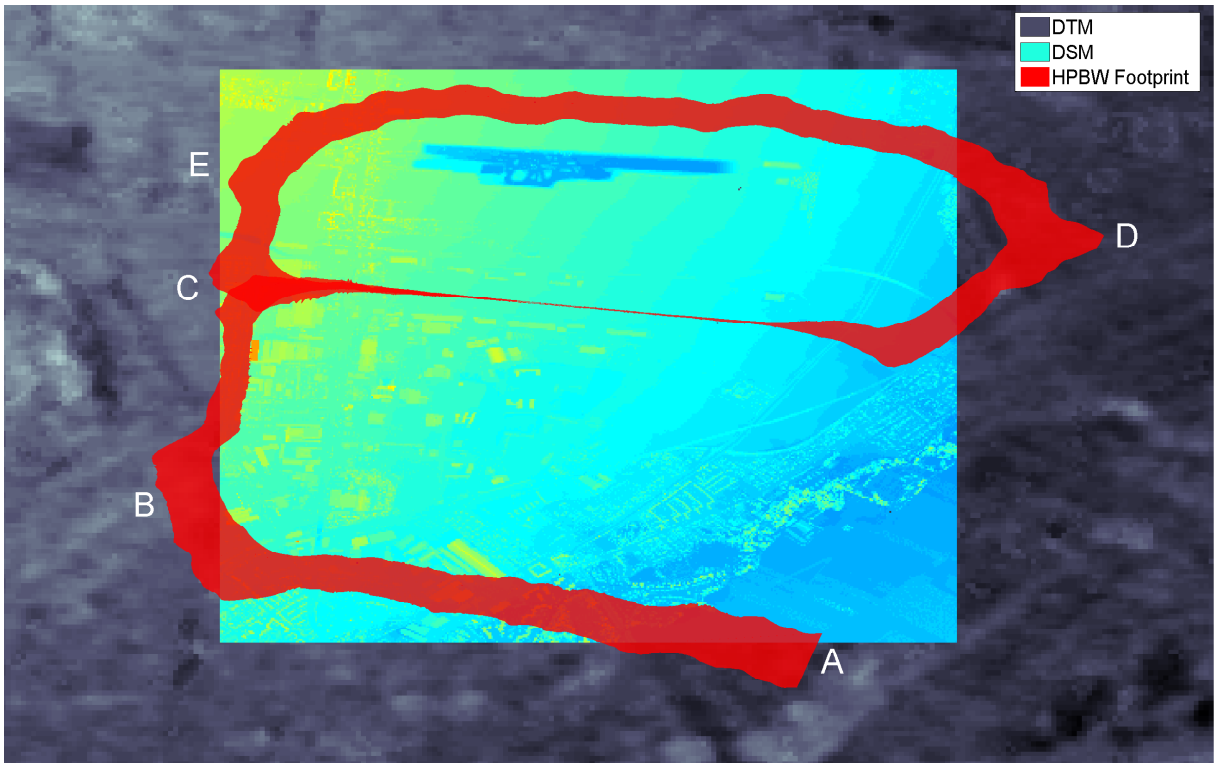

Figure 7.50: Flight test 1 - HPBW footprint

a resolution of about 1 m. The trajectory starts at the lower edge of the illustration (position A) and continuous with the downwind leg. Thereby, the borders between high- and low resolved DEM are crossed. The base leg is initiated at B, where the platform roll angle causes the footprint to exceed the highly resolved DEM again. This causes a degradation of the altimeter simulation model quality. The trajectory continues with the final approach, the decreasing height above ground reduces the HPBW footprint width. At letter D, the turn maneuver is initiated directly after the go-around. The trajectory is continued with the downwind leg and the base leg, indicated by the letter E before the final approach and landing.
The vertical situation of the measurements and altimeter simulation model results are given in figure 7.51.
The plot also features the normal height above ground. While this indication is equal to the pencil beam range of a Laser altimeter, for a Radar altimeter, the platform normal corresponds to the antenna center. Obviously, this is just valid if the antenna is mounted parallel to the platform fuselage, which is typically required for the antenna mounting. The three situations, where the simulation performance is expected to degrade (A-C) can be identified between $t = 64.1\,\text{min} - 64.5\,\text{min}$. During this period, the measurement errors exceed 100 m, while the simulated nadir error is about half of the measured deviation. This is mainly caused by the low-resolved DTM. Subsequently, the simulation model performs well. To quantify the results, the RMS error indications are given by table 7.13. The quality metric of the resulting assessment follows exactly the road map of the Laser altimeter comparison.
The match of the simulation results to the recorded Radar altimeter real data is within the accuracy and resolution of the applied DEM. As expected, the application of the high resolution DSM improves the fit of simulation and real data significantly.

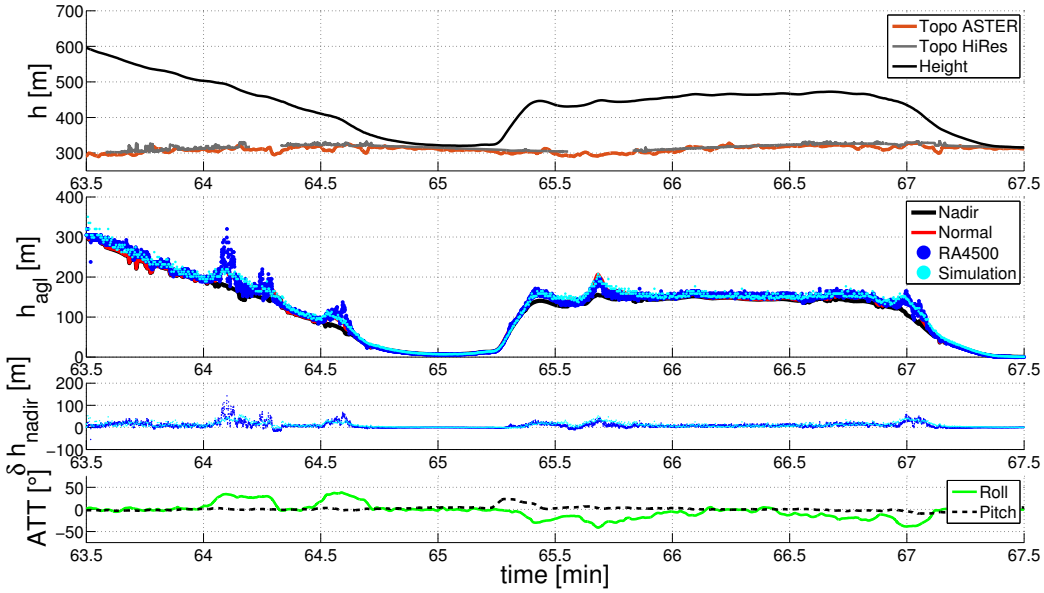

Figure 7.51: Flight test 1 - Radar altimeter simulation

	Total	**DTM**	**DSM**
RMS error	$\delta_{rms} = 10.0\,\mathrm{m}$	$\delta_{rms} = 11.0\,\mathrm{m}$	$\delta_{rms} = 5.1\,\mathrm{m}$

Table 7.13: Flight test 1 - Radar altimeter simulation error

The footprint of the second trajectory is illustrated in the same way in figure 7.52. The trajectory starts in the South at letter A. The final approach is initiated with a bank-to-turn at B, where the increased width of the footprint indicates the high roll angle. The glide path with decreasing height above ground enforces the reduction of the footprint width. The trajectory is continued with a 180° turn at C, and the downwind sector heading West.

The footprint at D, where the second approach is initiated, shows an artifact. In this situation, the high bank angles enforce the outer HPBW angle to exceed 90° and is thereby parallel to the Earth's surface or directing into the sky. In this situation, an intersection with the surface cannot be calculated.

The footprints of the second approach are similar to the first approach. The approach is aborted with a subsequent go-around and right turn maneuver. At letter E, again a 180° maneuver is flown with high roll angles $\phi \gg 60°$. In this situation, the outer half power beam width edges cannot be calculated, and therefore the footprint is discontinued. The approach ends with a standard approach leading to F and a subsequent landing. The vertical analysis is given in figure 7.53.

It provides a good fit between the measured and the simulated height above ground. The simulation model matches the recorded data, not only in the leveled flight situations, but also in the bank-to-turn maneuvers. The RMS errors are given in table 7.14.

The longer flight time above the low resolved DEM degrades the RMS results for the total trajectory. Additionally, the deviations of the bank-to-turn maneuvers are larger since they are flown above low-resolved DEM. The simulation model applied above DSM shows

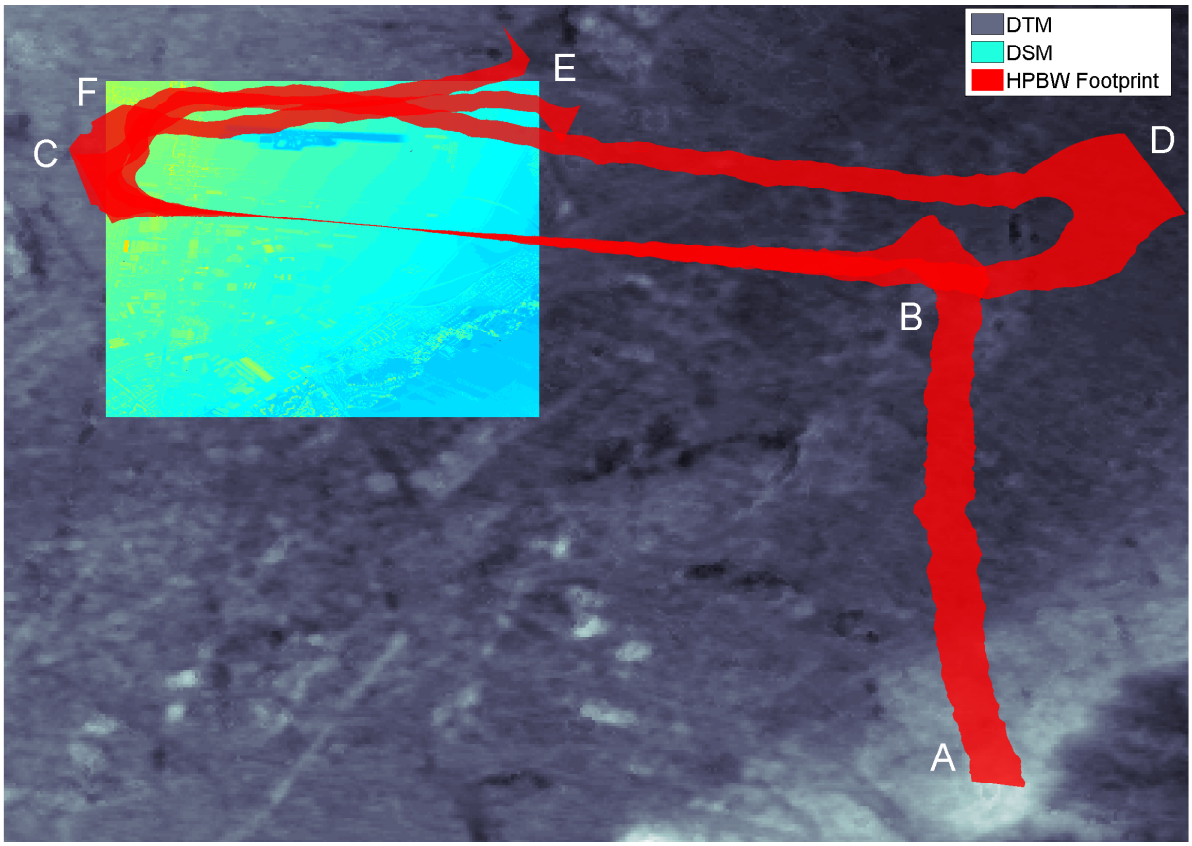

Figure 7.52: Flight test 2 - HPBW footprint

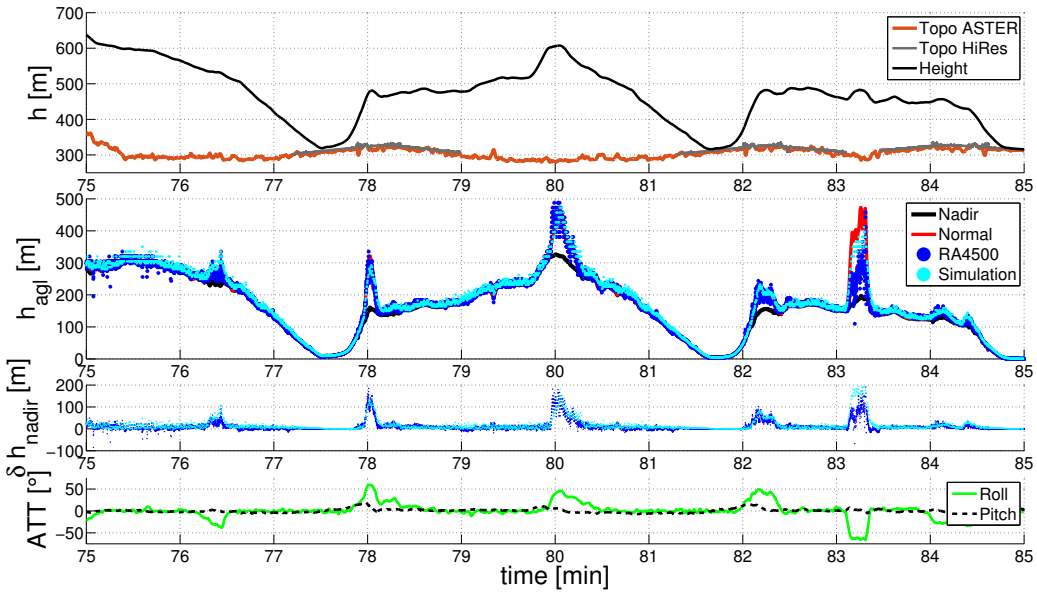

Figure 7.53: Flight test 2 - Radar altimeter simulation

an even better performance than in the first scenario. Finally, the footprint of the third trajectory is illustrated in figure 7.54.

The trajectory starts in the South at A, leading in a sustained left turn to the final approach at B. The bank angle is almost equal along the left turn. The vertical results of the third approach trajectory are plotted in 7.55.

	Total	DTM	DSM
RMS error	$\delta_{rms} = 17.0\,\mathrm{m}$	$\delta_{rms} = 18.4\,\mathrm{m}$	$\delta_{rms} = 4.4\,\mathrm{m}$

Table 7.14: Flight test 2 - Radar altimeter simulation error

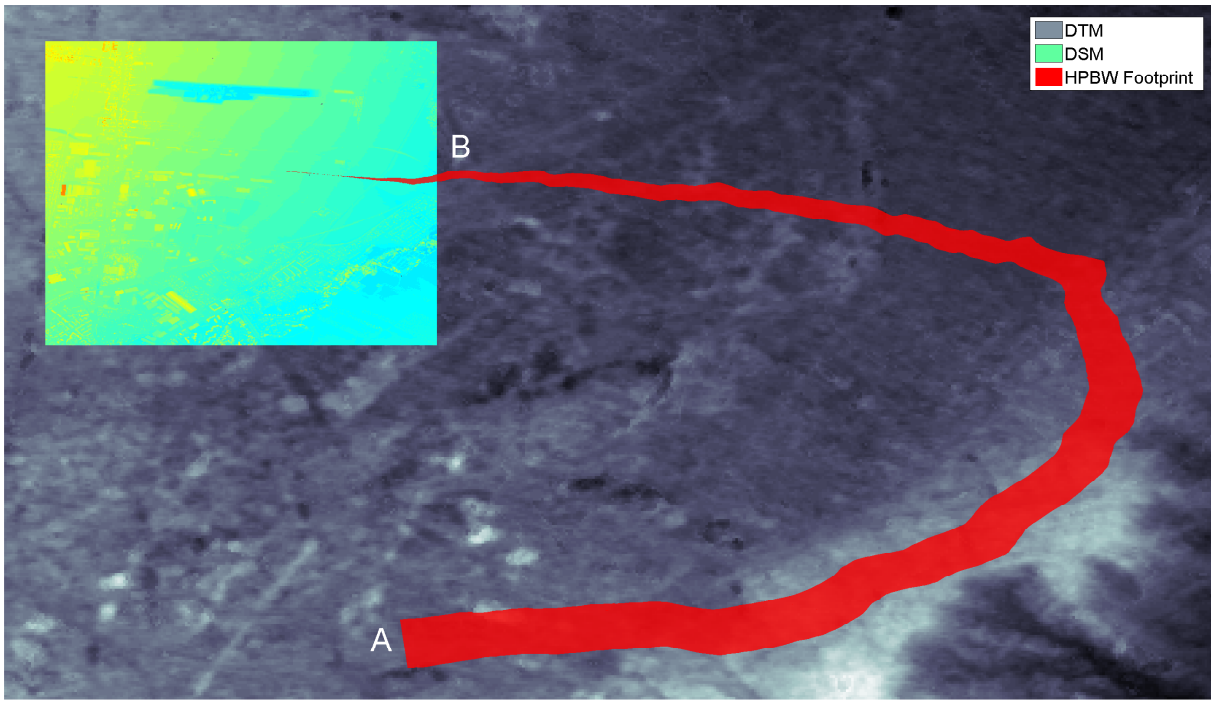

Figure 7.54: Flight test 3 - HPBW footprint

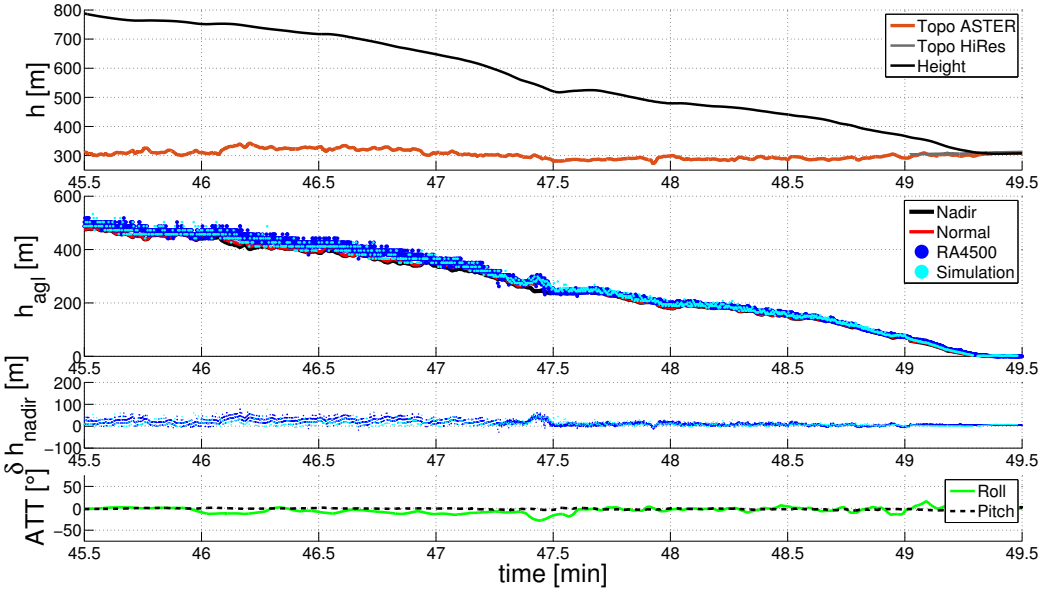

Figure 7.55: Flight test 3 - Radar altimeter simulation

While both other trajectories started at a height above ground of about $h_{agl} \approx 300\,\mathrm{m}$, this trajectory start significantly higher at $h_{agl} \approx 500\,\mathrm{m}$. The noise effects caused by

surface variation within the large beam-cone shape and the rounding effects of the receiver processing can be observed in the first seconds of the trajectory. Both effects are covered well by the simulation model and represent the characteristic of the real sensor. This is confirmed in the results of the RMS analysis in table 7.15.

	Total	**DTM**	**DSM**
RMS Error	$\delta_{rms} = 12.3\,\mathrm{m}$	$\delta_{rms} = 12.5\,\mathrm{m}$	$\delta_{rms} = 4.3\,\mathrm{m}$

Table 7.15: Flight test 3 - Radar altimeter simulation error

The RMS value for the entire trajectory is near to the RMS above DTM, which is caused by the long part of flight duration above DTM. Both DTM and DSM RMS errors are in the magnitude of the earlier simulations. Summarized it can be said, that the quality of the DEM has an higher influence on the Radar altimeter simulation model due to the size of the beam cone than on the Laser altimeter simulation model.

7.5.3 Validity Assessment

The validity assessment algorithm is applied as second step after comparing the simulation model to the recorded altimeter flight test data. The validation is based on the same trajectories as the ones used in the last section.

7.5.3.1 Laser Altimeter

For the validity assessment of the Laser altimeter measurements, the measurement values and the platform states and the surface environment are considered. Due to the pencil beam-shape characteristics of Laser altimeters, the validity range of the roll and pitch angle is limited which avoids an increase of slant range measurement errors. Additionally, the measured values are compared to the simulation model outputs. If the deviation between simulation and measurement exceeds the defined limit, the measurement is excluded. The settings of the Laser altimeter validity assessment algorithm are given in table 7.16.

Criteria	**Settings**
Roll angle	$\leq 10°$
Pitch angle	$\leq 10°$
Simulation model deviation	$\leq 5\,\mathrm{m}$

Table 7.16: Laser altimeter validity criteria

The Laser altimeter measurements and the validity assessment results are depicted in figure 7.56. Furthermore, invalid measurements are indicated in red color, valid measurements in blue. For the validity analysis, only the absolute height, the nadir height above ground error and the platform attitude are plotted.

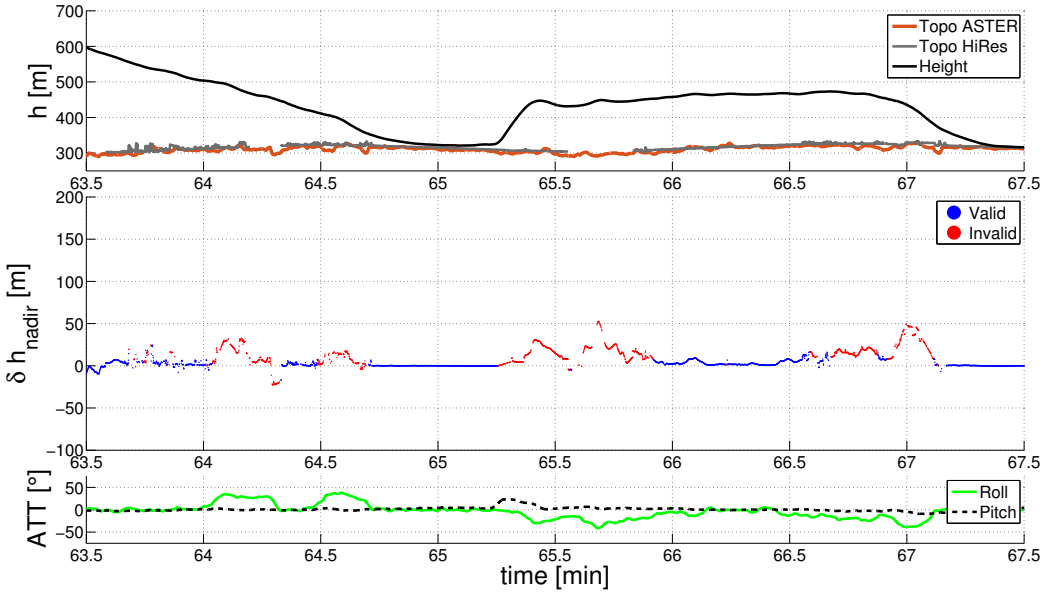

Figure 7.56: Flight test 1 - Laser altimeter validity assessment

The middle plot of the vertical analysis shows a very good detection rate of erroneous measurements. However, this methods strongly depends on the simulation model quality and thereby on the accuracy and resolution of the applied DEM. The RMS errors of the entire measurements are displayed with respect to the results of the validity assessment. The validity assessment results are given for the entire trajectory and for the sequences above the DTM and DSM, separately. Additionally, the exclusion rates, which provide the relation between excluded and total measurement numbers, are indicated for all three cases. The analysis is given in table 7.17.

		Validity assessment		
	Raw	**Total**	**DTM**	**DSM**
RMS error	$\delta h_{rms} = 11.5\,\mathrm{m}$	$\delta h_{rms} = 3.7\,\mathrm{m}$	$\delta h_{rms} = 5.0\,\mathrm{m}$	$\delta h_{rms} = 3.2\,\mathrm{m}$
Exclusion rate		35.4 %	60.0 %	23.3 %

Table 7.17: Flight test 1 - Laser altimeter validity assessment

For this recorded trajectory, the RMS error could be reduced by a factor of four for the entire measurements. The application of the DTM is slightly worse and requires a significantly higher exclusion rate, compared to the use of the DSM.
The vertical situation of the validity assessment is provided for the second trajectory by figure 7.57.
The validity assessment algorithm detects most of the measurement outliers. While most of the errors are caused by large platform angles, surface dependent errors can be observed for example at $t = 75.4\,\mathrm{min}$ and $t = 79.3\,\mathrm{min}$. The RMS errors of the algorithm performance is given in table 7.18.
The results of the first trajectory can be continued with this trajectory. While the error figures are approximately in the same magnitude, the exclusion rate for the DTM application was significantly reduced.

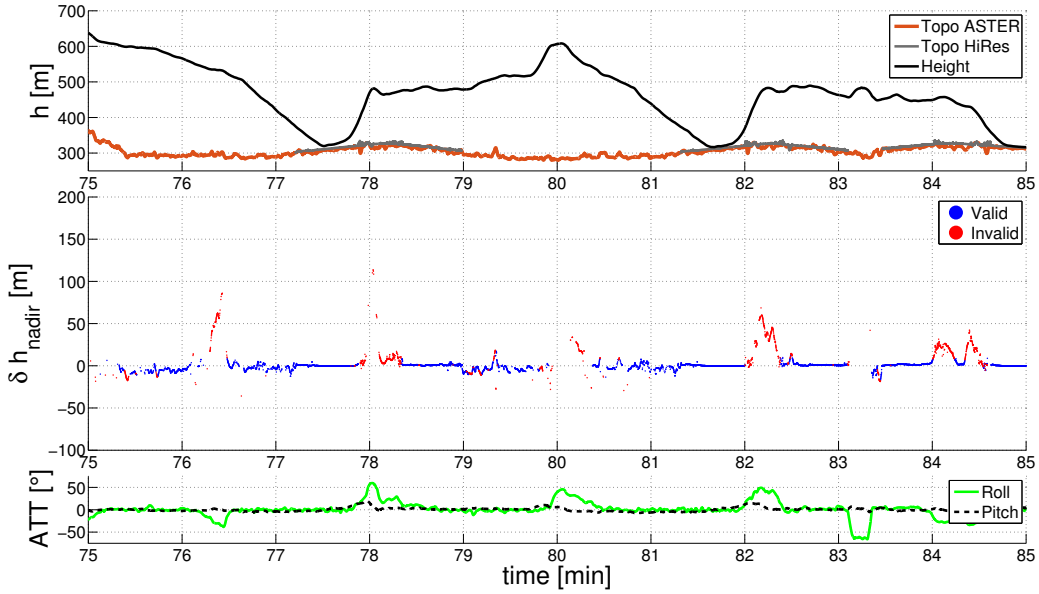

Figure 7.57: Flight test 2 - Laser altimeter validity assessment

		Validity assessment		
	Raw	**Total**	**DTM**	**DSM**
RMS error	$\delta h_{rms} = 11.1\,\text{m}$	$\delta h_{rms} = 3.3\,\text{m}$	$\delta h_{rms} = 4.7\,\text{m}$	$\delta h_{rms} = 1.3\,\text{m}$
Exclusion rate		17.9 %	22.3 %	13.9 %

Table 7.18: Flight test 2 - Laser altimeter validity assessment

The validity assessment of the third trajectory is the most representing result, due to the application-related scenario. The approach trajectory is flown under poor environmental conditions, including light fog. Obviously, erroneous measurements can be detected easily in the post-processing, but an in-flight evaluation of the altimeter measurement would support the pilots. The vertical validity indications are given in figure 7.58.
The erroneous reflection caused by the cloudy environment are excluded by the simulation model comparison. The performance measures are given in table 7.19.

		Validity assessment		
	Raw	**Total**	**DTM**	**DSM**
RMS error	$\delta h_{rms} = 151.1\,\text{m}$	$\delta h_{rms} = 3.0\,\text{m}$	$\delta h_{rms} = 4.7\,\text{m}$	$\delta h_{rms} = 0.5\,\text{m}$
Exclusion rate		72.2 %	86.3 %	23.5 %

Table 7.19: Flight test 3 - Laser altimeter validity assessment

While the majority of measurements above DTM surface is excluded, the remaining measurements can be improved to a quality comparable to the previous results.

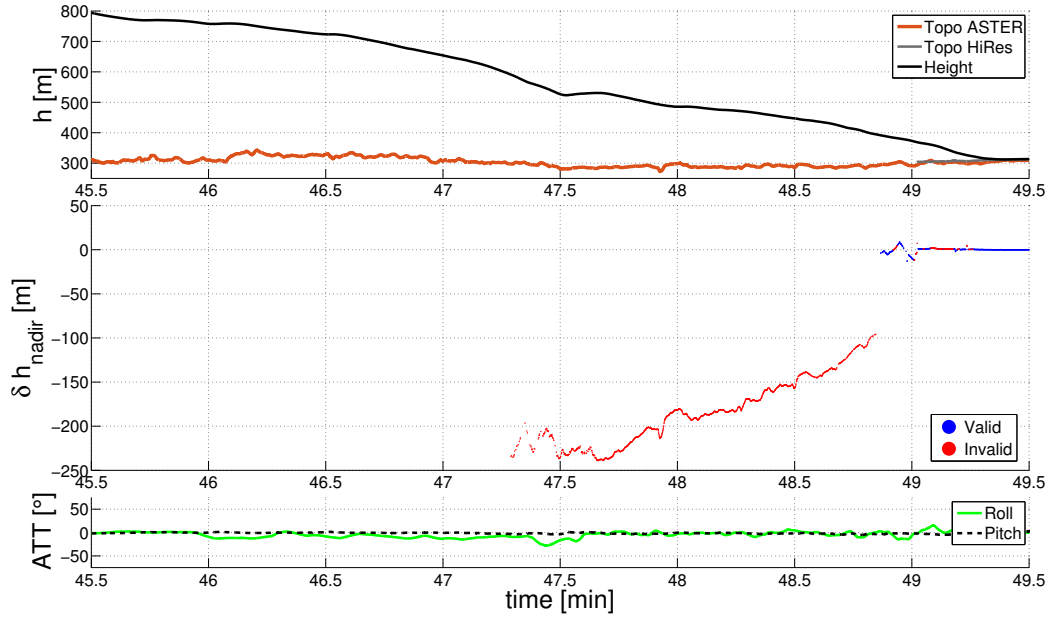

Figure 7.58: Flight test 3 - Laser altimeter validity assessment

7.5.3.2 Radar Altimeter

The same investigation as performed for the Laser altimeter is now done for the Radar altimeter. The parameter settings for the applied Radar altimeter model are given in table 7.20. Additionally to the criteria of the Laser altimeter validity assessment, the dispersion of simulated height is considered for the Radar altimeter. If the dispersion is excessively larger in relation to the height above ground, a measurement error is probable and the measurement is excluded.

Criteria	**Radar altimeter**
Roll angle	ϕ_{hpbw}
Pitch angle	θ_{hpbw}
Simulation model deviation	$\leq 10\,\mathrm{m}$
Received signal dispersion	$\sim h_{agl}$

Table 7.20: Radar altimeter validity criteria

The vertical situation of the first trajectory is given in figure 7.59.
The vertical situation shows a good detection rate of the validity assessment algorithm. The platform attitude is the driving factor, however some single outliers are detected with other criteria. The performance measures are given in table 7.21.
The RMS errors can be reduced by a factor of two using the DTM, and by a factor of three using the DSM. The vertical plots of the second trajectory are shown in figure 7.60. The vertical comparison provides similar results, the improvement by using the validity assessment algorithm is provided in table 7.22.
In this example, the error values are in the same magnitude compared to the first trajectory, however, the measurement error is significantly higher. Finally, the approach

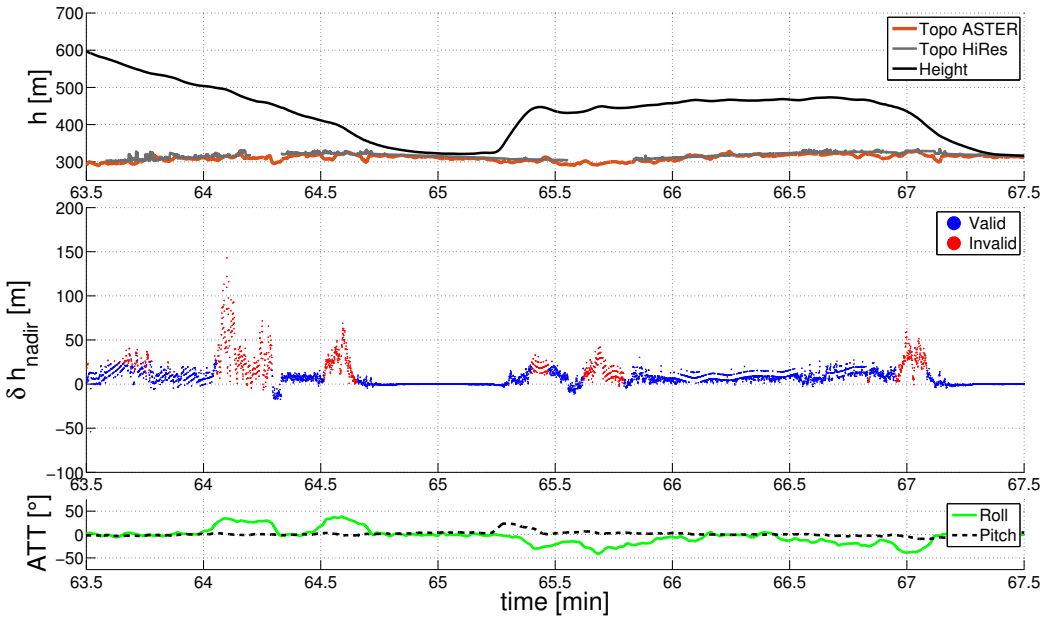

Figure 7.59: Flight test 1 - Radar altimeter validity assessment

		Validity Assessment		
	Raw	**Total**	**DTM**	**DSM**
RMS Error	$\delta h_{rms} = 15.8\,\text{m}$	$\delta h_{rms} = 8.6\,\text{m}$	$\delta h_{rms} = 9.7\,\text{m}$	$\delta h_{rms} = 5.0\,\text{m}$
Exclusion Rate		20.5 %	25.0 %	7.0 %

Table 7.21: Flight test 1 - Radar altimeter validity assessment

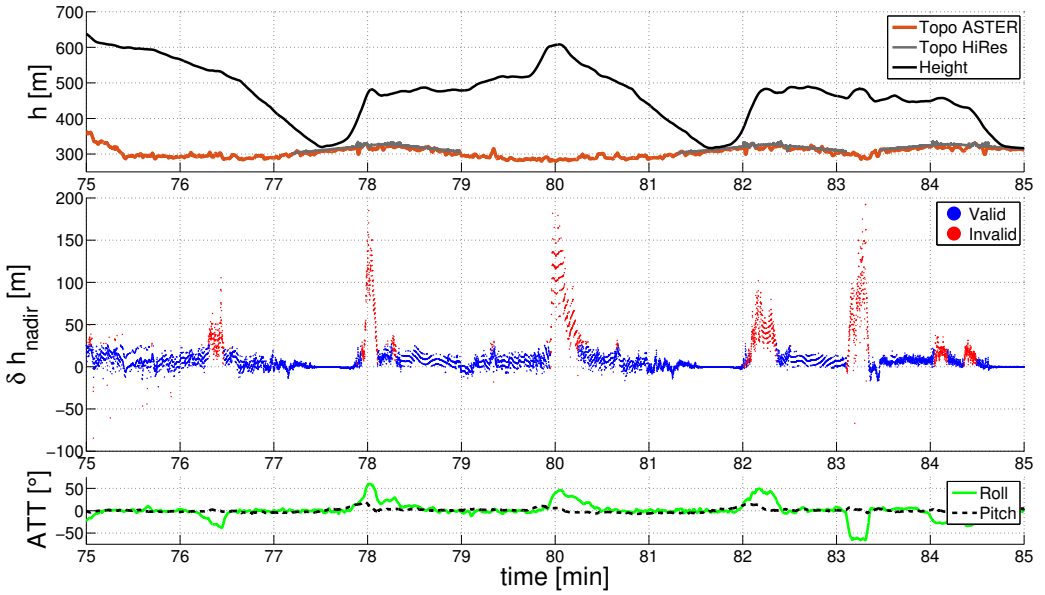

Figure 7.60: Flight test 2 - Radar altimeter validity assessment

trajectory is compared in figure 7.61.
In this example, the algorithm mainly excluded noisy measurements. The noise-like mea-

		Validity Assessment		
	Raw	**Total**	**DTM**	**DSM**
RMS Error	$\delta h_{rms} = 25.7\,\mathrm{m}$	$\delta h_{rms} = 8.1\,\mathrm{m}$	$\delta h_{rms} = 8.6\,\mathrm{m}$	$\delta h_{rms} = 5.4\,\mathrm{m}$
Exclusion Rate		15.6 %	18.2 %	0.6 %

Table 7.22: Flight test 2 - Radar altimeter validity assessment

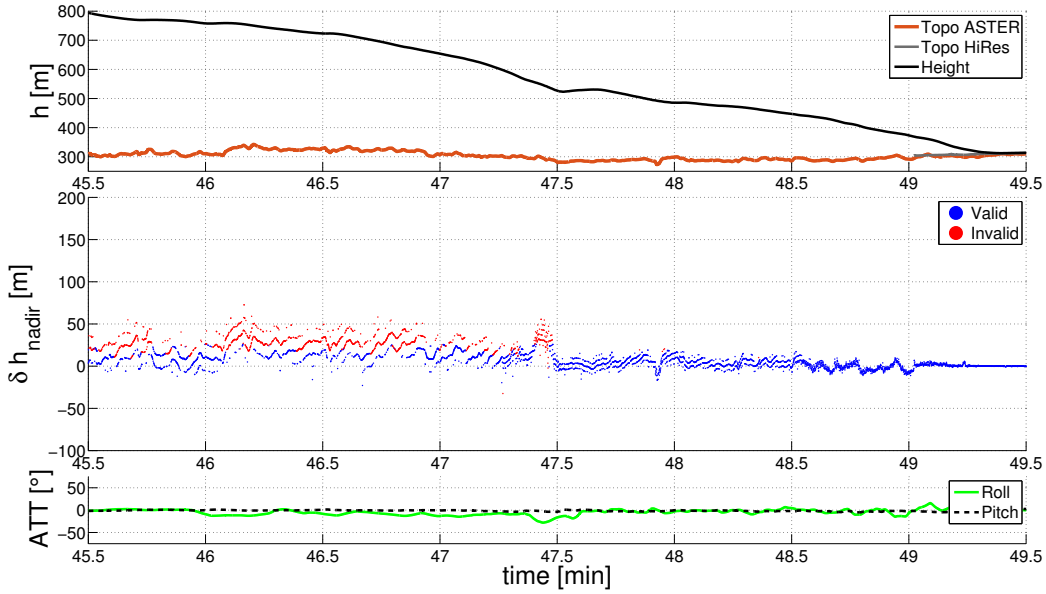

Figure 7.61: Flight test 3 - Radar altimeter validity assessment

surements are caused by bank-to-turn maneuvers. However, the roll and pitch limitation does not detect the outliers, the comparison with the simulation model can eliminate the erroneous measurements. The RMS error statistics in table 7.23 affirm these observations. The measurement error can be halved, the application of the DSM brings additional benefit and even reduces the error by a factor of ten.

		Validity assessment		
	Raw	**Total**	**DTM**	**DSM**
RMS error	$\delta h_{rms} = 16.8\,\mathrm{m}$	$\delta h_{rms} = 8.8\,\mathrm{m}$	$\delta h_{rms} = 9.0\,\mathrm{m}$	$\delta h_{rms} = 1.64\,\mathrm{m}$
Exclusion rate		23.8 %	24.9 %	0.0 %

Table 7.23: Flight test 3 - Radar altimeter validity assessment

7.5.4 Slant Range Compensation

To complete the real data evaluation, the compensation algorithm is applied to the three trajectories. The section outline is comparable to the previous considerations, the Laser altimeter compensation algorithm results are discussed first. Subsequently, the Radar

altimeter compensation results are analyzed.

7.5.4.1 Laser Altimeter

The evaluation of the Laser altimeter compensation results for the first trajectory is given in figure 7.62.

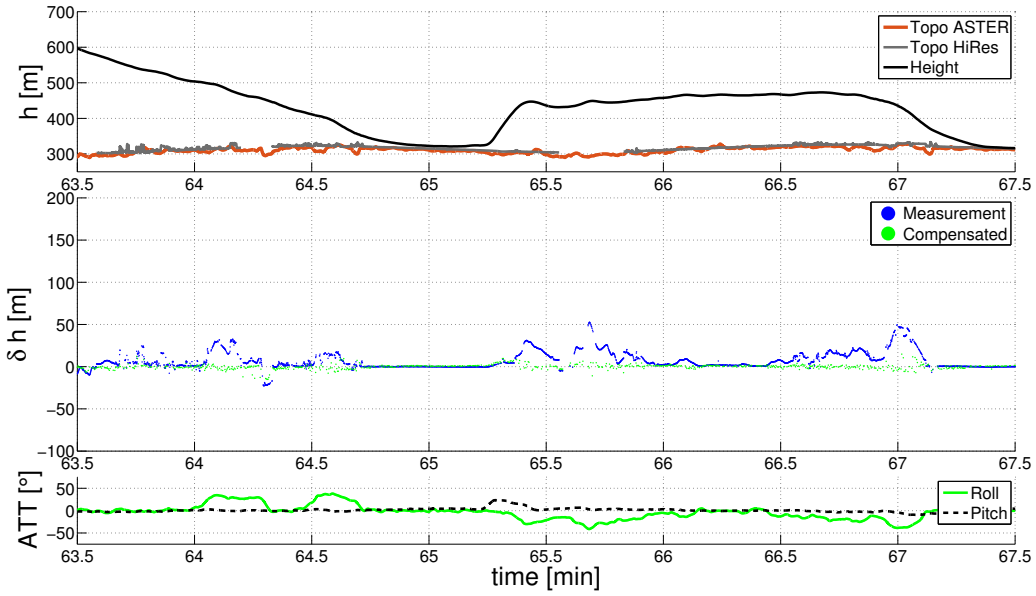

Figure 7.62: Flight test 1 - Laser altimeter slant range compensation

The upper graph of the figure shows the absolute height and the lower plot provides the platform attitude of the flown trajectory. The middle plot illustrates the compensation results and the original raw Laser altimeter measurements. Obviously, the Laser altimeter errors are reduced significantly by the introduced slant range compensation algorithm, which is used for a pencil beam measurement. The improvement is given in the familiar way as RMS errors in table 7.24.

	Raw	**Compensation**
RMS error	$\delta h_{rms} = 11.5\,\mathrm{m}$	$\delta h_{rms} = 3.0\,\mathrm{m}$

Table 7.24: Flight test 1 - Laser altimeter slant range compensation

The geometric compensation can reduce the measurement error by almost a factor of four. This result is comparable to the result of the validity assessment after excluding erroneous measurements. The compensation methods however do not exclude measurements and thereby provide a constant measurement update frequency. The results of the compensation algorithm for the measurement of the second trajectory are presented in figure 7.63.
The compensation results show a similar performance. Especially the errors induced by the bank-to-turn maneuvers are compensated. The compensation algorithm however can improve only available measurements, and thereby the outages of the recorded measurements are not compensated.

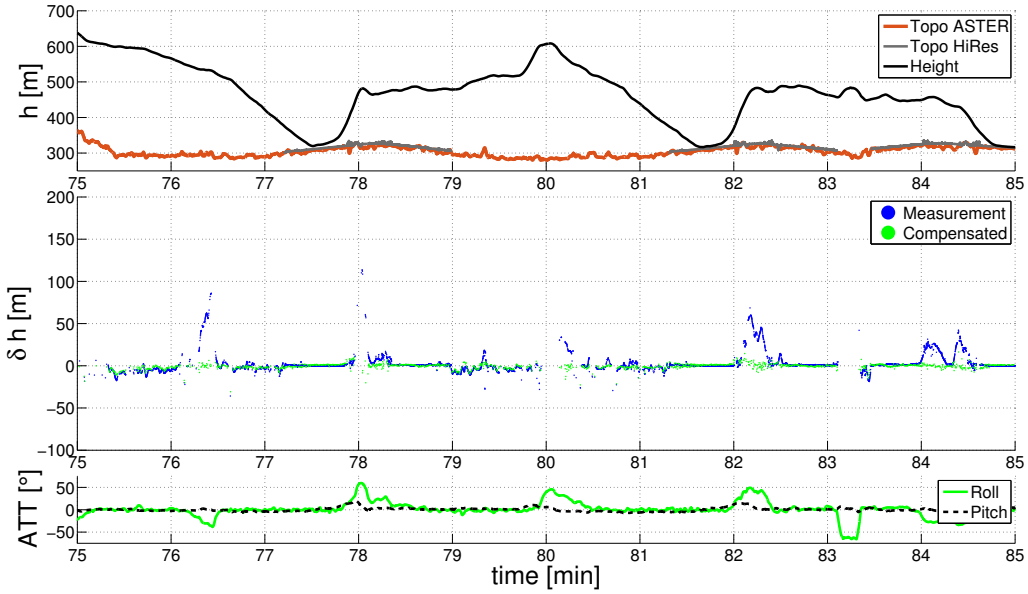

Figure 7.63: Flight test 2 - Laser altimeter slant range compensation

The RMS figures are given in table 7.25.

	Raw	Compensation
RMS error	$\delta h_{rms} = 11.1\,\mathrm{m}$	$\delta h_{rms} = 3.4\,\mathrm{m}$

Table 7.25: Flight test 2 - Laser altimeter slant range compensation

The RMS error for measurement and compensated height above ground are comparable to the results for the first trajectory. The improvement is between a factor of three and four. The measurements of the third trajectory cannot be processed by the compensation algorithm due to the large errors of the recorded height above ground measurements. The analysis is continued with the Radar altimeter compensation results.

7.5.4.2 Radar Altimeter

The compensation of Radar altimeter measurements is accomplished by a model which includes, in contrast to the Laser compensation algorithm, also the signal layer model. This signal layer model comprises the beam-shape, signal propagation effects and the receiver internal processing as described in section 2.2 and in section 3.3. The used antenna characteristics corresponds to the applied Sensor Systems S67-2002 antenna, which is integrated in the research aircraft (see figure 7.64)
For this analysis, the attitude only compensation is also applied for the Radar altimeter results. This compensation corresponds to the platform attitude compensation, assuming a measurement in direction of the antenna center. The vertical results for the first trajectory are given in figure 7.65.
The beam-shape compensation provides a significant improvement, compared to the attitude-only compensation and the raw measurements. Especially for higher heights

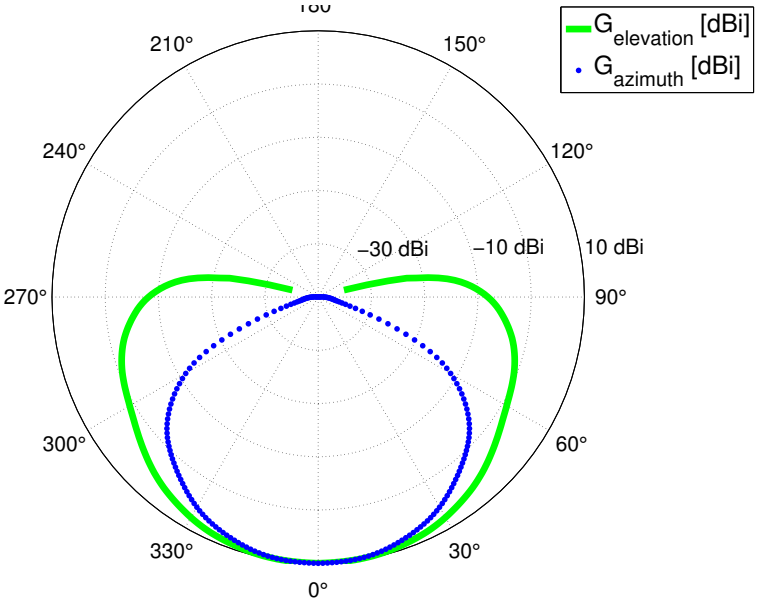

Figure 7.64: Sensor Systems S67-2002 antenna characteristics

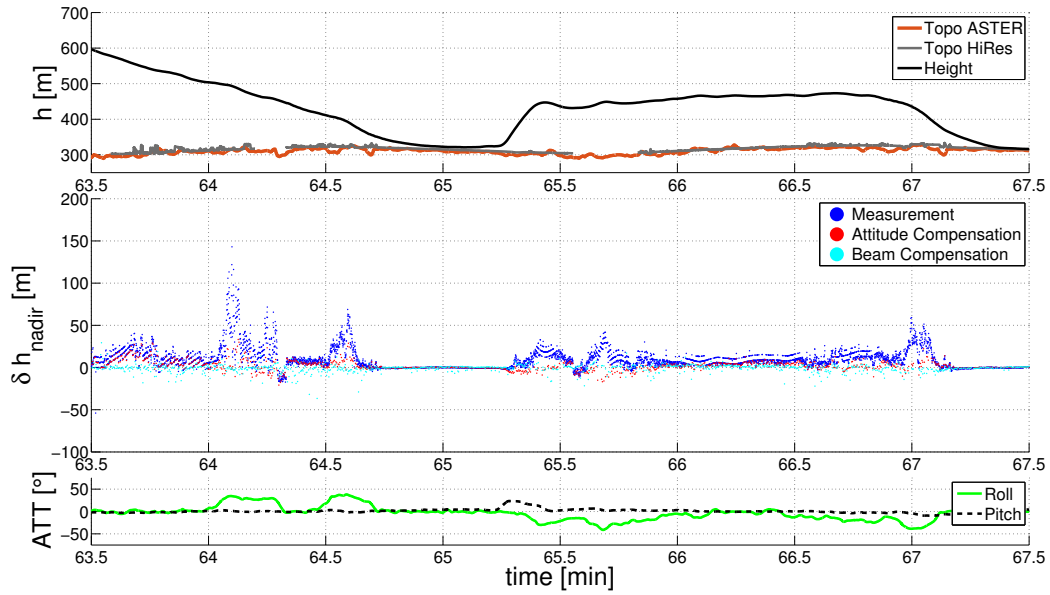

Figure 7.65: Flight test 1 - Radar altimeter slant range compensation

above ground at the beginning of the trajectory, the attitude compensation cannot completely compensate the error. The RMS figures are given in table 7.26.

		Compensation	
	Raw	**Attitude**	**Beam-shape**
RMS error	$\delta h_{rms} = 15.8\,\mathrm{m}$	$\delta h_{rms} = 6.6\,\mathrm{m}$	$\delta h_{rms} = 4.8\,\mathrm{m}$

Table 7.26: Flight test 1 - Radar altimeter slant range compensation

While the attitude compensation can improve the results by a factor of approximately

two, the beam-shape compensation yields an improvement of at least a factor of three. Following, the results of the second trajectory are presented in figure 7.66.

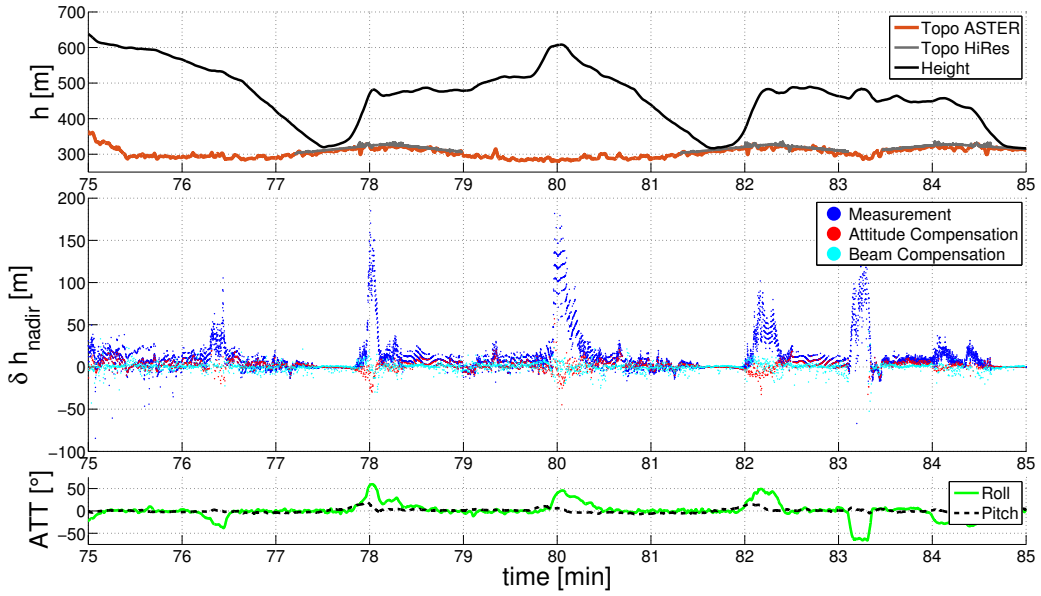

Figure 7.66: Flight test 2 - Radar altimeter slant range compensation

The enormous measurement errors can be reduced by both compensation algorithms. The analysis in table 7.27 affirms that the beam-shape compensation provides slightly better results. Both compensation algorithms can provide improvements, the attitude compensation can improve the measurement by a factor of four, the beam-shape compensation by a factor of five. The vertical situation of the last trajectory is given in figure 7.67.

		Compensation	
	Raw	**Attitude**	**Beam-shape**
RMS error	$\delta h_{rms} = 25.7\,\mathrm{m}$	$\delta h_{rms} = 6.6\,\mathrm{m}$	$\delta h_{rms} = 4.9\,\mathrm{m}$

Table 7.27: Flight test 2 - Radar altimeter slant range compensation

This chapter concludes with the results of the approach trajectory. The corresponding height above ground errors show the performance of both algorithms. The attitude compensation works well within a tolerance of about $\Delta h_{agl} \approx 200\,\mathrm{m}$. Beyond this tolerance, the beam-shape and the surface variation within the increasing footprint become a major influence. Therefore, the beam-shape compensation algorithm can provide better results in these situations and overall. The RMS figures are given in table 7.28. The results affirm the observations that the beam-shape compensation improves the measurement accuracy by a factor of approximately three.

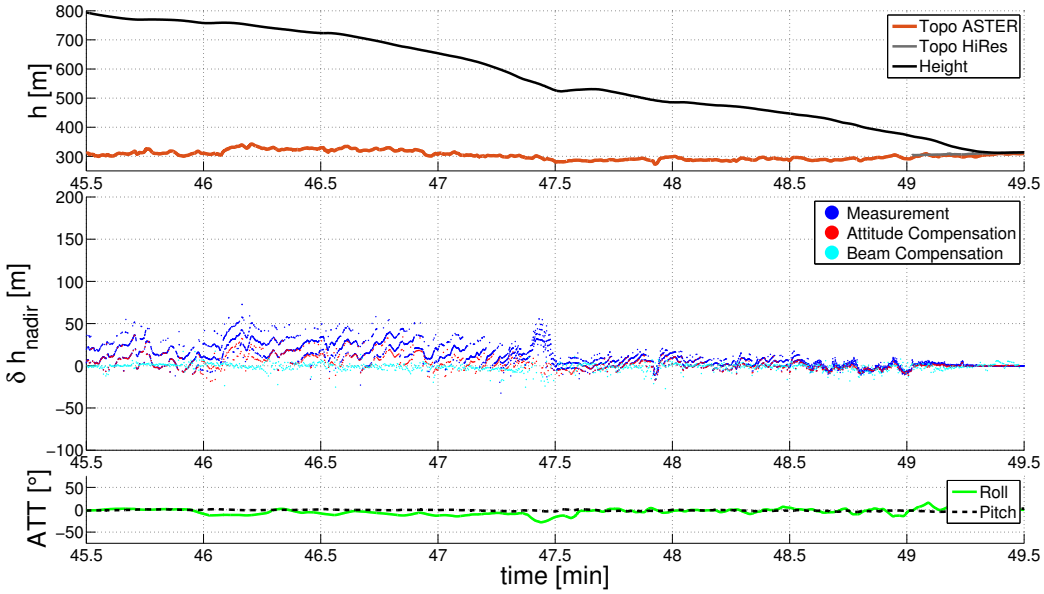

Figure 7.67: Flight test 3 - Radar altimeter slant range compensation

		Compensation	
	Raw	**Attitude**	**Beam-shape**
RMS error	$\delta h_{rms} = 16.8\,\mathrm{m}$	$\delta h_{rms} = 9.2\,\mathrm{m}$	$\delta h_{rms} = 5.0\,\mathrm{m}$

Table 7.28: Flight test 3 - Radar altimeter slant range compensation

Results

- Large raw measurement errors caused by surface variations and platform dynamics (Radar & Laser)
- Laser altimeter is sensitive to weather conditions (clouds & fog)
- Good fit of simulation model to raw measurements
- Improvement of the measurement accuracy by validity assessment
- Significant accuracy improvement by applying the compensation algorithm

Chapter 8

Conclusion

8.1 Detailed Summary

Functional Sensor Principles

This thesis started with the comparison of different altitude and height measurement methods used in aerospace applications. The time-of-flight measurement principle for height above ground measurements was introduced and the error characteristics of all methods were compared.
In order to model and simulate surface-ranging sensors, the functional principles of the three considered sensor classes ranging, range-scanning and range-imaging were introduced. Particularly the signal propagation effects on a Radar signal and its processing in the receiver were analyzed in detail.
The formal description of a slant range measurement was introduced including sensor mounting and measurement coordinate frames.

Sensor Modeling

A modular sensor simulation model including a geometric and a signal layer was developed. The model considers different types of DEMs including the Earth's surface in DTMs and the surface objects in DSMs. The bilinear interpolation of the surface was described to ensure a continuous DEM surface. To determine the geometric distance to the surface, a fast ray tracing algorithm using a tile prediction and an analytic intersection determination was implemented. For the closed solution of the intersection of the ray with a bilinear surface an approach using two auxiliary planes was used.
Based on the geometric distance, a simple ranging error model considering noise and scale factor errors was established. The detailed error model comprised signal propagation and signal processing. The beam shape was modeled using a large number of rays, angular distributed around the antenna boresight. A geodesic dome construction was used to ensure an uniform surface distribution of the rays.
The entire signal represented by multiple rays was reconstructed at the reception antenna and the internal receiver signal processing was simulated including the mix-down with the local oscillators and the low-pass filters. A baseband representation of the entire signal was calculated and used to reduce the computational load.
The simulation model, parametrized as Radar altimeter, was validated with real data which were recorded in a flight test campaign with an octo-copter. Three characteristic

trajectories was used to show the performance of the simulation model. The performance was quantified by comparing the simulated with the measured height, and the limitations of the simulation model were identified. The strong dependency on the currentness and accuracy of the applied DSM was identified in the validation steps.

Concept of Operation

The limitations of surface-ranging sensors were analyzed theoretically. Apart from environmental influences, ranging errors caused by the platform attitude, surface variations, the beam-shape and signal propagation effects were discussed. The influences of the error sources and their interactions were discussed in detail including their interactions.
The slant range errors were demonstrated on two simulated trajectories above a flat Earth's surface and with a realistic topographic elevation profile. The developed surface-ranging sensor simulation model was applied for this analysis.

Measurement Validity

To enhance the robustness of surface-ranging measurements, a method to assess the measurement validity was introduced. Apart from the sensor internal validity assessment, this method extends the validity consideration to the platform state and surrounding surface. Two different validity criteria sets for narrow and wide beam shaped sensors were defined.

Measurement Variance

The measurement variance was derived for the usage of the altimeter height as direct height above ground measurement, as slant range distance and as georeferenced measurement point. The beam-shape of different sensors was considered in the derivation. The derived variance was used to estimate the measurement quality for aiding a central navigation filter.

Slant Range Compensation

To not only detect erroneous measurements, to exclude them or to estimate their accuracy, three compensation methods to improve the measurement accuracy were introduced. The three methods are addressing different applications with different sensor and surface characteristics and available on-board computational power. The attitude compensation can be applied in missions above flat surface when a sensor with a narrow beam-shape is used. This compensation method corrects the measurement errors caused by the platform attitude. The range compensation can be used to compensate errors of the narrow beam-shape sensor if the mission profile is extended to rough surface. This extension considers the surface variations of the platform nadir and measurement point additionally to the platform attitude. The beam compensation can be applied independent of the overflown surface when it comes to sensors with wide beam-shape. In addition to the platform attitude and surface variation, this method also considers the beam-shape of the applied sensor.
The methods can be used as stand-alone compensation or integrated in the Kalman filter measurement matrix. Therefore, the measurement matrix was derived. The performance

of the compensation methods was validated on a recorded octo-copter trajectory with a significant accuracy improvement.

Basic SAN Concepts

As introduction to horizontal position and height estimation from surface measurements, the basic concepts of SAN were explained. Existing systems were categorized concerning the applied techniques and several background information.
A concept for a direct altimeter aiding to improve the horizontal position was introduced and discussed. Especially the pros and cons of the DEM linearization approach were discussed.
The batch processing with a matching metric and a grid-search algorithm was discussed in detail, which is the base for further improvements. For the integration of the measurement in a central navigation filter, a basic method to estimate the measurement covariance was introduced.

Information Exploitation

The influence of the elevation gradients on the shape of the matching matrix was analyzed. Based on the analysis results, an information exploitation method was introduced which selects the measurements with the highest impact on the matching metric. Thereby, the points with the highest elevation gradient improve the horizontal positioning information most. The algorithm was demonstrated in two synthetic examples as well as several real DEM regions showing performance improvements. Two matching results for a simulated trajectory above a DSM with and without the information exploitation method were compared and have shown the expected improvements.

Surface Sampling

The sampling of the overflown surface was discussed for two synthetic examples. The goal of this consideration was the reduction of ambiguities in the matching metric. The effects of an under-sampling were shown and the improvements by increasing the sampling was demonstrated. In combination with the information exploitation, this method can reduce the processed measurement points as well as the reduction of matching ambiguities.
The sampling of the surface was additionally considered in the frequency domain to analyze the information content of the overflown surface. This approach is based on a spatial Fourier transformation. The importance of the Nyquist-Shannon sampling theorem for spatial analysis was demonstrated by an example.

Translational Drift Estimation

The effects of the translational drift during each measurement interval was discussed and the benefits of an intrinsic compensation were shown. The relative compensation of the growing translational errors in the measurements with different time-stamps was demonstrated. With this method, the matching results can be improved in shape and accuracy.

Closed-loop Slant Range Compensation

The benefits of processing slant range compensated measurements in the matching metric were demonstrated in a synthetic example. A method to compensate slant range errors in the grid-search matching algorithm was introduced.
The grid-search algorithm was adjusted to the additional computational load required from the compensation algorithm. The optimized grid-search function calls were compared against a classical approach.
A detailed algorithm flow was used to explain the combination of a grid-search with a matching algorithm and a slant range compensation. The closed-loop slant range compensation was demonstrated in comparison to a conventional approach with significant improvements. A calculation-time efficient method which combines a regular grid for coarse search and a compensation algorithm for fine search was proposed.

Multi-beam SAN

The basic idea of increasing the measured information content was extended to a multi-beam SAN approach. Three different multi-beam sensor setups using fixed and steered beams were discussed. The performance of the three methods using fixed-beams, beam-switching and beam-steering were compared in simulation. All multi-beam methods have provided a performance impact compared to a single-beam approach.

Dead Reckoning SAN

The measurement concept of a dead-reckoning SAN was explained for range-scanning and range-imaging sensors to allow a DEM independent aiding. The difference and challenges of range-scanning measurements were discussed in detail and compared against a range-imaging measurement regarding the regular surface sampling, the sequential data collection and the time-to-overlap estimation. The sensor settings for different trajectory parameters were investigated for both kinds of sensors. The extension of the matching algorithm for a irregular point cloud processing was explained. The influence of the position error drift within the measurement period was discussed for range-scanning sensors in comparison to range-imaging sensors. The integration of a position error increment measurement aiding in a central navigation filter was proposed.

Flight Test Instrumentation

The integration of two altimeters and a reference sensor suite in the institute's research aircraft was shown. The sensor setup of the aircraft concerning the sensor mounting locations, the sensor interfaces and update frequencies was illustrated. For data logging, the FTI based on an automation computer was introduced which provides benefits concerning the modularity and extendability of the system. Apart from the hardware setup, the software structure and the data logging concept were explained including the buffer structure and the time stamping.
Apart from data logging, the in-flight data interpretation and visualization was discussed. Especially the bidirectional communication between the user interface, the FTI and the connected sensors was explained.

For developing and testing purposes, a FTI HIL setup was installed and the underlying principle was described.

Flight Emulation and Simulation

The simulation environment was described containing the three layers trajectory generation, sensor data generation and system simulation. A spline approach was chosen for trajectory generation to provide continuous trajectory states. It can be fed by real flight test data or from any kind of aerodynamic flight simulation. The tool was validated by an one hour free inertial integration to show that the numerical errors were dominating the error spectrum.
The vertical aiding of an INS with the introduced slant range compensation algorithm was demonstrated in an approach simulation. The result was compared against INS/GNSS results and a classical height above ground aiding with strong performance impacts.
As an alternative application, the use of the altimeter measurements as ground-clearance monitoring system was demonstrated. Especially in platforms without high computational capacity, this method is advantageous in an approach scenario. The system outputs a height integrity monitor as long as the platform horizontal guidance was on the defined path. Additionally, the glide slope deviation can be calculated with this approach.
The performance of the position aiding SAN was demonstrated along a highly dynamic trajectory. The introduced methods information exploitation, translational drift estimation, validity assessment, attitude compensation and closed-loop slant range compensation were applied cumulatively in four different setups. The results of the methods were demonstrated and subsequently the joined SAN algorithm performance was shown. Therefore, the algorithms were applied on three different scenario profiles of the trajectory. First, an additional aiding of the INS/GNSS system with the PPSAN algorithm was demonstrated which yields a performance gain. As second application, the PPSAN algorithm was used to bridge short sequence of GNSS degradation and finally, the aiding was used to bridge short GNSS outages. The PPSAN method was able to manage all scenarios with an positioning accuracy comparable to GNSS given sufficient sensor and DSM accuracies.
To demonstrate the benefits of a multi-beam approach, the simulation was repeated with four additional sensor setups including three, five, seven and nine measurements. In the GNSS degraded and denied scenarios, the methods were beneficial compared to the single measurement approach, whenever additional information can be measured.
The nine beam approach was compared with a single-beam method and an unaided INS in a long-term GNSS denied situation. While the unaided position solution drifts several meters, both SAN methods provide a stable position solution with slight benefits for the multi-beam approach in the provided scenario.
The performance of the dead-reckoning SAN method was demonstrated during a long-term GNSS outage with good results. However, the position error was drifting slightly compared to the absolute aiding of the PPSAN approach, the drift was reduced significantly compared to an unaided solution.
The recorded raw measurements of a Radar and a Laser altimeters were compared in three recorded flight test trajectories. The real data was compared against the simulation model results and the differences were quantified as RMS errors. The dependence on the applied DEM was demonstrated and illustrated in a beam footprint illustration for all trajectories. The validity assessment method was applied to the three trajectories and both sensors and

the performance impact was calculated. The method has improved the altimeter accuracy by a factor of three to four by detecting and excluding erroneous measurements. The compensation algorithm was furthermore applied with an improvement of a factor three to four to Laser altimeter measurements. For the Radar altimeter, the attitude compensation was compared with the beam compensation. While the attitude compensation improved the height measurement by a factor two to three, the beam compensation improved the measurement at least by a factor of three.

8.2 Significant Achievements beyond State-of-the-Art

Vertical aiding using an altimeter The improvement of vertical aiding of an INS/GNSS using surface-ranging sensors was the first problem discussed in this thesis. A combination of the validity assessment method and the slant range compensation was introduced and explained as solution approach. The method assumed a sufficiently good horizontal position estimation, a high precision DSM and a detailed sensor simulation model.
The developed high detail simulation model for surface-ranging sensors features the validity assessment algorithm as well as the slant range compensation approach. The model covers the geometric ranging as well as signal propagation effects including the beam-shape.
The performance demonstration of the validity assessment has shown an improvement between a factor of two and up to a factor of ten of the measurement accuracy. This was achieved by detecting and excluding erroneous measurements. This method can be applied to avoid height measurement errors whenever no continuous measurement is mandatory.
The performance of the slant range compensation algorithm has shown an accuracy improvement of a factor of four. With this method, a continuous measurement frequency with an increase accuracy can be guaranteed. The compensation algorithm has to be chosen dependent on the overflown surface and the altimeter beam-shape. For narrow beam-shapes, the attitude compensation can be used above flat surface and the range compensation above rough surface. Whenever a wide beam-shape altimeter is applied, the beam compensation provides the best compensation results and is recommended for this configuration.
With the ground clearance monitoring method, a measurement monitoring concept without the need of high computational power has been introduced. This method can be applied to smaller unmanned aircraft with the nominal height above ground measurement as prior knowledge. With this information, the current measurement can be validated for a further use.

Improvement of SAN The accuracy improvement of SAN was the second main focus of this thesis. It was demonstrated that the matching metric based algorithms can be improved by a section of the measurement concerning their accuracy and their information content.
The detailed sampling of the surface in combination with the information exploitation algorithm ensure a significant accuracy improvement of the SAN position estimation. By taking the translational drift during the measurement time interval into account, additional benefits concerning the matching matrix shape and accuracy were achieved.

The closed-loop slant range compensation applies the introduced compensation algorithm to the horizontal positioning problem with significant improvements. The extension of the sensor setup by multi-beam measurements improved the accuracy and robustness further. The simulation of the single-beam approach with the introduced method has shown a high accuracy position estimation, whenever the surface is rough enough. The high frequency sampling and the information exploitation method is mandatory to achieve a position accuracy in a comparable scale as GNSS. Depending on the quality of the used INS, it is recommended to apply the translational drift estimation. If a wide-beam altimeter, such as a Radar is used for SAN, the closed-loop slant range compensation brings an additional performance impact. Apart from the beam-shape, the compensation of the platform attitude is mandatory for high dynamic aircraft. The extension of the configuration by a multi-beam setup is recommended whenever the expected information above the mission elevation profile is too low. Thereby, the multi-beam measurement with fixed-beams or the beam-switching method increase the measured information content. In case of the beam-steering approach, the sensor can be steered to maximize the measured information content. This method is recommended for trajectories above a surface with poor features.

Dead-reckoning approach to SAN As solution for the third problem, a DEM independent SAN method, an autarchical dead-reckoning approach to SAN was introduced. This method can stabilize the position drift above an unknown surface. The applied methods are similar to the methods used for VSAN and PPSAN algorithm. The extension of the algorithm to address the novel sensor setup are discussed separately.
If an integration of a DRSAN is intended, the higher cost and integration effort of a range-imaging or range-scanning sensor in comparison to the costs of the used INS have to be evaluated. It is recommended to use a range-imaging sensor due to the snapshot measurement characteristics rather than a range-scanning sensor, not at least due to the easier implementation in the aircraft. Whenever the costs for range-scanning or range-imaging sensors decrease, this method can be an alternative navigation system. Currently the application of a navigation grade INS seems more economical to become independent of GNSS than the integration of two range-scanning or one range-imaging sensors.

8.3 Outlook

Most methods introduced in this thesis rely strongly on the accuracy and currentness of the used DEM model. Performance improvements are expected whenever DEM with a finer resolution and higher accuracy are available. Not only the measurement accuracy, but also the currentness is influencing the performance. Seasonal dependencies of the DEM can be managed with a characterization of the surface regarding the vegetation or forest type. The reflectivity of the surface is another important influence which is not considered due to missing surface information. With a surface database including the surface reflectivity characteristics, the simulation model and thereby the compensation and positioning algorithm performance can be improved. The consideration of the environmental condition in the simulation model can be another information to improve the introduced methods.

Bibliography

[1] European Aviation Safety Agency. *Authority, Organisation and Operations Requirements for Aerodromes*.

[2] Kjetil Bergh Anonsen and Oddvar Hallingstad. Terrain aided underwater navigation using point mass and particle filters.

[3] ASTER GDEM Validation Team. *ASTER Global Digital Elevation Model Version 2 – Summary of Validation Results*, 2011.

[4] C. A. Baird, F. B. Snyder, and M. Beierle. Terrain-aided altitude computations on the AFTI/F-16. In *Position Location and Navigation Symposium., IEEE PLANS*, 1990.

[5] A. Bar-Gill, P. Ben-Ezra, and I. Bar-Itzhack. Improvement of terrain-aided navigation via trajectory optimization. *Control Systems Technology, IEEE Transactions on Control Systems Techology*, 2(4):336–342, Dec 1994.

[6] F. Barthelmes. *Definition of functionals of the Geopotential and their Calculation from Spherical Harmonic Models*. Deutsches GeoForschungszentrum, Helmholtz-Zentrum Potsdam.

[7] Bayerische Vermessungsverwaltung. http://www.vermessung.bayern.de/.

[8] L. Beller. Analyse von Schrägmessungen bei Radar Höhenmessern. Bacherlorarbeit, Lehrstuhl für Flugsystemdynamik, 2013.

[9] Bennett. Enhanced Navigation and Displays from Passice Terrain Referenced Avionics.

[10] Peter J. Bennett. The Use of Digital Map Data for Airborne Operations. 1998.

[11] O. Bergem. *Bathymetric Navigation of autonomous Underwater Vehicles Using a Multibeam Sonar and a Kalman Filter With Relative Measurement Covariance Matrices*. PhD thesis, University of Trondheim, 1993.

[12] N. Bergman. Deterministic and Stochastic Bayesian Methods in Terrain Navigation. 1998.

[13] N. Bergman. *Recursive Bayesian Estimation Navigation and Tracking Applications*. PhD thesis, Department of Electrical Engineering Linköping University, 1999.

[14] N. Bergman, L. Ljung, and F. Gustafsson. Terrain navigation using Bayesian statistics. *IEEE Control Systems*, 1999.

[15] H. E. Bingöl, B. Akin, and O. Koc. Radar altimeter as a navigation aid using hierarchical elevation map clustering. In *Position Location and Navigation Symposium (PLANS), 2012 IEEE/ION*, pages 377–381, April 2012.

[16] R. Braff. Integrated GNSS/Altimeter Landing System. In *Proceedings of the 20th International Technical Meeting of the Satellite Division of The Institute of Navigation (ION GNSS), Fort Worth, TX*, 2007.

[17] B. Braun. *High Performance Kalman filter Tuning for Integrated Navigation Systems*. PhD thesis, TU München, Institute of Flight System Dynamics, 2016.

[18] C. Brenner. Aerial Laser Scanning. Technical report, Institute of Cartography and Geoinformatics, University of Hannover.

[19] I. N. Bronstein. *Taschenbuch der Mathematik*. Verlag Harri Deutsch, 2005.

[20] G. Brooker. *Introduction to Sensors for Ranging and Imaging*. Yes Dee Publishing Pvt Ltd, 2009.

[21] Jack L. Bufton. Laser Altimetry Measurements from Aircraft and Spacecraft. In *Proceedings of the IEEE*, 1989.

[22] Bundesnetzagentur. *Frequenzplan gemäß § 54 TKG über die Aufteilung des Frequenzbereichs von 9 kHz bis 275 GHz auf die Frequenznutzungen sowie über die Festlegungen für diese Frequenznutzungen*. 2015.

[23] J. Campbell, M. Uijt de Haag, and F. van Graas. Terrain Reference Navigation using Airborne LAser SCAnner (ALASCA) - Preliminary Flight Test Results. In *Proceedings of the 60th Annual Meeting of The Institute of Navigation, Dayton, OH*, 2004.

[24] J. Campbell, M. Uijt de Haag, and F. van Graas. Terrain Referenced Precision Approach Guidance. In *Proceedings of the National Technical Meeting of The Institute of Navigation, San Diego, CA*, 2005.

[25] J. Campbell, M. Uijt de Haag, and F. van Graas. Terrain-Referenced Precision Approach Guidance: Proof-of-Concept Flight Test Results. *NAVIGATION, Journal of the Institute of Navigation, Volume 54, Number 1*, 2007.

[26] J. Campbell, M. Uijt de Haag, F. van Graas, and S. Young. Light Detection and Ranging-Based Terrain Navigation - A Concept Exploration. In *Proceedings of the 16th International Technical Meeting of the Satellite Division of The Institute of Navigation (ION GPS/GNSS), Portland, OR*, 2003.

[27] J. L. Campbell. *Application of Airborne Scanner - Aerial Navigation*. PhD thesis, School of Electrical Engineering and Computer Science and the Russ College of Engineering and Technology, 2006.

[28] M. V. Couch. Proven Technology for Low Flying Aircraft. 1998.

[29] M. Cowie, N. Wilkinson, and R. Powlesland. Latest Development of the TERPROM Digital Terrain System (DTS). Atlantic Inertial Systems,Plymouth, England.

[30] J. Dambeck. Lecture Slides "Navigation and Datafusion". Institute of Flight System Dynamics, TU München, 2015.

[31] M. Uijt de Haag and A. Vadlamani. Flight Test Evaluation of Various Terrain Referenced Navigation Techniques for Aircraft Approach Guidance. In *2006 IEEE/ION Position, Location, And Navigation Symposium*, 2006.

[32] M. Uijt de Haag, D. Venable, M. Smearcheck, J. L. Campbell, and M. M. Miller. Flash-LADAR Inertial Navigator Aiding. In *2006 IEEE/ION Position, Location, And Navigation Symposium*, 2006.

[33] M. Uijt de Haag, D. Venable, and A. Soloviev. Implementation of a Flash-LADAR aided inertial navigator. In *2008 IEEE/ION Position, Location and Navigation Symposium*, 2008.

[34] Maarten Uijt de Haag, A. Vadlamani, J. L. Campbell, and J. Dickman. Application of laser range scanner based terrain referenced navigation systems for aircraft guidance. In *Third IEEE International Workshop on Electronic Design, Test and Applications (DELTA'06)*, 2006.

[35] Diamond Aicraft Industries. *Airplane Flight Manual DA 42 NG.*

[36] N. El-Sheimy, C. Valeo, and A. Habib. *Digital terrain modeling.* Artech House, 2005.

[37] J. A. Farrell. *Aided navigation - GPS with high rate sensors.* Electronic engineering. McGraw-Hill, 2008.

[38] J. L. Farrell. *Integrated aircraft navigation.* Academic Press, New York [u.a.], 1976.

[39] Federal Aviation Administration. Installation of Terrain Awarneness and Warning System (TAWS) Approved for Part 23 Airplanes.

[40] Federal Aviation Administration. TSO-C87, Airborne Low-Range Radio Altimeter.

[41] S. Fleischmann. Modellierung eines Flash LADAR Navigationssystems. Semesterarbeit, Lehrstuhl für Flugsystemdynamik, 2012.

[42] J. R. Fountain. Digital terrain systems. In *Airborne Navigation Systems Workshop, IEEE*, 1998.

[43] FreeFlight Systems. *Equipment Installation Manual for FreeFlight Systems RA-4000 and RA-4500 Radar Altimeters.*

[44] S.b Fritz. Modellierung eines Laserscanner. Semesterarbeit, Lehrstuhl für Flugsystemdynamik, 2011.

[45] J. P. Golden. Terrain Contour Matching (TERCOM): A Cruise Missile Guidance Aid. *SPIE Image Processing for Missile Guidance*, 1980.

[46] P. D. Groves. *Principles of GNSS, Inertial, and Multisensor Integrated Navigation Systems.* Artech House, 2nd edition, 2013.

[47] A. J. Henley. Terrain aided navigation: current status, techniques for flat terrain and reference data requirements. In *Position Location and Navigation Symposium (IEEE PLANS)*, 1990.

[48] B. Hofmann-Wellenhof, K. Legat, and M. Wieser. *Navigation*. Springer, Wien [u.a.], 2003.

[49] Intermap. Nextmap product handbook.

[50] International Civil Aviation Organization (ICAO). *Annex 10 to the Convention on Internatinal Civil Aviation*. International Standards and Recommended Pratices, 2006.

[51] David Jensen. PTAN's Potential. 2004.

[52] Jet Propulsion Laboratory. http://www.jpl.nasa.gov/srtm/.

[53] Myron Kayton and Walter R. Fried. *Avionics Navigation Systems*. John Wiley and Sons, Inc., 2nd edition, 1997.

[54] Wang Kedong and Yong Yang. Influence of Application Conditions on Terrain-Aided Navigation. In *Proceedings of the 8th World Congress on Intelligent Control and Automatio*, 2010.

[55] U. Kiencke and H. Jäkel. *Signale und Systeme*. Oldenbourg, 3rd edition, 2005.

[56] Thomas Köhler, Franz Tumbrägel, and Jürgen Beyer. Reliable Autonomous Precise Integrated Navigation RAPIN for Present and Future Air-Vehicles. In *AGARD MSP Symposium on "System Design Consideration for Unmanned Tactical Aircraft (UTA)*, 1997.

[57] Diane E. Di Massa. *Terrain-Relative Navigation for Massa Autonomous Underwater Vehicles*. PhD thesis, Massachusetts Institue of Technology, 1997.

[58] S. Merhav. *Aerospace sensor systems and applications*. Springer, 1996.

[59] J. Metzger. *Optimierung des Akquisitions- und Tracking-Verhaltens zentraler und modularer Terrainnavigationssysteme*. PhD thesis, Universität Karlsruhe (TH), 2006.

[60] J. Metzger, O. Meister, G. F. Trommer, F. Tumbrägel, and B. Taddiken. Covariance Estimation for Terrain Referenced Navigation with a Comparison Technique. In *Proceedings of the 60th Annual Meeting of The Institute of Navigation, Dayton, OH*, 2004.

[61] J. Metzger, J. Wendel, and G. F. Trommer. Comparison of Different Terrain Referenced Navigation Techniques. In *Proceedings of the 58th Annual Meeting of The Institute of Navigation and CIGTF 21st Guidance Test Symposium, Albuquerque, NM*, 2002.

[62] Alberto Moreira, Gerhard Krieger, Irena Hajnsek, Sebastian Riegger, and Eckard Settelmeyer. TanDEM-X: A TerraSAR-X Add-On Satellite for Single-Pass SAR Interferometry. 2004.

[63] National Imagery and Mapping Agency (NIMA). World Geodetic System 1984.

[64] National Imagery and Mapping Agency (NIMA). Performance Specification Digital Terrain elevation Data (DTED), 1996.

[65] A. Nebylov. *Aerospace Sensors*. Momentum Press, 2012.

[66] I. Nygren. *Terrain Navigation for Underwater Vehicles*. PhD thesis, KTH Electrical Engineering, 2005.

[67] S. Paris and J.-P. Le Cadre. Planification for Terrain- Aided Navigation. In *Proceedings of the Fifth International Conference on Information Fusion*, 2002.

[68] M. Perrett and J. Krempasky. Terrain Aiding for Precision Navigation in Heavy GPS Jamming. In *Proceedings of the 14th International Technical Meeting of the Satellite Division of The Institute of Navigation (ION GPS), Salt Lake City, UT*, 2001.

[69] Michael A. G. Peters. Development of a trn/ins/gps integrated navigation system.

[70] John E. Pritchett and Alan J. Pue. Robust Guidance and Navigation for Airborne Vehicles Using GPS Terrain Aiding.

[71] quantum-system GmbH. http://www.quantum-systems.com.

[72] S. Rapp. Simulation und Analyse eines laserbasierten Indoor-Navigationssystems. Bacherlorarbeit, Lehrstuhl für Flugsystemdynamik, 2011.

[73] F. W. Riedel, S. M. Hall, J. D. Barton, J. P. Christ, B. K. Funk, T. D. Milnes, P. E. Neperud, and D. R. Stark. Guidance and Navigation in the Global Engagement Department. *Johns Hopkins APL Technical Digest, Volume 29, Number 2*, 2010.

[74] A. J. Robins. Recent Developments in the "TERPROM" Integrated Navigation System. In *Proceedings of the 44th Annual Meeting of The Institute of Navigation, Annapolis, Maryland*, 1988.

[75] M. Shamiyeh. Analyse der Korrelations-Metrik eines DALS Navigationssystems. Bachelorarbeit, Lehrstuhl für Flugsystemdynamik, 2012.

[76] J. Shan and C. K. Toth. *Topographic Laser Ranging and Scanning*. Taylor & Francis Inc, 2008.

[77] J. Sickle. *Basic GIS coordinates*. CRC Press, 2004.

[78] George N. Siouris. *Missile Guidance & Control Systems*. Springer, 2004.

[79] smart microwave sensors GmbH. http://www.smartmicro.de/.

[80] A. Soloviev. Tight Coupling of GPS, Laser Scanner, and Inertial Measurements for Navigation in Urban Environments. In *Proceedings of IEEE/ION PLANS, Monterey, CA*, 2008.

[81] A. Soloviev, D. Bates, and F. van Graas. Tight Coupling of Laser Scanner and Inertial Measurements for a Fully Autonomous Relative Navigation Solution. *NAVIGATION, Journal of the Institute of Navigation, Volume 54, Number 3*, 2007.

[82] P. Spiegel, B. Braun, J. Dambeck, and F. Holzapfel. Altimeter Slant Range Analysis and Compensation. In *Institute of Navigation, International Technical Meeting (ITM), San Diego (CA)*, 2014.

[83] P. Spiegel, J. Dambeck, and F. Holzapfel. Improvement of Surface Navigation. In *Institute of Navigation, Position Location and Navigation Symposium (PLANS), Savannah (GA)*, 2016.

[84] P. Spiegel, J. Dambeck, and F. Holzapfel. Slant Range Analysis and Inflight Compensation of Radar Altimeter Flight Test Data. *NAVIGATION*, Vol. 63(No. 4):pp. 491–507, Winter 2016.

[85] P. Spiegel, M. Kriegel, J. Dambeck, and F. Holzapfel. Slant Range Analysis and Inflight Compensation of Radar Altimeter Flight Test Data. In *Institute of Navigation, International Technical Meeting (ITM), Dana Point (CA)*, 2015.

[86] F. T. Ulaby. *Handbook of Radar Scattering Statistics for Terrain.* Artech House Remote Sensing Library, 1989.

[87] A. K. Vadlamani. Performance Improvement Methods for Terrain Database Integrity Monitors and Terrain Referenced Navigation. Master's thesis, Ohio University, Computer Science (Engineering), 2004.

[88] A. K. Vadlamani. *Airborne Laser Scanner Aided Inertial for Terrain Referenced Navigation in Unknown Environments.* PhD thesis, Ohio University, Computer Science (Engineering), 2010.

[89] A. K. Vadlamani and M. Uijt de Haag. Aerial Vehicle Navigation Over Unknown Terrain Environments using Flash LADAR and Inertial Measurements. In *Proceedings of the 2007 National Technical Meeting of The Institute of Navigation, San Diego, CA*, 2007.

[90] A. K. Vadlamani and M. Uijt de Haag. Tight Integration of Dual ALS and IMU for Autonomous Aerial Vehicle Navigation. In *Proceedings of the 20th International Technical Meeting of the Satellite Division of The Institute of Navigation (ION GNSS), Fort Worth, TX*, 2007.

[91] A. K. Vadlamani and M. Uijt de Haag. Dual Airborne Laser Scanners Aided Inertial for Improved Autonomous Navigation. *IEEE Transactions on Aerospace and Electronic Systems*, 2008.

[92] A. K. Vadlamani and M. Uijt de Haag. Flight test results of loose integration of dual airborne laser scanners (DALS)/INS. In *2008 IEEE/ION Position, Location and Navigation Symposium*, 2008.

[93] A. K. Vadlamani and M. Uijt de Haag. Synthesis of Airborne Laser Measurements for Navigation Algorithms. *IEEE Sensors Journal*, 2008.

[94] A.K. Vadlamani and M. Uijt de Haag. Use of Laser Range Scanners for Precise Navigation in Unknown Environments. In *Proceedings of the 19th International Technical Meeting of the Satellite Division of The Institute of Navigation (ION GNSS), Fort Worth, TX*, 2006.

[95] D. Vaman. Terrain Referenced Navigation: History, Trends and the Unsued Positential.

[96] G. Vosselman and H.-G. Maas. *Airborne and terrestrial laser scanning*. CRC Press, 2010.

[97] J. Wendel. *Integrierte Navigationssysteme*. Oldenbourg, 2007.

[98] J. Wendel, O. Meister, R. Monikes, and G. F. Trommer. Time-Differenced Carrier Phase Measurements for Tightly Coupled GPS/INS Integration. In *2006 IEEE/ION Position, Location, And Navigation Symposium*, 2006.

[99] W. Wiesbeck. *Lecture Script "Radar System Engineering"*. Institut für Hochfrequenztechnik und Elektronik (IHE), Karlsruher Institut für Technologie.

[100] WorldDEM. www.geo-airbusds.com/worlddem/.

[101] Y. M. Yoo, S. M. Lee, and C. G. Park. New Terrain Roughness Index for Update of Profile Based TRN. In *Proceedings of the ION Pacific PNT Meeting, Honolulu, Hawaii*, 2003.

[102] S. H. Yun, W. Lee, and C. G. Park. Covariance calculation for batch processing terrain referenced navigation. In *IEEE/ION Position, Location and Navigation Symposium - PLANS*, 2014.

Appendix A

Isotropic Radiator

The derivation of the power density of an isotropic radiator is based on the distribution of the transmitted power on the surface of a sphere. A sphere with a radius d has the surface area A_{sphere} given by equation A.1 [19].

$$A_{sphere} = 4\pi d^2 \tag{A.1}$$

The power density at the distance d initiated by the transmitted power P_{tx} is calculated by equation A.2.

$$S_{target} = \frac{P_{tx}}{4\pi d^2} \tag{A.2}$$

With this equation, the basic Radar equation can be derived.

Appendix B

Signal Mixer

Assuming two independent signals $s_1(t)$ and $s_2(t)$ with their frequencies f_1 and f_2 given by equation B.1.

$$\begin{aligned} s_1(t) &= a_1 \cos(2\pi f_1 t) \\ s_2(t) &= a_2 \cos(2\pi f_2 t) \end{aligned} \tag{B.1}$$

The both signals are mixed in a multiplicative frequency mixer illustrated in B.1. The output signal is given by equation B.2.

$$\begin{aligned} s_{out}(t) &= s_1(t) \cdot s_2(t) \\ &= a_1 a_2 \cos(2\pi f_1 t) \cos(2\pi f_2 t) \end{aligned} \tag{B.2}$$

With the addition theorem for trigonometric functions given in B.3 [19], the output signal of the frequency mixer can be calculated to equation B.4. The frequencies of the input and the output signals are illustrated in B.2, the time domain representation is given in figure B.3. A detailed signal processing consideration is given in [55].

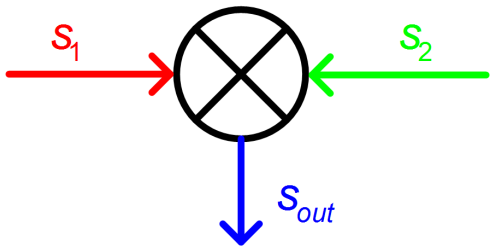

Figure B.1: Frequency mixer block diagram

$$\cos(x)\cos(y) = \frac{1}{2}(\cos(x-y) + \cos(x+y)) \tag{B.3}$$

$$\begin{aligned} s_{out}(t) &= \frac{a_1 a_2}{2}(\cos(2\pi f_1 t - 2\pi f_2 t) + \cos(2\pi f_1 t + 2\pi f_2 t)) \\ &= \frac{a_1 a_2}{2}(\cos(2\pi(f_1 - f_2)t + \cos(2\pi(f_1 + f_2)t))) \end{aligned} \tag{B.4}$$

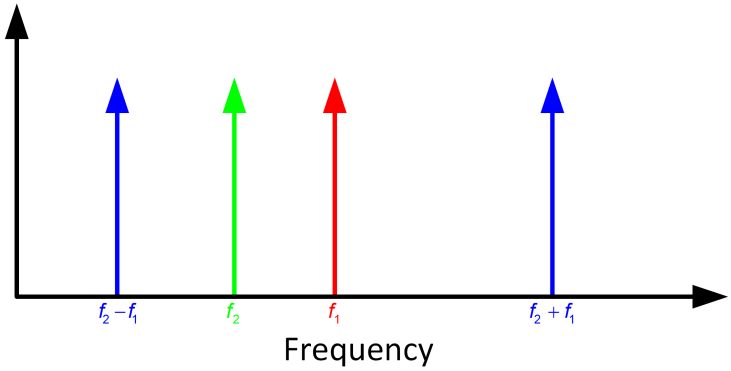

Figure B.2: Mixer frequency domain

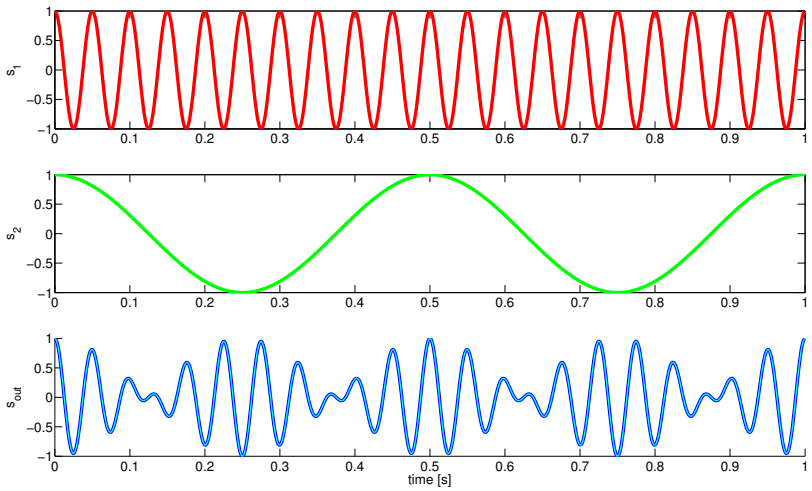

Figure B.3: Mixer Time domain

Appendix C

Slant Range Perturbation

C.1 Footprint Perturbation

The footprint perturbation of a slant range measurement is derived in this section. The basic equation is given in C.1.

$$\mathbf{x}_e\left(M\right) = \mathbf{x}_e\left(P\right) + \mathbf{R}_{en}\mathbf{R}_{nb}\left(\mathbf{R}_{bs}\mathbf{R}_{sm}\mathbf{d}_m - \mathbf{x}_b\left(S\right)\right) \tag{C.1}$$

For the perturbation, the rotational errors are expressed as rotation between a tilted and the corresponding error-free coordinate frames. The rotation matrices are denoted $\mathbf{R}_{n\tilde{n}}$, $\mathbf{R}_{\tilde{s}s}$ and $\mathbf{R}_{\tilde{m}m}$. With the perturbation approach, the equation can be written to C.2.

$$\begin{aligned}\tilde{\mathbf{x}}_e\left(M\right) + \delta\mathbf{x}_e\left(M\right) = \tilde{\mathbf{x}}_e\left(P\right) + \delta\mathbf{x}_e\left(P\right) + \\ \mathbf{R}_{en}\mathbf{R}_{n\tilde{n}}\mathbf{R}_{\tilde{n}b}\left(\mathbf{R}_{b\tilde{s}}\mathbf{R}_{\tilde{s}s}\mathbf{R}_{s\tilde{m}}\mathbf{R}_{\tilde{m}m}\left(\tilde{\mathbf{d}}_m + \delta\mathbf{d}_m\right) - \left(\tilde{\mathbf{x}}_b\left(S\right) + \delta\mathbf{x}_b\left(S\right)\right)\right)\end{aligned} \tag{C.2}$$

The products are following expanded and the footprint error is isolated, the result is given by equation C.3.

$$\begin{aligned}\delta\mathbf{x}_e\left(M\right) =& \tilde{\mathbf{x}}_e\left(P\right) + \delta\mathbf{x}_e\left(P\right) - \tilde{\mathbf{x}}_e\left(M\right) - \mathbf{R}_{en}\mathbf{R}_{n\tilde{n}}\mathbf{R}_{\tilde{n}b}\tilde{\mathbf{x}}_b\left(S\right) - \mathbf{R}_{en}\mathbf{R}_{n\tilde{n}}\mathbf{R}_{\tilde{n}b}\delta\mathbf{x}_b\left(S\right) \\ &+ \mathbf{R}_{en}\mathbf{R}_{n\tilde{n}}\mathbf{R}_{\tilde{n}b}\mathbf{R}_{b\tilde{s}}\mathbf{R}_{\tilde{s}s}\mathbf{R}_{s\tilde{m}}\mathbf{R}_{\tilde{m}m}\tilde{\mathbf{d}}_m + \mathbf{R}_{en}\mathbf{R}_{n\tilde{n}}\mathbf{R}_{\tilde{n}b}\mathbf{R}_{b\tilde{s}}\mathbf{R}_{\tilde{s}s}\mathbf{R}_{s\tilde{m}}\mathbf{R}_{\tilde{m}m}\delta\mathbf{d}_m\end{aligned} \tag{C.3}$$

Rotations by small enough angles can be approximated with the relation in equation C.4.

$$\mathbf{R}\left(\delta\boldsymbol{\psi}\right) \approx \begin{pmatrix} 1 & -\delta\psi & \delta\vartheta \\ \delta\psi & 1 & -\delta\varphi \\ -\delta\vartheta & \delta\varphi & 1 \end{pmatrix} \tag{C.4}$$

Introducing the skew symmetric matrix $\boldsymbol{\Psi}$, the expression can be decomposed to equation C.5.

$$\mathbf{R}\left(\delta\boldsymbol{\psi}\right) \approx \mathbf{I}_3 + \boldsymbol{\Psi} \tag{C.5}$$

The error angles in this use case fulfill the requirement and therefore the approximations given by equation C.6 are valid.

$$\begin{aligned}\mathbf{R}_{n\tilde{n}} &\approx (\mathbf{I}_3 + \boldsymbol{\Psi}_{n\tilde{n}}) \\ \mathbf{R}_{\tilde{s}s} &\approx (\mathbf{I}_3 + \boldsymbol{\Psi}_{\tilde{s}s}) \\ \mathbf{R}_{\tilde{m}m} &\approx (\mathbf{I}_3 + \boldsymbol{\Psi}_{\tilde{m}m})\end{aligned} \tag{C.6}$$

With this approximation, the equation can be written to C.7.

$$\begin{aligned}\delta\mathbf{x}_e(M) \approx& \tilde{\mathbf{x}}_e(P) + \delta\mathbf{x}_e(P) - \tilde{\mathbf{x}}_e(M) \\ &- \mathbf{R}_{en}(\mathbf{I}_3 + \boldsymbol{\Psi}_{n\tilde{n}})\mathbf{R}_{\tilde{n}b}\tilde{\mathbf{x}}_b(S) - \mathbf{R}_{en}(\mathbf{I}_3 + \boldsymbol{\Psi}_{n\tilde{n}})\mathbf{R}_{\tilde{n}b}\delta\mathbf{x}_b(S) \\ &+ \mathbf{R}_{en}(\mathbf{I}_3 + \boldsymbol{\Psi}_{n\tilde{n}})\mathbf{R}_{\tilde{n}b}\mathbf{R}_{b\tilde{s}}(\mathbf{I}_3 + \boldsymbol{\Psi}_{\tilde{s}s})\mathbf{R}_{s\tilde{m}}(\mathbf{I}_3 + \boldsymbol{\Psi}_{\tilde{m}m})\tilde{\mathbf{d}}_m \\ &+ \mathbf{R}_{en}(\mathbf{I}_3 + \boldsymbol{\Psi}_{n\tilde{n}})\mathbf{R}_{\tilde{n}b}\mathbf{R}_{b\tilde{s}}(\mathbf{I}_3 + \boldsymbol{\Psi}_{\tilde{s}s})\mathbf{R}_{s\tilde{m}}(\mathbf{I}_3 + \boldsymbol{\Psi}_{\tilde{m}m})\delta\mathbf{d}_m \\ \approx& \tilde{\mathbf{x}}_e(P) + \delta\mathbf{x}_e(P) - \tilde{\mathbf{x}}_e(M) - \mathbf{R}_{en}\mathbf{I}_3\mathbf{R}_{\tilde{n}b}\tilde{\mathbf{x}}_b(S) \\ &- \mathbf{R}_{en}\mathbf{I}_3\mathbf{R}_{\tilde{n}b}\delta\mathbf{x}_b(S) - \mathbf{R}_{en}\boldsymbol{\Psi}_{n\tilde{n}}\mathbf{R}_{\tilde{n}b}\tilde{\mathbf{x}}_b(S) - \mathbf{R}_{en}\boldsymbol{\Psi}_{n\tilde{n}}\mathbf{R}_{\tilde{n}b}\delta\mathbf{x}_b(S) \\ &+ \mathbf{R}_{en}\mathbf{I}_3\mathbf{R}_{\tilde{n}b}\mathbf{R}_{b\tilde{s}}\mathbf{I}_3\mathbf{R}_{s\tilde{m}}\mathbf{I}_3\tilde{\mathbf{d}}_m + \mathbf{R}_{en}\mathbf{I}_3\mathbf{R}_{\tilde{n}b}\mathbf{R}_{b\tilde{s}}\mathbf{I}_3\mathbf{R}_{s\tilde{m}}\mathbf{I}_3\delta\mathbf{d}_m \\ &+ \mathbf{R}_{en}\boldsymbol{\Psi}_{n\tilde{n}}\mathbf{R}_{\tilde{n}b}\mathbf{R}_{b\tilde{s}}\mathbf{I}_3\mathbf{R}_{s\tilde{m}}\mathbf{I}_3\tilde{\mathbf{d}}_m + \mathbf{R}_{en}\boldsymbol{\Psi}_{n\tilde{n}}\mathbf{R}_{\tilde{n}b}\mathbf{R}_{b\tilde{s}}\mathbf{I}_3\mathbf{R}_{s\tilde{m}}\mathbf{I}_3\delta\mathbf{d}_m \\ &+ \mathbf{R}_{en}\mathbf{I}_3\mathbf{R}_{\tilde{n}b}\mathbf{R}_{b\tilde{s}}\boldsymbol{\Psi}_{\tilde{s}s}\mathbf{R}_{s\tilde{m}}\mathbf{I}_3\tilde{\mathbf{d}}_m + \mathbf{R}_{en}\mathbf{I}_3\mathbf{R}_{\tilde{n}b}\mathbf{R}_{b\tilde{s}}\boldsymbol{\Psi}_{\tilde{s}s}\mathbf{R}_{s\tilde{m}}\mathbf{I}_3\delta\mathbf{d}_m \\ &+ \mathbf{R}_{en}\boldsymbol{\Psi}_{n\tilde{n}}\mathbf{R}_{\tilde{n}b}\mathbf{R}_{b\tilde{s}}\boldsymbol{\Psi}_{\tilde{s}s}\mathbf{R}_{s\tilde{m}}\mathbf{I}_3\tilde{\mathbf{d}}_m + \mathbf{R}_{en}\boldsymbol{\Psi}_{n\tilde{n}}\mathbf{R}_{\tilde{n}b}\mathbf{R}_{b\tilde{s}}\boldsymbol{\Psi}_{\tilde{s}s}\mathbf{R}_{s\tilde{m}}\mathbf{I}_3\delta\mathbf{d}_m \\ &+ \mathbf{R}_{en}\mathbf{I}_3\mathbf{R}_{\tilde{n}b}\mathbf{R}_{b\tilde{s}}\mathbf{I}_3\mathbf{R}_{s\tilde{m}}\boldsymbol{\Psi}_{\tilde{m}m}\tilde{\mathbf{d}}_m + \mathbf{R}_{en}\mathbf{I}_3\mathbf{R}_{\tilde{n}b}\mathbf{R}_{b\tilde{s}}\mathbf{I}_3\mathbf{R}_{s\tilde{m}}\boldsymbol{\Psi}_{\tilde{m}m}\delta\mathbf{d}_m \\ &+ \mathbf{R}_{en}\boldsymbol{\Psi}_{n\tilde{n}}\mathbf{R}_{\tilde{n}b}\mathbf{R}_{b\tilde{s}}\mathbf{I}_3\mathbf{R}_{s\tilde{m}}\boldsymbol{\Psi}_{\tilde{m}m}\tilde{\mathbf{d}}_m + \mathbf{R}_{en}\boldsymbol{\Psi}_{n\tilde{n}}\mathbf{R}_{\tilde{n}b}\mathbf{R}_{b\tilde{s}}\mathbf{I}_3\mathbf{R}_{s\tilde{m}}\boldsymbol{\Psi}_{\tilde{m}m}\delta\mathbf{d}_m \\ &+ \mathbf{R}_{en}\mathbf{I}_3\mathbf{R}_{\tilde{n}b}\mathbf{R}_{b\tilde{s}}\boldsymbol{\Psi}_{\tilde{s}s}\mathbf{R}_{s\tilde{m}}\boldsymbol{\Psi}_{\tilde{m}m}\tilde{\mathbf{d}}_m + \mathbf{R}_{en}\mathbf{I}_3\mathbf{R}_{\tilde{n}b}\mathbf{R}_{b\tilde{s}}\boldsymbol{\Psi}_{\tilde{s}s}\mathbf{R}_{s\tilde{m}}\boldsymbol{\Psi}_{\tilde{m}m}\delta\mathbf{d}_m \\ &+ \mathbf{R}_{en}\boldsymbol{\Psi}_{n\tilde{n}}\mathbf{R}_{\tilde{n}b}\mathbf{R}_{b\tilde{s}}\boldsymbol{\Psi}_{\tilde{s}s}\mathbf{R}_{s\tilde{m}}\boldsymbol{\Psi}_{\tilde{m}m}\tilde{\mathbf{d}}_m + \mathbf{R}_{en}\boldsymbol{\Psi}_{n\tilde{n}}\mathbf{R}_{\tilde{n}b}\mathbf{R}_{b\tilde{s}}\boldsymbol{\Psi}_{\tilde{s}s}\mathbf{R}_{s\tilde{m}}\boldsymbol{\Psi}_{\tilde{m}m}\delta\mathbf{d}_m\end{aligned} \tag{C.7}$$

For linearizing the perturbation, all bilinear error terms are neglected, the result is given by equation C.8.

$$\begin{aligned}\delta\mathbf{x}_e(M) \approx& \delta\mathbf{x}_e(P) - \tilde{\mathbf{x}}_e(M) + \tilde{\mathbf{x}}_e(P) + \mathbf{R}_{en}\mathbf{R}_{\tilde{n}b}\mathbf{R}_{b\tilde{s}}\mathbf{R}_{s\tilde{m}}\tilde{\mathbf{d}}_m - \mathbf{R}_{en}\mathbf{R}_{\tilde{n}b}\tilde{\mathbf{x}}_b(S) \\ &- \mathbf{R}_{en}\mathbf{R}_{\tilde{n}b}\delta\mathbf{x}_b(S) - \mathbf{R}_{en}\boldsymbol{\Psi}_{n\tilde{n}}\mathbf{R}_{\tilde{n}b}\tilde{\mathbf{x}}_b(S) \\ &+ \mathbf{R}_{en}\mathbf{R}_{\tilde{n}b}\mathbf{R}_{b\tilde{s}}\mathbf{R}_{s\tilde{m}}\delta\mathbf{d}_m + \mathbf{R}_{en}\boldsymbol{\Psi}_{n\tilde{n}}\mathbf{R}_{\tilde{n}b}\mathbf{R}_{b\tilde{s}}\mathbf{R}_{s\tilde{m}}\tilde{\mathbf{d}}_m \\ &+ \mathbf{R}_{en}\mathbf{R}_{\tilde{n}b}\mathbf{R}_{b\tilde{s}}\boldsymbol{\Psi}_{\tilde{s}s}\mathbf{R}_{s\tilde{m}}\tilde{\mathbf{d}}_m + \mathbf{R}_{en}\mathbf{R}_{\tilde{n}b}\mathbf{R}_{b\tilde{s}}\mathbf{R}_{s\tilde{m}}\boldsymbol{\Psi}_{\tilde{m}m}\tilde{\mathbf{d}}_m\end{aligned} \tag{C.8}$$

With the relation in equation C.9 the equation can be furthermore reduced, the resulting error equation is given by equation C.10.

$$\tilde{\mathbf{x}}_e(M) = \tilde{\mathbf{x}}_e(P) + \mathbf{R}_{en}\mathbf{R}_{\tilde{n}b}\mathbf{R}_{b\tilde{s}}\mathbf{R}_{s\tilde{m}}\begin{pmatrix}0\\0\\\tilde{d}_m\end{pmatrix} - \mathbf{R}_{en}\mathbf{R}_{\tilde{n}b}\tilde{\mathbf{x}}_b(S) \tag{C.9}$$

$$\begin{aligned}\delta\mathbf{x}_e(M) \approx& \delta\mathbf{x}_e(P) - \mathbf{R}_{en}\mathbf{R}_{\tilde{n}b}\delta\mathbf{x}_b(S) - \mathbf{R}_{en}\boldsymbol{\Psi}_{n\tilde{n}}\mathbf{R}_{\tilde{n}b}\tilde{\mathbf{x}}_b(S) \\ &+ \mathbf{R}_{en}\mathbf{R}_{\tilde{n}b}\mathbf{R}_{b\tilde{s}}\mathbf{R}_{s\tilde{m}}\delta\mathbf{d}_m + \mathbf{R}_{en}\boldsymbol{\Psi}_{n\tilde{n}}\mathbf{R}_{\tilde{n}b}\mathbf{R}_{b\tilde{s}}\mathbf{R}_{s\tilde{m}}\tilde{\mathbf{d}}_m \\ &+ \mathbf{R}_{en}\mathbf{R}_{\tilde{n}b}\mathbf{R}_{b\tilde{s}}\boldsymbol{\Psi}_{\tilde{s}s}\mathbf{R}_{s\tilde{m}}\tilde{\mathbf{d}}_m + \mathbf{R}_{en}\mathbf{R}_{\tilde{n}b}\mathbf{R}_{b\tilde{s}}\mathbf{R}_{s\tilde{m}}\boldsymbol{\Psi}_{\tilde{m}m}\tilde{\mathbf{d}}_m\end{aligned} \tag{C.10}$$

C.2 Slant Range Perturbation

The perturbation of the measurement equation is derived in this section. The basic measurement equation is given in C.11.

$$\mathbf{d}_m = \mathbf{R}_{ms}\mathbf{R}_{sb}\left(\mathbf{R}_{bn}\mathbf{R}_{ne}\left(\mathbf{x}_e\left(M\right) - \mathbf{x}_e\left(P\right)\right) + \mathbf{x}_b\left(S\right)\right) \tag{C.11}$$

The perturbation is similar to the footprint perturbation, the equation is given in C.12.

$$\begin{aligned}&\tilde{\mathbf{d}}_m + \delta\mathbf{d}_m = \mathbf{R}_{m\tilde{m}}\mathbf{R}_{\tilde{m}s}\mathbf{R}_{s\tilde{s}}\mathbf{R}_{\tilde{s}b}\\ &\left(\mathbf{R}_{b\tilde{n}}\mathbf{R}_{\tilde{n}n}\mathbf{R}_{ne}\left(\tilde{\mathbf{x}}_e\left(M\right) + \delta\mathbf{x}_e\left(M\right) - \tilde{\mathbf{x}}_e\left(P\right) - \delta\mathbf{x}_e\left(P\right)\right) + \tilde{\mathbf{x}}_b\left(S\right) + \delta\mathbf{x}_b\left(S\right)\right)\end{aligned} \tag{C.12}$$

With the small angle rotation matrix approximations given by equation C.13 (based on equation C.5), the equation can be expanded to C.16, with the intermediate steps in equation C.14 and equation C.15.

$$\begin{aligned}\mathbf{R}_{\tilde{n}n} &\approx \left(\mathbf{I}_3 + \boldsymbol{\Psi}_{\tilde{n}n}\right)\\ \mathbf{R}_{s\tilde{s}} &\approx \left(\mathbf{I}_3 + \boldsymbol{\Psi}_{s\tilde{s}}\right)\\ \mathbf{R}_{m\tilde{m}} &\approx \left(\mathbf{I}_3 + \boldsymbol{\Psi}_{m\tilde{m}}\right)\end{aligned} \tag{C.13}$$

$$\begin{aligned}\tilde{\mathbf{d}}_m + \delta\mathbf{d}_m \approx &\left(\mathbf{I}_3 + \boldsymbol{\Psi}_{m\tilde{m}}\right)\mathbf{R}_{\tilde{m}s}\left(\mathbf{I}_3 + \boldsymbol{\Psi}_{s\tilde{s}}\right)\mathbf{R}_{\tilde{s}b}\left(\mathbf{R}_{b\tilde{n}}\left(\mathbf{I}_3 + \boldsymbol{\Psi}_{\tilde{n}n}\right)\mathbf{R}_{ne}\right.\\ &\left.\left(\tilde{\mathbf{x}}_e\left(M\right) + \delta\mathbf{x}_e\left(M\right) - \tilde{\mathbf{x}}_e\left(P\right) - \delta\mathbf{x}_e\left(P\right)\right) + \tilde{\mathbf{x}}_b\left(S\right) + \delta\mathbf{x}_b\left(S\right)\right)\end{aligned} \tag{C.14}$$

$$\begin{aligned}\tilde{\mathbf{d}}_m + \delta\mathbf{d}_m \approx &\left(\mathbf{I}_3\mathbf{R}_{\tilde{m}s}\mathbf{I}_3\mathbf{R}_{\tilde{s}b} + \boldsymbol{\Psi}_{m\tilde{m}}\mathbf{R}_{\tilde{m}s}\mathbf{I}_3\mathbf{R}_{\tilde{s}b} + \mathbf{I}_3\mathbf{R}_{\tilde{m}s}\boldsymbol{\Psi}_{s\tilde{s}}\mathbf{R}_{\tilde{s}b} + \boldsymbol{\Psi}_{m\tilde{m}}\mathbf{R}_{\tilde{m}s}\boldsymbol{\Psi}_{s\tilde{s}}\mathbf{R}_{\tilde{s}b}\right)\\ &\left(\mathbf{R}_{b\tilde{n}}\mathbf{I}_3\mathbf{R}_{ne}\tilde{\mathbf{x}}_e\left(M\right) + \mathbf{R}_{b\tilde{n}}\mathbf{I}_3\mathbf{R}_{ne}\delta\mathbf{x}_e\left(M\right) - \mathbf{R}_{b\tilde{n}}\mathbf{I}_3\mathbf{R}_{ne}\tilde{\mathbf{x}}_e\left(P\right)\right.\\ &- \mathbf{R}_{b\tilde{n}}\mathbf{I}_3\mathbf{R}_{ne}\delta\mathbf{x}_e\left(P\right) + \mathbf{R}_{b\tilde{n}}\boldsymbol{\Psi}_{\tilde{n}n}\mathbf{R}_{ne}\tilde{\mathbf{x}}_e\left(M\right) + \mathbf{R}_{b\tilde{n}}\boldsymbol{\Psi}_{\tilde{n}n}\mathbf{R}_{ne}\delta\mathbf{x}_e\left(M\right)\\ &\left.- \mathbf{R}_{b\tilde{n}}\boldsymbol{\Psi}_{\tilde{n}n}\mathbf{R}_{ne}\tilde{\mathbf{x}}_e\left(P\right) - \mathbf{R}_{b\tilde{n}}\boldsymbol{\Psi}_{\tilde{n}n}\mathbf{R}_{ne}\delta\mathbf{x}_e\left(P\right) + \tilde{\mathbf{x}}_b\left(S\right) + \delta\mathbf{x}_b\left(S\right)\right)\end{aligned} \tag{C.15}$$

$$
\begin{aligned}
\tilde{\mathbf{d}}_m + \delta\mathbf{d}_m \approx & \mathbf{R}_{\tilde{m}s}\mathbf{R}_{\tilde{s}b}\mathbf{R}_{b\tilde{n}}\mathbf{R}_{ne}\tilde{\mathbf{x}}_e\left(M\right) + \mathbf{R}_{\tilde{m}s}\mathbf{R}_{\tilde{s}b}\mathbf{R}_{b\tilde{n}}\mathbf{R}_{ne}\delta\mathbf{x}_e\left(M\right) \\
& - \mathbf{R}_{\tilde{m}s}\mathbf{R}_{\tilde{s}b}\mathbf{R}_{b\tilde{n}}\mathbf{R}_{ne}\tilde{\mathbf{x}}_e\left(P\right) - \mathbf{R}_{\tilde{m}s}\mathbf{R}_{\tilde{s}b}\mathbf{R}_{b\tilde{n}}\mathbf{R}_{ne}\delta\mathbf{x}_e\left(P\right) \\
& + \mathbf{R}_{\tilde{m}s}\mathbf{R}_{\tilde{s}b}\mathbf{R}_{b\tilde{n}}\boldsymbol{\Psi}_{\tilde{n}n}\mathbf{R}_{ne}\tilde{\mathbf{x}}_e\left(M\right) + \mathbf{R}_{\tilde{m}s}\mathbf{R}_{\tilde{s}b}\mathbf{R}_{b\tilde{n}}\boldsymbol{\Psi}_{\tilde{n}n}\mathbf{R}_{ne}\delta\mathbf{x}_e\left(M\right) \\
& - \mathbf{R}_{\tilde{m}s}\mathbf{R}_{\tilde{s}b}\mathbf{R}_{b\tilde{n}}\boldsymbol{\Psi}_{\tilde{n}n}\mathbf{R}_{ne}\tilde{\mathbf{x}}_e\left(P\right) - \mathbf{R}_{\tilde{m}s}\mathbf{R}_{\tilde{s}b}\mathbf{R}_{b\tilde{n}}\boldsymbol{\Psi}_{\tilde{n}n}\mathbf{R}_{ne}\delta\mathbf{x}_e\left(P\right) \\
& + \mathbf{R}_{\tilde{m}s}\mathbf{R}_{\tilde{s}b}\tilde{\mathbf{x}}_b\left(S\right) + \mathbf{R}_{\tilde{m}s}\mathbf{R}_{\tilde{s}b}\delta\mathbf{x}_b\left(S\right) + \boldsymbol{\Psi}_{m\tilde{m}}\mathbf{R}_{\tilde{m}s}\mathbf{R}_{\tilde{s}b}\mathbf{R}_{b\tilde{n}}\mathbf{R}_{ne}\tilde{\mathbf{x}}_e\left(M\right) \\
& + \boldsymbol{\Psi}_{m\tilde{m}}\mathbf{R}_{\tilde{m}s}\mathbf{R}_{\tilde{s}b}\mathbf{R}_{b\tilde{n}}\mathbf{R}_{ne}\delta\mathbf{x}_e\left(M\right) - \boldsymbol{\Psi}_{m\tilde{m}}\mathbf{R}_{\tilde{m}s}\mathbf{R}_{\tilde{s}b}\mathbf{R}_{b\tilde{n}}\mathbf{R}_{ne}\tilde{\mathbf{x}}_e\left(P\right) \\
& - \boldsymbol{\Psi}_{m\tilde{m}}\mathbf{R}_{\tilde{m}s}\mathbf{R}_{\tilde{s}b}\mathbf{R}_{b\tilde{n}}\mathbf{R}_{ne}\delta\mathbf{x}_e\left(P\right) + \boldsymbol{\Psi}_{m\tilde{m}}\mathbf{R}_{\tilde{m}s}\mathbf{R}_{\tilde{s}b}\mathbf{R}_{b\tilde{n}}\boldsymbol{\Psi}_{\tilde{n}n}\mathbf{R}_{ne}\tilde{\mathbf{x}}_e\left(M\right) \\
& + \boldsymbol{\Psi}_{m\tilde{m}}\mathbf{R}_{\tilde{m}s}\mathbf{R}_{\tilde{s}b}\mathbf{R}_{b\tilde{n}}\boldsymbol{\Psi}_{\tilde{n}n}\mathbf{R}_{ne}\delta\mathbf{x}_e\left(M\right) - \boldsymbol{\Psi}_{m\tilde{m}}\mathbf{R}_{\tilde{m}s}\mathbf{R}_{\tilde{s}b}\mathbf{R}_{b\tilde{n}}\boldsymbol{\Psi}_{\tilde{n}n}\mathbf{R}_{ne}\tilde{\mathbf{x}}_e\left(P\right) \\
& - \boldsymbol{\Psi}_{m\tilde{m}}\mathbf{R}_{\tilde{m}s}\mathbf{R}_{\tilde{s}b}\mathbf{R}_{b\tilde{n}}\boldsymbol{\Psi}_{\tilde{n}n}\mathbf{R}_{ne}\delta\mathbf{x}_e\left(P\right) + \boldsymbol{\Psi}_{m\tilde{m}}\mathbf{R}_{\tilde{m}s}\mathbf{R}_{\tilde{s}b}\tilde{\mathbf{x}}_b\left(S\right) \\
& + \boldsymbol{\Psi}_{m\tilde{m}}\mathbf{R}_{\tilde{m}s}\mathbf{R}_{\tilde{s}b}\delta\mathbf{x}_b\left(S\right) + \mathbf{R}_{\tilde{m}s}\boldsymbol{\Psi}_{s\tilde{s}}\mathbf{R}_{\tilde{s}b}\mathbf{R}_{b\tilde{n}}\mathbf{R}_{ne}\tilde{\mathbf{x}}_e\left(M\right) \\
& + \mathbf{R}_{\tilde{m}s}\boldsymbol{\Psi}_{s\tilde{s}}\mathbf{R}_{\tilde{s}b}\mathbf{R}_{b\tilde{n}}\mathbf{R}_{ne}\delta\mathbf{x}_e\left(M\right) - \mathbf{R}_{\tilde{m}s}\boldsymbol{\Psi}_{s\tilde{s}}\mathbf{R}_{\tilde{s}b}\mathbf{R}_{b\tilde{n}}\mathbf{R}_{ne}\tilde{\mathbf{x}}_e\left(P\right) \\
& - \mathbf{R}_{\tilde{m}s}\boldsymbol{\Psi}_{s\tilde{s}}\mathbf{R}_{\tilde{s}b}\mathbf{R}_{b\tilde{n}}\mathbf{R}_{ne}\delta\mathbf{x}_e\left(P\right) + \mathbf{R}_{\tilde{m}s}\boldsymbol{\Psi}_{s\tilde{s}}\mathbf{R}_{\tilde{s}b}\mathbf{R}_{b\tilde{n}}\boldsymbol{\Psi}_{\tilde{n}n}\mathbf{R}_{ne}\tilde{\mathbf{x}}_e\left(M\right) \\
& + \mathbf{R}_{\tilde{m}s}\boldsymbol{\Psi}_{s\tilde{s}}\mathbf{R}_{\tilde{s}b}\mathbf{R}_{b\tilde{n}}\boldsymbol{\Psi}_{\tilde{n}n}\mathbf{R}_{ne}\delta\mathbf{x}_e\left(M\right) - \mathbf{R}_{\tilde{m}s}\boldsymbol{\Psi}_{s\tilde{s}}\mathbf{R}_{\tilde{s}b}\mathbf{R}_{b\tilde{n}}\boldsymbol{\Psi}_{\tilde{n}n}\mathbf{R}_{ne}\tilde{\mathbf{x}}_e\left(P\right) \\
& - \mathbf{R}_{\tilde{m}s}\boldsymbol{\Psi}_{s\tilde{s}}\mathbf{R}_{\tilde{s}b}\mathbf{R}_{b\tilde{n}}\boldsymbol{\Psi}_{\tilde{n}n}\mathbf{R}_{ne}\delta\mathbf{x}_e\left(P\right) + \mathbf{R}_{\tilde{m}s}\boldsymbol{\Psi}_{s\tilde{s}}\mathbf{R}_{\tilde{s}b}\tilde{\mathbf{x}}_b\left(S\right) \\
& + \mathbf{R}_{\tilde{m}s}\boldsymbol{\Psi}_{s\tilde{s}}\mathbf{R}_{\tilde{s}b}\delta\mathbf{x}_b\left(S\right) + \boldsymbol{\Psi}_{m\tilde{m}}\mathbf{R}_{\tilde{m}s}\boldsymbol{\Psi}_{s\tilde{s}}\mathbf{R}_{\tilde{s}b}\mathbf{R}_{b\tilde{n}}\mathbf{R}_{ne}\tilde{\mathbf{x}}_e\left(M\right) \\
& + \boldsymbol{\Psi}_{m\tilde{m}}\mathbf{R}_{\tilde{m}s}\boldsymbol{\Psi}_{s\tilde{s}}\mathbf{R}_{\tilde{s}b}\mathbf{R}_{b\tilde{n}}\mathbf{R}_{ne}\delta\mathbf{x}_e\left(M\right) - \boldsymbol{\Psi}_{m\tilde{m}}\mathbf{R}_{\tilde{m}s}\boldsymbol{\Psi}_{s\tilde{s}}\mathbf{R}_{\tilde{s}b}\mathbf{R}_{b\tilde{n}}\mathbf{R}_{ne}\tilde{\mathbf{x}}_e\left(P\right) \\
& - \boldsymbol{\Psi}_{m\tilde{m}}\mathbf{R}_{\tilde{m}s}\boldsymbol{\Psi}_{s\tilde{s}}\mathbf{R}_{\tilde{s}b}\mathbf{R}_{b\tilde{n}}\mathbf{R}_{ne}\delta\mathbf{x}_e\left(P\right) + \boldsymbol{\Psi}_{m\tilde{m}}\mathbf{R}_{\tilde{m}s}\boldsymbol{\Psi}_{s\tilde{s}}\mathbf{R}_{\tilde{s}b}\mathbf{R}_{b\tilde{n}}\boldsymbol{\Psi}_{\tilde{n}n}\mathbf{R}_{ne}\tilde{\mathbf{x}}_e\left(M\right) \\
& + \boldsymbol{\Psi}_{m\tilde{m}}\mathbf{R}_{\tilde{m}s}\boldsymbol{\Psi}_{s\tilde{s}}\mathbf{R}_{\tilde{s}b}\mathbf{R}_{b\tilde{n}}\boldsymbol{\Psi}_{\tilde{n}n}\mathbf{R}_{ne}\delta\mathbf{x}_e\left(M\right) \\
& - \boldsymbol{\Psi}_{m\tilde{m}}\mathbf{R}_{\tilde{m}s}\boldsymbol{\Psi}_{s\tilde{s}}\mathbf{R}_{\tilde{s}b}\mathbf{R}_{b\tilde{n}}\boldsymbol{\Psi}_{\tilde{n}n}\mathbf{R}_{ne}\tilde{\mathbf{x}}_e\left(P\right) \\
& - \boldsymbol{\Psi}_{m\tilde{m}}\mathbf{R}_{\tilde{m}s}\boldsymbol{\Psi}_{s\tilde{s}}\mathbf{R}_{\tilde{s}b}\mathbf{R}_{b\tilde{n}}\boldsymbol{\Psi}_{\tilde{n}n}\mathbf{R}_{ne}\delta\mathbf{x}_e\left(P\right) \\
& + \boldsymbol{\Psi}_{m\tilde{m}}\mathbf{R}_{\tilde{m}s}\boldsymbol{\Psi}_{s\tilde{s}}\mathbf{R}_{\tilde{s}b}\tilde{\mathbf{x}}_b\left(S\right) + \delta\mathbf{x}_b\left(S\right)
\end{aligned}
\tag{C.16}
$$

The bilinear terms are furthermore neglected, the result is given in C.17.

$$
\begin{aligned}
\tilde{\mathbf{d}}_m + \delta\mathbf{d}_m \approx & \mathbf{R}_{\tilde{m}s}\mathbf{R}_{\tilde{s}b}\mathbf{R}_{b\tilde{n}}\mathbf{R}_{ne}\tilde{\mathbf{x}}_e\left(M\right) + \mathbf{R}_{\tilde{m}s}\mathbf{R}_{\tilde{s}b}\mathbf{R}_{b\tilde{n}}\mathbf{R}_{ne}\delta\mathbf{x}_e\left(M\right) \\
& - \mathbf{R}_{\tilde{m}s}\mathbf{R}_{\tilde{s}b}\mathbf{R}_{b\tilde{n}}\mathbf{R}_{ne}\tilde{\mathbf{x}}_e\left(P\right) - \mathbf{R}_{\tilde{m}s}\mathbf{R}_{\tilde{s}b}\mathbf{R}_{b\tilde{n}}\mathbf{R}_{ne}\delta\mathbf{x}_e\left(P\right) \\
& + \mathbf{R}_{\tilde{m}s}\mathbf{R}_{\tilde{s}b}\mathbf{R}_{b\tilde{n}}\boldsymbol{\Psi}_{\tilde{n}n}\mathbf{R}_{ne}\tilde{\mathbf{x}}_e\left(M\right) - \mathbf{R}_{\tilde{m}s}\mathbf{R}_{\tilde{s}b}\mathbf{R}_{b\tilde{n}}\boldsymbol{\Psi}_{\tilde{n}n}\mathbf{R}_{ne}\tilde{\mathbf{x}}_e\left(P\right) \\
& + \mathbf{R}_{\tilde{m}s}\mathbf{R}_{\tilde{s}b}\tilde{\mathbf{x}}_b\left(S\right) + \mathbf{R}_{\tilde{m}s}\mathbf{R}_{\tilde{s}b}\delta\mathbf{x}_b\left(S\right) + \boldsymbol{\Psi}_{m\tilde{m}}\mathbf{R}_{\tilde{m}s}\mathbf{R}_{\tilde{s}b}\mathbf{R}_{b\tilde{n}}\mathbf{R}_{ne}\tilde{\mathbf{x}}_e\left(M\right) \\
& - \boldsymbol{\Psi}_{m\tilde{m}}\mathbf{R}_{\tilde{m}s}\mathbf{R}_{\tilde{s}b}\mathbf{R}_{b\tilde{n}}\mathbf{R}_{ne}\tilde{\mathbf{x}}_e\left(P\right) + \boldsymbol{\Psi}_{m\tilde{m}}\mathbf{R}_{\tilde{m}s}\mathbf{R}_{\tilde{s}b}\tilde{\mathbf{x}}_b\left(S\right) \\
& + \mathbf{R}_{\tilde{m}s}\boldsymbol{\Psi}_{s\tilde{s}}\mathbf{R}_{\tilde{s}b}\mathbf{R}_{b\tilde{n}}\mathbf{R}_{ne}\tilde{\mathbf{x}}_e\left(M\right) - \mathbf{R}_{\tilde{m}s}\boldsymbol{\Psi}_{s\tilde{s}}\mathbf{R}_{\tilde{s}b}\mathbf{R}_{b\tilde{n}}\mathbf{R}_{ne}\tilde{\mathbf{x}}_e\left(P\right) \\
& + \mathbf{R}_{\tilde{m}s}\boldsymbol{\Psi}_{s\tilde{s}}\mathbf{R}_{\tilde{s}b}\tilde{\mathbf{x}}_b\left(S\right)
\end{aligned}
\tag{C.17}
$$

With the relation in equation C.18, the result can be reduced to C.19

$$
\tilde{\mathbf{d}}_m \approx \mathbf{R}_{\tilde{m}s}\mathbf{R}_{\tilde{s}b}\left(\mathbf{R}_{b\tilde{n}}\mathbf{R}_{ne}\tilde{\mathbf{x}}_e\left(M\right) - \mathbf{R}_{b\tilde{n}}\mathbf{R}_{ne}\tilde{\mathbf{x}}_e\left(P\right) + \tilde{\mathbf{x}}_b\left(S\right)\right) \tag{C.18}
$$

$$
\begin{aligned}
\delta\mathbf{d}_m \approx & \mathbf{R}_{\tilde{m}s}\mathbf{R}_{\tilde{s}b}\mathbf{R}_{b\tilde{n}}\mathbf{R}_{ne}\delta\mathbf{x}_e\left(M\right) - \mathbf{R}_{\tilde{m}s}\mathbf{R}_{\tilde{s}b}\mathbf{R}_{b\tilde{n}}\mathbf{R}_{ne}\delta\mathbf{x}_e\left(P\right) \\
& + \mathbf{R}_{\tilde{m}s}\mathbf{R}_{\tilde{s}b}\mathbf{R}_{b\tilde{n}}\boldsymbol{\Psi}_{\tilde{n}n}\mathbf{R}_{ne}\tilde{\mathbf{x}}_e\left(M\right) - \mathbf{R}_{\tilde{m}s}\mathbf{R}_{\tilde{s}b}\mathbf{R}_{b\tilde{n}}\boldsymbol{\Psi}_{\tilde{n}n}\mathbf{R}_{ne}\tilde{\mathbf{x}}_e\left(P\right) \\
& + \mathbf{R}_{\tilde{m}s}\mathbf{R}_{\tilde{s}b}\delta\mathbf{x}_b\left(S\right) + \boldsymbol{\Psi}_{m\tilde{m}}\mathbf{R}_{\tilde{m}s}\mathbf{R}_{\tilde{s}b}\mathbf{R}_{b\tilde{n}}\mathbf{R}_{ne}\tilde{\mathbf{x}}_e\left(M\right) \\
& - \boldsymbol{\Psi}_{m\tilde{m}}\mathbf{R}_{\tilde{m}s}\mathbf{R}_{\tilde{s}b}\mathbf{R}_{b\tilde{n}}\mathbf{R}_{ne}\tilde{\mathbf{x}}_e\left(P\right) + \boldsymbol{\Psi}_{m\tilde{m}}\mathbf{R}_{\tilde{m}s}\mathbf{R}_{\tilde{s}b}\tilde{\mathbf{x}}_b\left(S\right) \\
& + \mathbf{R}_{\tilde{m}s}\boldsymbol{\Psi}_{s\tilde{s}}\mathbf{R}_{\tilde{s}b}\mathbf{R}_{b\tilde{n}}\mathbf{R}_{ne}\tilde{\mathbf{x}}_e\left(M\right) - \mathbf{R}_{\tilde{m}s}\boldsymbol{\Psi}_{s\tilde{s}}\mathbf{R}_{\tilde{s}b}\mathbf{R}_{b\tilde{n}}\mathbf{R}_{ne}\tilde{\mathbf{x}}_e\left(P\right) \\
& + \mathbf{R}_{\tilde{m}s}\boldsymbol{\Psi}_{s\tilde{s}}\mathbf{R}_{\tilde{s}b}\tilde{\mathbf{x}}_b\left(S\right)
\end{aligned}
\tag{C.19}
$$